Advancing Extended Source Analysis in VHE Gamma-Rays: From Background Estimation to Pulsar Environment Studies

Fortschritte in der Analyse ausgedehnter Quellen in VHE-Gammastrahlen: Von der Hintergrundabschätzung zu Studien von Pulsarumgebungen

Vorgelegt von
Tina Wach
aus Erlangen

Der Naturwissenschaftlichen Fakultät
der Friedrich-Alexander-Universität Erlangen-Nürnberg
zur Erlangung des Doktorgrades Dr. rer. nat.

Abstract

γ-ray sources associated with pulsars make up a significant fraction of the identified Galactic TeV source population. Recent studies have uncovered a new subtype of this source class, degree scale γ-ray emission formed around middle-aged pulsars, the pulsar halo. This source class has the potential to provide valuable insights not only into the evolution of pulsars but also into the propagation of cosmic rays in the interstellar medium. However at this point, only a few such sources have been detected, complicating the separation of the properties of the population from the properties of individual sources.

The detection of such largely extended sources in the TeV energy range has mainly been facilitated by wide-field survey instruments, while Imaging Atmospheric Cherenkov Telescopes are better suited for providing a detailed description of the morphology of sub-degree scale γ-ray sources. To this point, however, the only facility which can survey the southern TeV sky, is the High Energy Stereoscopic System (H.E.S.S.), an IACT array located in Namibia. This work aims to improve the detection capability of IACT arrays for largely extended sources by developing a novel background estimation approach, which, in contrast to classical background estimation techniques, does not rely on a source-free region in the observation.

This background estimation technique is used in an analysis of the region around PSR B1055-52. The middle-aged pulsar, previously grouped with Geminga and PSR B0656+14 as the 'Three Musketeers' due to their similar properties, has long been suspected to host a TeV halo. Through the application of two different advanced background estimation methods, this work is able to significantly detect degree scale emission in the region, with properties indicating that this marks the first detection of a pulsar halo in the southern hemisphere. From this, a diffusion model is employed to derive the diffusion properties of the cosmic ray leptons in the region around the pulsar. This study confirms the unexpected finding of sub-ISM diffusion in other pulsar halos, suggesting that the sphere of influence of the pulsar, either trough self-generated turbulence or magnetic field effects, may extend further than previously thought.

Zusammenfassung

Ein erheblicher Teil der identifizierten galaktischen γ-Strahlenquellen im TeV Energiebereich wird mit Pulsaren assoziiert.Jüngste Studien haben einen neuen Untertyp dieser Quellenklasse entdeckt, γ-Strahlungsemissionen auf der skala von Grad die sich um mittelalte Pulsare bilden – sogenannte Pulsarhalos. Mithilfe dieser Quellenklasse können wertvolle Erkenntnisse, nicht nur über die Entwicklung von Pulsaren, sondern auch über die Ausbreitung der kosmischen Strahlung im interstellaren Medium, gewonnen werden. Bisher wurden jedoch nur wenige dieser Quellen nachgewiesen, was es erschwert, die Eigenschaften der gesamten Population von denen einzelner Quellen zu unterscheiden. Der Nachweis solcher ausgedehnten Quellen im TeV-Energiebereich wurde bisher hauptsächlich durch Instrumente für Weitfeldbeobachtungen erreicht, während Imaging Atmospheric Cherenkov Teleskope (IACT) besser geeignet sind, die Morphologie von Gammastrahlenquellen unterhalb der Gradskala detailliert zu beschreiben. Bislang ist jedoch nur das High Energy Stereoscopic System (H.E.S.S.), ein IACT-Array in Namibia, in der Lage, den südlichen TeV-Himmel zu untersuchen. Diese Arbeit zielt darauf ab, die Nachweisfähigkeit von IACT-Arrays für großräumig ausgedehnte Quellen zu verbessern, indem eine neuartige Hintergrundschätzungsmethode entwickelt wird, die im Gegensatz zu klassischen Techniken keine quellenfreie Region in der Beobachtung voraussetzt.

Diese Technik zur Abschätzung des Hintergrunds wird in einer Analyse der Region um PSR B1055-52 verwendet. Der mittelalte Pulsar, der aufgrund seiner ähnlichen Eigenschaften mit Geminga und PSR B0656+14 als einer der "Drei Musketiere" bezeichnet wird, wurde lange als Kandidat für einen TeV-Halo gehandelt. Durch die Anwendung zweier verschiedener fortschrittlicher Hintergrundschätzungsmethoden gelingt es in dieser Arbeit, eine signifikante Emission in der Region zu entdecken, deren Eigenschaften darauf hindeuten, dass dies der erste Nachweis eines Pulsarhalos in der südlichen Hemisphäre ist. Aus den Eigenschaften der γ-Strahlenemission werden dann mit Hilfe eines Diffusionsmodells die Diffusionseigenschaften der hochenergetischen Leptonen in der Region um den Pulsar abgeleitet. Diese Studie bestätigt die unerwartete Beobachtung einer sub-ISM-Diffusion in anderen Pulsarhalos und legt nahe, dass die Einflusssphäre des Pulsars – entweder durch selbstinduzierte Turbulenzen oder magnetische Feldeffekte – weiter reichen könnte als bisher angenommen.

Contents

1 Cosmic Rays

In 1909, the German physicist Theodor Wulf developed a device capable of measuring ionization, an early form of the electroscope (Wulf, 1910). His experiments, as well as contemporaneous experiments conducted by Domenico Pacini (Pacini, 1912), unveiled the presence of constant ionizing radiation, which at first was attributed to radioactive material on Earth. Experiments conducted by Victor Hess in 1912 confirmed that the rate of this ionizing radiation decreases with increasing altitude up to $\sim 1\,\mathrm{km}$, supporting the theory of radioactive material on Earth being responsible for this ionization. For higher altitudes, however, his experiments revealed that after reaching $\sim 1\,\mathrm{km}$, the rate of the ionizing radiation increases again towards higher altitudes (Hess, 1912). This discovery led Hess to propose the existence of cosmic rays, ionizing particles coming from beyond the Earth's atmosphere.

After this discovery many experiments have been conducted to understand the composition of these particles and their interactions with the atmosphere. In the late 20th century the detection techniques had improved, and it was established that these particles, the cosmic rays, originate from astrophysical environments. Therefore, cosmic rays were recognized as important astrophysical messengers, bridging the gap between astrophysics and particle physics (see Kampert (2001) and references therein).

The cosmic ray population consists of a variety of hadrons and leptons with different masses. Their energy spectrum is shown in Figure 1.1. The discussion of its distinct features across different energy ranges given here follows Longair (2011).

At low energies (below $\sim 1 \cdot 10^9\,\mathrm{eV}$), the spectrum shows a pronounced cutoff due to ionization losses as well as shielding by the solar wind. This effect also introduces seasonal fluctuations due to solar modulation.

The earth's magnetic field also plays a crucial role at these low energies. To describe the deflection of cosmic rays by a magnetic field, the rigidity R is used. It is defined as:

$$R = \frac{pc_0}{Ze}\,, \tag{1}$$

with p the momentum of the particle, c_0 the vacuum speed of light, Z the atomic number and e the elementary charge. Particles with the same rigidity experience the same deflection in a magnetic field, independent of their mass or charge. This makes rigidity an important parameter for the acceleration, propagation, and detection of cosmic rays.

The Earth's magnetic field imposes a cutoff rigidity, below which cosmic rays are deflected and cannot reach Earth. This cutoff rigidity depends on the rigidity of the cosmic rays, the magnetic field at the location, and the incident trajectory. The cutoff rigidity for a cosmic ray arriving vertically at the geomagnetic equator is estimated to $R \approx 15\,\mathrm{GV}$ (Bütikofer, 2018). The cutoff rigidity, combined with instrumental effects, is one of the limiting factors for the low end of the cosmic ray spectrum measured at earth.

Above $10 \cdot 10^9\,\mathrm{eV}$, where these effects no longer play a crucial role, the cosmic ray spectrum can be approximated by a power-law of the form:

$$\frac{\mathrm{d}N}{\mathrm{d}E} \propto E^{-\alpha} \tag{2}$$

with α the spectral index varying for different energies.

Up to particle energies of $3 \cdot 10^{15}$ eV, cosmic rays are believed to be accelerated predominantly by sources within our galaxy and remain confined by the Galactic magnetic field. In this energy range, the cosmic-ray population is predominantly composed of protons. The spectrum of cosmic rays in this energy range can be characterized by a spectral index of $\alpha \approx 2.7$ (Becker Tjus and Merten, 2020). Towards higher energies, the magnetic confinement is less efficient, causing the spectrum to soften to $\alpha \approx 3.0$. This break in the spectrum is referred to as the spectral knee. An alternative explanation for the occurrence of this break is that it denotes the maximum energy up to which galactic sources can accelerate protons (Alves Batista et al., 2019a).

Beyond the spectral knee, the cosmic-ray spectrum becomes increasingly dominated by heavier nuclei, each reaching their respective maximum energies. This scenario suggests the presence of multiple spectral breaks associated with different cosmic-ray species and is in accordance with the existence of a rigidity dependent cutoff, where the maximum energy $E_{\max}(Z)$ up to which various elements can be accelerated is defined as $E_{\max}(Z) = Z \cdot E_{\max}(Z = 1)$ (Peters, 1961). This postulation is supported by the detection of the second knee at $\sim 10 \cdot 10^{16}$ eV, corresponding to a sharp decrease in the abundance of heavy elements (Apel et al., 2011).

At even higher energies of $7 \cdot 10^{18}$ eV, the spectrum hardens again and can be described by a spectral index of $\alpha \approx 2.3$ (Becker Tjus and Merten, 2020). This second feature is often referred to as the ankle and interpreted as the rise of an extragalactic component to the cosmic ray flux. This is supported by the composition, which at these energies is again dominated by protons. Another feature recently identified by the Pierre Auger Observatory (The Pierre Auger Collaboration, 2015) is the instep at $\sim 1.4 \cdot 10^{19}$ eV, most likely corresponding to a change in the particle composition of the flux again, this is however still highly debated at the time of writing (Aab et al., 2020). The all-particle cosmic ray spectrum ultimately cuts off at around $5 \cdot 10^{19}$ eV. This can be explained by a combination of the maximum acceleration energy of the heaviest nuclei being reached and the Greisen-Zatsepin-Kuzmin (GZK) cutoff. The latter describes the energy loss of the particles due to interactions with the cosmic microwave background (CMB) photons (Greisen, 1966; Zatsepin and Kuz'min, 1966). The GZK cutoff determines that protons with an energy of $> 10^{20}$ eV can only originate from sources with a distance of less than 130 Mpc or a redshift of $z = 0.034$ (Scully and Stecker, 2002).

1.1 Cosmic-ray Acceleration

The detection of cosmic rays at energies up to $5 \cdot 10^{19}$ eV raises the question of how these particles achieve such extreme energies. Currently, there are two different mechanisms under discussion, bottom-up or top-down acceleration. The top-down acceleration describes the decay of extremely high-energy particles or particle production due to topological defects. These mechanisms are, however, still highly debated and not regarded as the main effect for the production of cosmic rays at $E > 1$ PeV, and will, therefore not be discussed in detail. A recent review of the mechanisms is given in de Vega and Sanchez (2003). In the bottom-up scenario, a low-energy cosmic ray is accelerated in astrophysical environments, for which powerful acceleration mechanisms are necessary. The following is a brief overview of possible acceleration mechanisms, based on the discussions given in Bell (2013) and Caprioli (2023).

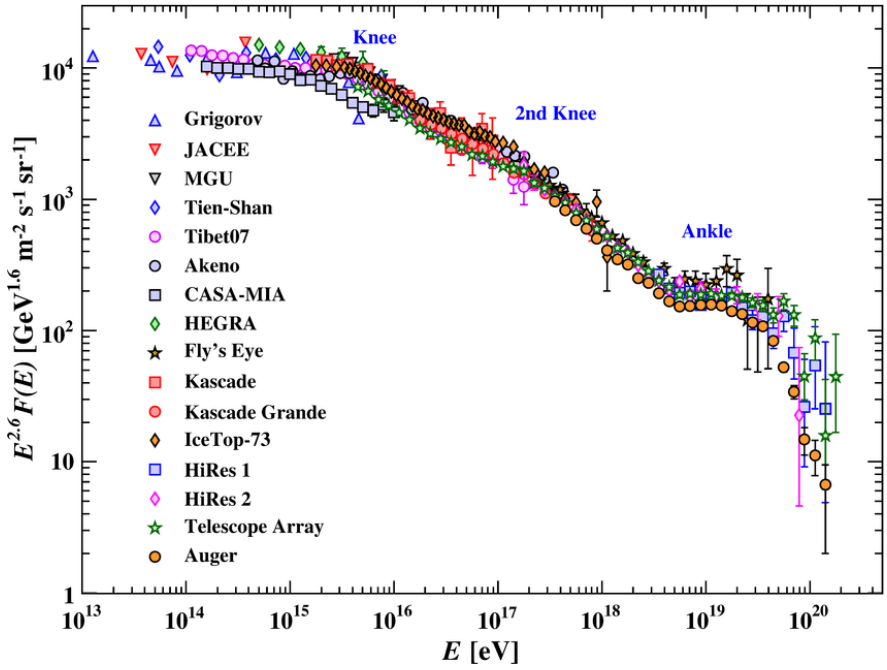

Figure 1.1: The all particle cosmic ray spectrum as observed by different instruments. The different spectral features are highlighted. Figure taken from Tanabashi et al. (2018).

1.1.1 Second Order Fermi-Acceleration

The first particle acceleration mechanism discussed is the second-order Fermi acceleration, which was proposed by Enrico Fermi in Fermi (1954). He theorized the acceleration of particles as an elastic reflection of the cosmic ray on moving magnetic field structures such as clouds. Two possible scenarios can occur in this interaction. A 'head-on' collision happens when the particle is moving towards a turbulent magnetic structure. In this case the particle gains energy in the interaction. A 'tail-on' collision means the particle is moving away from the magnetic turbulence but is overtaken by it. In this case, the relative velocity of the collision is low, which results in a low energy gain or even energy loss, depending on the movement of the turbulence relative to the particle.

While the chances of a particle undergoing a 'head-on' or 'tail-on' collision are approximately isotropically distributed in the rest frame of the magnetic turbulence, the relative motion of the particle changes this symmetry. Particles are more likely to encounter the turbulence head-on because their flux relative to the turbulence is boosted by a factor of u/c, with u the average speed of the magnetic turbulence and c the speed of light in the medium. While this relative motion results in a preference for 'head-on' collisions, the net energy gain still depends on the square of the relative velocities, and its sign is, therefore, randomly distributed.

The average fractional energy exchange per collision is of order u/c, but because of the random nature of the scatterings, an average over many scatterings leads to the cancellation of first-order terms, with only second-order terms remaining. This leads to

a mean energy gain per interaction given by:

$$\frac{\Delta E}{E} = \left(\frac{u}{c}\right)^2 . \tag{3}$$

This effect is therefore only efficient enough to explain the acceleration of cosmic rays to the observed energies in extreme scenarios, such as the jets of active galactic nuclei (Winchen and Buitink, 2018; Meli, 2012).

1.1.2 First Order Fermi-Acceleration

A more effective acceleration mechanism was also proposed by Fermi. The first-order Fermi acceleration, or diffusive shock acceleration, involves the interaction of particles with shock fronts (Fermi, 1949). Shock fronts form when a flow of material (e.g., gas or plasma) is accelerated to speeds exceeding the speed of sound in the medium. The shock compresses the medium, which leads to the creation of two distinct regions: a region of undisturbed material ahead of the shock (upstream region) and a region of compressed and heated material behind the shock (downstream region). The compression ratio r, which is the factor by which the density of the medium increases due to the shock, depends on the properties of the medium:

$$r = \frac{\rho_2}{\rho_1} = \frac{\gamma + 1}{\gamma - 1} , \tag{4}$$

with $\rho_{1/2}$ the upstream/downstream densities and γ the adiabatic index. Assuming a strong shock in a non-relatvistic monoatomic gas ($\gamma = 5/3$), the compression rate is usually assumed to be $r \sim 4$, with other factors such as the magnetic field further modifying this relation (Caprioli and Haggerty, 2019).

The crossing of cosmic rays through these up- and downstream regions can cause low-frequency oscillations in the plasma, so-called Alfvén waves (Alfvén, 1942). These instabilities propagate along the magnetic field lines with wavelengths comparable to the Larmor radius, [1] r_L:

$$r_L = \frac{\gamma m c^2}{ZeBc_0} , \tag{5}$$

with γ being the Lorentz factor, m the particle mass, Ze the particle charge, c_0 the speed of light in vacuum, B the magnetic field strength. If the wavelength of the Alfvén waves is equal to the Larmor radius, strong interactions between the cosmic rays and the magnetic fluctuations scatter the particles and create a diffusive random walk pattern of cosmic rays along the field lines and repeated interactions between the particles and the shock front (Kulsrud and Pearce, 1969; Skilling, 1975a; Skilling, 1975b; Skilling, 1975c). When a particle crosses the shock front from the upstream into the downstream side, the diffusive random walk can lead to it either remaining in the downstream region, exciting the acceleration process and contributing to the overall cosmic ray spectrum, or crossing the shock front again into the upstream region while gaining more energy. In the rest frame of the particle, the upstream or downstream side of the shock front approach the particle with a speed of $u_{1/2} = 3u/4$, where $u_{1/2}$ is the upstream/downstream velocity,

[1] The radius of a circular motion of a charged particle in a uniform magnetic field

due to the compression ratio for strong shocks. This results in a net energy gain of the particle for a full crossing of:

$$\frac{\Delta E}{E} \propto \frac{u}{c} \,. \tag{6}$$

From this, the energy of the particle after n crossings can be computed as:

$$E_n = E_0 \left(1 + \frac{\Delta E}{E}\right)^n \,, \tag{7}$$

with E_0 the injection energy of the particle, while the number of particles present in the shock front N can be computed as:

$$N = N_0 (1 - P_{\text{esc}})^n \,, \tag{8}$$

with P_{esc} the particle escape probability and N_0 the number of particles initially present in the shock. Equation (7) and Equation (8) can be combined to yield a description of the particle spectrum. This requires the assumption that the cosmic ray distribution is isotropic and that the shock velocity is much smaller than the velocity of the cosmic ray. Additionally required is the inability of cosmic rays to escape far upstream and downstream. With these requirements, the particle spectrum is described as:

$$\frac{\mathrm{d}N}{\mathrm{d}E} \propto \left(\frac{E}{E_0}\right)^{-\alpha} \,, \tag{9}$$

with $\alpha \approx 2$. A more detailed explanation is given in Bell (2013).

The maximum energy cosmic rays can achieve through diffusive shock acceleration depends on the rigidity of the particle. The Larmor radius defined in Equation (5) can also be expressed in terms of rigidity R as $r_L = Rc_0/B$. This means that particles with low rigidity will have a small Larmor and will leave the acceleration site before gaining large energies. Particles with high energies will be confined for a longer time and cross the shock more often. This leads to the preferential acceleration of heavier particles, explaining why the iron knee is located at higher energies than the proton knee. Additional processes influencing the maximum energy of an acceleration site are the magnetic field strength, the size of the acceleration region, the shock velocity, and the lifetime of the acceleration site (Perri et al., 2022). The first-order Fermi acceleration is believed to be one of the main acceleration mechanisms responsible for the acceleration of particles to the highest energies.

1.2 Acceleration Sites

However, even considering first-order Fermi acceleration, a single shock crossing is not enough to explain the observed cosmic ray energies. A cosmic ray needs to be accelerated repeatedly, which can be most efficiently achieved if the particle is confined to the acceleration site, as once the particle has escaped the acceleration region it is generally assumed that it is unable to further gain energy. From this, it can be inferred that the maximum energy ϵ_{max} is reached when the Larmor radius of the particle equals the extension of the accelerator:

$$\epsilon_{\text{max}} = Zec_0 B R_{\text{acc}} \,, \tag{10}$$

where Ze is the electric charge of the accelerated particle, B the magnetic field of the environment and R_{acc} the extension of the acceleration region (Hillas, 1984). This simple equation assumes the idealized condition of a perfectly confined particle moving with a speed close to the speed of light and should, therefore, only be seen as a first-order approximation. For sub-relativistic particles, the factor β (with $\beta = u/c$) is used as a correction for the slow motion (Matthews and Taylor, 2021). When the energy gain is mostly due to diffusive shock acceleration, the equation is modified by multiplying it with the shock velocity u/c, and for non-idealised systems an acceleration efficiency η (with $\eta < 1$) is included (Alves Batista et al., 2019b).

This requirement for the maximum energy is usually referred to as the Hillas criterion. Not taking into account further effects, such as limitations due to energy loss, potential acceleration sites are plotted as a function of their extension and magnetic field in Figure 1.2. Also shown as lines in the Figure are the minimally necessary magnetic field and extension to accelerate protons up to energies beyond the respective features of the cosmic ray spectrum. While objects like supernova remnants, pulsars, and pulsar wind nebulae (PWNe) are capable of accelerating cosmic rays up to $10^{15}\,\mathrm{eV}$, they cannot be responsible for cosmic rays detected at the highest end of the cosmic ray spectrum. Only extragalactic objects like active galactic nuclei (AGN) or gamma-ray bursts (GRBs) are theoretically capable of accelerating particles up to the energies observed at the highest end of the cosmic ray spectrum. A thorough review of the acceleration of particles above $\sim 10^{17}\,\mathrm{eV}$ can be found in (Blasi, 2014).

1.3 Transport Mechanisms

Aside from the acceleration of cosmic rays to very high energies, it is also important to understand the properties of the propagation of the cosmic rays in the interstellar medium (ISM). For this purpose, the population of cosmic rays can be split into primary particles and secondary particles. The primary particles are directly produced and accelerated in astrophysical sources. The secondary cosmic rays are caused by interactions of primary cosmic rays with the ambient medium, nuclear fragmentation, or radioactive decay of the primaries. The ratio between primary and secondary cosmic rays can then be used to test different propagation models (Strong and Moskalenko, 2000; de la Torre Luque, 2022). The currently favoured model for galactic cosmic ray propagation is a diffusion model, following a hypothesis about the behaviour of turbulent fluid presented in Kolmogorov (1991). Applied to cosmic ray propagation, this theory postulates that turbulent magnetic fields in space cause cosmic rays to diffuse randomly. The cosmic rays are scattered by irregularities in the magnetic field, and this scattering results in diffusion. The diffusion coefficient depends on the energy of the cosmic rays and the properties of the turbulence. A thorough review of the current state of research in this field can be found in Amato and Casanova (2021). Since this work focuses on signal from astrophysical sources within the galaxy, the propagation of cosmic rays from extragalactic sources is not addressed here. A comprehensive overview of the topic can, however, be found in Kuempel (2014)

1.4 Gamma-ray production

Studies of the cosmic ray spectrum and composition are very valuable to understanding the production and diffusion mechanisms of highly relativistic particles in the galaxy and

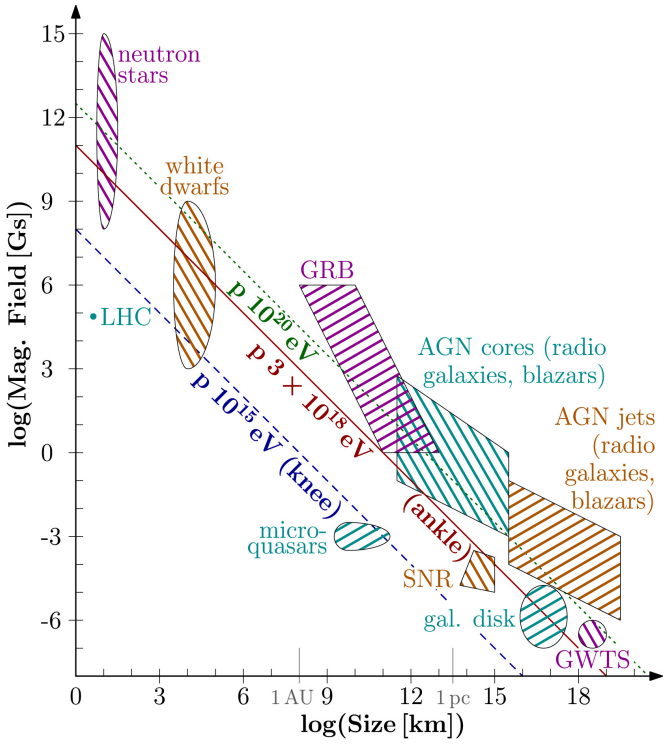

Figure 1.2: Hillas diagram depicting the relation between magnetic field strength and source extension for various astrophysical sources. The diagonal lines depict the boundary above which a source is able to accelerate protons up to the respective energies of the spectral knee, ankle and the cutoff of the cosmic ray spectrum at 10^{20} eV. Figure taken from Becker Tjus and Merten (2020)

beyond. The cosmic ray particles themselves can however not be used to gain insights into individual sources due to their deflection in the interstellar or intergalactic magnetic fields. To overcome this hurdle and trace the particle acceleration sites directly, Cocconi (1960) proposed the usage of detectors sensitive to highly energetic photons produced through interactions of the accelerated cosmic rays with the ambient photon fields of the ISM. Since these γ-rays have no electric charge, they propagate undisturbed by magnetic fields and can be traced back to their origin. While some interactions between cosmic rays and particle populations of the ISM take place after the cosmic rays have propagated away from the source, forming a diffuse γ-ray background, the probability of these interactions is highly enhanced in the vicinity of cosmic ray accelerators through an increased matter density in those regions. Therefore, the mechanisms under which these γ-rays are produced are highly dependent on not only the density but also the type of incident CR. The following discussion of the different possible interaction mechanisms is in accordance with Aharonian (2004).

1.4.1 Bremsstrahlung and Pair-Production

Bremsstrahlung is electromagnetic radiation produced by a charged particle, typically an electron, which is decelerated due to the influence of another charged particle, such as a hydrogen nucleus. This energy change of the initial charged particle results in the emission of photons. The photons produced in the interaction can either escape, or if enough energy has been transferred to the photon, it can interact with another electron or nucleus in the material and produce an electron-positron pair. This particle pair can again lose energy through bremsstrahlung, creating a particle cascade. An important parameter for the development of such cascades is the amount of matter a particle can traverse before it has lost $1/e$ of its energy. This parameter is referred to as the radiation length, X_0, and can be expressed as:

$$X_0 = \frac{7}{9} \cdot (n\,\sigma_0)^{-1} \tag{11}$$

with n the number density of the gas and σ_0 the cross section of bremsstrahlung or pair-production. A highly relativistic lepton is able to produce high energy γ-rays in this manner until it has reached its critical energy ($E_{\mathrm{crit}} = 350\,\mathrm{MeV}$ for hydrogen gas (Aharonian, 2004)), after which ionization losses dominate.

Using the expression for the radiation length defined in Equation (11), the average energy loss rate can be described as:

$$\left(\frac{\mathrm{d}E_e}{\mathrm{d}t}\right)_{\mathrm{br}} = \left(\frac{c\,m_p\,n}{X_0}\right)\epsilon_e \tag{12}$$

with the corresponding electron lifetime t_{br}:

$$t_{\mathrm{br}} = -\frac{E_e}{\mathrm{d}E_e/\mathrm{d}t} \approx 4 \cdot 10^7 \cdot \left(\frac{n}{1\,\mathrm{cm}^{-3}}\right)^{-1}\ \mathrm{yr}\ . \tag{13}$$

1.4.2 Electron-Positron Annihilation

The electron-positron annihilation process mainly involves the interaction of relativistic positrons with thermal electrons of the ambient medium through $e^+e^- \rightarrow 2\gamma$.

The estimated annihilation lifetime for relativistic positrons is:

$$t_{\mathrm{ann}} = \frac{8}{3\sigma_T^2 cn}\frac{\varepsilon_+}{\ln(2\varepsilon_+)-1} \approx 4\times 10^6 \frac{\varepsilon_+}{\ln(2\varepsilon_+)-1}\left(\frac{n}{1\ \mathrm{cm}^{-3}}\right)^{-1}\ \mathrm{yr}\,, \tag{14}$$

where ε_+ is the positron energy. When comparing this annihilation time to the bremsstrahlung cooling time in Equation (13), one finds that for positrons with $E_+ = \epsilon_+ \cdot m_e c_0^2 > 16\,\mathrm{MeV}$, the annihilation time is shorter than the bremsstrahlung cooling time. This implies that annihilation dominates over bremsstrahlung for positrons with energies of less than 16 MeV. A more thorough discussion of this process can be found in Section 3.1.2 in Aharonian (2004).

1.4.3 Synchrotron Radiation

γ-rays produced by relativistic charged particles moving in a magnetic field are referred to as synchrotron radiation. While the charged particle moves through the magnetic field, it experiences a Lorentz force perpendicular to the field lines of the ambient magnetic field. This induces a circular motion around the field line. The average energy loss rate of an electron through this acceleration can be described by:

$$-\left(\frac{\mathrm{d}E}{\mathrm{d}t}\right) = \frac{2}{3}\frac{e^2}{m_e^2 c^3}\gamma^2(e\beta B_\perp)^2 = \frac{4}{3}\sigma_T c_0 \beta^2 \gamma^2 U_B \tag{15}$$

with $U_B = B^2/8\pi$ the energy density of the magnetic field, $\beta = u/c$ the particle speed, γ the Lorentz factor and $\sigma_T \approx 6.65\cdot 10^{-25}\,\mathrm{cm}^2$ the Thomson cross-section. The proportionality $\mathrm{d}E/\mathrm{d}t \propto \gamma^2/m_e^2$ follows from Equation (15). Using $\gamma^2 \propto 1/m^2$, the energy loss depends on the mass of the particle as $\mathrm{d}E/\mathrm{d}t \propto \gamma^2/m_e^2 \propto 1/m_e^4$. This results in the energy loss for protons being $(m_e/m_p)^4 \approx 10^{-13}$ times slower.

The energy loss can be translated into the synchrotron cooling time t_{syn}:

$$t_{\mathrm{syn}} = \frac{E}{-\mathrm{d}E/\mathrm{d}t} \propto \frac{1}{EB^2}\,. \tag{16}$$

Using this equation and the dependence of the energy loss on the mass, Aharonian (2004) shows that the time needed for radiation of a synchrotron γ-ray to be emitted by a proton is $(m_e/m_p)^{5/2} \approx 10^8$ times longer than the cooling time of a lepton.

This effect is even more pronounced for cosmic ray particles with higher mass, therefore making the detection of synchrotron emission a clear indicator that the parent cosmic ray population contains electrons.

The energy of the emitted synchrotron photons can be related to the energy of the parent lepton via (Funk, 2015):

$$E_{\mathrm{syn}} = 0.2\frac{B}{10\mu\mathrm{G}}\left(\frac{E_e}{1\,\mathrm{TeV}}\right)^2\ \mathrm{eV}\,. \tag{17}$$

Assuming a parent population of TeV electrons, this results in a peak in the spectrum at around 0.2 eV. The spectral shape of the γ-ray emission produced due to synchrotron emission can be seen in Figure 1.3. Besides the maximum, this spectrum also shows a pronounced cutoff at $\sim$ GeV energies. This cutoff is a result of different effects. The inverse proportionality between the synchrotron cooling time and the lepton energy

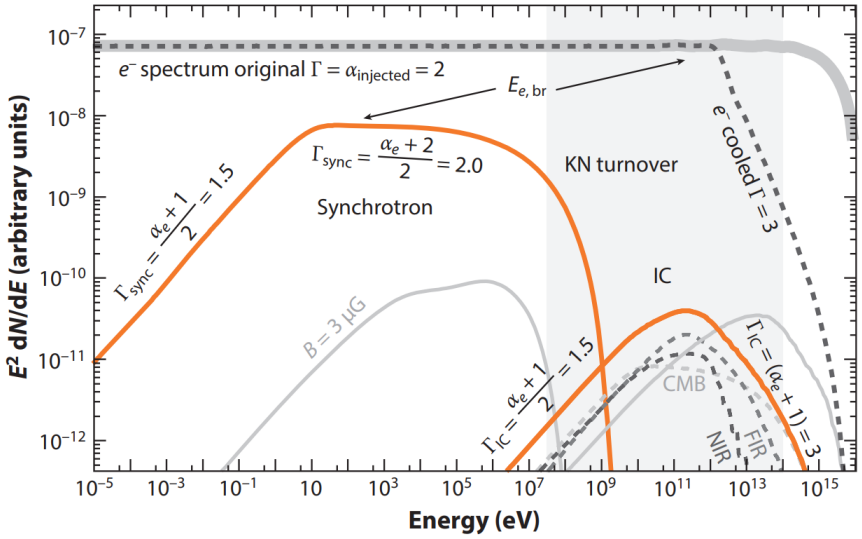

Figure 1.3: Example spectral energy distribution of high energy cosmic ray electrons, as well as the γ-rays spectrum resulting from synchrotron radiation and Inverse Compton scattering. Figure taken from Funk (2015)

shown in Equation (16), leads to a spectral break due to the domination of radiative losses at higher energies. At even higher energies, the Klein-Nishina (KN) regime, the energy of the emitted photon approaches a significant fraction of the electron energy, resulting in a softening of the spectrum. This break occurs at energies where the cooling time scales approach the age of the source (Funk, 2015).

1.4.4 Inverse Compton Scattering

Compton scattering describes a highly energetic photon scattering off a low energetic charged particle and losing energy in the process. Inverse Compton (IC) scattering describes the opposite, the low energetic photon gains energy through the collision with a relativistic charged particle. The latter is the relevant process in the astrophysical context, describing the upscattering of photons, mostly originating from stellar radiation fields and dust in the ISM, to very-high energy (VHE) γ-rays by interacting with accelerated cosmic rays, mainly electrons and positrons.

Following the calculation outlined in Section 13.2.2 in Vink (2020), the relation between the initial photon energy and the energy after the collision can be calculated as:

$$\frac{\nu'}{\nu} = \frac{1 - \beta\cos(\Theta)}{1 - \beta\cos(\Theta - \alpha) + \frac{h\nu}{\gamma m_e c^2}(1 - \cos(\alpha))} \tag{18}$$

with Θ the angle between the photon and electron before the collision. Using Equation (18), the process can be divided into two regimes. For non-relativistic electrons, the photon energy in the rest frame of the electron is smaller than the electron mass $h\nu \ll \gamma m_e c^2$. In this case, $\nu' \approx \nu$, and the electron loses energy continuously over many interactions. This energy range is called the Thomson regime. For relativistic electrons with $h\nu > \gamma m_e c^2$, the electron loses a significant portion of its energy in every interaction. This is referred to as the Klein-Nishina regime.

The overall IC scattering cross section σ_{IC} can be approximated with:

$$\sigma_{\mathrm{IC}} = \frac{3\sigma_T}{8\kappa_0}\left[\left(1-\frac{2}{\kappa_0}-\frac{2}{\kappa_0^2}\right)\ln\left(1+2\kappa_0\right)+\frac{1}{2}+\frac{4}{\kappa_0}-\frac{1}{2(1+2\kappa_0)^2}\right] \tag{19}$$

with $\kappa_0 = \omega_0\epsilon_e$ the product of the energies of the interacting photon ω_0 and electron ϵ_e (Aharonian, 2004). In the Thomson regime this simplifies to $\sigma_{\mathrm{IC}} \approx \sigma_{\mathrm{T}}(1-2\kappa_0)$ while it decreases with κ_0 in the Klein-Nishina regime to $\sigma_{\mathrm{IC}} \approx (3/8)\sigma_{\mathrm{T}}\kappa_0^{-1}\ln(4\kappa_0)$.

In addition to the different interaction cross sections, the energy loss rate shows a different dependence on the electron energy:

$$\left(\frac{\mathrm{d}E}{\mathrm{d}T}\right)_{\mathrm{T}} = \frac{4}{3}\sigma_{\mathrm{T}}c\omega_0 n_{\mathrm{ph}}\epsilon_e^2 \tag{20}$$

$$\left(\frac{\mathrm{d}E}{\mathrm{d}T}\right)_{\mathrm{KN}} = \frac{3}{8}\frac{\sigma_{\mathrm{T}}cn_{\mathrm{ph}}}{\omega_0}\cdot\left(\ln\left(4\kappa_0\right)-11/6\right) \tag{21}$$

with n_{ph} the photon number density. The energy loss rate in the Klein-Nishina regime is therefore almost energy independent, while the energy loss in the Thomson regime depends on ϵ_e^2. This implies that in the Thomson regime, the electron spectrum hardens with increasing energy, while it softens in the Klein-Nishina regime. IC scattering is possible with all charged particles, however, the interaction of ISM photons with cosmic ray protons is suppressed by a factor of $(m_e/m_p)^4$.

For lepton energies in the Thomson regime, efficient upscattering takes place, and the spectrum of the resulting γ-ray emission steadily increases. Beyond the transition into the Klein-Nishina energy regime, the leptons lose a large fraction of their energy per interaction, reducing the number of upscattered photons. This interplay leads to a peak in the γ-ray spectrum, which can be seen in Figure 1.3. Assuming a population of electrons that all have the same energy, the γ-ray spectrum resulting from IC scattering of these highly energetic cosmic-ray leptons on target photons can be described by a black-body spectrum that peak at (Funk, 2015):

$$E_{\mathrm{IC}} = 5\cdot 10^9 \frac{E_\gamma}{10^{-3}\,\mathrm{eV}}\left(\frac{E_e}{1\,\mathrm{TeV}}\right)^2\,\mathrm{eV}\,, \tag{22}$$

where E_γ is the photon field.

1.4.5 Pion Decay

While previously discussed radiation mechanisms involve mainly leptons, the pion decay channel is a radiation mechanism exclusive to hadronic cosmic rays. The hadronic cosmic rays collide with atomic nuclei present in the local medium, resulting in the formation of hadrons consisting of two quarks, so-called mesons. These particles only have a short lifetime and decay into lower-mass mesons, muons, neutrinos, electrons and positrons, as well as photons. While this radiation mechanism is often referred to as pion decay, since pions (π^0, $\pi^\pm$) are the most abundantly produced mesons, a contribution from other mesons, especially kaons and hyperons, is not excluded.

Once a proton exceeds the energy $E_{\mathrm{thr}} = 2m_\pi c^2(1+m_\pi/4m_p) \approx 280\,\mathrm{MeV}$, pions can be produced in collisions with the ambient medium. The neutral pions then decays

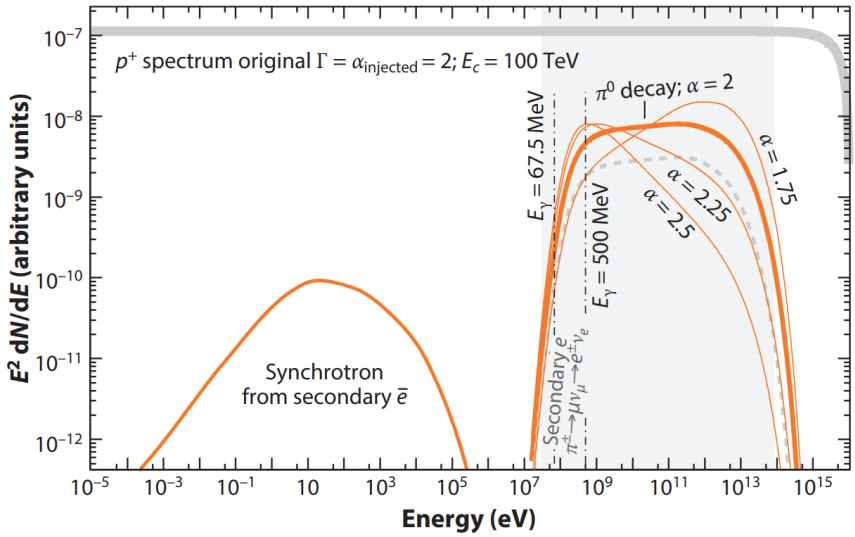

Figure 1.4: Spectral energy distribution of high energy cosmic ray protons, as well as the γ-rays spectrum resulting from collisions of these protons with the ambient medium. Figure taken from Funk (2015)

after a mean lifetime of $t_{\pi^0} = 8.4 \cdot 10^{-17}$ s (Navas et al., 2020) to $\pi^0 \to \gamma\gamma$. The charged pions decay after $t_{\pi^\pm} = 2.6 \cdot 10^{-8}$ s (Navas et al., 2020) as:

$$\begin{aligned} \pi^\pm &\to \mu^\pm + \nu_\mu \\ \mu^\pm &\to e^\pm + \nu_e + \nu_\mu \end{aligned} \tag{23}$$

Through this channel, γ-rays are produced directly by the meson decay, as well as by synchrotron cooling of the resulting electrons/positrons. The direct decay of neutral pions results in a distinct feature in the γ-ray spectrum at the threshold energy of $E_\gamma = 67.5\,\text{MeV}$ (half of the rest mass of the neutral pion), the so-called pion bump and is therefore characteristic only for hadronic γ-rays (for more information see (Stecker, 1971)). As shown in Aharonian (2004) (Section 3.1.3.1), the cooling time for this process is almost energy-independent above $\approx 1\,\text{GeV}$, implying that the γ-ray spectrum can be used to gain direct information about the acceleration spectrum of the parent proton population. Figure 1.4 shows an example γ-ray spectrum resulting from the pion decay.

1.4.6 Summary

While Bremsstrahlung may well be relevant for the production of γ-rays in e.g. solar flares or the production of VHE γ-rays in environments with a high gas density, due to the relation of the energy loss rate (Equation (12)) to the number density of the gas, the energy losses from synchrotron and IC scattering generally dominate over the losses by bremsstrahlung and pair production for relativistic electrons.

A thorough comparison between the energy losses of cosmic rays from synchrotron and IC scattering is given in Aharonian et al. (1997). Assuming the photons of both radiation mechanisms arise from the same parent electron population, the photon

energies are related as:

$$\frac{E_{\mathrm{syn}}}{1\,\mathrm{keV}} \approxeq 0.07 \frac{E_{\mathrm{IC}}}{1\,\mathrm{TeV}} \frac{B_{\mathrm{IC}}}{10^{-5}\,\mathrm{G}}\,. \tag{24}$$

With the flux ratio depending only on the magnetic field:

$$F_{\mathrm{IC}} \approx 0.1 F_{\mathrm{syn}} \left(\frac{10^{-5}\,\mathrm{G}}{B}\right)^2\,, \tag{25}$$

indicating a domination of the IC Flux for magnetic fields below $3.2\,\mu$G.

While all possible production mechanisms have been well studied in Laboratory settings, the identification of the underlying physical process in the various astrophysical accelerators is not a straight forward process, and very often the same γ-ray spectrum can be reproduced using different radiation mechanisms or more than one radiation mechanism can be present in the same source.

As discussed above, the identification of a pion-bump in the spectrum is a clear indicator of the acceleration of hadronic cosmic rays at a shock front, for example, in an SNR. However, the production of positrons and electrons from the decay of charged particles at the same acceleration site means that a contribution from synchrotron or IC scattering is likely to also be observed. Similarly, as discussed later in Chapter 4, an acceleration of hadronic cosmic rays is possible in environments where predominantly the acceleration of leptons is expected (e.g. Pulsar Wind Nebulae).

1.5 Overview of known γ-ray Sources

The above-mentioned fundamental radiative mechanisms responsible for γ-ray emission provide the foundation for understanding astrophysical objects that act as gamma-ray sources and their observed γ-ray spectra. Using the characteristics of the different radiative mechanisms, as well as combining information from observations over a large range of photon energies, many γ-ray sources have related to different source types.

The individual sources can be broadly clustered in two different categories depending on their location, galactic and extragalactic sources. The galactic γ-ray source population is thought to consist predominantly of PWNe and Supernova Remnants (SNR), whereas the extragalactic γ-ray source population consists primarily of AGNs and GRBs.

Figure 1.5 shows the VHE γ-ray sky as observed by *Fermi*-LAT. There are three distinct features that are observable for γ-ray telescopes, the galactic diffuse emission, individual point sources and extended sources, and the isotropic gamma-ray background (IGRB) or extragalactic background. A brief overview of the main γ-ray source classes is given in this section, while a more in-depth overview of Supernova explosions, as well as pulsars and their environments, is given in Chapter 4.

Supernova Remnants

SNR are the expanding shells of gas and debris left behind after a supernova explosion. The supersonic expansion of the ejected stellar material creates a shock front in the surrounding interstellar medium. These shock fronts then act as acceleration sites for diffuse cosmic rays, resulting in a γ-ray spectrum that is dominated by a hadronic component at higher energies and a leptonic synchrotron component dominating at lower energies. A more detailed review of Supernova explosions and their remnants can

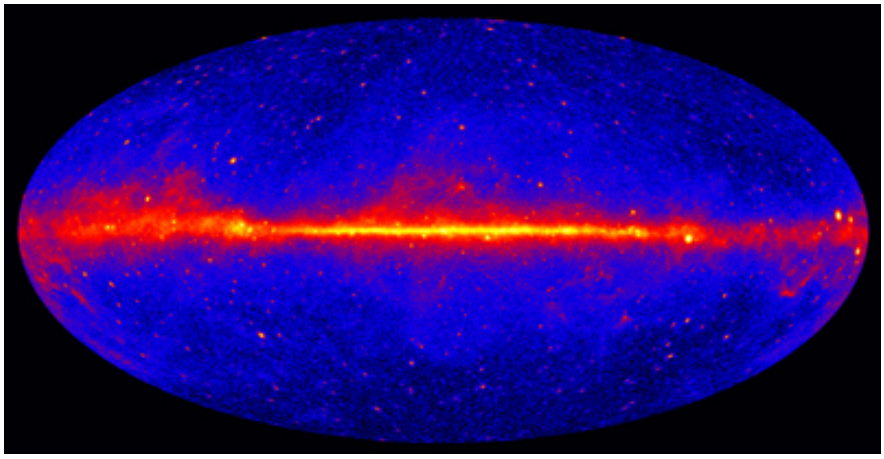

Figure 1.5: All-sky map of γ-rays above 1 GeV as seen by the *Fermi*-LAT detector based on 5 years of continuos data acquisition. `Image Credit: NASA/DOE/Fermi LAT Collaboration`

be found in Section 4.1, and a thorough review of SNRs in a multi-wavelength context can be found in Vink (2020).

Pulsars and their Nebulae

During the supernova explosion, the progenitor star collapses into either a rapidly rotating neutron star (NS) or a black hole, depending on the progenitor mass. If the magnetic and rotation axis of the NS are misaligned, electrons and positrons accelerated from the surface of the star can escape over open field lines. This results in beamed electromagnetic radiation.

These relativistic electromagnetic particles interact with the surrounding medium, creating a standing shock wave. The electrons and positrons from the pulsar wind are then accelerated at the shock wave through diffusive shock acceleration and produce a γ-ray signal through synchrotron radiation and IC scattering with photons from the CMB, starlight, or the synchrotron photons themselves. This extended γ-ray bright region around the pulsar is referred to as PWN and is today the most numerous class of galactic γ-ray sources known. A more thorough discussion on the formation of pulsars and their environments can be found in Section 4.

Active Galactic Nuclei

AGNs are active supermassive black holes situated at the centre of galaxies. Infalling matter onto the black hole powers the formation of relativistic jets of collimated plasma, which are aligned along the rotational axis of the black hole. Cosmic rays are accelerated in these jets, giving rise to an observable γ-ray signal.

The nature of these jets, as well as the composition of the accelerated particles, is still poorly understood. In particular, the contribution of hadronic and leptonic models to the observed γ-ray emission is still debated. A thorough review, including an in-depth discussion of the hadronic and leptonic models for AGNs can be found in Dermer and Giebels (2016).

Gamma-ray Bursts

GRBs are extremely energetic, short-lived γ-ray signals. Their signal is thought to be caused by the death of massive stars or mergers of binary compact objects, which result in the formation of an ultrarelativistic shock front. The signal observed from the GRBs is therefore twofold, first, highly energetic γ-rays are produced in the inner shell while the burst occurs, resulting in a millisecond to hundreds of seconds long flash. Then, a delayed, less energetic afterglow results from the acceleration of cosmic rays on the shock front, which quickly decelerates and merges with the ISM. This stage can last up to several months. The origin of the emission from GRBs is still uncertain, and it may involve both leptonic and hadronic processes (Gill and Granot, 2022).

GRBs are, so far, the most energetic explosions that have been observed. The brightest GRB observed to date is GRB 221009A, with photons of $\approx 10\,\mathrm{TeV}$ being detected (Cao et al., 2023b). This would imply a proton acceleration up to $\sim 10^3\,\mathrm{EeV}$ (He et al., 2024). A comprehensive review of GRB formation and classification can be found in Luongo and Muccino (2021).

Stellar Clusters

Young ($< 30\,\mathrm{Myr}$) and massive stellar clusters have recently emerged as potential γ-ray sources due to their spatial coincidence with the detection of extended γ-ray emission (Bartoli et al., 2014; Abramowski et al., 2012; H.E.S.S. Collaboration et al., 2011). These clusters harbor a large number of massive stars that individually steadily lose mass via stellar winds. In stellar clusters, a collective wind forms which is believed to be a region of efficient acceleration of nucleons. These can then interact with the stellar wind itself and produce γ-rays via the decay of neutral pions. For a cluster age of $> 3\,\mathrm{Myr}$, this effect is combined with the increased chance of massive stars in the cluster undergoing a Supernova explosion, further contributing to the acceleration of cosmic rays in the region. A more in-depth discussion on stellar clusters as γ-ray sources can be found in Morlino et al. (2021a) and Celli et al. (2024).

Stellar Binaries

The different types of stellar binaries are very diverse, resulting in vastly different multiwavelength spectra for the different combinations of stellar objects. However, only a handful of them are known γ-ray emitters. These divide into four different categories: microquasars which are powered by accretion onto a black hole or neutron star, colliding wind binaries powered by interactions of the stellar winds; novae which are created by a thermonuclear runaway process in white dwarfs and pulsar binaries which are powered by the interaction between the relativistic wind of a pulsar and the wind of a massive companion star. Since in each of these cases, particle acceleration occurs through distinct mechanisms resulting in gamma-ray emission via leptonic and hadronic processes, a thorough study of the resulting spectra, as well as the orbital modulation, can be crucial to identifying the underlying acceleration mechanism. A review of the classification of binaries as well as their particle acceleration is given in Dubus (2015)

Galactic Diffuse Emission and Extragalactic Background

Galactic diffuse γ-ray emission arises predominantly from interactions of relativistic cosmic rays with the local ISM as well as radiation fields. The diffuse emission, therefore, traces the distribution of gas and dust and is very bright in the galactic centre region, as well as along the galactic plane. This diffuse emission has been observed from GeV (Ackermann et al., 2012) up to hundreds of TeV (Cao et al., 2023c). These measurements are not only central to estimating its contribution in specific sky regions when analysing specific γ-ray sources but can also be used to study the propagation of cosmic rays in the Galaxy and probe the content of the ISM itself. A more in-depth analysis of the implications of galactic diffuse emission measurements by *Fermi*-LAT on the cosmic ray and ISM distribution is given in Ackermann et al. (2012).

The isotropic gamma-ray background (IGRB) is an isotropic distribution over the entire sky. It consists of diffuse γ-rays from two different contributions, unresolved extragalactic sources from γ-ray emitters which are too faint to be observed with the respective telescope or still unknown source populations, and a possible contribution from cosmological processes like dark matter annihilation or decay. This makes the IGRB for a given study dependent on the amount of resolved sources and, therefore on the sensitivity of the instrument. A more often referred to quantity is the extragalactic background (EGB), which consists of the sum of the IGRB and the resolved extragalactic sources. More information on the implications of extragalactic diffuse γ-rays in the TeV energy range can be found in Dwek and Krennrich (2013). For even higher energies, the EGB can be neglected as the universe is essentially opaque to γ-rays with energies higher than 100 TeV, due to electron-positron pair production on extragalactic background light.

2 Gamma-ray Detection Techniques

γ-rays span a wide range of energies, from $\sim 100\,\mathrm{keV}$ to $\sim 100\,\mathrm{TeV}$. Due to limitations of the current detection techniques (see Section 2.1.2 for more information), the current energy threshold above which γ-rays can be extensively studied is $\approx 1\,\mathrm{MeV}$. Photons between $\approx 1\,\mathrm{MeV}$ and $100\,\mathrm{GeV}$ are referred to as high-energy (HE) γ-rays while very-high-energy (VHE) γ-rays are in the range between $100\,\mathrm{GeV}$ and $100\,\mathrm{TeV}$.

The current γ-ray detectors are broadly divided into two categories: space-based detectors, which detect HE γ-rays, and ground-based detectors, which detect VHE γ-rays. This distinction needs to be made due to the steep γ-ray spectrum. While space-based detectors are able to observe the HE γ-ray range, only few γ-rays are expected to be measured at the highest energies, and the possibly employable detection area of these detectors could not collect a sufficient γ-ray flux. A detection of γ-rays from the surface of the earth, where large detection areas can be used, however is only possible for VHE γ-rays, since earth's atmosphere is opaque to γ-rays and the signal from HE γ-rays is too weak to be picked up by the currently employed detectors.

This work mainly focuses on the ground-based detector High Energy Stereoscopic System (H.E.S.S.). In the analysis of the γ-ray sources presented in Section 5 and Section 6, data from other experiments is also utilised. These experiments include the space-based detector *Fermi*-LAT, the High-Altitude Water Cherenkov Observatory (HAWC) and the Large High Altitude Air Shower Observatory (LHAASO). The next chapter provides a short introduction to the space-based detectors and especially *Fermi*-LAT, before ground-based detectors will be discussed in detail.

2.1 Space-based γ-ray Detectors

Due to the opacity of the earth's atmosphere to γ-rays, direct detection is not possible from within the atmosphere. Space-based detectors are, therefore a vital instrument to observe the γ-ray sky, especially in the MeV to GeV range, where γ-rays do not carry enough energy to be observed by ground-based instruments (for more details see Section 2.2.1).

2.1.1 Overview

The first γ-ray observations were acquired by a detector mounted on a satellite, which was launched in 1961, consisting of a Photo multiplier and a crystal scintillator (Kraushaar et al., 1965). Not long after, the first γ-ray survey was performed by a similar detector onboard the third Orbiting Space Observatory (OSO-3) (Kraushaar et al., 1972). Since then the understanding of the γ-ray sky over a large energy range up to $\sim 1\,\mathrm{TeV}$ has drastically increased with the two most important space-based γ-detectors being the Energetic Gamma Ray Experiment Telescope (EGRET, (Fichtel et al., 1994)) and its successor the Large Area Telescope (LAT), (Atwood et al., 2009a) mounted on the *Fermi* Gamma-ray Space Telescope (Thompson and Wilson-Hodge, 2022). Using the LAT it has become possible to detect γ-rays from space up to energies above $300\,\mathrm{GeV}$, creating an overlap with the detection capability of many ground-based detectors. Space-based γ-ray detection does, however, have its limitations. Due to the relatively strict weight limitations of mounting the detector to a satellite, it has not been possible to design a

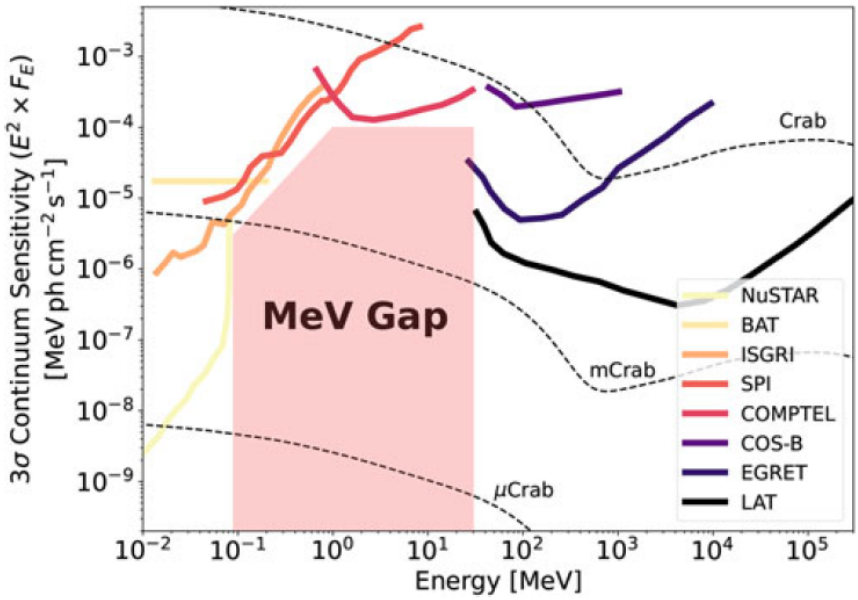

Figure 2.1: $3\,\sigma$ sensitivity curve of past and current hard X-ray and γ-ray detectors for an exposure of 12 days. Figure taken from Bambi and Santangelo (2024).

detector with a detection area of $> 1\,\mathrm{m}^2$, making the detection of several TeV γ-rays unfeasible.

At energies smaller than 10 MeV, the interaction of photons with matter starts to be dominated by Compton scattering rather than pair-production (Thompson, 2015). In this case containing the photon in the small detector and reconstructing its initial parameters becomes challenging. An additional complication for the detection of photons at this energy is the high rate of cosmic ray events. A combination of these effects results in a 'MeV Gap' in the sensitivity of past and current detectors. This is illustrated when comparing the sensitivity curves - showing the minimum detectable photon flux within a specified observation time as a function of energy - of space-based detectors in Figure 2.1.

More information regarding the development in the field of space-based telescopes and a comparison between EGRET and LAT can be found in Thompson (2015).

2.1.2 *Fermi*-LAT

The LAT is a pair-conversion detector that can detect γ-rays in an energy range of $\sim 20\,\mathrm{MeV}$ to $> 300\,\mathrm{GeV}$ by providing an environment in which the highly energetic γ-rays undergo pair production. The effective detection area, referring to the area of the detector sensitive to the detection of γ-rays after considering inefficiencies, geometric constraints, and reconstruction failures, is $< 1\,\mathrm{m}^2$ with a field of view (FoV) of 2.4 sr. Since its launch in 2008, it has observed the sky almost continuously.

Design

The discussion about the LAT and its detection capabilities given in this Section follows the information provided in Atwood et al. (2009b).

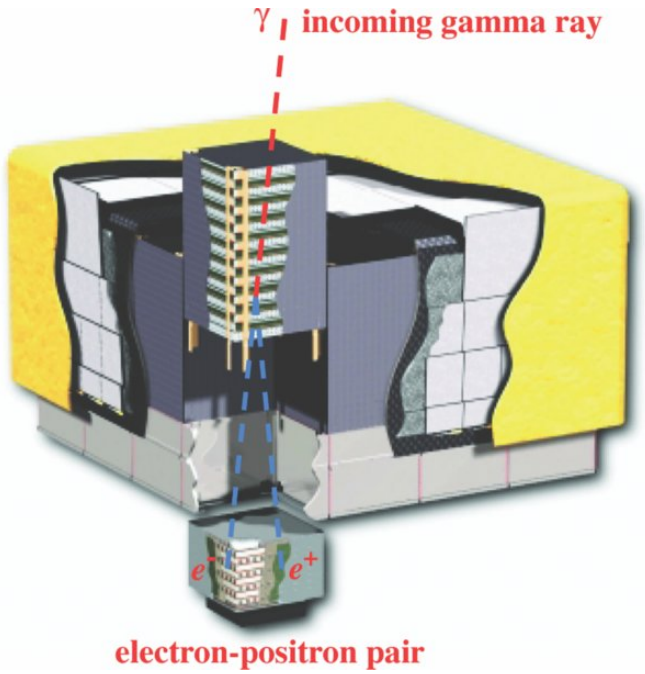

Figure 2.2: Schematic of the LAT on board the *Fermi* satellite. Indicated in white are the ACD tiles around a tracker module and the calorimeter. Figure taken from Atwood et al. (2009b).

The detector consists of several different layers in which different signal properties can be obtained. A schematic of the structure of the LAT detector is shown in Figure 2.2. The primary particles first pass through an Anti-Coincidence Detector (ACD), which is used to distinguish between γ-ray and cosmic ray events. After that, the particle enters the tracker which consists of several layers of dense material, in which the photon undergoes pair-production. From there, the lepton pair enters a calorimeter, in which the energy of the electron and positron are measured.

The ACD consists of plastic scintillator tiles which are read out by two wavelength-shifting fibres coupled to silicon photomultipliers (SiPMs). These SiPMs are more compact and lighter compared to Photo Multiplier Tubes (PMTs) and, therefore, better suited for use in the compact design of the LAT. When a charged particle passes through the scintillator tiles, it produces a strong signal, while γ-rays typically do not deposit a large amount of energy in the ACD, providing a strong indication for background rejection.

The γ-ray, after passing through the ACD, enters the tracker and interacts with the tracker material. In the MeV to GeV energy range the primary interaction of photons and matter is pair-conversion into an electron-positron pair in the Coulomb field of an atomic nucleus. In the LAT tungsten foil converters are used to facilitate the pair-conversion. Due to the inverse proportionality of the atomic number (Z) with the radiation length X_0 (see Equation (11)), a material with a high atomic number is desirable to ensure a high interaction probability of the γ-ray. The path of the charged leptons in the high-Z material is not straight due to interactions with the material

through multiple Coulomb scattering. The scattering angle is given in a Gaussian approximation as:

$$\Theta_0 = \frac{13.6\,\mathrm{MeV}}{vp}\sqrt{x/X_0}\,(1 + 0.038\ln(x/X_0)) \tag{26}$$

with v and p the velocity and momentum of the particle and x the thickness of the material (Lynch and Dahl, 1991). Therefore, the high-Z material is disadvantageous because of the large Coulomb scattering angle. To solve this problem, the converting material in the LAT is broken into 16 thin layers, between which silicon-strip detectors (SSDs) are located to track the lepton path through the successive planes.

After exiting the conversion tracker, the electron-positron pair resulting from the incident γ-ray passes through a calorimeter where the energy of the e^+ and e^- is measured. 96 optically isolated CsI crystals are located in each calorimeter module, and the scintillation light is read out by PIN photodiodes mounted on both ends of the crystals. This segmentation of the calorimeter allows for the imaging of the spatial development of successive pair conversions and annihilations (shower development), providing an additional channel to distinguish between CR-induced hadronic air showers and leptonic air showers (see Section 2.2.1).

The LAT is designed to measure γ-rays up to 300 GeV. For measuring γ-rays up to such energies, a heavy calorimeter ($\sim$ 1800 kg) is necessary to contain the full development of the shower initiated by the electrons and positrons (Atwood et al., 2009b). However, a dense, high-mass calorimeter also increases the chance of Compton scattering in the electromagnetic shower. If the electrons and positrons then enter the ACD, it can lead to the event being flagged as a cosmic ray event. These false negatives are called the backsplash effect. To suppress the effect, the ACD is segmented, and only the segment near the incident candidate is considered.

The trigger of the LAT is formed from the tracker, the calorimeter, and the ACD subsystems, with the tracker being the principal trigger. A first-level trigger is the coincident detection of a charged particle in at least three successive layers in the tracker area, with the efficiency of this first-level trigger for charged particles being almost 100% (Atwood et al., 2009b).

Event Reconstruction

For the event reconstruction, information from all subsystems is combined. The term event in this context refers to a signal that triggers the detector and can be reconstructed. Once the detector has been triggered, the tracker signal is used to reconstruct the trajectory of the incident γ-ray by measuring the angle and separation of the electron-positron pair and the reconstructed energy is gained from the energy deposited in the calorimeter. The reconstruction of the events track and energy relies on Monte Carlo simulations.

The direction of the incident γ-rays can be estimated using an approximation of the opening angle between both particles to $\Theta \propto 0.8E_\gamma^{-1}$ with E_γ in the MeV range (Olsen, 1963). Above 100 MeV the opening angle is small enough that the track directions can be used directly to reconstruct the direction of the incident photon (Thompson, 2015).

The spatial response of the detector to a point source, or Point Spread Function (PSF) of the SSDs, is limited by multiple Coulomb scattering of the e^+ and e^-, as

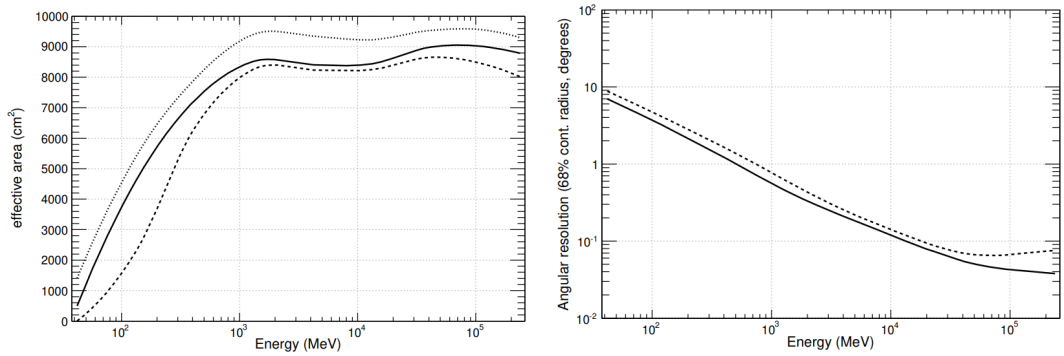

Figure 2.3: Performance of the LAT. Left: Effective detection area versus energy for different levels of background rejection. Right: 68% containment radius for 'front' events with different incidence angles of 0° (solid curve) and 60° (dashed curve). Figures taken from Atwood et al. (2009b).

well as bremsstrahlung. It is, therefore, important to measure the direction of the leptons directly after the pair conversion. In its current form, *Fermi*-LAT is limited to a PSF of $> 3\,^\circ$ at energies around 100 MeV (Atwood et al., 2009b). The tracker itself is divided into two regions. The 'front' region, with thin converters of $0.03X_0$, is used to optimize the PSF, especially at low energies. The 'back' region with thicker converters of $\approx 0.18X_0$, maximizes the effective detection area at the cost of a slightly worse PSF compared to the 'front' region (roughly a factor two at 1 GeV). The relation between effective detection area and PSF with energy is shown in Figure 2.3.

The particle track reconstruction is done employing two track-finding algorithms that compare a particle track hypothesis to the readout of the sensors. The first algorithm, `Calorimeter-Seeded Pattern Recognition (CSPR)`, uses a rough estimate of the total energy deposited in the calorimeter. This information is then used to combine different hits along possible path trajectories using Kalman fitting (Kalman, 1960). Only the track with the smallest χ^2 is retained by the algorithm. The second algorithm, the `Blind Search Pattern Recognition (BSPR)` operates similarly to the CSPR, but without calorimeter information by identifying at least 3 hits along a possible particle trajectory. The resulting paths are combined into vertices to evaluate if some of these tracks result from the same parent particle, and the energy is estimated from the amount of multiple scattering between different possible tracks.

For energies $E_\gamma \gg 2m_e$, with m_e the rest mass of the electron and positron, only a negligible amount of energy is not transferred to the lepton pair. Energy reconstruction is done by evaluating the total energy and location of the triggered CsI crystals. Three different algorithms are used for the exact energy reconstruction of every event: fitting the shower profile (SP) for initial energies above 1 GeV, a maximum likelihood (LK) fit on the correlations of deposited energy for initial energies below 300 GeV and a parametric correction (PC). The reconstructed particle track is used to account for leakage out of the calorimeter or in between the calorimeter modules. Then, a classification tree is used to average over the results to find the most probable reconstructed energy and track. At energies below ~ 100 MeV it also becomes important to account for energy lost in the tracker ($\sim 0.5E_{\rm tot}$, with $E_{\rm tot}$ the total energy of the primary

γ-ray), using the number of hit silicon strips.

Background Rejection

Due to backsplash it is not possible to reject all ACD-triggered events. If, however, the ACD trigger is used in comparison with the reconstructed particle track, a likelihood of the event being a cosmic ray can be established. The topology of the shower initiated in the calorimeter provides further means to distinguish between background and signal (see Section 2.2.1 for more information). Using the system trigger described above, as well as event reconstruction, the cosmic ray background can be reduced by a factor of 10^6 while keeping more than 75% of the γ-ray events (γ-efficiency) (Atwood et al., 2009b).

The importance of background rejection and signal retainment can vary for different target observations. It is for example, important to reject a sufficient amount of background for extended, diffuse sources, while it is more important to retain almost all γ-rays in the analysis of point-like, short-lived signals like GRBs. LAT, therefore provides 3 different classes for the processing of the data:

1. 'Transient': This class maximises the effective area with a high residual background rate of 2 Hz. It is used for monitoring transient objects like GRBs,

2. 'Source': This class has a residual background rate of 0.4 Hz and is used for detection of point sources or slightly extended sources below 1°

3. 'Diffuse': This class is suitable for the study of the weakest diffuse sources by providing a residual background rate of 0.1 Hz.

After the signal processing, it is reasonable to assume that the remaining misclassified cosmic rays, as well as earth albedo γ-rays, and diffuse or unresolved extra-galactic γ-rays are isotropically distributed. To derive this remaining γ-ray flux, a template is created from a fit to the all-sky emission in regions with galactic latitude of $|b| > 30°$.

Galactic Diffuse Background Model

While accounting for isotropic background emission is important for a precise estimation of the flux from γ-ray sources, the HE γ-ray sky is dominated by galactic diffuse emission resulting from interactions of cosmic rays with interstellar gas and radiation fields. The γ-ray emission produced through this process is spatially coincident with the distribution of the interstellar gas density, which is highest in the galactic plane. In order to compute a spatial model of the diffuse emission (Galactic interstellar emission model - IEM), several different physical templates were used and the emission is modelled as a linear combination of these templates. The computation of this model is described in detail in Ackermann et al. (2012). With auxiliary notes detailing the changes made for more advanced models computed since the initial publication[2].

One of the templates used describes the cosmic ray transport in the galaxy. To derive this template, the numerical code GLAPROP, which calculates the propagation

[2]Information for the new version, `gll_iemv07.fits` can be found at `https://fermi.gsfc.nasa.gov/ssc/data/analysis/software/aux/4fgl/Galactic_Diffuse_Emission_Model_for_the_4FGL_Catalog_Analysis.pdf`

of relativistic charged particles and gives an estimate of the diffuse emission which is produced during their propagation (Porter et al., 2017).

The distribution of diffuse interstellar gas, meaning gas not gravitationally bound in other structures, can in first order be measured by H1 and CO gas. For the computation of the background model template, the H14PI all-sky survey (HI4PI Collaboration et al., 2016) and the CfA CO survey (Dame and Thaddeus, 2004) were used. These channels are chosen since both are relatively easy to excite through collisions and H1 is optically thin for the ISM with a typical gas temperature of $T_K > 50\,\mathrm{K}$ (Kulkarni and Heiles, 1988). For the CO emission line, this is not the case, and CO can only be used as an accurate tracer for molecular gas through its virial mass if it is gravitationally bound. These conditions do not apply in the ISM and further tracers are needed to determine the full amount of molecular gas (Planck Collaboration et al., 2011). Assuming that gas and dust are well mixed as they are produced by the same astrophysical sources, the dust column density presents a reasonable tracer. The dust optical depth map at 353 GHz from Planck Collaboration et al. (2011) was therefore additionally used as a template for the galactic diffuse emission.

Besides the spatial templates derived from particle propagation and target material distribution, patches were defined. These patches consist of regions with established large scale γ-ray residuals, like the the large radio lobe Loop 1 (Haslam et al., 1982), the *Fermi*-bubbles, which are 'lobes' extending out from the Galactic centre region (Su et al., 2010), as well as the Galactic centre GeV excess (Hooper and Goodenough, 2011). The patches for these objects are defined from the residual γ-ray intensity after the fit of the overall model derived from the physical templates and removal of known γ-ray sources. 8 years of data, reconstructed using the 'Source' class, were used for this purpose. The energy range in which the data was analysed, and therefore also in which the background model is valid, is 50 MeV - 1 TeV. This process has been iteratively repeated as the patch itself is part of the background model, and the resulting background is smoothed with a 3° Gaussian kernel.

Single sources were excluded from the background model using the 4FGL catalog (Abdollahi et al., 2020). The contribution of unresolved extragalactic sources to the isotropic background is estimated from a population synthesis presented in Acero et al. (2016), while unresolved galactic sources were estimated to mostly be concentrated in the galactic plane ($|b| < 10°$) with a flux contribution of around 3% (Acero et al., 2015).

The last two contributing templates account for diffuse γ-ray emission from cosmic ray interactions in the fine layer of dust and soil on the Moon's surface (Moskalenko et al., 2008; Ackermann et al., 2016) and the cosmic ray interactions in the outer solar atmosphere (Ackermann et al., 2016) as well as IC scattering in the solar radiation field (Abdo et al., 2011). The IEM computed for the 3FGL with 4 years of observation data can be seen in Figure 2.4.

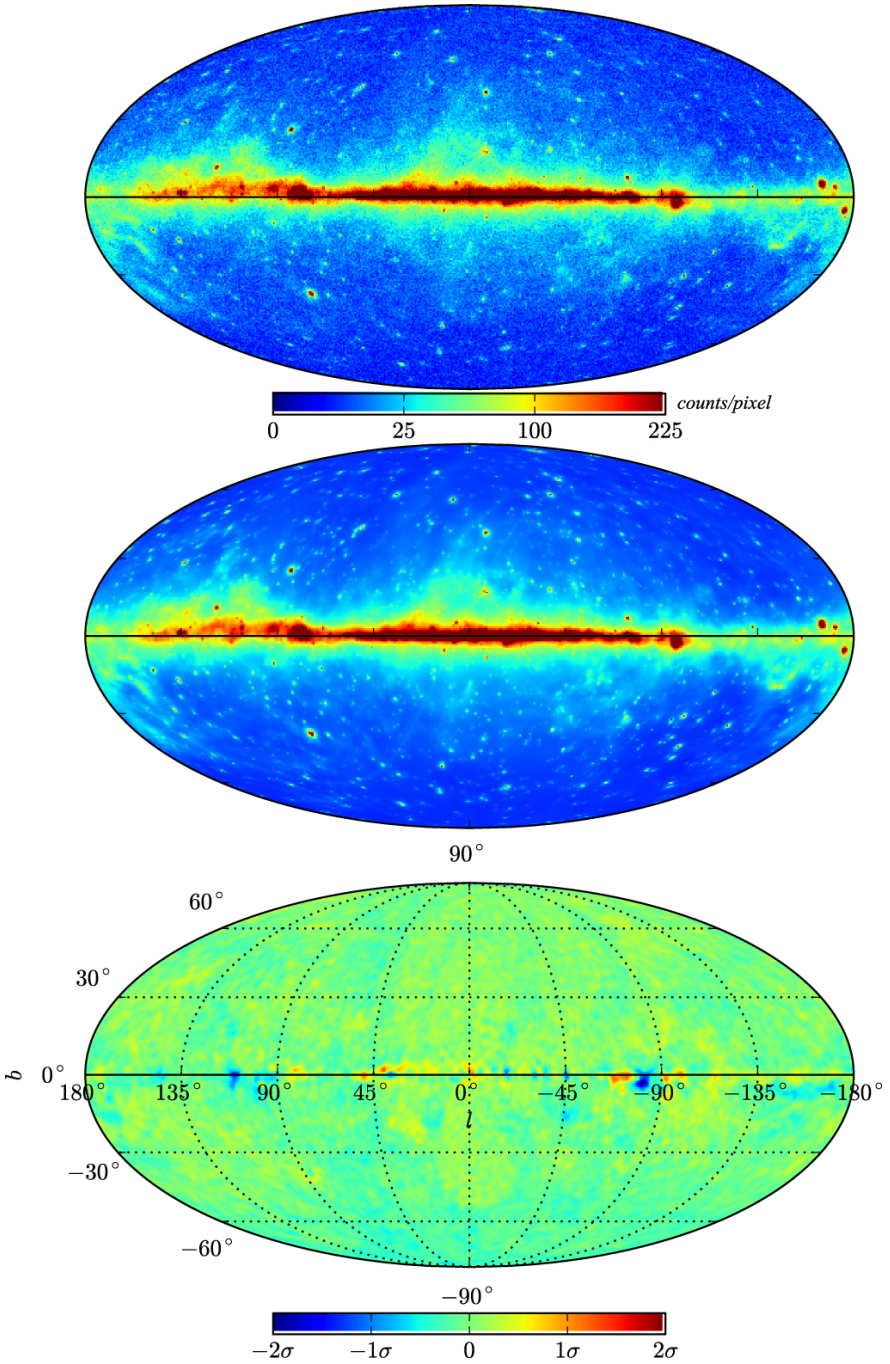

Figure 2.4: All-sky projection of 4 years of data aquired by the LAT between 0.36 – 50 GeV. Top: data after inital rejection of cosmic ray events. Middle: Predicted interstellar emission model. Bottom: Residuals after subtraction of the the IEM. Figure taken from Ackermann et al. (2012).

2.2 Ground-based Instruments

Earth's atmosphere is only transparent for photons in certain regions of the electromagnetic spectrum, the so-called atmospheric windows. The three main windows lie in the optical, infrared, and radio, while photons with a energy above $\sim 10\,\mathrm{eV}$ interact strongly with atoms or molecules in the atmosphere (Alavipanah et al., 2008). This interaction of X-ray and γ-ray photons, as well as cosmic rays, leads to a cascade of secondary particles which can be traced using instruments on the ground.

The properties of the particle cascade can be used to distinguish between γ-ray and cosmic ray initiated air showers and to reconstruct the energy and direction of the primary particle. The current generation of ground-based detectors achieve a peak sensitivity at a few TeV for Imaging Atmospheric Cherenkov Telescopes (IACTs) and a few tens of TeV for Water Cherenkov Detectors (WCDs) with detection areas $> 10^4\,\mathrm{m}^2$ for both detector types.

2.2.1 Air showers

An air shower is a cascade of particle decays, scattering, and collisions initiated by a γ-ray or a cosmic ray entering the atmosphere. These showers can be divided into two categories: hadronic showers initiated by a charged hadron and electromagnetic showers which are caused by a photon or lepton. This Section will give an overview of the development of both kinds of air showers and their detection using IACTs and WCDs, before the Section 2.3 gives an in-depth discussion about the H.E.S.S. array of IACTs. The Section follows Bambi and Santangelo (2024). A thorough review of air showers and their development can be found in Grieder (2010).

Electromagnetic Air Showers

An incoming highly energetic γ-ray will produce a relativistic electron-positron pair in the Coulomb field of nuclei in the atmosphere. The produced lepton pair will travel further into the atmosphere and produce additional photons via bremsstrahlung. These, in turn, can produce additional lepton pairs via pair production if their energy is sufficient, and the cascade can reach down to sea level.

Due to this interaction cascade, the dominating factor responsible for the spatial distribution of the electromagnetic shower is the interaction cross-section of pair-production and bremsstrahlung. Since their Feynman diagrams are variations of each other, the cross-section is related, and one finds for their radiation lengths: $X_0^{\mathrm{pair}} = (7/9)X_0^{\mathrm{brems}}$ (Bambi and Santangelo, 2024).

After travelling a distance x, the energy of a particle can be described as:

$$E(x) = E_0 \exp\left(-\frac{x}{X_0}\right), \tag{27}$$

with x given in units of atmospheric depth, defined as:

$$x(z) = \int_l \varrho(z)\mathrm{d}l\,, \tag{28}$$

with $z = l \cdot \cos\Theta$ the vertical height above sea level for small zenith angles ($\Theta < 65°$) and $\varrho(z) = \varrho_0 \exp(-z/H)$ the height dependent atmospheric density. Quoting the depth x

in units of g cm^{-2} and scaling it by the radiation length X_0 is commonly done to remove the effect of changing atmospheric density with height. Assuming dry air and a nominal atmospheric pressure, the radiation length can be approximated as $X_0 = 36.6\,\mathrm{g\ cm^{-2}}$ (Navas et al., 2020).

A simple analytical derivation of the shower development assuming only bremsstrahlung and pair-production with $X_0^{\mathrm{pair}} = X_0^{\mathrm{brems}}$ and an equal distribution of the parent particle energy on the two secondary particles at each step is given in Heitler (1954). From this model, it can be assumed that every particle produces two additional particles after propagating $X_0 \ln(2)$. A visualization of this model is shown in Figure 2.5.

Pair production in the shower is possible until the energy of the photons in the cascade reaches energies below $2m_e$. In this regime, only bremsstrahlung can further contribute to the cascade until the critical energy E_c is reached. At this energy ionization takes over as the dominant energy loss and the shower development rapidly slows. This critical energy is $E_c = 88\,\mathrm{MeV}$ for electrons and $E_c = 86\,\mathrm{MeV}$ for positrons for interactions in air (Navas et al., 2020).The time scale for the development of the whole shower is around a few microseconds.

The cascade formation for an incoming relativistic cosmic ray electron or positron is similar to the development of a γ-ray-initiated shower. The lepton will produce a photon either by annihilation in the case of a positron or bremsstrahlung in the case of an electron or positron. The mean free path of the electron in the atmosphere is slightly shorter compared to the γ-rays, this results in a higher point of first interaction and a shower maximum which is located further up in the atmosphere, as well as a more broad distribution at telescope level (Karpov et al., 2006). An additional effect relevant for cosmic ray electrons is that they are subject to synchrotron and inverse Compton energy losses while travelling through space. A significant contribution of electrons to the rate of air showers is, therefore, only expected for either low-energy cosmic ray electrons ($E_e < 100\,\mathrm{GeV}$) or locally accelerated electrons at higher energies (Grieder, 2010).

The height of the first interaction in the atmosphere is subject to strong variation due to the low atmospheric density at these altitudes and contributes significantly to strong variations in the shower development. After the first interaction, which is expected to occur roughly at a height of $\sim 35\,\mathrm{km}$ above sea level, the number of particles in the air shower increases until the shower reaches a maximum and ionization losses dominate. The atmospheric depth x_{max} of this maximum depends on the initial particle energy following Equation (27):

$$x_{\mathrm{max}} = X_0 \ln\left(\frac{E_\gamma}{E_c}\right). \tag{29}$$

For a γ-ray with an energy of 1 TeV, the shower maximum is located at an atmospheric depth of $\sim 10\,\mathrm{km}$. The development of the shower depends on atmospheric depth, but also on barometric pressure and temperature as they change the atmospheric density. The zenith angle also has a big influence as a higher zenith angle is equivalent to a higher amount of transversed medium.

Using an approximation from Hillas (1982), the number N of electrons and positrons

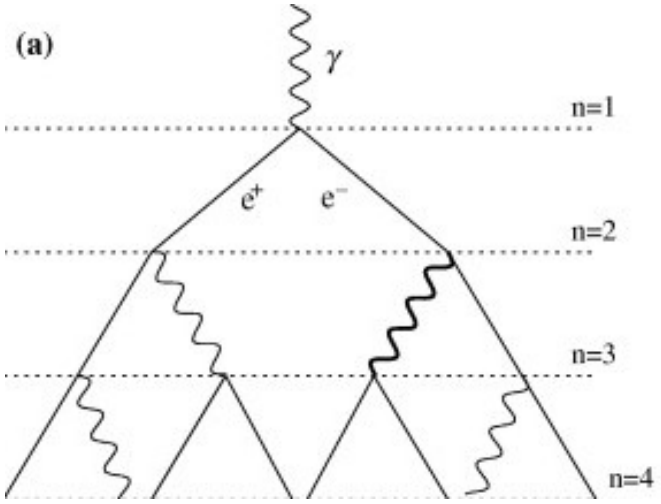

Figure 2.5: Illustration of the Heitler Model for a electromagnetic shower initiated by a VHE γ-ray. Figure adapted from Matthews (2005).

in the shower can be described by:

$$N(x) = \frac{0.31}{\sqrt{\ln\left(E_\gamma/E_c\right)}} \exp\left[\frac{x}{X_0}(1 - 1.5 \ln s)\right], \tag{30}$$

with the shower age $s = 3 \cdot (1 + 2\ln\left(E_\gamma/E_c\right)/(x/X_0))^{-1}$ describing the developmental stage of the shower ($s < 1$ for young showers; $s > 1$ for old showers which have already reached their maximum). The number of particles at the shower maximum is roughly $N(x_{\max}) \sim 10^3 E_\gamma/\,\mathrm{TeV}$ (Bambi and Santangelo, 2024). This, however, only includes the number of charged particles, photons are excluded.

The cascade develops along a narrow axis in the longitudinal direction and is broadened by Multiple Coulomb scattering and deflection of the charged particles in the earth's magnetic field. This radius of the shower containing 90% of the particles is characterized by the Molière radius $R_M = 0.24 X_0/\varrho$. At sea level, the Molière radius can be estimated to $R_M \sim 80\,\mathrm{m}$, increasing with increasing altitude due to decreasing density of the atmosphere (Bambi and Santangelo, 2024).

To achieve a good reconstruction of the γ-ray properties, detecting as many of the secondary particles as possible is vital. Due to this, a good understanding of the radial extent of the particle shower on the ground is important information to factor into the design of a ground-based γ-ray detector.

Hadronic Air Showers

Air showers initiated by relativistic cosmic rays are referred to as hadronic air showers or extensive air showers. Just like the showers initiated by γ-rays, the interaction of a cosmic ray with the atmosphere results in a particle cascade, which propagates longitudinally along the initial direction of the incident cosmic ray.

Contrary to electromagnetic air showers, which involve only leptons and photons, hadronic air showers involve strong interactions that produce mostly mesons (pions and kaons) and some light baryons. Because the mean free path of a particle is mass

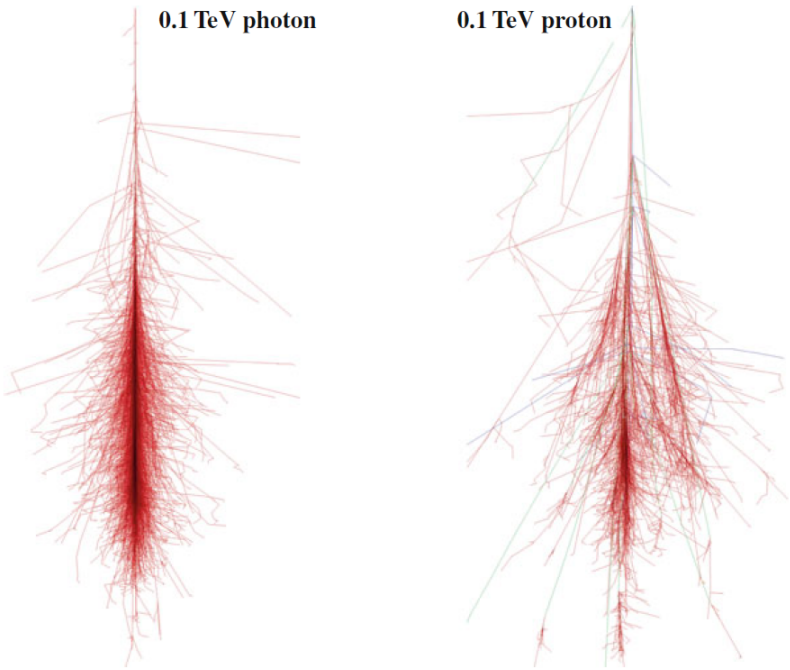

Figure 2.6: Simulated air shower development initiated by a 0.1 TeV photon on the left and a 0.1 TeV proton on the right. The height of first interaction was assumed as 30 km above sea level. The leptons and photons are shown in red, while muons and hadrons are shown in green. Figure taken from Bambi and Santangelo (2024).

dependent, the height of the first interaction of the cosmic ray and, therefore, also the shower maximum is directly proportional to the primary mass A. An additional feature of the hadronic cascades is that $x_{\max}$ does not only depend on the primary energy but also on the depth at which the particle undergoes highly inelastic collisions and loses a majority of its energy. When compared to electromagnetic showers, hadronic showers are subject to larger fluctuations in their development.

In contrast to the rather narrow scattering angles from multiple Coulomb scattering in electromagnetic showers, the strong interactions impart a large transverse momentum on their secondary particles, and scattering processes take place in the cascade. This leads to a large lateral spread of the shower, which is the primary characteristic by which the different kinds of showers are distinguished. The differences in the lateral spread and development of the shower cascade for both electromagnetic showers and hadronic showers at the same incident energy can be seen in Figure 2.6.

Even with these differences, it is not trivial to distinguish between electromagnetic and hadronic air showers. A major factor that complicates the identification is that the resulting cascade is not only hadronic. Roughly one-third of the produced pions are neutral pions, which further decay into two photons, resulting in an electromagnetic subshower. The charged pions, as well as kaons, which are present in the shower, decay into neutrinos and muons. As the shower development progresses and more pions and hadrons, as well as some of the resulting muons, decay, the electromagnetic component can start to dominate the shower development, complicating the identification of the primary particle. This effect dominates if a photon has been produced at a large atmospheric depth and close to the primary shower axis. In this case, Grieder (2010) estimates that an average hadronic air shower contains over 90% of electromagnetic particles at sea level.

2.2.2 Cherenkov Radiation

When a charged particle moves in a medium it causes the distribution of charge of the atoms and molecules to change. This results in a temporary polarization of the medium, which relaxes by emitting electromagnetic waves once the particle has passed. If the particle moves with a speed lower than the speed of light in the medium ($v_{\text{particle}} < c_0/n$ with n the refractive index of the medium), the medium responds gradually, and the waves of the resulting dipole field are typically randomly phased and can interfere destructively. If the particle moves with a speed of $v > c_0/n$, the waves of the resulting field are all in phase under a certain angle Θ_{Ch} to the particle track and add up coherently to a plain wave following Huygens construction (Grieder, 2010). This relation is visualized in Figure 2.7, the coherent radiation is referred to as Cherenkov radiation.

The emission angle of the Cherenkov photons Θ_{Ch} is given by:

$$\cos\left(\Theta_{\text{Ch}}\right) = \frac{c}{vn(z)}\,, \tag{31}$$

with the refractive index $n(z)$, which, for the atmosphere, can be approximated as:

$$n(z) = 1.0 + 0.000283\frac{\varrho(z)}{\varrho(z=0)}\,, \tag{32}$$

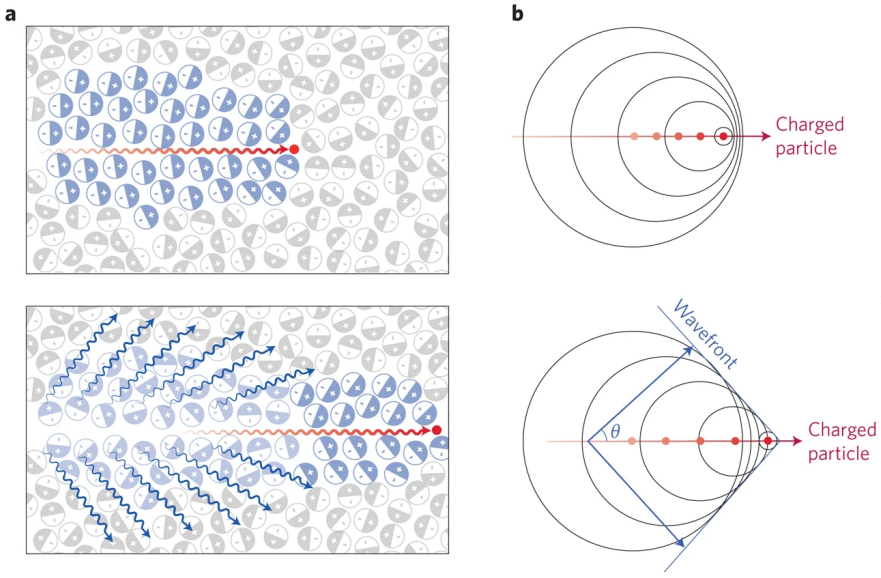

Figure 2.7: Schematic of the polarization of a medium from a charged particle travelling with non-relativistic (top) and relativistic (bottom) velocities. The emission of the Cherenkov photons and the geometric expansion of the wave front resulting from the presence of the relativistic particle are shown on the right. Figure taken from Shaffer et al. (2017).

with $\varrho(z)$ the atmospheric density at a height z.

In an air shower, each relativistic charged particle that moves faster than the speed of light in air produces Cherenkov radiation. The radiation can be observed in a cone around the trajectory of the relativistic particle under the angle Θ_{Ch}. The Cherenkov angle depends on the altitude of emission, increasing towards sea level as the air density increases. The Cherenkov flash produced by a shower typically lasts around 5 ns, and the amount of emitted light can be used as a measure of the primary particle's energy. The minimum energy for the production of Cherenkov radiation is given as:

$$E_{\mathrm{min}} = \frac{m_0 c^2}{\sqrt{1 - n^{-2}}} \tag{33}$$

with m_0 the particle mass. At sea level, this results in a threshold energy of $E_{\mathrm{th}} = 21\,\mathrm{MeV}$ for an electron.

The energy loss of the highly relativistic charged particle due to Cherenkov radiation can be approximated as:

$$\left(\frac{\mathrm{d}E}{\mathrm{d}l}\right)_{\mathrm{Ch}} = \frac{1}{2}\left(\frac{Ze\omega}{c}\right)^2 (\eta - 1) \ln\left(\frac{\eta}{\eta - 1}\right), \tag{34}$$

with Ze the charge of the particle, ω the angular frequency of the Cherenkov radiation and $\eta = 1 + A/\omega_0$ with ω_0 the frequency of the first resonance in the spectrum. Typical values for ω_0 are $\omega_0 = 6 \cdot 10^{15}\,\mathrm{s}^{-1}$, resulting in a typical energy loss of a few keV per centimetre (Grieder, 2010). This energy loss is almost negligible compared to the loss by ionization and excitation.

Equation (34) can be transformed to yield the number of emitted Cherenkov photons as:

$$\frac{\mathrm{d}^2 N}{\mathrm{d}\lambda \mathrm{d}x} = \frac{2\pi\alpha}{\lambda} \cdot Z^2 \left(1 - \frac{1}{\beta^2 n(\lambda)^2}\right) , \tag{35}$$

with α the fine structure constant and Z the charge of the particle (Čerenkov, 1937). This shows that the number of Cherenkov photons N_{Ch} is proportional to the energy of the primary particle, and the majority of the emission is expected for lower frequency particles.

The atmosphere is, however, not transparent for ultraviolet wavelengths due to the increase of the interaction cross-section of Rayleigh scattering with increasing particle energy. This results in the Cherenkov flash being detected within $300\,\mathrm{nm} < \lambda < 450\,\mathrm{nm}$, peaking at the low wavelengths, which accounts for the blue shade of the Cherenkov emission (Grieder, 2010). Due to this relation, the Cherenkov photons themselves suffer little absorption in the atmosphere and can still be observed at sea level even when most of the shower particles have already died out. As seen in Equation (35), the number of Cherenkov photons also depends on the density of the atmosphere. This changes not only with the height above sea level, but also with e.g. temperature, humidity, and air pressure.

Following Equation (32), the refractive index of the atmosphere at sea level can be estimated as $n = 1.00029$, for standard atmospheric conditions. This leads to a Cherenkov light cone with a relatively small opening angle of around $\sim 1.3^\circ$ at sea level. A schematic of the development of the Cherenkov cone around the shower axis is shown in Figure 2.8. The arrival distribution of the Cherenkov photons is relatively compact and the Cherenkov light pool, which is the area on the ground illuminated by Cherenkov photons, shows a disk-like shape with a over-density of light around the outer ring and a distribution area with a radius of around 100 m for a primary particle with an energy in the TeV range (Konopelko et al., 1997). The outer edge of this light pool is created around the shower axis from the envelope of all Cherenkov photons and the middle of the ring structure is filled by the emission of Cherenkov photons under different angles from the individual charged particles.

2.2.3 Imaging Atmospheric Cherenkov Telescopes

The Cherenkov light produced in air by the charged particles in a shower can be detected by ground-based telescopes, so-called Imaging-Atmospheric-Cherenkov Telescopes (IACTs). These telescopes employ big mirror dishes in order to collect as much of the light of the Cherenkov light pool as possible and focus the collected light on a camera.

The cameras need to be equipped with fast electronics to be able to resolve the signal, which only lasts a few tens of nanoseconds. They typically consist of individually detecting pixels, usually photomultiplier tubes (PMTs). The signal from the individual camera pixels is typically read out once a specified threshold criterion - the trigger threshold - is achieved. For measurements with individual telescopes, the trigger consists of a certain number of pixels measuring a light yield above a certain threshold.

As stated in the previous section, Cherenkov light is mainly emitted in the optical. This provides a challenge to the IACTs since it limits their observation time. Contrary to the space-based telescopes, IACTs are limited to a small duty cycle of night-time measurements with breaks during full moon. Also, contrary to space-based instruments,

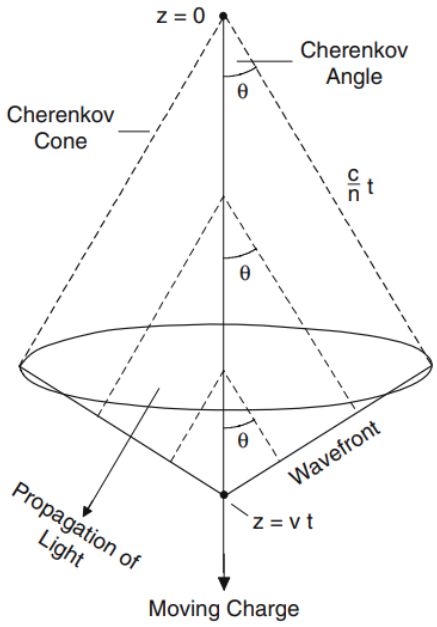

Figure 2.8: Schematic showing the basic geometry of the Cherenkov light created from the particles in an EAS. Figure taken from Grieder (2010).

IACTs are not able to observe the whole sky. Depending on their location on Earth, each IACT array has a blind spot.

A further limiting factor for the observation of γ-ray sources with IACTs is the limited FoV, with current arrays possessing a FoV of $< 6°$. This results in the need for pointed observations, where the telescope is pointed to observe only a small portion of the sky. This is usually done by introducing a time-binning which divides the total observation time per night into shorter observation 'runs'.

The pointing of these observations is usually done in 'wobble' mode, which means the camera is not directly pointed at the target of interest but pointed slightly offset from the target source in alternating directions. In a successive observation run of the same target, the wobble offset is chosen in a different direction along Right Ascension or Declination. This creates a grid of four pointing positions around the source. This offset helps to mitigate potential gradients in the camera and makes background estimation possible (for more information see Chapter 3.1). Depending on the energy range that is studied, it is also not advisable to observe at zenith angles higher than 60°, as the increased path length through the atmosphere significantly attenuates the Cherenkov light yield and increases the background signal towards low energies.

Cherenkov telescopes image in angular space. This means that photons emitted under the same angle, regardless of their point of origin, are focused onto the same spot on the camera by the telescope's optical system. For a narrow air shower initiated by a γ-ray this results in a characteristically elliptical camera image, due to the low transverse momentum of the secondary particles, as well as the inclination of the shower axis to the telescope. The length of the elliptical parametrisation can be used to estimate the point of first interaction, as it corresponds to the height difference between the bottom and the top of the shower.

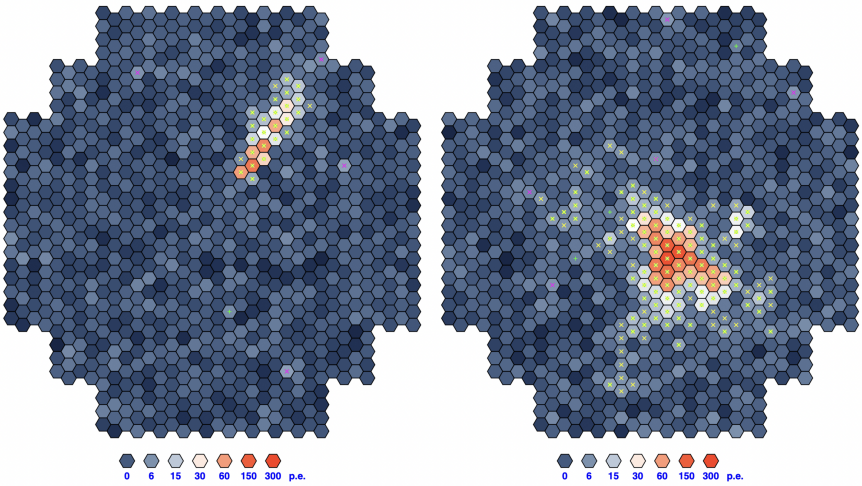

Figure 2.9: Geometrical differences between the images of a γ-ray-induced shower (left) and hadron-induced shower (right) as imaged by an IACT. Figure taken from Völk and Bernlöhr (2009).

Contrary to the narrow, elliptical images for the γ-ray initiated showers, the more numerous hadronic showers result in a more irregular image due to the large transverse momentum given to the secondary particles, which directly affects the angular distribution of the Cherenkov light and the presence of subshowers. The differences in spatial distribution between hadronic and electromagnetic air showers in the camera of an IACT are shown in Figure 2.9.

Due to the large extension of the Cherenkov cone of the shower it is not feasible to build a telescope with a collection area that is able to collect all light from the shower. As a compromise, multiple IACTs can be combined to form a telescope array. These arrays consist of a number of telescopes spread over a large area. For IACT arrays, the trigger criterion is typically set to a certain number of telescopes reaching a trigger threshold within a certain time window. The number of telescopes triggering on the same air shower is referred to as multiplicity. Requiring multiplicity > 1 helps to capture more of the air shower to reconstruct the location of the shower core and distinguish between hadronic and leptonic air showers and avoid triggering on night sky background (NSB) light. In the case of IACTs, this background light consists of light pollution, moonlight or starlight, or air glow from excited nitrogen atoms in the atmosphere.

Due to the above-mentioned restrictions like the necessity of pointed observations and reduction of light pollution, much consideration needs to be done when choosing a location for an IACT.

A further limiting parameter is that the height of the shower maximum depends on the energy of the primary γ-ray or cosmic ray (Equation (29)). For old showers where ionization losses have taken over, the shower fades out slowly with increasing atmospheric depth, and only the muons and neutrinos reach sea level. In order to observe a large portion of the shower and lower the energy threshold for both IACTs and Water Cherenkov Detectors (see Section 2.2.4), it is therefore vital to not only

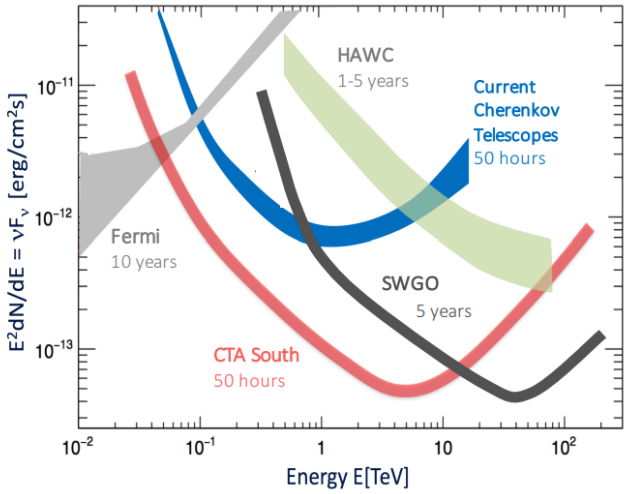

Figure 2.10: Point-source sensitivity curves for current IACTs, compared to Fermi-LAT and current Water Cherenkov Telescopes. Figure taken from Hinton and Ruiz-Velasco (2020).

minimize light pollution but also place the detector at a sensible altitude. While WCDs should be located close to the shower maximum, the optimal height for IACTs is at a lower altitude of $\sim 2000\,\mathrm{m}$ to maximize Cherenkov light collection efficiency while maintaining a sufficiently large detection area and managing background contamination (Szanecki et al., 2014). The magnetic field strength of the earth also has to be taken into consideration when choosing a potential site, as it deflects charged particles in the air shower, broadening the shower unnecessarily.

The first IACT array to start operating was the Whipple Observatory, which was built in Arizona. It observed the γ-ray sky in an energy range from 300 GeV to 10 TeV and made its first discovery, the Crab Nebula, in 1989 (Weekes et al., 1989). Since the beginning of ground-based γ-ray observations with the Whipple observatory, many other IACTs have started to operate, with the current field being dominated by the Very Energetic Radiation Imagaing Telescope Array System (VERITAS) in Arizona (Bradbury, 1999), the Major Atmospheric Gamma Imaging Cherenkov Telesopces (MAGIC) in La Palma (Lombardi, 2011) and the High Energy Stereoscopic System (H.E.S.S.) in Namibia (Aharonian et al., 2006a). In the future, the Cherenkov Telescope Array Observatory (CTAO) will be built in Chile and La Palma. This addition is expected to result in great improvements in our knowledge of the γ-ray sky by significantly enhancing the sensitivity compared to the current generation of IACTs (Morcuende et al., 2023). The sensitivity for the current generation of ground-based detectors, taking systematic errors into account, compared to the sensitivity of Fermi-LAT and CTAO is shown in Figure 2.10.

2.2.4 Particle Detector Arrays

In contrast to Cherenkov Telescopes, particle detector arrays directly detect secondary particles in order to sample the shower distribution. To observe a large number of secondary particles, these detectors usually cover areas ranging from $10^4\,\mathrm{m}^2$ to $10^6\,\mathrm{m}^2$

and are built at $\sim 4000\,\mathrm{m}$ to be located close to the shower maximum. They typically consist of a large number of different detection stations. These, in turn, consist of scintillation plates coupled with PMTs, Resistive Plate Chambers (RPCs), or water tanks that observe Cherenkov light from the passage of secondary particles through the water. The detectors use particle densities and their arrival times to reconstruct the shower development and primary particles. The total energy deposited in either the water tanks or the scintillators is compared to Monte Carlo Simulations to obtain the energy of the primary particle.

The angular resolution of these detectors is limited by their time resolution, which needs to be able to resolve the arrival time of the shower front, but especially by large fluctuations in the height of the first interaction, which can fluctuate up to one radiation length for electromagnetic particles ($X_0 = 37\,\mathrm{g/cm^2}$). The angular resolution improves for higher energies since more secondary particles are produced in the shower, which reduces statistical uncertainties in the timing and position measurements.

The energy threshold of the detector depends on both the detection area and the spacing between the detection stations. A lower threshold can be achieved by a dense array, which eliminates sampling fluctuations but also drastically increases the cost. Decreasing the detector area, however, leads to losing information about the shower from the outer parts of the cascade. Due to this trade-off, arrays are often built with a dense inner array and a sparse outer array. The detection area also limits the maximum energy up to which particles can be detected since measuring showers extended outside of the detector increases the uncertainty of the energy estimation. In the case of very high particle energies ($> 10\,\mathrm{PeV}$), the particle density near the shower core can additionally saturate the detectors, further complicating the detection capabilities.

Since these detectors detect the air shower particles directly and do not rely on the Cherenkov light produced in air, they have a 24-hour duty cycle and a wide FoV, surveying the whole visible sky. The downside of these detectors is that their angular resolution is on the scale of degrees compared to sub-degree resolutions achieved by IACTs. A thorough review of particle detector arrays is given in Bambi and Santangelo (2024), while a brief overview of two currently operating particle detector arrays, HAWC and LHAASO, is given below. Public data from both arrays will be used in the analysis presented in Chapter 5.

The High-Altitude Water Cherenkov Observatory (HAWC) (Abeysekara et al., 2023) is a WCD consisting of 300 Water Cherenkov tanks of 5 m height and 7.32 m diameter. Each tank has 4 upward-facing PMTs mounted at the bottom and contains more than 10 radiation lengths of water. This depth guarantees that incident leptons are fully absorbed and the detector acts as a calorimeter. HAWC can detect γ-rays and cosmic rays between $\sim 100\,\mathrm{GeV}$ and a few 100 TeV. The energy range is limited at the lower end by ionization losses in the shower and for the highest energies by the limited detection area. HAWC has an angular resolution of $\sim 0.5^\circ$ at 1 TeV and monitors around 15% of the sky at any given time.

The new generation of particle detector arrays has been inaugurated with the Large High Altitude Air Shower Observatory (LHAASO) in China (Cao et al., 2019). The array consists of a $1.3\,\mathrm{km^2}$ particle detector array (KM2A), a $78000\,\mathrm{m^2}$ Water Cherenkov Detector array (WCDA), and 18 air Cherenkov telescopes (WFCTA). KM2A is an array of scintillator detectors designed to detect γ-rays with energies between 30 TeV up to 1 PeV, as well as $0.01 - 100\,\mathrm{PeV}$ cosmic rays. The angular resolution is $\sim 0.5^\circ$

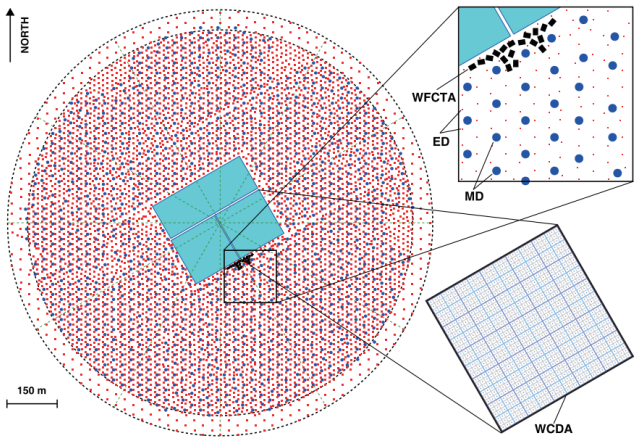

Figure 2.11: Schematic of the Layout of LHAASO, indicating the different detectors. Figure taken from Cao et al. (2019).

at 100 TeV. Also part of KM2A is an array of muon detectors, which are underground water Cherenkov detectors. These detectors are effectively shielded from all particles in the shower except penetrating muons. The muon tanks are used as an effective tool for background rejection.

The WCDA consists of three water pools filled with purified water. Those pools are equipped with $\sim$ 3000 PMTs placed at their bottom. They can detect γ-rays from 100 GeV up to 100 TeV. The angular resolution of the WCDA is limited by the timing resolution as well as the spacing between the PMTs at the bottom of the pools, effectively resulting in a resolution of $\sim 0.3°$ at 1 TeV.

The WFCTA is an array of Cherenkov Telescopes (CTs) with a FoV of 16°, which measure Cherenkov light from cosmic-ray induced air showers between 10 TeV and $\sim$ 1 PeV. Due to their focus on highly energetic cosmic-ray events, the detectors have a 24 hr duty cycle with the goal to study the cosmic ray energy spectrum and composition.Their large FoV is realised by employing lenses instead of mirrors and makes these telescopes ideal for identifying the geometry and composition of the air shower from the secondary particles produced at lower altitudes and reconstructing the primary particle. The WFCTA is used for composition studies but also contributes significantly to the background rejection for measurements of the WCDA and KM2A. A schematic of the layout of LHAASO can be seen in Figure 2.11.

Figure 2.12: The H.E.S.S. array in Namibia is arranged along a square with a side length of 120 m and four telescopes, each featuring segmented mirrors arranged in a Davies-Cotton design. The fifth telescope is placed in the center of the array and features segmented mirrors arranged in a parabolic design. Image Credit: Maria Clementina Medina

2.3 High-Energy Stereoscopic System

The High Energy Stereoscopic System (H.E.S.S.) is an IACT array located at a height of 1835 m above sea level in the Khomas Highlands in Namibia. Initially, the array consisted of 4 identical IACTs (CT 1-CT 4), which are arranged in a square with a side length of 120 m. This side length was chosen with respect to the expected Cherenkov light pool diameter of ~ 250 m in air, in order to facilitate the detection of the shower by multiple telescopes and maximize the effective detection area.

Each of the four telescopes features a large reflector dish with an effective mirror surface area of 107 m^2 and a total reflector diameter of 13 m. Each reflector dish consists of 382 small and identical hexagonal mirrors arranged to approximate a parabolic shape (Fegan, 2024). The shorter focal length of each segment helps reduce spherical aberrations, leading to a sharper image on the camera, and is more cost-effective and easier to install. Each of these mirrors is pointed towards a common focal point, where a fast-imaging camera is located. A schematic of the design is shown in Figure 2.13. With this geometry, the four telescopes are able to observe a FoV of 5°. Further details of the optical structure are given in Bernlöhr et al. (2003).

The fast-imaging cameras consist of 960 individual pixels, each of them featuring a FoV of 0.16 °. Each pixel consists of a Winston cone, which is a hexagonal light guide focusing the light on a round PMT. While the camera reads out the signal, no further photons can be measured. This results in a short time window in which no new data can be acquired. This time window is often referred to as deadtime, and the total observation time needs to be corrected for it. The deadtime for these cameras is estimated to be around $\sim 450\,\mu$s (Giavitto et al., 2017).

The readout is triggered based on the signal seen in different sectors, which are groups of 64 neighbouring pixels. The H.E.S.S. telescopes can be operated under two

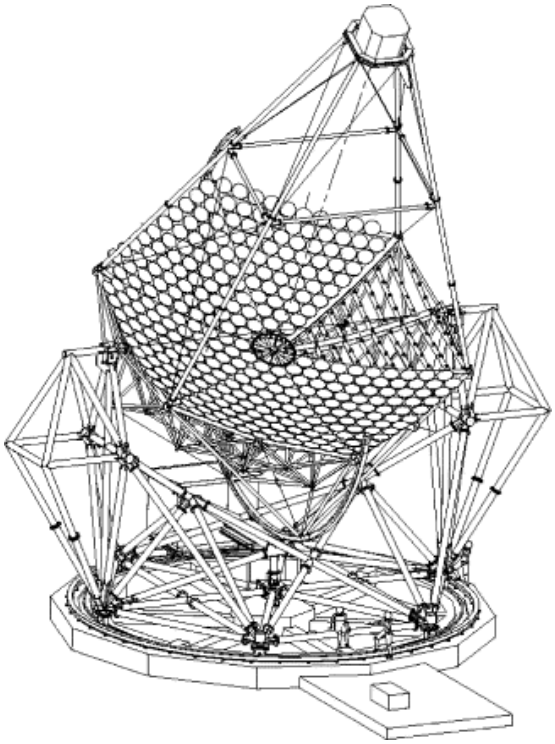

Figure 2.13: Schematic of the H.E.S.S. telescopes showing the Davies-Cotton design of the reflector dish. Figure taken from Bernlöhr et al. (2003)

different telescope triggers. The monoscopic (mono) trigger acts when a number of pixels within a sector all observe a signal above a threshold within a nanosecond window. The stereoscopic trigger acts when two telescopes send a monoscopic trigger within a coincidence window. The telescopes are usually operated using the stereoscopic trigger. Detailed information on the trigger system is given in (Funk et al., 2004).

The design introduced above is referred to as Phase-I (Aharonian et al., 2006b). Since the commissioning of H.E.S.S. in 2003, Phase-II commenced with the addition of a fifth telescope (CT 5) in the centre of the array in 2012 (Bolmont et al., 2014). The layout of this array can be seen in Figure 2.12. CT 5 has a light collection area of $614\,\mathrm{m}^2$, with a reflector diameter of 28 m, a FoV of $3.2\,^\circ$ and a camera equipped with 2048 pixels. Instead of using the Davies-Cotton design, a parabolic mirror was introduced, which reduces the slight time delay that is introduced due to the varying optical path lengths from the different Davies-Cotton segments. This updated mirror design, as well as the larger light collection area, allows CT 5 to reduce the energy threshold of the system from $\sim 100\,\mathrm{GeV}$ to $\sim 30\,\mathrm{GeV}$.

The camera of CT 5 follows the same design as the camera of the four smaller telescopes, just with an increased number of PMTs to 2048. Applying a stereo trigger between one of the smaller telescopes and CT 5 has increased the overall array trigger rate, since its increased sensitivity to lower energetic photons allows the telescope to observe air showers which would otherwise have only triggered one of the small telescopes and been rejected as mono triggers.

This increased trigger rate resulted in the need for a further hardware upgrade in 2016 (Giavitto et al., 2017). Allowing for a deadtime of $450\,\mu\mathrm{s}$ was acceptable for

CT 1-CT 4, since the telescopes observed higher energetic air shower. After adding CT 5, however, this large deadtime results in the loss of a substantial fraction of the signal. To reduce the deadtime, upgrades to the cameras were done by installing the NECTAR analogue memory chip (Naumann et al., 2012), which was able to decrease the deadtime to $\sim 7\,\mu$s. This third hardware phase of the H.E.S.S. array is referred to as Phase-IU.

An additional hardware update for the camera in CT 5 followed in 2019, where an advanced prototype of FlashCam, developed for CTA, was installed in CT 5. The camera features 1758 PMTs, still connected to Winston cones, but triggers without any deadtime(Bi et al., 2022).

2.3.1 Calibration

The calibration of the PMTs and the electronic's response is essential for a successful air shower reconstruction. The calibration is extensively described in (Aharonian et al., 2004), and a summary is given below.

Camera Calibration

In order to gauge the random noise created due to spontaneous or thermal emission of electrons in the PMTs or electronic noise in the amplifier, pedestal measurements are conducted every few thousand runs. The pedestal, which is the mean Analog-to-Digital Converter (ADC) value of the camera without any light, is measured and recorded while the shutters of the camera are closed, and the result per pixel is later subtracted from the PMT signal.

Another parameter that needs to be taken into account is the variability of the light transmission of the Winston cones and the detection efficiency of the PMTs. This varies for every pixel and needs to be taken into account when reconstructing the energy of the Cherenkov photons. For this purpose, a flat field coefficient F_i is introduced. A LED flash, which is positioned in the centre of the mirror dish, is used to illuminate the camera, and the deviation from the mean value across all pixels is estimated for every pixel and stored. These flat fielding runs are also repeated every few thousand runs.

The gain, or the amplification factor, of the telescopes is measured by shining an LED flasher onto each pixel. This LED flash is calibrated to generate exactly one photoelectron (p.e.) in this pixel, and the result per pixel is recorded. The gain is then acquired by fitting a Poissonian signal convoluted with the instrument response to the pixel-wise distribution of ADC counts. H.E.S.S. has a high gain channel for faint Cherenkov signals and a low gain channel, which is used for air showers produced by high-energetic γ-rays, which would saturate the camera if the high gain channel were used. Both channels are calibrated using the single photoelectron measurements.

Optical Efficiency

Besides accurately interpreting the signal from the camera electronics, it is also important to take losses from other factors, such as reduced reflectivity of the mirrors from dust collection and transmissivity of the Winston cones, into account. These factors are considered by monitoring the optical efficiency of the telescopes.

This can be achieved by using the distinct signal observed from muons in hadronic air showers. With a lifetime of 2.2 s (Bambi and Santangelo, 2024), the main energy loss

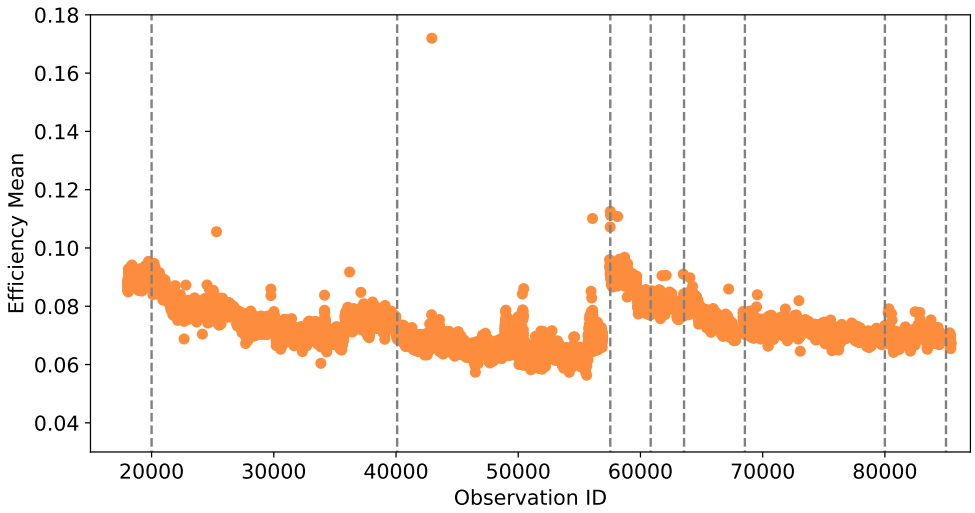

Figure 2.14: Evolution of the muon efficiency of CT 3 for the data acquisition in Phase I. Only the muon efficiency for observations for which more than 52 muons were observed is depicted. This threshold is set to filter observations with technical problems and corresponds to the $2\,\sigma$ deviation from the mean number of muons per run in Phase I. The boundaries of the optical phases are shown in gray.

channel of muons produced by the decay of mainly charged pions is ionization rather than decay. Therefore, a significant fraction of muons reaches the ground and due to their large mass, they do not significantly suffer from multiple Coulomb scattering. This results in a direct propagation to Earth in a straight line. Because the Cherenkov telescopes image in angular space, the absence of scattering causes all Cherenkov photons emitted at a fixed angle Θ_{Ch} around the muon's path to reach the reflector under approximately the same incident angle and the light is focused on the same point in the focal plane of the camera. Since the complete azimuth component of the Cherenkov light pool is imaged, the signal in the camera has a characteristic ring-shape, with the ring radius corresponding to Θ_{Ch}. Vacanti et al. (1994) showed that this ring radius is directly related to the number of observed photons. This relation can then be used to compute the muon efficiency of the telescopes $\eta = N_{\mathrm{obs}}/N_{\mathrm{exp}}$, with N_{obs} the number of observed photons and N_{exp} the number of expected photons.

The development of the muon efficiency of the H.E.S.S. telescopes over Phase I is shown in Figure 2.14. The muon efficiency decreases over time mainly due to the degradation of the reflectivity of the mirrors as well as Winston cones. This is a result of dust accumulating on the surface and UV degradation of the mirrors. Upward jumps in the muon efficiency are correlated with changes in the hardware of the experiment or cleaning of the mirrors or Winston cones. A period of relatively stable muon efficiency is referred to as optical phase, and a constant optical efficiency is assumed. The boundaries of these optical phases are shown as grey dashed lines in Figure 2.14.

2.3.2 Event Reconstruction

After the calibration of the instrument, an accurate understanding of the energy deposited in the camera is gained. From this, the properties of the primary particle,

which induced the extensive air shower, can be reconstructed. This section will give an overview of the steps necessary to process the data which will later be analysed.

Image Cleaning

Before the parameters of the primary γ-ray are reconstructed from the camera signal, the images are cleaned. In this step, signal which is induced by NSB, the passage of bright stars or camera noise, is removed. This is necessary to ensure that these random signals are not included in the parametrization of the emission and the reconstruction of the primary particle energy. The cleaning is done by retaining only signal in pixels that are above a certain threshold and have at least one neighbouring pixel that is above a certain threshold. The pixel threshold is chosen such that no NSB pixel passes the cut. For H.E.S.S. in its current operation, it is standard to only retain signal in pixels which themselves show signal above 5 pe and have one neighbouring pixel which has above 10 pe, or vice versa (Aharonian et al., 2006b).

Hillas Reconstruction

The standard approach used for the reconstruction of the γ-ray properties in H.E.S.S. is the Hillas parametrization, which extracts key features of the Cherenkov signal through geometrical parametrization (Hillas, 1982). In order to gain a good understanding of the dependence of the geometry of this elliptical approximation on the properties of the γ-ray, Monte Carlo simulations are used to generate lookup tables that relate the width and length extracted from the signal to the γ-ray properties. The `CORSIKA` package introduced in Heck et al. (1998) is used to simulate the propagation of electromagnetic and hadronic air showers in the atmosphere and the `sim_telarray` software package (Bernlöhr, 2008a) is used to simulate the detector response for different detector conditions, incident particle energies, as well as zenith and azimuth angles.

Direction Reconstruction

The elliptical shape of the image is created because the majority of particles travel along the shower axis without gaining a large transverse momentum (see Section 2.2.1). The major axis of the ellipse in the camera can, therefore, be used to reconstruct the shower axis, which is the extension of the initial direction of the primary particle. The precision of this reconstruction can be increased significantly by combining the information about the shower axis from more than one telescope. A schematic of this is shown in Figure 2.15.

Another important parameter, the impact parameter, can be gained from the major axis of the elliptical parametrization as the distance between the intersection of the shower axis with the ground (impact point) and the telescope. For vertical showers, this distance is almost zero, while increasing with increasing zenith angle. When this information is combined with timing information (an increase in zenith angle corresponds to a delay in triggering between different telescopes) as well as the orientation of the major axis, the zenith angle of the primary particle can be reconstructed.

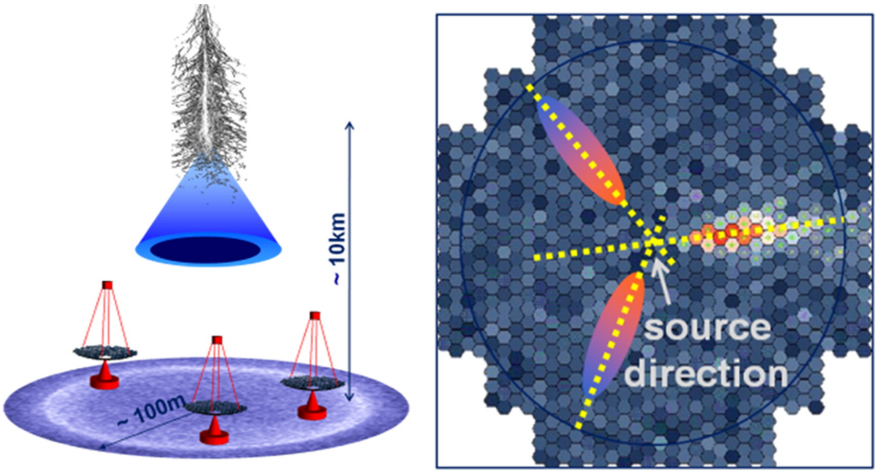

Figure 2.15: Left: Schematic of the principle of air shower detection using Cherenkov telescopes (not to scale). Right: Example of a cleaned shower image, and the direction reconstruction using the principle of stereoscopy. Figure taken from Naumann et al. (2012)

Energy reconstruction

The energy reconstruction is based on the image amplitude, which quantifies the total charge observed in all pixels that survive the cleaning and impact distance to the camera centre. The result is then scaled with the optical efficiency of the telescope and together with the impact parameter and geometry of the parametrized signal, compared to the lookup tables computed from Monte Carlo simulations. The result is averaged over all participating telescopes.

2.3.3 Background Rejection

The Hillas parameters are not just used to reconstruct the primary particle properties, but also for background rejection. As mentioned in Section 2.2.1, hadronic air showers result in less well-behaved camera images due to the large spread of the secondary particles. To reject events with such a broad distribution on the camera, the properties of the signal from the observations are again compared to the results in the lookup tables. This is done for all participating telescopes i and a mean reduced scaled width (MRSW) and length (MRSL) are computed for every event:

$$\mathrm{MRSW} = \frac{1}{N} \sum_{i}^{N} \frac{p_i - p_{\mathrm{exp,i}}}{\sigma_i} \,, \tag{36}$$

with N the number of telescopes, p_i either the length or width of the ellipse, $p_{\mathrm{exp,i}}$ the expected value from the simulations and σ_i the spread derived from the lookup tables. Applying a cut on MRSL, MRSW and image amplitude helps to distinguish between the two different types of air showers. An additional parameter that is used for background rejection is a Θ^2-cut. Θ is the distance between the reconstructed direction and the true direction, which is defined as the position of a known or suspected γ-ray source.

By limiting an acceptable Θ^2 to be slightly larger than the expected source, a large portion of background, which is flatly distributed over the camera, can be reduced.

Especially in the low energy regime, it is not always easy to distinguish hadronic from electromagnetic air showers. By applying tighter selection criteria on these parameters, a higher background rejection can be achieved. However, this also results in a higher rejection rate of true γ-ray events. It is, therefore, advisable to use different thresholds for studies that focus on observing largely extended sources than for studies which observed, e.g. transients, where it is important to retain as many γ-rays as possible. The different thresholds between which an event is accepted as γ-ray can be seen in Table 2 in Aharonian et al. (2006b). For extended sources, the Θ^2 is dropped entirely.

Since these thresholds have been defined and H.E.S.S. started data acquisition, several improvements have been made. The γ-hadron separation is now done using a boosted decision tree (BDT) machine learning algorithm. The BDT is trained on MRSL and MRSW, as well as the shower maximum and an average spread in energy reconstruction. This training is done in different energy and zenith angle bands and the classifier is used for background rejection. Ohm et al. (2009) has shown that this implementation has increased the sensitivity by 20%. Another major improvement, especially for direction reconstruction, was the implementation of the Image Pixel-wise fit for Atmospheric Cherenkov Telescopes (ImPACT). Instead of just comparing image parameters with simulations, ImPACT is a fit of image templates, generated in simulations, to the actual shower image. Parsons and Hinton (2014) showed that this fit improves the angular resolution over all energies and the energy reconstruction by 50% in the low energy range. The use of this algorithm even decreases the time necessary to detect a source by $\sim 50\%$ for a variety of sources.

2.3.4 Instrument Response

The response of a telescope to an incoming signal is described by the Instrument Response Functions (IRFs). These functions are folded with the reconstructed signal to estimate the true properties of the signal. For observations to be described by the same IRFs, a stable optical efficiency needs to be assumed. For H.E.S.S., this is done by recomputing IRFs for every optical phase.

IRFs consist of a point spread function (PSF), effective area (A_{eff}) as well as an energy dispersion ΔE. The instrument response can be calculated as:

$$R(p, E|p_{\text{true}}, E_{\text{true}}) = A_{\text{eff}}(p_{\text{true}}, E_{\text{true}}) \times \text{PSF}(p|p_{\text{true}}, E_{\text{true}}) \times \Delta E(E|p_{\text{true}}, E_{\text{true}}) \quad (37)$$

with p the measured direction of the event and p_{true} the true direction.

The PSF describes the distribution of Θ^2 with energy. It is computed from simulations for observations of point-like sources. For H.E.S.S., it is assumed to be around 0.1° at a zenith angle of 10° (Aharonian et al., 2006b).

The effective area corresponds to the area in which the array is sensitive to signals from the air shower, accounting for detection efficiency and instrumental response. This area is energy dependent, approaching a constant value for the highest energies as the showers become brighter. It is defined as:

$$A_{\text{eff}}(\Theta, E, \Phi) = A_{\text{geom}} \cdot \eta(\Theta, E, \Phi)\,, \quad (38)$$

with A_{geom} the area of the detector, which in case of IACT arrays corresponds to the sum of the physical area of the mirrors of the telescopes, and the detection efficiency $\eta(\Theta, E, \Phi)$. The effective area decreases for lower energies since the Cherenkov light

pool is less extended. The same dependence is observed for increasing zenith angles due to light attenuation. The effective area ties directly into the reconstruction of the γ-ray flux, since the event rate is given as:

$$R = \int A_{\text{eff}}(\Theta, E, \Phi) \cdot \Phi(E) \mathrm{d}E \,, \tag{39}$$

with Φ the γ-ray flux from a observed source.

The energy dispersion is given as the deviation between reconstructed energy E_{reco} and the true energy E_{true} from simulations:

$$\Delta E = \frac{E_{\text{reco}} - E_{\text{true}}}{E_{\text{true}}} \,. \tag{40}$$

An example energy dispersion matrix can be seen in Figure 2.16. The mean of the distribution for each true energy is referred to as the energy bias and shown as black line in Figure 2.16. The curve shows that the discrepancy between true and reconstructed energy is very large towards low and very high energies. For low-energy events, E_{reco} is strongly overestimated. This effect is caused by the low light yield of the Cherenkov pool at these energies. Not only does the chance to include more hadronic events increase, the chance of stereoscopy measurements also decreases because of the smaller extension of the light pool. This, as well as intrinsic fluctuations in the shower development, increases the uncertainty of the energy reconstruction. This increase in systematic effect becomes a problem since the event reconstruction includes a cut on image amplitude, which means that only fluctuations toward higher energies are kept. For high-energy events, E_{reco} is underestimated. This effect is caused by the limited detection area, which, for these highly energetic events, is not able to catch the whole Cherenkov light pool, as well as the saturation of the detector. Because of these edge artifacts, it is common to include a cut on the energy bias, discarding low and high energy events with more than 10% energy bias for the analysis.

2.3.5 Systematic Uncertainties

The steps outlined above to reconstruct the γ-ray signal from the camera image show that using IACTs to observe γ-rays is no easy task. The response of the telescopes to varying observation conditions is obtained from Monte Carlo simulations and applied to the respective observation run. It is, however, not possible to sample a dense grid of observation conditions and create IRFs for all possible combinations. The IRFs of an observation run are obtained by interpolating between Monte Carlo-generated IRFs. With this method, a satisfactory result can be obtained, but three main contributions to the uncertainties remain: the development of the shower in the atmosphere, the response of the optical system, and the camera response. These systematic uncertainties, if not accounted for, introduce significant biases in the reconstructed spatial distribution of the γ-rays and the source flux, which are critical parameters for studying astrophysical sources.

Telescope Response

A large part of systematic uncertainties is the response of the optical system. The mirrors of the reflector dish degrade over time due to aging or environmental factors like

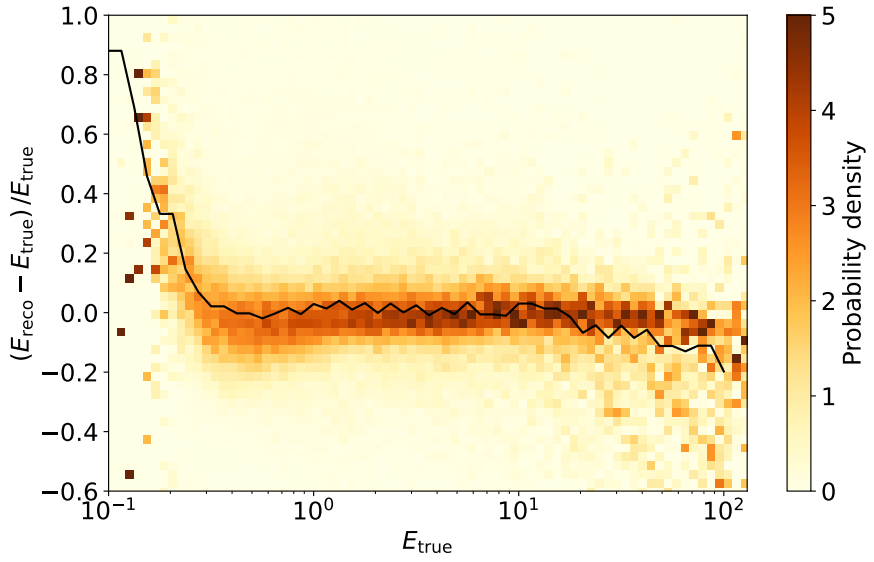

Figure 2.16: Example distribution of the energy dispersion for one observation run. The energy bias is indicated by the black line.

UV exposure. Additionally, both the mirrors as well as the Winston cones accumulate dust over time, worsening the mirror reflectivity and the throughput of the cones. This results in a dip in optical efficiency. In the case of rain, or just regular cleaning, the optical efficiency improves. This can, in part, be corrected by using the muon efficiency, a small systematic uncertainty, however, remains.

The camera itself is also a source of systematic uncertainty, as each PMT has a different optical response. This is in theory, accounted for by running flat fielding and single-pe observations. These are, however, only performed sporadically and changes arising in between those periods can lead to systematic changes in the camera response.

Event Reconstruction

The atmosphere is the largest of all systematic uncertainties. The energy of the primary γ-ray is reconstructed from the intensity of the detected shower. As mentioned in Section 2.2.1, the energy deposited in the shower particles at a given height is directly influenced by the density of the atmosphere. Using simulations with a wrong aerosol content, which largely influences the atmospheric transparency to optical light, leads to over- or underestimating the energy of the primary particle. Changes in the atmospheric density correspond to variations in pressure, temperature, or humidity and need to be considered in the choice of simulations. An additional factor that needs to be taken into account is the light attenuation from clouds and dust.

Another important factor is the difference between the reconstructed and the true source position. A discrepancy cannot only occur due to uncertainties in the reconstruction of the shower axis, but also due to offsets of the pointing position of the camera from the nominal pointing. This mainly happens due to bending of the telescope structure under the weight of the heavy camera. The effect is estimated by the acquisition of dedicated observation runs to compare the measured position of known bright stars with their catalogue position. For H.E.S.S. this uncertainty has been estimated to 20″

(Acero et al., 2010).

Background Rejection

A major aspect of the systematic uncertainties is the γ-hadron separation. The wrong classification of many hadronic air showers as being induced by γ-rays can lead to signal attenuation due to the increased background noise and induce a bias in the reconstructed spatial distribution and source spectrum. The removal of too many γ-ray induced events leads to a systematic underestimation of the γ-ray flux from the source. A more thorough discussion of systematic uncertainties on the estimation of the remaining γ-like background is given in Section 3.1.

2.3.6 3D Maximum-Likelihood Analysis using `gammapy`

In the beginning of data analysis with H.E.S.S. and other IACTs, the source properties have been extracted using proprietary analysis software. For H.E.S.S., this has been the HESS Analysis Package (HAP) (Aharonian et al., 2006b). In recent years, however, the development of software tools has gone more towards open source tools to increase the availability and facilitate the joint analysis of data from different instruments. This has been realized in the `gammapy` package (Donath et al., 2023; Deil et al., 2020). This section will be a short description of the analysis workflow employed in `gammapy`, which is used in the following Chapters. A more thorough description can be found in Donath et al. (2023)

After a set of observation runs has been selected, the events and their corresponding IRFs are filled into a common physical coordinate system, which is referred to as `Map geometry`. This `Map geometry` can have up to 3 dimensions, two spatial and an energy dimension. After this step, the residual γ-like background is estimated and subtracted from the number of events (for more information see Chapter 3.1). The events, together with the IRFs and the background, are then bundled together in a `Dataset`. Different models can be assigned to this dataset. For a 3d analysis, these models are convolutions of a spatial and a spectral model. After a model has been assigned to the dataset, its parameters can be optimised through a maximum likelihood fit.

The maximum likelihood analysis is a way to quantify if a Hypothesis $\mathcal{H}$ can be supported using the given data. In order to identify the set of parameters θ of a model $\mathcal{M}(\theta)$ which describes the observed γ-ray emission best, the likelihood function $\mathcal{L}(\mathcal{H})$ is maximized (Fisher, 1922a). After the best parameter set for a given model has been identified, different models can be compared by calculating the ratio of the likelihoods of the models:

$$\lambda = \frac{\mathcal{L}(\mathcal{M}_0(\theta_0))}{\mathcal{L}(\mathcal{M}_1(\theta_1))}\,, \tag{41}$$

with $\mathcal{L}(\mathcal{M}_0(\theta_0))$ the null hypothesis and $\mathcal{L}(\mathcal{M}_1(\theta_1))$ the alternative hypothesis. The likelihood ratio test (Fisher, 1922b) can, however, only be used when the two tested models are nested. The ratio can then be translated into a significance σ, by computing the test statistics (Wilks, 1938):

$$TS = -2\log(\lambda)\,, \tag{42}$$

and using the relation $TS \sim \chi^2_k$ with k the number of free parameters of the model. From this, a p-value can be determined by integrating the χ^2 distribution from the

observed TS value. The p-value gives an estimation of how likely it is that the observed signal could be produced by background fluctuations. The significance is then computed by identifying the number of standard deviations for which the area in the upper tail of the Gaussian distribution is equal to the p-value. For γ-ray data, the null-hypothesis is often chosen as a background-only hypothesis, and the significance of adding a source model is computed. It can, however, also be used for nested models directly or by comparing the TS between a background only and different source models hypotheses.

This process can be done for individual observations in a joint likelihood analysis, which gives the total likelihood as a sum of the log-likelihoods for each observation run or in a stacked analysis, where the IRFs are averaged over the observation runs and only one log-likelihood is computed over all observations. The latter case is often used to reduce computation time for large datasets.

3 Background estimation for highly extended sources

Recent results from the Water Cherenkov Detectors, HAWC (Abeysekara et al., 2017a) and LHAASO (Cao et al., 2023a), have demonstrated that while IACTs excel at differentiating and precisely measuring the extension of γ-ray sources due to their superior angular resolution, they struggle with detecting large-scale extended emission. This is mainly caused by the limited FoV of IACTs, which, unlike survey instruments that continuously monitor the overhead sky, need to be pointed at a specific target and can only observe a region spanning a few degrees. As a result, distinguishing between cosmic ray contamination, diffuse γ-ray emission, and the actual signal is rather difficult in regions around extended γ-ray structures. This can lead to the underestimation of the emission and source extension (Abdalla et al., 2021).

As outlined in Section 2.3.3, the separation of cosmic ray and γ-ray events is no easy task. For IACTs, the application of Boosted Decision Trees (BDTs) has brought significant improvements in this regard, especially at low energies (Ohm et al., 2009). In this method, a series of image parameters obtained from γ-ray simulations and observation runs with no strong γ-ray emission (OFF runs) are combined as input for a classifier. The classifier assigns a probability to every event, indicating whether it is more background-like or signal-like while taking correlations between different parameters into account. The improved separation power is well observable when comparing the overlap of the distributions of the individual parameters for cosmic rays and γ-rays (Figure 3.1 on the left), with the overlap of the output of the classifier (Figure 3.1 on the right). While the application of the BDT algorithm has brought significant improvement in the sensitivity of H.E.S.S. up to 20%, an overlap between the two distributions still remains. The estimation of the remaining contamination from γ-like cosmic rays is a main source of systematic uncertainties and, if done wrong, can introduce major errors in the spectral and spatial analysis of γ-ray sources. This section first outlines classical background estimation techniques for IACTs before it introduces a new method that can be employed in regions containing large, extended γ-ray structures for which classical background estimation cannot be used to obtain precise results.

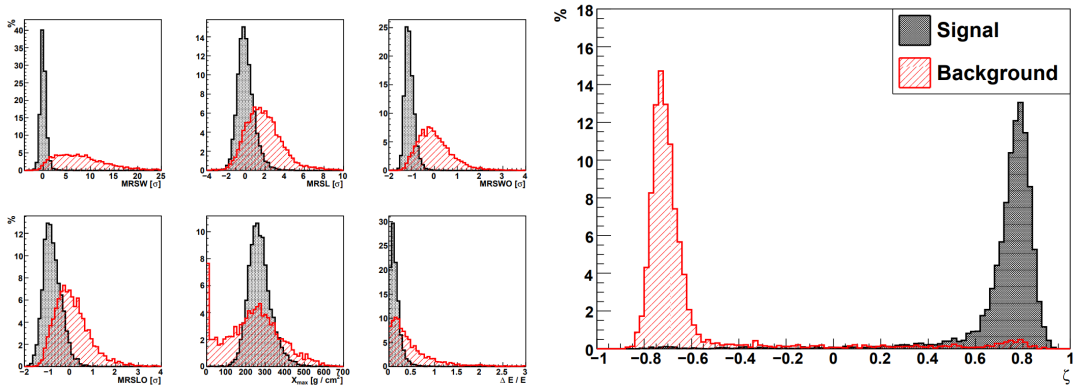

Figure 3.1: Distribution of image parameters from simulated γ-ray and cosmic ray events. Left: Distributions of the six image parameters that are used to train the γ-hadron separation classifier. Right: Distribution of the output parameter of the classifier. Image taken from Ohm et al. (2009).

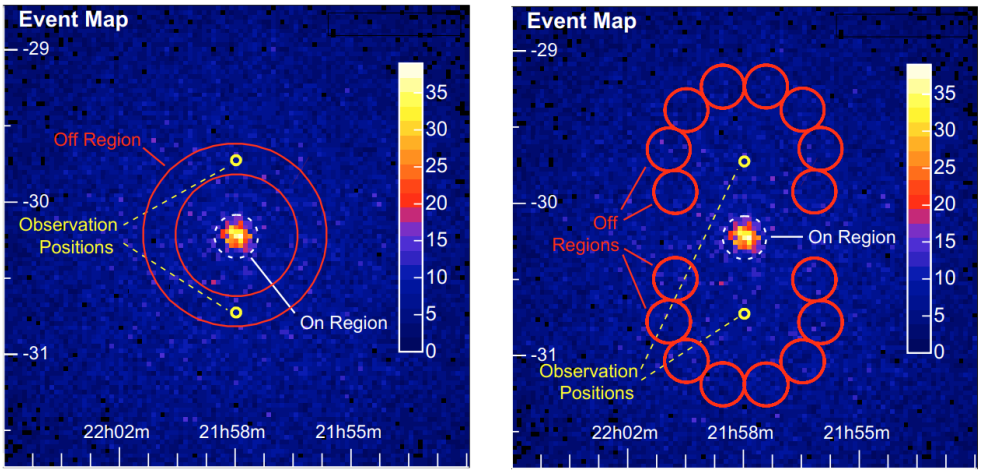

Figure 3.2: Counts map derived from 5 hours of observations on PKS 2155−304. The wobble pointing positions are indicated in yellow, and the background estimation regions are indicated in red. Left: Schematic illustration of the ring background method. Right: Illustration of the reflected regions background method. Figure taken from Berge et al. (2007).

3.1 Classical Background Estimation for IACTs

In order to facilitate background estimation in IACT observation, the wobble-mode technique was introduced. In this method, the telescope alternates between pointing positions that are offset from the source by a small angle in different directions, allowing for observations of the source and empty regions, which are used for the background estimation, at the same time. The number of events from the γ-ray source is estimated from $N_{\text{excess}} = N_{\text{ON}} - \alpha N_{\text{OFF}}$ with N_{ON} the number of counts in a test region, N_{OFF} the number of counts in a empty region in the observation and α a normalisation factor. The normalization accounts for differences in the acceptance of the detector and different zenith angles.

3.1.1 Ring Background Method

In the ring background method, N_{OFF} is estimated from an annular region centered around a trial source position. The ring size is typically chosen such that $\Omega_{\text{ON}}/\Omega_{\text{OFF}} = 1/7$, with Ω the solid angle of the respective region. Here, the normalization factor α can be approximated by the solid angle ratio combined with an additional acceptance correction to account for varying distances between the observation pointing and the pixel positions in the ring. A schematic visualization of this method can be seen on the left in Figure 3.2.

3.1.2 Reflected Regions Background

This method estimates the background from a number n_{OFF} of source-free regions. These OFF regions have the same extension and shape as the ON region. In contrast to the ring background method, where the ring is placed around the trial source position, the reflected regions method uses regions symmetrically distributed around the pointing

positions. An illustration can be seen on the right in Figure 3.2. The number of background estimation regions depends on the extension of the source as well as the number of additional sources in the FoV, with which they must not overlap. Generally, it is recommended to use as many OFF regions as possible. Since the OFF regions are chosen as symmetrically distributed around the pointing position, no variations in the detector acceptance are expected. The normalization is therefore given as $\alpha = 1/n_{\mathrm{OFF}}$.

3.1.3 ON-OFF Method

This method uses separate, dedicated observations of a γ-ray free region to estimate the background. In order to achieve a comparable background rate in the empty field and target observations, it is important that the observation conditions, including atmospheric conditions and observation length, are comparable. This is typically achieved by alternating between observation runs on the target source (ON runs) and OFF runs. These OFF runs are usually acquired from a region offset in right ascension from the source to ensure a comparable zenith angle.

This, however, means that double the amount of data needs to be taken for an analysis. Also, alternation between ON and OFF runs does not ensure that the same observation conditions are present. Due to rapid changes in the atmospheric conditions, like temperature or humidity, as well as changes in the night sky background light or the optical response of the telescope, large systematic errors can be introduced in the analysis. Despite these challenges, this background estimation method is particularly advantageous for analysing regions containing extended emission since it does not require any assumptions about source morphology or detector acceptance to be made.

3.1.4 Background Model Template

The above outlined methods are well-suited for point-like or slightly extended sources in regions with a low source density. For extended sources, however, using the ring background method or the reflected regions background method can introduce significant biases, since the spatial extent depends strongly on the initial guess of the source extension. Both of these methods depend on knowledge of the spatial distribution of the γ-ray source population in the observed region and are, therefore, not particularly suitable for sky surveys. To address these limitations, Mohrmann et al. (2019a) introduced a 3-dimensional background model template. This template is constructed from archival H.E.S.S. observation runs of regions outside of the galactic plane ($|l| > 60\,^\circ$ and $|b| > 5\,^\circ$) to avoid contamination from diffuse γ-ray emission. Its construction is done in bins according to the optical phase of the telescope array, as well as the zenith and azimuth angle, with a linear interpolation between the bins to ensure a smooth transition. Regions containing known γ-ray sources are removed from these observations, and the background event distribution is estimated from the remaining data. The model is then folded with the acceptance of the detector and assigned to every observation.

Because the background model template is constructed from a large number of observations taken under similar conditions, this method is highly stable and suffers little from statistical fluctuations in the background estimate. This stability has also been proven to be beneficial in detecting extended emission around sources, which have previously been categorized as point-like or only minimally extended. One such example

is the analysis of HESS J1813−173, where its application revealed a second, diffuse component (for more information see Chapter **??**).

This template model is, however, still not suitable for detecting large diffuse structures which fill the FoV of the IACTs. In order to account for differences in the observation conditions, which cause discrepancies between the background rate $R_{\mathrm{BG}}*$ of the observations and the predicted rate R_{BG}, described by a power-law model, the template is normalized to each observation outside of γ-ray source regions using:

$$R^*_{BG} = \Phi \cdot R_{BG} \cdot (E/E_0)^{-\delta}\,, \tag{43}$$

where E_0 is the reference energy, and the spectral tilt δ and background normalisation Φ. These are determined through a 3D likelihood fit of the background model template to an emission-free region in the observation. This, however, means that the background model template approach still requires at least some emission-free region in the FoV, otherwise, the diffuse regions of γ-ray emission can be absorbed into the background.

3.2 Run Matching Approach

The overview given above about the background estimation methods used for IACT data analysis shows that only the three-dimensional background template model and the ON-OFF method are suitable for the detection of large extended structures, with both bringing in their own disadvantages. In this work, these disadvantages are alleviated by combining the two approaches. For this purpose, pairs of ON and OFF runs are selected according to quantitative criteria (described in section 3.2.2), and the normalisation of the background model template for each pair is determined from the OFF run. This normalisation is then applied to the ON run. Due to this approach, the background rate is not estimated from just one OFF run, but many. This enables us to decrease the dependence of the background rate on the particular OFF run selected and thus to lower the uncertainty of the background estimate.

The following section outlines the development of this new method using the data structure of the H.E.S.S. array. Since this method relies only on standard Python packages along with the open-source package `gammapy` (Deil et al., 2020; Donath et al., 2023), it is in accordance with the goal of the Very-high-energy Open Data Format Initiative (VODF; Khelifi et al. 2023) to achieve a common, software-independent data format and develop open-source analysis software (Nigro et al., 2021). This also means that the method can easily be adapted to other telescope arrays and is not restricted to the usage by H.E.S.S.. Hereafter, the template constructed in Mohrmann et al. (2019a) is referred to as the 'background model template'; the standard method which has already been employed by the Whipple Observatory as the 'classical ON/OFF method' (Weekes et al., 1989); and the method developed in this work as the 'run-matching approach'. After the development has been outlined, the validation of this pipeline using data on 4 sources from the first H.E.S.S. public data release (H.E.S.S. Collaboration, 2018a), as well as 3 sky regions from which no γ-ray emission is expected, will be described. Some of the information in this section has already been published in Wach et al. (2024).

For the classical ON/OFF method, a comparable system acceptance is the most important factor. While the use of a background model template allows relaxed matching

criteria between the ON and the OFF run with respect to the classical ON-OFF matching, finding a comparable OFF run is nevertheless a critical aspect of the background estimation. For this work, only observations with pointing position at a Galactic latitude of $|b| \geq 10°$ are considered as OFF runs. With these selection cuts, regions including many known γ-ray sources, as well as diffuse γ-ray emission, can be avoided. Furthermore, runs that pass tight quality cuts (see section 3.2.1) are considered, and it is required that all four small telescopes participate in both the ON and OFF run. As small changes of the atmosphere and degradation of the system can be absorbed by the fit of the background model template (see section 3.3), the run pairs do not need to be acquired in the same night but can be up to a few years apart. It is, however, important to match runs using the same hardware configuration. Therefore, optical phases are taken into account. These are periods of stable optical efficiency between abrupt changes due to, for example, cleaning of the Winston cones or mirror recoating (for more information see Section 2.3). Typically, these phases span at least one year for the H.E.S.S. telescopes, therefore enabling the choice of many possible OFF runs for one ON run. The optical phases used for this work can be found in Table A.2.

3.2.1 Data Quality

The data acquired from H.E.S.S. can be reconstructed for different array configurations. The reconstruction can be done for hybrid mode (operation of all 5 telescopes combined), stereo mode (only considering CT 1-CT 4) and mono mode (CT 5 only). For this study, only data acquired in stereo mode is used. For all observations used, the data reduction was performed using HAP, the H.E.S.S. analysis package described in Aharonian et al. 2006b, and reconstructed using the ImPACT algorithm (Parsons and Hinton, 2014). The quality of H.E.S.S. observations can be divided into three categories. Data that were acquired under good atmospheric conditions and show a good system response are categorized as spectral quality runs. Data acquired under non-ideal atmospheric conditions and system response cannot be used to reliably reconstruct the energy of the events but can still be used to enhance statistics of a dataset for source detection. These observations are categorized as detection quality runs. Observation runs failing even these criteria, or observations which are shorter than 10 minutes are categorized as failed runs.

The goodness of the system response for an observation run, and therefore its category, is determined by monitoring different system parameters. To ensure a good stereoscopic reconstruction of the events, a threshold on the participation fraction is set. This parameter is a measure of which fraction of the operational telescopes of the array recorded the event. The functionality of the tracking system of the cameras is monitored using the deviation between the nominal pointing position and the actual pointing of the telescopes as well as the root mean square of the telescope pointing deviation in altitude and azimuth. Bright stars in the FoV of the telescope can cause an excess current in the PMTs and damage them. To avoid this, the transit of bright stars through the camera pixels is predicted, and the relevant pixels are turned off in advance. Other transiting objects like meteors and airplanes might also induce very bright light signals, this is handled by the installation of an over-current protection for the PMTs, which switches the affected pixel off. If the over-current protection triggers for more than 50 pixels or more than 120 pixels in total are switched off per camera,

the observation run is flagged as a failed run.

The quality of the sky conditions is determined from the trigger rate. In case clouds or excessive dust is present, large fluctuations in the trigger rate can be observed due to the absorption of Cherenkov light. This is monitored by looking at the overall trigger rate (`True_Rate_mean`), as well as the deviation between the trigger rate at the start and end of the observation (`True_Rate_Delta_1`), and the steepness of the fluctuations (`True_Rate_Delta_2`). Aside from fluctuations in the trigger rate, the atmospheric quality can also be quantified using the Cherenkov transparency coefficient (Hahn et al., 2014a):

$$\tau = \frac{1}{N \cdot k_N} \sum_i t_i = \frac{1}{N \cdot k_N} \sum_i \frac{R_i^{\frac{1}{1.7-\Delta}}}{\mu_i \cdot g_i}\,, \tag{44}$$

with the number of participating telescopes N, the average amplification gain of the photosensors g_i, and the trigger rate R_i. The term Δ allows for higher order corrections, k_N is a scaling factor (Hahn et al., 2014b), and μ_i is the muon efficiency of observation i. The latter quantity specifies how many photoelectrons are detected per incident photon from a muonic event in the camera and is, therefore, a measure of the optical performance of the telescopes. The exact thresholds for these quality criteria depend on the H.E.S.S. phase, as well as on the detector configuration. The data quality thresholds for stereo mode for Phase I can be seen in tabulated form in Appendix A.1. For Phase II and Phase IU the stereo quality cuts have not changed, except for an additional limit on the trigger rate of at least 1200 Hz also for the detection quality.

3.2.2 Matching Parameters

Previous works employing the classical ON/OFF method have shown that a variety of parameters influence the background rate and need to be considered in the matching process (Flinders, 2016; Abeysekara, 2019; H.E.S.S. Collaboration et al., 2023; Veh, 2018). In this study, the influence of the tested matching parameters on the background rate has been estimated by calculating a distance correlation (Székely et al., 2007) between the matching parameters and the number of background events estimated from an OFF region using the background model template. In contrast to the Pearson correlation coefficient, the distance correlation can account for nonlinear association between parameters without the need to take inter-parameter correlations into account.

Among the tested parameters are the zenith angle of the observation, due to its influence on the Cherenkov light yield from the air shower, as well as the dead-time-corrected observation time. The influence of NSB light is also tested since it is expected that some NSB events will remain in the data even after the observation runs have been cleaned. Another important matching parameter is the muon efficiency ε_μ, which, as described above, is a measure of the optical performance of the telescopes. To evaluate the differences in atmospheric conditions, two quantities were investigated. The first parameter is the Cherenkov transparency coefficient, and the second matching parameter is the effective sky temperature, measured with infrared radiometers (Aye et al., 2003) mounted to each telescope.

As the influence of the matching parameters can vary following major changes in the hardware configuration of the telescope array, the distance correlation coefficients for the different matching parameters, except the zenith angle, have been calculated for each of the three hardware phases of the H.E.S.S. telescopes. For the construction

of the background model template, the zenith angles of the OFF runs were grouped into bins with a size dependent on the available statistics. These zenith angle bins were adopted as a validity range of the zenith angle deviation for this work in order to ensure compatibility with the background model template and can be seen in Table 3.1. In order to have a comparable background model template between ON and OFF runs, the azimuth angle bins from Mohrmann et al. (2019a) were also adopted for this study. A summary of all significant matching parameters, as well as allowed deviations and correlation coefficients for this work, can be found in Table 3.2.

Additionally, correlation coefficients were computed using only low-energy events in order to prove the validity of these coefficients for the energy range in which the most misclassified cosmic rays are expected. No significant dependence on the threshold energy was found (see Appendix A.3).

Table 3.1: The bounds and number of observations N_{obs} for the zenith angle Θ_z binning used for the construction of the background model template and run matching approach.

Θ_z [°]	N_{obs}
$0 - 10$	99
$10 - 20$	392
$20 - 30$	650
$30 - 40$	444
$40 - 45$	300
$45 - 50$	306
$50 - 55$	150
$55 - 60$	61

Table 3.2: Matching parameters used for the OFF run estimation. Additionally given are the respective allowed deviations of all parameters and their distance correlation (Székely et al., 2007) with the background rate.

Matching parameter	Valid parameter range	Correlation d_{corr}		
		Phase I	Phase II	Phase IU
Zenith Angle Θ_z	within zenith bins	0.36	0.32	0.45
Trigger Rate r	$\Delta r < 25\%$	0.42	0.66	0.46
Duration t	$\Delta t < 7\%$	0.64	0.68	0.71
Transparency Coeff. τ	$\Delta \tau < 6\%$	0.43	0.66	0.55
Radiometer Temp. R_T	$\Delta R_T < 50\%$	0.23	0.51	0.48
Muon Efficiency ε_μ	$\Delta \varepsilon_\mu < 11\%$	0.42	0.37	0.16
NSB	$\Delta \mathrm{NSB} < 80\%$	0.32	0.25	0.24

3.2.3 Fractional run difference

The deviations of the matching parameters are then used to quantify the difference between an ON and OFF run, by calculating the fractional run difference f:

$$f = \sum_j d_{corr,j} \cdot \frac{|x^j_{\text{on}} - x^j_{\text{off}}|}{x^j_{\text{on}}}\,, \tag{45}$$

where j is one of the matching parameters, and $d_{corr,j}$ is the distance correlation for the respective matching parameter. The observation with the smallest fractional run difference is chosen as the OFF run for the corresponding ON run. This approach ensures that the best match does not depend on the order in which the OFF runs are compared to the ON run.

If no OFF run fulfilling all matching criteria can be found, only the parameters with the largest influence (top half of Table 3.2) are used for the matching. In this case, the fractional run difference computed with all matching parameters can be large, and the suboptimal matching is then taken into account by increased systematic errors (as described in section 3.4).

3.3 Background estimation

3.3.1 General method

After matching every ON run with an OFF run, the background model template was normalised to the OFF run. During this process, the background rate R_{BG} is corrected for minor discrepancies stemming from varying observation conditions between the average run used for the templated construction and the nominal observation conditions, employing the relation given in Equation 43, as described in section 3.1.4.

For every ON and OFF run, the energy at which the deviation between true and reconstructed energy —referred to as the energy bias— reaches 10% was estimated. This energy was then set as a safe energy threshold and the data at lower energies were discarded. The maximally allowed offset between the reconstructed event direction and the pointing position of the telescope was 2.0°. `gammapy version 1.2` (Deil et al., 2020; Donath et al., 2023) was used to create a dataset with a square region geometry of $4° \times 4°$ centred around the pointing position of the OFF run. This `MapDataset` combines information such as a counts map (the observed number of events passing selection cuts in each bin), expected background map, and exposure. The size of the geometry was chosen such that all of the data within the above-mentioned thresholds were included in the analysis. For a correct description of the amount of cosmic-ray background in the observation, it is important to ensure that no γ-ray source is present in the region to which the parameters of the background model template are fitted.

Therefore, the regions containing previously identified extragalactic γ-ray sources in the OFF run were excluded from the fit of the background model template. Additionally, we excluded a circular region with a radius of 0.5° around the observation target of the respective OFF run to minimise the amount of γ-ray emission included due to subthreshold γ-ray sources. The background model template was then fit to the OFF run. Thereafter, only the adjusted background model template was used.

In addition to minimising the deviations between ON and OFF run by comparing the fractional run deviation and identifying the best-matching OFF run, deviations

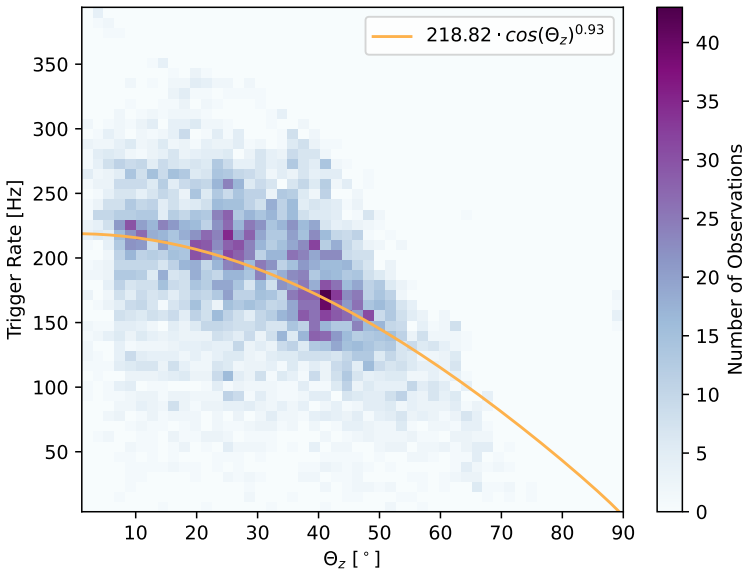

Figure 3.3: Dependence of the array trigger rate of the four small H.E.S.S. telescopes on the zenith angle of the measurement for the first optical phase. A fit of Eq. (47) to the data yields the parameters used for the background correction.

between the observations can be accounted for by applying correction factors. One correction applied accounts for the deviation in duration (observation time during which the telescope system can trigger on a signal) between the ON and OFF runs:

$$b_{i,ON} = \frac{b_{i,OFF} \cdot t_{ON}}{t_{OFF}} \,, \tag{46}$$

where b_i is the total number of background events per spatial pixel and t is the total duration of the observation.

The second correction applied accounts for the deviation in zenith angle of the observation. Because of the matching within the zenith angle bins used in the computation of the background model template (see Table 3.1), some run pairs can have a deviation of up to 5° in zenith angle Θ_z. The correction factor to account for this deviation is calculated using:

$$b_{ON} = b_{OFF} \cdot p_1 \cos\left(\Theta_z\right)^{p_2} . \tag{47}$$

This correction follows the relation between the cosmic-ray rate —and therefore also the trigger rate, which is dominated by hadronic background events— and the zenith angle of the measurement, established in Lebohec and Holder (2003). The parameters p_1 and p_2 were estimated for every optical phase by fitting Eq. (47) to the trigger rate of the H.E.S.S. array for all observations performed in the respective optical phase. An example of such a fit to the trigger rates can be seen in Fig. 3.3. The fit parameters for all optical phases, as well as more information about their computation, can be found in Appendix A.2.

In the next step, another `MapDataset` was created and filled with the reconstructed events observed in the ON run. The background model template was then assigned to this dataset, and the spectral tilt δ and background normalisation Φ derived following

Equation (43) from the fit of the template to the OFF run were assumed for this dataset. This allows for the background rate to be adjusted to the different observation conditions without the need to have γ-ray emission-free regions in the ON run.

3.3.2 Creation of validation datasets

In order to validate the above-described background estimation method, the background rate and source parameters achieved by applying the run-matching approach should be compared to the standard background model template method. To achieve this, validation datasets consisting of observations of gamma-ray sources that are either point-like or exhibit only marginal extension, facilitating the application of both methods, were constructed for the different background estimation techniques. For ease of reference, these different cases have been given numbers, and an overview can be found in Table 3.3. First, a standard analysis of all ON runs for a region of interest (ROI) is performed as a reference. For this purpose, all observations of the target region are identified, the background model template is fitted to each ON run, and the resulting `MapDatasets` are 'stacked', which means the measured data are summed over all observations, averaged instrument response functions (IRFs) are created, and only one `MapDataset` is returned for every ROI. Hereafter, this dataset is referred to as Case 0. Another dataset was constructed following the same steps, this time with the run-matching approach, but without corrections, in order to estimate the background rate. Hereafter, this is referred to as Case 1. We constructed one dataset where only the correction for the differences in duration was applied (Case 2) and another where both corrections were applied (Case 3). Two more datasets were constructed to estimate the influence of the systematic errors introduced due to the run-matching (see section 3.4); these are labelled Case 4+ and Case 4-, respectively, for increased and decreased background count rate.

Table 3.3: Overview of the identifiers used for the datasets in this validation.

Case	Description
Case 0	standard background model template analysis
Case 1	run-matching approach
Case 2	Case 1 with a duration correction
Case 3	Case 2 with a zenith angle correction
Case 4+	Case 3 with added systematic uncertainties
Case 4-	Case 3 with subtracted systematic uncertainties

3.3.3 Derivation of the correlation coefficients and validity intervals

The influence of the respective matching parameters on the background rate was estimated by analysing archival H.E.S.S. data obtained for the γ-ray source PKS 2155−304 using the direct application of the background model template (Case 0).

PKS 2155−304 was chosen as a test region as it has been continuously monitored since the commissioning of the first H.E.S.S. telescope and a large amount of data with varying observation conditions has been acquired. Additionally, the γ-ray signal in this ROI is contained in a small, well-known region, resulting in a small uncertainty in

the background rate. The background model template was fitted to each observation in this dataset, and the number of background events was estimated. The data were then split into three groups depending on the hardware configuration of the telescope array. A total of 791 observations distributed over the three hardware phases was used. A distance correlation coefficient between the different matching parameters and the background rate was then computed. The results can be seen in Table 3.2. To estimate the valid range for every matching parameter, the background rate estimated for Case 0 was compared with that resulting from the run-matching approach (Case 3) for a large number of observations. To this end, all observation pairs from the sets of observations on PKS 2155−304 indicated in Table 3.4 were used.

For each of these observations, all possible OFF runs were identified, the background rate of all pairs for Case 0 and Case 3 computed, and the deviation of these calculated as follows:

$$\Delta R_{BG} = \frac{R_{BG,0} - R_{BG,3}}{R_{BG,3}}\,, \tag{48}$$

with $R_{BG,0}$ the background rate of the dataset for Case 0 and $R_{BG,3}$ the background rate for Case 3. Additionally, the deviation between all matching parameters of ON and OFF runs was calculated for each observation pair as $\Delta x = (x_{\mathrm{on}} - x_{\mathrm{off}})/x_{\mathrm{on}}$, where x is a given matching parameter. Then the mean background rate deviation $\overline{\Delta R_{\mathrm{BG}}}$ per Δx was computed, and the valid parameter range was defined as the Δx at which $|\overline{\Delta R_{\mathrm{BG}}}| > 10\%$. This computation is performed individually for all four telescopes, and the smallest value is identified as the upper bound of the validity range. A visualisation of the distribution of $\overline{\Delta R_{BG}}$ and its mean for the Muon efficiency can be seen in Fig. 3.4.

3.4 Systematic errors

In order to estimate the systematic uncertainties introduced by employing the run-matching approach, the background rates for Case 0 were compared to the rates obtained for Case 3. Because of strong variations in the optical efficiency of the telescopes, the systematic uncertainty can vary for observations obtained at different times. To account for this effect, the systematic uncertainties should be computed for each individual analysis by selecting observations recorded in a short time span around the recording of the ON runs used for the source analysis. In order to validate this background estimation technique, ON runs from three different time periods will be used. To account for this, three different sets of observations for the estimation of the systematic uncertainties were computed. For all three sets, observations on the source PKS 2155−304 were used, excluding the observations that are part of the public data release.

For each of these observations, all possible OFF runs were identified, and the background rate of all pairs for Case 0 and Case 3 was computed. Then, the deviation of these two rates was obtained as indicated in Eq. 48. This deviation, which can be used as a measure of the systematic shift, was calculated for all run pairs, and the results were grouped according to the fractional run difference of the respective OFF run. Although this comparison is a good estimation of the systematic uncertainty introduced by the run-matching approach, it is limited by the available statistics, and a coarse bin size of $\Delta f = 0.1$ was chosen. Subsequently, the standard deviation of the background deviation was computed in each bin with more than ten entries to ensure

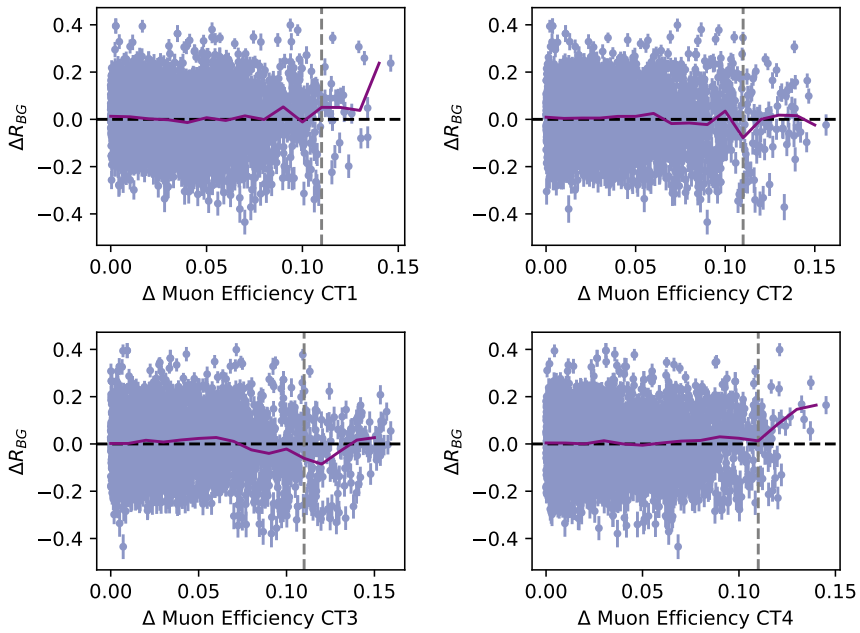

Figure 3.4: Background rate deviation ΔR_{BG} per difference in muon efficiency for each ON-OFF run pair in set 3 (see Table 3.4 for more information on the set). The case of no deviation between the background rates is depicted by the black dashed line, and the mean of ΔR_{BG} is depicted by the purple line.

sufficient statistics for a stable result. The standard deviation is then used as systematic uncertainty on the background count rate for a run pair with the respective fractional run deviation. Table 3.4 provides further properties of the three sets that were used to estimate the systematic uncertainties for the analyses of the validation datasets.

Table 3.4: Properties of the sets of observations from which the systematic uncertainties were estimated and the corresponding source analysis they were used for.

Set	Optical phase	N_{ON}	N_{OFF}	Analysis Region
Set 1	1b	49	284	Crab Nebula, MSH 15−52, RX J1713.7−3946
Set 2	1c	38	2170	PKS 2155−304, Sculptor Dwarf Galaxy
Set 3	2c2	27	631	Reticulum II, Tucana II

A visualisation of the systematic shift for all three sets can be seen in Fig. 3.5. The systematic errors for set 1 and set 2 are comparable, whilst the errors for set 3 are marginally smaller. This is most likely caused by a camera update in 2016. Set 3 also extends to higher fractional run deviations f, because a greater number of observations on extragalactic sources was acquired in this time period.

The systematic uncertainty on the background rates derived from these tests is then translated to a systematic uncertainty on the source flux by computing two additional datasets for all validation regions. These are computed by using the fractional run difference of every run pair to identify their expected systematic uncertainty and increase

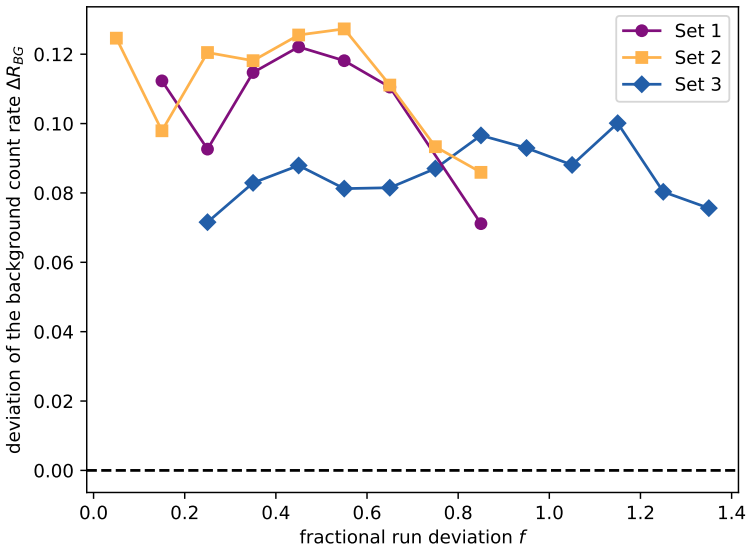

Figure 3.5: Systematic uncertainties on the background count rate introduced by using a run-matching approach for different fractional run deviations f for all datasets. A description of the respective sets can be found in Table 3.4

or decrease the background counts per pixel using the corresponding systematic factor. These datasets are identified as Case 4+ for the increased background rate and Case 4- for the decreased background rate.

3.5 Validation

To validate the run-matching approach, data from the H.E.S.S. public dataset release (H.E.S.S. Collaboration, 2018a) was analysed using the run matching approach (Case 3), and the results were compared to an analysis using the background model template (Case 0) and to the results reported in Mohrmann et al. (2019a). The observations on PKS 2155−304 were selected to be acquired in time intervals where the source does not undergo γ-ray outbursts. A second dataset on PKS 2155−304 was used to demonstrate the performance of the background estimation technique also for datasets with large statistics. For this purpose, the observation run list from the study presented in H.E.S.S. Collaboration et al. (2018a) was utilized. Additionally, this work uses observations of sky regions devoid of γ-ray emission (which are referred to as empty-field observations hereafter) acquired with the H.E.S.S. telescope array. These datasets contain observations on the dwarf galaxies Reticulum II, Tucana II, and Sculptor Dwarf Galaxy.

The public data release only contains data passing a tight quality selection (for more information, see Aharonian et al., 2006a). Therefore, all observations that are part of the data release can be used for this validation study. The empty-field observations were filtered to only contain observations that pass spectral quality cuts. The properties of these datasets are listed in Table 3.5.

The spectral and morphological properties of the γ-ray emission from all sources contained in the public data release (see Table 3.5) were acquired by performing a three-dimensional fit of a spectromorphological model to the dataset. A stacked analysis

was performed using `gammapy`.

All datasets were prepared using a spatial pixel size of 0.02°. The spatial extension of the `MapDataset`s for each analysis region was chosen such that all events recorded in the observations were included in the analysis, and the energy axis for each dataset was chosen to be logarithmically spaced, with eight bins per decade.

Table 3.5: Analysis datasets used in this study.

Target	Type	Extension	Runs	Time [h]	Zenith angle	$\overline{f}$
Reticulum II	dSph	None	16	7.0	$34° - 50°$	0.24
Tucana II	dSph	None	14	6.2	$35° - 38°$	0.28
Sculptor Dwarf Galaxy	dSph	None	22	10.0	$11° - 19°$	0.22
Crab Nebula[a]	PWN	Point-like	4	1.9	$45° - 49°$	0.35
PKS 2155−304 (steady)[a]	AGN	Point-like	6	2.8	$23° - 37°$	0.89
MSH 15−52[a]	PWN	Extended	15	6.8	$36° - 39°$	0.22
RX J1713.7−3946[a]	SNR	Extended	15	7.0	$16° - 26°$	0.58
RX J1713.7−3946 (large)[b]	SNR	Extended	153	51.0	$17° - 59°$	0.57

[a] This dataset is part of the first public data release of the H.E.S.S. collaboration (H.E.S.S. Collaboration, 2018a)
[b] More information on this dataset can be found in H.E.S.S. Collaboration et al. (2018a)

3.5.1 Validation with empty-field observations

The quality of the background estimation was assessed via the Li&Ma (1983) significance distribution. For an empty sky region, a Gaussian distribution centred around $\mu = 0$, with a standard deviation of $\sigma = 1$ is expected, since the fluctuations of the background counts are Poisson distributed.

To test for the correct description of the background, the three datasets comprised of observations centred on the dwarf spheroidal galaxies Reticulum II and Tucana II, as well as the dwarf galaxy Sculptor are computed. These regions were chosen because no significant γ-ray emission from the sources and within a region with a diameter of 4° around the sources has been observed with H.E.S.S. (Abdallah et al., 2020; Abramowski et al., 2014b). Therefore, the regions can be used for an estimation of the background rate without contamination from a mismodeled γ-ray source.

For all regions, the significance of the number of events passing selection cuts in excess of the background prediction in every pixel was computed. The correlation radius used for the computation of the significance is 0.06° for all empty-field observations. This approximately corresponds to the point-spread function of H.E.S.S.. A Gaussian model is fitted to a histogram of the pixel significances with the fit results for the different regions given in Table 3.6. An example distribution for the region around the dwarf spheroidal galaxy Tucana II and the corresponding Gaussian fit can also be seen in Fig. 3.6.

For Case 0, all three regions show a distribution centred around zero and a standard deviation of approximately 1.0, confirming that no γ-ray sources are present. The mean of the distributions for Case 1 indicates an over-prediction of cosmic-ray background of up to 20%. This over-prediction is slightly decreased if a duration correction is

Table 3.6: Fit parameters of a Gaussian distribution to the Li&Ma (1983) significance values of the background events derived from the empty-field observations. The uncertainties are of the order of 10^{-4} to 10^{-5} on all fit parameters.

Case	Reticulum II		Tucana II		Sculptor	
	μ	σ	μ	σ	μ	σ
Case 0	−0.06	1.04	−0.05	1.01	−0.10	1.04
Case 1	−0.11	1.04	−0.08	1.05	−0.15	1.03
Case 2	−0.08	1.04	−0.07	1.06	−0.14	1.03
Case 3	−0.08	1.04	−0.06	1.06	−0.14	1.03
Case 4+	−0.30	1.03	−0.24	1.04	−0.42	1.01
Case 4-	0.15	1.06	0.12	1.07	0.15	1.07

applied (Case 2) and is further reduced once the zenith correction is applied for all three empty-field regions.

The Gaussian fit to the significance histograms of these datasets shows that the nominal value derived for the Case 0 datasets is included in the range covered by the systematic error for all datasets. An example of the shift on the significance distribution caused by the inclusion of the systematic errors can be seen in Fig. 3.7.

To rule out a potentially energy-dependent behaviour of the goodness of the background estimation, the observations of all three empty-field regions were used. For this purpose, the data from the Case 0 and Case 3 datasets of each region were divided into eight logarithmically spaced energy bins, from 0.1 TeV to 10 TeV. This binning was chosen so that each bin included two energy bins of the initial dataset. The data above 10 TeV were not included in this comparison due to insufficient gamma-ray statistics.

To check for variation in background counts as a function of energy due to the run matching, the background counts per energy bin for all empty-field region observations for Case 0 (N^0_{BKG}) and Case 3 (N^3_{BKG}) have been computed. Then the ratio between these counts N^3_{BKG}/N^0_{BKG} per energy bin has been calculated. Figure 3.8 shows this ratio, the shaded band depicts the error on the number of background counts estimated from the systematic error on the run pairs. It can be seen that the number of background counts for the Case 3 datasets is slightly underestimated for lower energies and slightly overestimated for higher energies compared to the number of counts derived for the Case 0 datasets. This deviation is, however, found to be below 6% for all energies.

Significance histograms were also computed for all bins, and a Gaussian fit was performed. The significance histograms, as well as the Gaussian fits for all bins for the dataset around Sculptor, can be seen in Figure 3.9 and Table 3.7. Figure 3.9 shows that the fluctuations are indeed Poissonian distributed at low energies. At higher energies, the statistics decrease drastically, and the background template is fitted to the few events that are still present. This creates a truncation effect in the significance distribution. A Gaussian fit in these bins, however, still shows a good agreement between Case 0 and Case 3. The results for the regions around Reticulum II and Tucana II have been summarised in the Appendix in Table A.4 and Table A.5, respectively. For the three data sets, a Gaussian fit to the significance distribution yields comparable results between the Case 0 and Case 3 datasets in all energy bins.

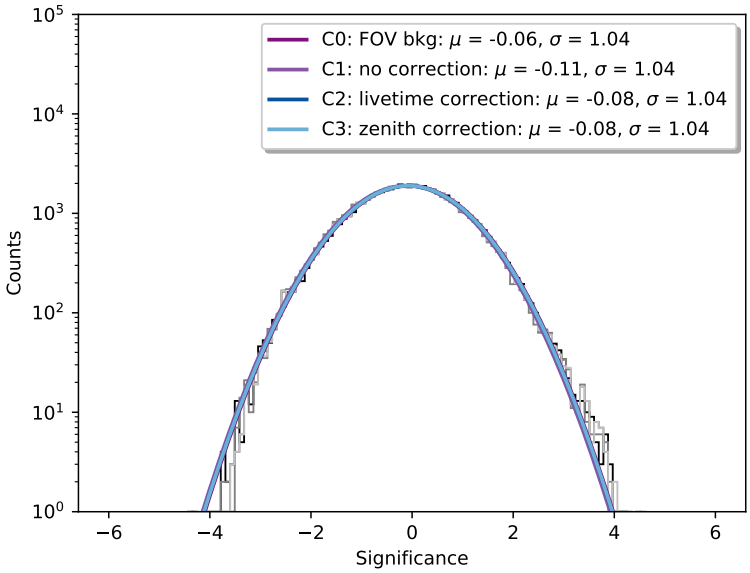

Figure 3.6: Li&Ma (1983) significance distribution of the observations in the region around the dwarf spheroidal galaxy Reticulum II. Depicted are the distributions for four different estimates of the background; see Table 3.6. Each of the distributions is shown as a histogram in grey, while a Gaussian fit to each distribution is shown by the coloured lines.

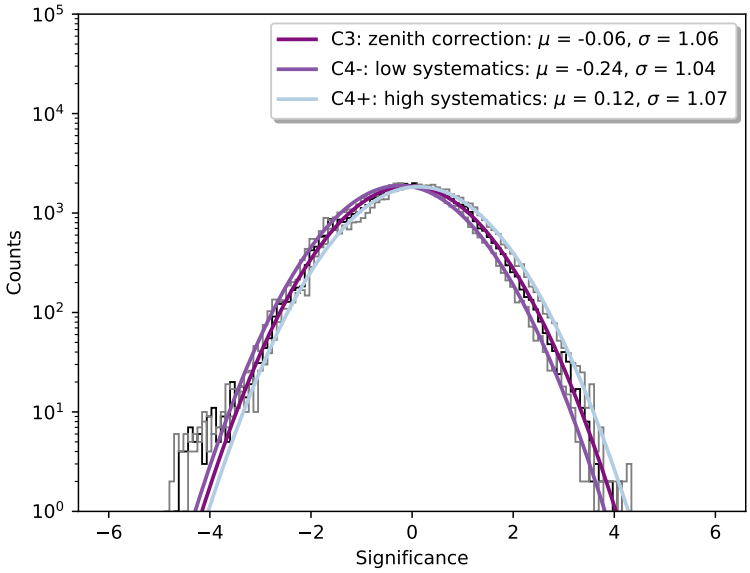

Figure 3.7: Li&Ma (1983) significance distributions of background counts in the region around the dwarf spheroidal galaxy Tucana II for the different background estimation methods.

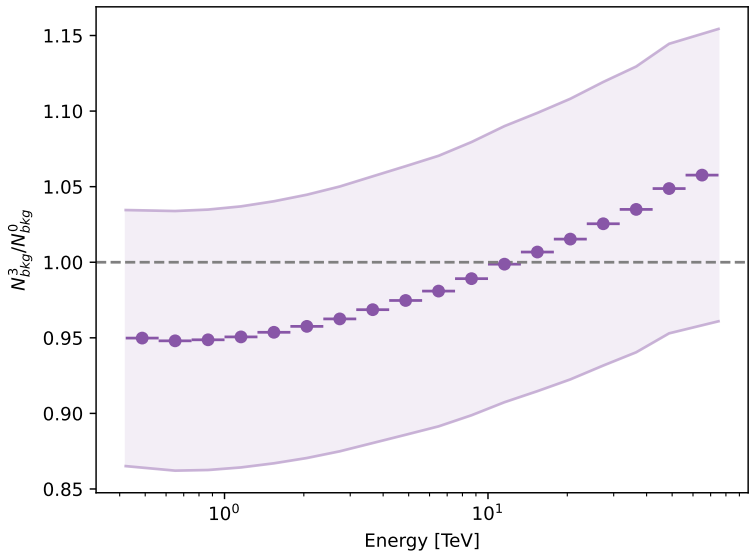

Figure 3.8: The ratio between the number of background counts for the Case 0 (N^0_{BKG}) and Case 3 (N^3_{BKG}) datasets in energy bins. This rate was computed using all observations of the empty-field regions.

3.5.2 Public data release

After verifying the background prediction in an empty sky region, the best-fit values for a source analysis should be verified between the different background estimation techniques. To this end, we analysed data from the public data release of H.E.S.S. (H.E.S.S. Collaboration, 2018a) for both background estimation methods and compared the results to those derived in Mohrmann et al. (2019a). A simple power law was chosen as a spectral model for all datasets, and in all cases, the flux normalisation $\mathrm{N_0}$ at a reference energy E_0 and the spectral index Γ were used as fit parameters. The power-law model is defined as:

$$\frac{\mathrm{dN}}{\mathrm{dE}} = \mathrm{N_0} \cdot \left(\frac{\mathrm{E}}{\mathrm{E_0}}\right)^{-\Gamma} . \tag{49}$$

The reference energy for all datasets was chosen to be equal to the values used in Mohrmann et al. (2019a), for the sake of comparison, and can be found in Table 3.8.

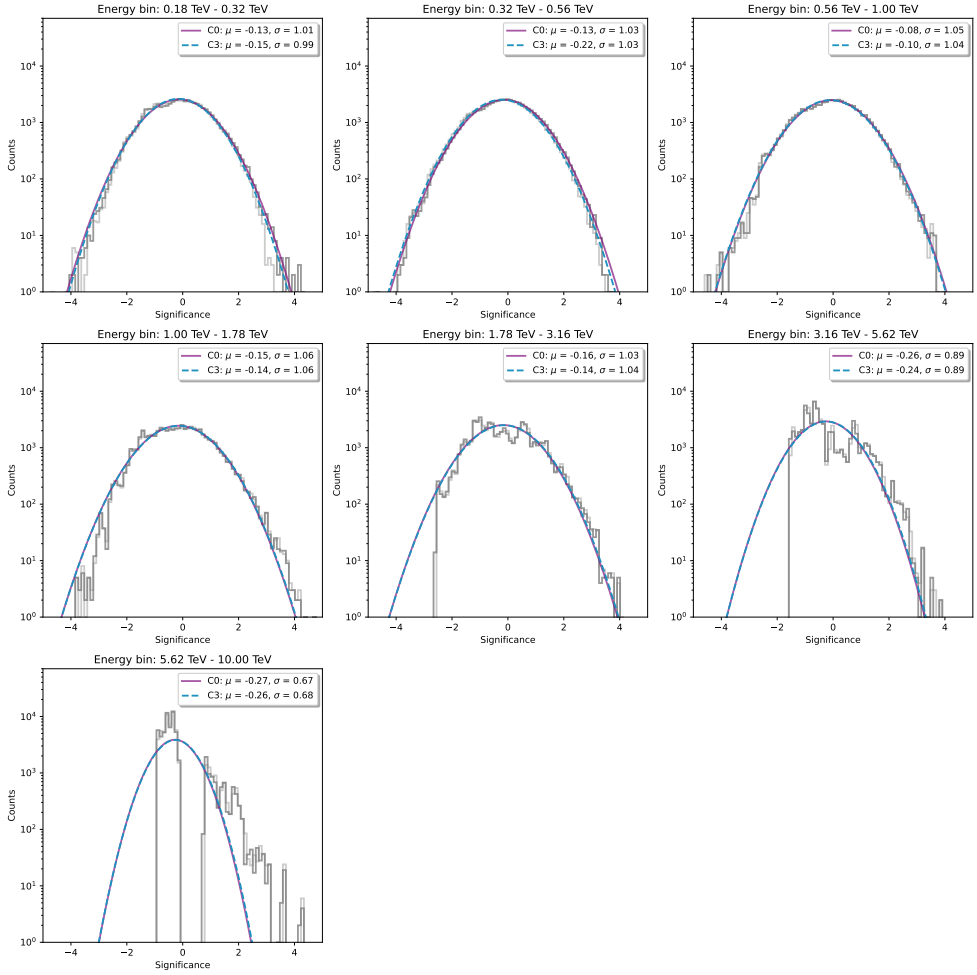

Figure 3.9: Significance distribution for the region around Sculptor in energy bins. A Gaussian fit to the histogram for Case 0 is depicted by the solid purple line, and a fit to the Case 3 dataset is depicted by the blue dashed line. The number of events in the last energy bin is too sparse for a good fit, however, the distributions of the significance values are comparable.

Table 3.7: The fit parameters of the Gaussian fit to the significance distributions estimated from the region around Sculptor.

Energy bin [TeV]	Case 0		Case 3		Case 4+		Case 4-	
	μ	σ	μ	σ	μ	σ	μ	σ
0.18 - 0.32	−0.13	1.01	−0.12	1.02	−0.37	1.00	0.14	1.06
0.32 - 0.56	−0.13	1.03	−0.19	1.03	−0.58	1.00	0.23	1.09
0.56 - 1.00	−0.08	1.05	−0.12	1.04	−0.39	1.03	0.18	1.07
1.00 - 1.78	−0.15	1.06	−0.18	1.06	−0.36	1.03	−0.02	1.09
1.78 - 3.16	−0.16	1.03	−0.18	1.03	−0.30	1.01	−0.06	1.06
3.16 - 5.62	−0.26	0.89	−0.28	0.88	−0.34	0.87	−0.21	0.90
5.62 - 10.00	−0.27	0.67	−0.28	0.67	−0.32	0.66	−0.25	0.68

Table 3.8: The best-fit parameters for all sources analysed in this study. Ref. denotes the values given in Mohrmann et al. (2019a), C 0 are the values derived from the case 0 dataset and C 3 the values for the analysis of the case 3 dataset.

		RA [°]	Dec [°]	r_0 [°]	e [°]	ϕ [°]	E_0 [TeV]	N_0 [10^{-12} cm^{-2}s^{-1}TeV^{-1}]	Γ
Crab Nebula	Ref.	83.619 ± 0.003	22.025 ± 0.002	−−	−−	−−	1.45	17.3 ± 0.8	2.69 ± 0.07
	C 0	83.628 ± 0.002	22.026 ± 0.002	−−	−−	−−	1.45	16.8 ± 0.7	2.73 ± 0.06
	C 3	83.629 ± 0.002	22.027 ± 0.002	−−	−−	−−	1.45	16.1 ± 0.7	2.67 ± 0.06
PKS 2155−304	Ref.	329.73 ± 0.007	-30.227 ± 0.006	−−	−−	−−	0.65	22.1 ± 2.2	3.50 ± 0.23
	C 0	329.72 ± 0.005	-30.224 ± 0.004	−−	−−	−−	0.65	17.1 ± 1.8	3.73 ± 0.21
	C 3	329.72 ± 0.006	-30.227 ± 0.005	−−	−−	−−	0.65	16.8 ± 1.7	3.68 ± 0.2
MSH 15−5*2*	Ref.	228.55 ± 0.01	-59.171 ± 0.007	0.196 ± 0.007	0.801 ± 0.038	151 ± 6.0	1.4	2.91 ± 0.14	2.41 ± 0.05
	C 0	228.56 ± 0.04	-59.175 ± 0.003	0.170 ± 0.004	0.739 ± 0.020	145.4 ± 2.2	1.4	3.35 ± 0.24	2.42 ± 0.08
	C 3	228.56 ± 0.02	-59.170 ± 0.001	0.169 ± 0.001	0.765 ± 0.034	149 ± 7.8	1.4	3.26 ± 0.34	2.40 ± 0.08
RX J1713.7−3946	Ref.	−−	−−	−−	−−	−−	1.15	13.3 ± 0.5	2.21 ± 0.04
	C 0	−−	−−	−−	−−	−−	1.15	14.1 ± 0.7	2.26 ± 0.05
	C 3	−−	−−	−−	−−	−−	1.15	14.9 ± 0.7	2.17 ± 0.04

Note: The parameters r_0, e, Φ are the major axis, eccentricity, and position angle of the elliptical disk used to describe the emission from MSH 15−5*2*. Due to the complex spatial shape of RX J1713.7−3946 no spatial model was used to describe the emission. Instead, a template has been created from the excess observed in the data and only a spectral model was applied to the excess region. These fit parameters are compared to reference values from Mohrmann et al. (2019a). The reference energy E_{ref} was fixed for the likelihood-minimisation.

The correlation radius used for the computation of the significance maps and histograms for all datasets is 0.06°, except the dataset centred on the Crab Nebula, which is 0.1°, because of the small size and limited statistics of the dataset.

For the sake of comparing the best-fit results between this analysis and the results obtained in Mohrmann et al. (2019a), the same spatial models are chosen. It should be noted that these models should not be interpreted as yielding the most accurate description of the region. The Crab Nebula, as well as PKS 2155−304, are described using a point source model. For a more in-depth discussion of these sources, see Aharonian et al. (2024) and H.E.S.S. Collaboration et al. (2017), respectively. The pulsar wind nebula MSH 15−5*2* (analysed in detail in Aharonian et al. (2005)) is described by an elongated disc model. For the supernova remnant RX J1713.7−3946, no predefined spatial model could be used because of the complicated morphology of the source. For this reason, an 'excess template' was constructed. This was done by fitting the background model template to the observations outside of the source region and then subtracting the best-fit model derived in this fit from the data. To minimise the bias introduced by the statistical fluctuations in the observed data, the template was smoothed using a two-dimensional cubic spline function. In the last step negative values in the template have been replaced by zero. More information describing the newest results for the emission from RX J1713.7−3946 can be found in H.E.S.S. Collaboration et al. (2018a).

An additional challenge for the analysis of these datasets is that, depending on the source location, misclassified cosmic rays are not the only source of background events. Observations centred in the Galactic plane will also include events from the Galactic diffuse emission (Abramowski et al., 2014a). For the background estimation employing the background model template, the Galactic diffuse emission can be partly absorbed by increasing the normalisation of the background model template. In the case of the run-matching approach, the background model template is normalised on observations outside of the Galactic plane, and so absorption of the diffuse emission into the background is not possible.

This effect has been observed in the analysis of the datasets centered on the regions around the sources MSH 15−5*2*, located at a Galactic latitude of $b = -1.19°$, and RX J1713.7−3946, with a Galactic latitude of $b = -0.47°$. For both datasets, an excess signal across the whole FoV was detected at low energies. Whilst it is likely that the observed excess emission is Galactic diffuse emission, the data used in this validation are not extensive enough to model this signal or derive any of its physical properties. Therefore, we adopted a strict energy threshold for the analysis of the regions around MSH 15−5*2* and RX J1713.7−3946, effectively excluding the energy range in which a significant influence of diffuse emission can be observed for H.E.S.S.. This energy threshold was evaluated for each individual analysis for Case 3. To this end, we estimated the number of background and signal events in a source-free region in the stacked dataset. The first energy bin after which the absolute difference between the number of signal and background events is less than 10% was adopted as an energy threshold for the analysis. For the analysis of both MSH 15−5*2* and RX J1713.7−3946, this resulted in an energy threshold of 560 GeV.

In addition to the increased energy thresholds, a second modification of the background estimation needs to be included for the datasets for MSH 15−5*2* and RX J1713.7−3946. Because they were taken in 2004, shortly after the commissioning of the H.E.S.S. array,

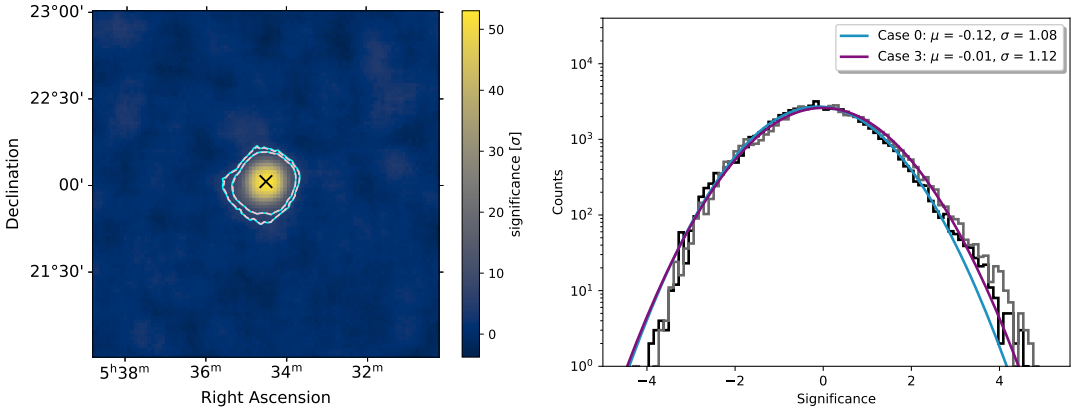

Figure 3.10: The Region around the Crab Nebula as seen with the H.E.S.S. Telescopes. Left: Li&Ma (1983) significance map of the region with $5\,\sigma$ and $8\,\sigma$ contours. The contours from case 0 are depicted in blue, while the contours from case 3 are depicted in pink. The best-fit position is indicated by the black cross. Right: Significance distribution of the background in the FoV.

the optical phase is very short due to the fast system degradation, and few observations were taken outside of the Galactic plane in this time period. For this reason, an insufficient number of OFF runs can be found within this optical phase, and the first two optical phases have been combined.

The best-fit parameters for the datasets created using the run-matching approach for all sources can be found in Table 3.8. Additionally, the best-fit values derived in the previous analysis are indicated in the table for comparison, as are the results derived from the Case 0 datasets. A visual comparison of the fit parameters for all sources can be found in Appendix A.4.

Table 3.9: Gaussian distribution of the Li&Ma (1983) significance values of the background events derived for each of the datasets in the H.E.S.S. public data release. The uncertainties on μ and σ are of the order of 10^{-4} to 10^{-5} for all regions.

Case	Crab Nebula		PKS 2155−304		MSH 15−52		RX J1713.7−3946		RX J1713.7−3946 2	
	μ	σ	μ	σ	μ	σ	μ	σ	μ	σ
Case 0	−0.12	1.08	−0.11	1.04	−0.16	1.04	−0.26	1.02	−0.20	1.05
Case 3	−0.01	1.12	−0.17	1.03	−0.29	1.02	−0.29	1.03	−0.18	1.05
Case 4+	−0.34	1.18	−0.34	1.06	−0.68	1.05	−0.56	1.07	−0.81	1.11
Case 4-	0.36	1.08	0.01	1.02	0.14	1.00	0.00	1.00	−0.51	1.23

Point-like sources

The comparison of the best-fit parameters for the analysis of the γ-ray emission from the Crab Nebula and PKS 2155−304 can be found in Table 3.8. The left panel of Fig. 3.10 shows a significance map for the region around the Crab Nebula. Indicated in the significance map are the $5\,\sigma$ and $8\,\sigma$ contours for Case 3 in dashed pink lines, and the contours for Case 0 as solid blue lines. The contours show good agreement.

The right panel of Fig. 3.10 shows the distribution of significance entries in the respective maps. A region of 0.5 ° radius around the source has been excluded to avoid contamination of residual γ-ray emission. The significance map and histogram of the region around PKS 2155−304 can be found in Appendix A.5 (Figure A.9). The distribution of the background counts shows a shift between the datasets for Case 0 and Case 3, indicating a slight over-prediction of the background rate for the Case 3 dataset. This shift is, however, within the expected range derived from a study of the influence of the systematic uncertainties (see Table 3.9)

The best-fit results of the likelihood minimisation for the Crab Nebula can be seen in Table 3.8. All parameters except the best-fit position are comparable within statistical errors with the results derived in Mohrmann et al. (2019a). The comparability of the right ascension between Case 0 and Case 3 suggests that a change in pointing reconstruction might be responsible for this deviation. A similar deviation can be observed for the best-fit parameters of PKS 2155−304 (see Figure A.2), where we also see a slight decrease in flux normalisation compared to the results derived in Mohrmann et al. (2019a). In each region, the Spectral Energy Distribution (SED) were computed. For the computation of the SED points, the flux normalisation of the respective source model was refitted in every energy bin, and from this, a mean flux per energy bin was derived. If the fit of the model in the respective energy bin shows a significance above $2\,\sigma$, an SED point is derived. Otherwise, an upper limit is calculated. For the calculation of the SED points of all datasets, 12 logarithmically spaced energy bins between 0.1 TeV and 100 TeV are used.

Good agreement is seen for both sets of SEDs depicted in Figure A.5 and Figure A.6. Only in one energy bin, around 3 TeV, is the deviation above $1\,\sigma$ between the SEDs derived from the Crab Nebula. A possible reason for this deviation is the change in the binning of the background model template that has been incorporated since the publication of Mohrmann et al. (2019a).

MSH 15−5*2*

A significance map of the region around MSH 15−5*2* can be seen in Appendix A.5 (Figure A.10) alongside the distribution of background. In this region, a shift of the background distribution towards a smaller number of cosmic-ray signals can be observed. This shift is most likely caused by a lack of OFF runs in this optical phase, making it necessary to choose OFF runs from the next optical phase. It is, therefore, possible that the time-span between the ON and OFF runs is larger than 4 years, resulting in a high probability that the optical efficiency of the telescopes between the two observations differs substantially. The shift can, however, be accounted for by the systematic uncertainty introduced by the run-matching approach.

The best-fit values for all parameters agree within the error (see Fig. 3.11). The strong dependence of the source extension on the correct estimation of the background rate is clearly shown by the large systematic errors, which are introduced by the systematic uncertainty on the run-matching results. The SED derived for this source shows a good agreement within the errors with the SED computed in Mohrmann et al. (2019a) (see (Figure A.7).

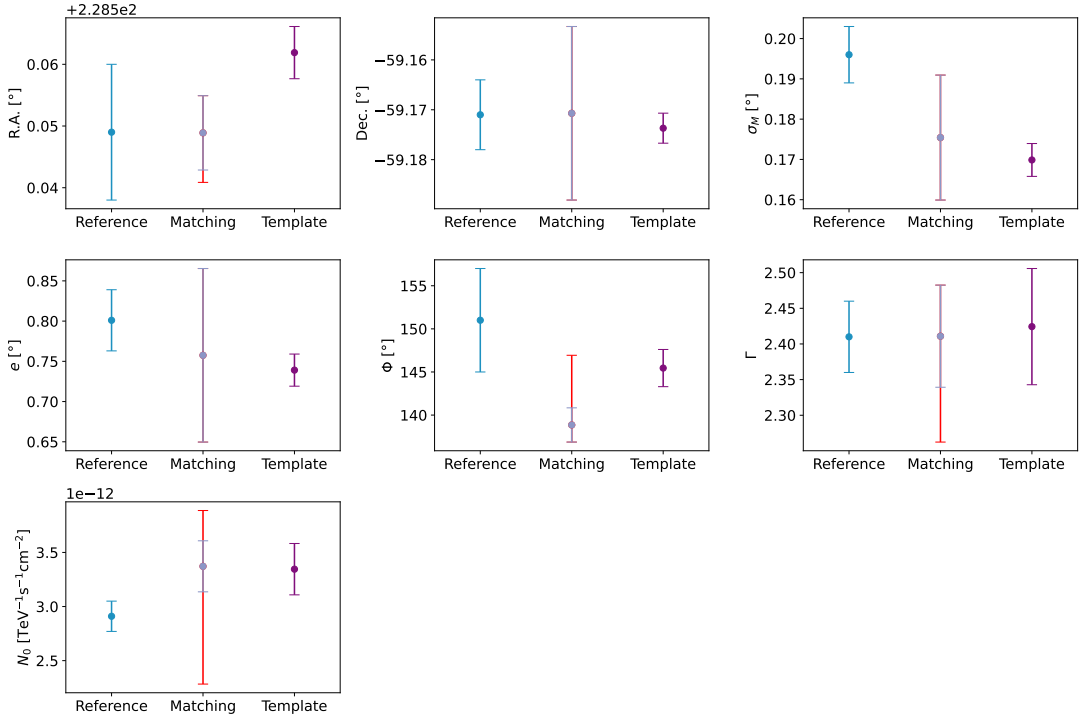

Figure 3.11: Comparison between the best-fit values for all parameters of the elongated model used to describe the emission from MSH 15−5*2*. The reference values were taken from Mohrmann et al. (2019a). Here, 'matching' refers to the values derived using the run-matching approach for the background estimation, while 'template' refers to the background model template. The systematic uncertainties introduced when using the run-matching approach are indicated in red.

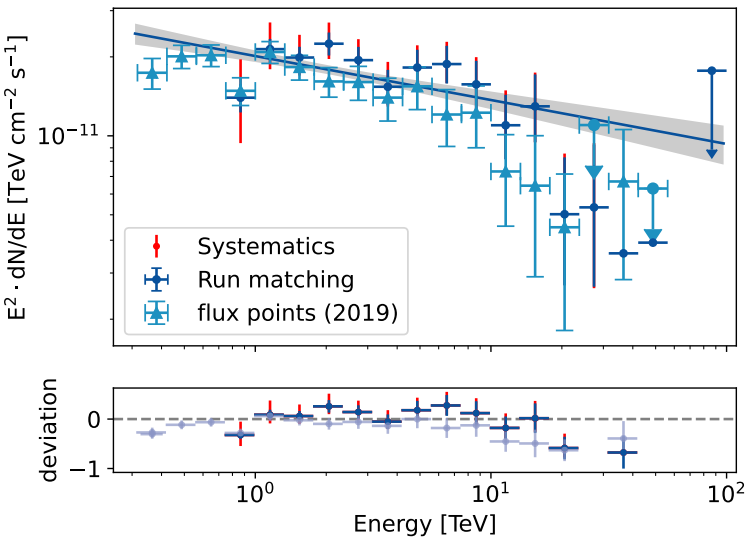

Figure 3.12: SED of RX J1713.7−3946 derived in the present analysis compared to the SED derived by Mohrmann et al. (2019a). The systematic uncertainties added by the run-matching approach are indicated in red in the upper panel. The lower panel shows the deviation between the SED derived in both analyses and the best-fit model derived from the Case 3 dataset.

3.5.3 RX J1713.7−3946

Figure A.11 shows a significance map and distribution for the region around RX J1713.7−3946. Good agreement between the background rate estimated for Case 0 and Case 3 is again seen. The best-fit parameters can be seen in Figure A.3. The spectral index and flux normalisation for RX J1713.7−3946 agree with the results of the likelihood minimisation within the error. A comparison of the SEDs for RX J1713.7−3946 can be seen in Fig. 3.12. The upper panel of the figure shows a comparison of the SED derived using the run-matching approach with that derived by Mohrmann et al. (2019a), while the lower panel shows the deviation between the two sets of SEDs. Again, a good agreement can be observed.

To verify that this background estimation is also stable for a large number of observations, we analysed a dataset containing 57.0 hours of observations centred on RX J1713.7−3946. The dataset has been presented in H.E.S.S. Collaboration et al. (2018a) and has only been slightly modified to remove observations that fail the spectral quality criteria. The significance map and distribution can be seen in Figure A.12 and the spectrum in comparison with the SED derived in H.E.S.S. Collaboration et al. (2018a) in Figure A.8. A comparison of the fit parameters for both background estimation techniques can be seen in Figure A.4. This analysis shows that the run matching approach is even more robust and better agreements between the Case 0 and Case 3 dataset analysis can be achieved for datasets containing a large amount of data.

3.6 Conclusion

This section presents the development of a method to combine the classical ON/OFF background estimation technique used by IACT arrays with a 3D background model template (Mohrmann et al., 2019a). This combination of techniques makes it possible to remove a major restriction of each method. As the 3D background model template has been created from a large number of OFF runs, it is robust and not subject to large statistical uncertainties. However, this method requires source-free regions in the FoV of the observation in order to normalise the background estimation for varying observation conditions. The classical ON/OFF background estimation does not require a source-free region but is nevertheless very sensitive to variations in observation conditions.

This work shows that it is possible to achieve a good agreement with the previously published results for all types of sources. Nonetheless, the datasets used here already give an indication of the limitations of this technique. To achieve a comparable background rate between ON and OFF runs, the two need to be chosen from periods with comparable optical efficiency. Due to the limited number of available OFF runs in these periods, large systematic errors can be introduced on the source parameters. This effect can be mitigated by constructing a background model template suitable for long-term hardware conditions, with corrections to the normalisation designed to account for short-term variations, thereby expanding the pool of viable OFF runs for these periods.

While this study presents a detailed analysis of the systematic uncertainty on the run-matching approach, an additional source of uncertainty —not examined in detail here— is introduced because of the stacking of the observations. This method of combining the observations for the analysis can produce a slight gradient in the number of background counts over the FoV. While this effect is small, it should nevertheless be kept in mind when interpreting the results achieved with this method and becomes particularly relevant for large, extended sources.

An additional problem of this framework is how to treat the Galactic diffuse emission. In this work, the energy threshold has been increased to exclude the influence of the diffuse emission, but this is not ideal. A better approach would be to construct an additional spectromorphological template from interstellar gas tracers.

While these disadvantages show that the run-matching approach presented here cannot compete with the 3D background model template method in regions containing few sources with a small extension, the non-dependence on source-free regions in the observation is a major advantage in sky regions with many sources or for the detection of diffuse extended structures, which cannot be observed using the background model template alone. The presented background estimation technique is an extension of the background estimation using a 3D background model template, offering the possibility to still profit from the small statistical uncertainty of the background model template, even for regions filled with significant emission, where this method can traditionally not be used. This application is vital considering that there are currently no survey instruments observing the southern γ-ray sky, restricting the observable source population to structures that can be detected with the comparatively small FoV of the H.E.S.S. array. The combined method presented here also has the potential to increase the population of sources observable with CTAO (Cherenkov Telescope Array Consortium et al., 2019), opening up the possibility of using the superior angular resolution to expand our knowledge of large extended structures previously uniquely detected by the Water Cherenkov Detectors.

4 Introduction to Pulsars and their Environments

This chapter will give an introduction to the evolution of pulsar environments. Afterwards two specific pulsars, in different evolution states, PSR J1813−1749 and PSR J1057−5226 are introduced in detail. For both of these regions data acquired with H.E.S.S. and Fermi-LAT are analysed and possible injection scenarios are evaluated.

4.1 Supernovae and their Remnants

Supernovae, the explosion of certain types of stars, can be broadly sorted into two categories with distinct progenitors and explosion mechanisms: core-collapse supernovae and thermonuclear supernovae. The latter are thought to be caused by runaway thermonuclear fusion, which is caused by a white dwarf exceeding a maximum stable mass, the Chandrasekhar limit, after which electron degeneracy pressure in the core can no longer counter gravitational pressure. Thermonuclear supernova explosions leave no remnant behind. More information about this type of supernova explosion can be found in Liu et al. (2023). This work focuses on the remnants of the second kind of explosion, the core-collapse supernova explosion, which occurs for massive stars and is the key mechanism behind the formation of pulsars. An in-depth discussion can be found in Vink (2020) and Bambi and Santangelo (2024).

A star forms from the accumulation of gas in the interstellar medium. Assuming an ideal gas and that gravitational energy and internal energy are in equilibrium, one can derive an expression for the gas density ϱ depending on mass M and temperature T:

$$\varrho \propto T^3 M^{-2} \,. \tag{50}$$

From this, it can be inferred that if gravity is the only energy-generation process, a contracting mass heats up. So as the star forms and gains density, its central temperature keeps rising. Once the temperature reaches $\sim 10^7\,\mathrm{K}$ hydrogen fusion to helium starts in the core. At this stage, the contraction of the star due to gravitational pressure is stopped by the thermal pressure from the nuclear fusion as well as electron degeneracy pressure. Once all hydrogen is burned, the thermal energy is not able to counter gravity anymore and the core contracts again. This contraction leads to an increase in temperature until the ignition of helium burning in the core. The star, depending on its mass, progresses through several successive fusion stages, forming a shell-like structure as fusion continues in the surrounding layers.

For a very massive star ($M > 10 M_\odot$) the fusion processes continue until the formation of an iron core. As iron has the highest binding energy per nucleon, its fusion is an endothermic reaction, making further fusion not energetically favourable. In this stage, thermal pressure is only generated from burning of the outer shells, resulting in a growing iron core. This thermal pressure is not able to counter gravity, which leads to further contraction and heating of the core. The temperature increase leads to photodisintegration of the iron nuclei, resulting in the presence of many protons and neutrons and heating the core further. At these high densities, electron capture becomes possible, which leads to the reaction $\mathrm{p} + e^- \rightarrow \mathrm{n} + \nu_e$, and significantly reduces the only force which still counters gravity, electron degeneracy pressure. This leads to a

rapid collapse of the core under the gravitational pressure.

Once the core has collapsed to nuclear density, the neutron degeneracy pressure is able to counter the gravitational pressure, and the collapse stalls. This sudden stop results in the formation of a shock wave, which propagates outward. Simulations of this process show that the initially outward propagating shock wave stalls due to the pressure of the still infalling material. The reason for the outward propagation of the shock wave after it has been stalled is not clear yet. The standard evolution model of supernovae explosions currently explains the outward propagation and the expulsion of all material above the core into the ISM due to interactions of the highly energetic neutrinos with the infalling matter (Bethe and Wilson, 1985). However, overcoming the ram pressure of the inward falling material would require that $\sim 99\%$ of the total energy of the collapse is carried away by neutrinos, and the feasibility of such a high rate is still highly debated (Liebendörfer et al., 2001; Sumiyoshi et al., 2005).

The whole explosion process takes place on a timescale of milliseconds and releases several solar masses of ejecta into the ISM with a speed of $\sim 10^4\,\mathrm{kms}^{-1}$ and an energy of $\sim 10^{51}\,\mathrm{erg}$ (Slane, 2017). As the ejecta expand into the ambient medium, they sweep up, compress and heat the surrounding medium. This creates a contact discontinuity between the shocked ejecta and the ambient medium, which results in the formation of a strong outward-moving shock front. This shock is referred to as forward shock and its formation is generally seen as the birth of the supernova remnant (SNR). The evolution of this remnant can broadly be divided into four phases.

Shortly after the explosion, the ejecta propagate outward into a dense region that has been heavily influenced by the stellar wind of the progenitor star. The shock front forms and expands outward, while the ejecta behind the forward shock expand adiabatically into the surrounding medium, cooling them to low temperatures. Due to the accumulation of material, the forward shock gradually slows down, while the ejecta behind the shock are still expanding outward at high speeds. This builds up pressure in the shocked surrounding medium, which in turn pushes back against the freely expanding ejecta, forming a reverse shock that moves inward (in the frame of the ejecta). This phase is referred to as the free expansion phase and ends when $M_{\mathrm{swept}} \sim M_{\mathrm{ejecta}}$. The duration of this phase depends strongly on the mass and energy of the ejecta, but also on the stellar wind of the progenitor, which strongly influences the density of the region in which the forward shock expands (Cardillo et al., 2015).

The next phase is referred to as the Sedov-Taylor phase and is characterised by a mass domination of the swept-up ISM over the ejecta and adiabatic expansion. The reverse shock has usually traversed most of the ejecta and heated them significantly. The phase ends when radiative losses become dominant.

Once radiative cooling becomes significant, the remnant enters the snow-plow phase. In this phase the remnant is still expanding, but mainly due to thermal pressure. The phase ends when no more expansion is possible.

In the final phase, the shock front slows to subsonic speeds and merges with the ISM. A thorough review of the different phases is given in Vink (2020).

The development of the core after the explosion depends on the initial mass and the abundance of elements heavier than helium, the metallicity of the progenitor. For progenitors with a low metallicity and an initial mass of smaller than $20 - 25\,M_{\odot}$, the neutron degeneracy pressure is not able to counter the gravitational pressure and the

core collapses, creating a black hole. Kochanek (2015) has presented observational evidence that it is also possible for heavy progenitors to collapse directly into a black hole without undergoing a supernova explosion. In the majority of supernova explosions, the progenitors have a mass lower than $\sim 20 - 25\,M_\odot$. In this case, the neutron degeneracy pressure is enough to counter the gravitational pressure, stopping the collapse and leaving behind a very dense object, which is referred to as neutron star.

Stars in an intermediate mass range of $8\,M_\odot < M < 10\,M_\odot$ can also undergo a supernova explosion in case they have a degenerate oxygen-neon-magnesium core. In this scenario, the supernova explosion occurs before the iron-burning stage is initiated. Since the mass of the progenitor is lower, the gravitational pressure is not as strong, and an equilibrium between electron degeneracy pressure and gravitational pressure is reached after Carbon burning in the core is completed. No further contraction happens and the star continues with shell burning until the mass of the core approaches the Chandrasekhar limit of $M = 1.38\,M_\odot$ (Chandrasekhar, 1931). At this point, the temperature is high enough for electron capture to set in, reducing the electron degeneracy pressure. This results in a runaway process that leads to a supernova explosion. In this case the explosion is referred to as an electron capture supernova explosion, and the core is expected to be a neutron star. SN 1054, associated with the Crab Nebula, is believed to be such an electron capture supernova due to the low explosion energy and specific observational properties, such as its faint ejecta mass (Hillebrandt, 1982).

Stars with masses below $8\,M_\odot$ do not undergo supernova explosions. After exhausting hydrogen in the core, the star expands, and helium fusion begins. Strong stellar winds cause mass loss, and eventually, the outer layers are expelled, forming a planetary nebula. The remnant is a carbon-oxygen white dwarf, supported by electron degeneracy pressure, which remains stable as long as its mass stays below the Chandrasekhar limit. If the star is part of a binary system, the white dwarf can accrete mass from its companion. If it approaches the Chandrasekhar limit, a thermonuclear runaway ignites carbon fusion, leading to a Type Ia supernova, which completely disrupts the star. More information on the evolution of low mass stars can be found in Luhman (2012).

4.2 Pulsars

In both core-collapse supernovae and electron-capture supernovae, the remnant is a very dense object ($\varrho \sim 10^{17}\,\mathrm{kg/m^3}$), referred to as a neutron star. During the collapse, the radius of the progenitor shrinks from $10^4 - 10^6\,\mathrm{km}$ to $\sim 10\,\mathrm{km}$ (Vidaña, 2018), conserving both the magnetic flux $\Phi = B \cdot A$, with A the surface area of the star and the angular momentum $L = I \cdot \omega$, with $I = M \cdot R^2$ the moment of inertia. This leads to very high magnetic fields in the order of $10^8 - 10^{15}\,\mathrm{G}$ and rapid rotation of the neutron star with spin periods $P = 2\pi/\omega$ of around $0.03 - 3\,\mathrm{s}$.

The existence of these rapidly rotating, neutron-dense objects as remnants after a supernova explosion has first been postulated in Baade and Zwicky (1934). Since then, models describing possible radiation from these objects, as well as theories about the state of matter in their dense interiors, have undergone numerous revisions. To this day, there is no universally accepted model for the composition and equation of state of neutron star matter (Vidaña, 2018).

There has, however, been significant progress in understanding the potential radiation emitted by these sources. In 1967, F. Pacini postulated that a rapidly rotating neutron star with a strong magnetic field could emit significant radiation across the electromagnetic spectrum (Pacini, 1967). In the same year, a sky survey of a large radio telescope at the Mullard Radio Astronomy Observatory revealed radio signals that were periodically appearing at a fixed position in the sky with high regularity (Hewish et al., 1968). These pulses with a period of $P = 1.34\,\mathrm{s}$ were shown to originate from a compact object, which was termed pulsar due to the short time intervals and precise periodicity of the signal. Shortly after the discovery of the pulsed radio emission, Gold (1968) made the connection between the discovered pulsating object and the theory postulated by Pacini, stating that pulsars are neutron stars that emit radiation from their magnetic poles. This connection has since then been established by observational evidence, such as the precise periodicity of many pulsars, as well as their detection at the centres of supernova remnants.

The strong magnetic field of the rotating neutron star induces an electric field on the stars surface. This electric field, in turn, accelerates charged particles from the surface along the magnetic field lines. These charged particles are thought to be mainly electrons and positrons, though contributions from ions cannot be neglected (Lemoine et al., 2015; Amato et al., 2003a). The primary particles, accelerated along the magnetic field lines, emit high-energy gamma rays via curvature radiation and IC scattering. These photons then undergo pair production, initiating electron-positron cascades that fill the region around the star. When the magnetic axis and the rotation axis are aligned, the charged particles stay trapped on the symmetric field lines and can be detected as an isotropic signal around the neutron star (Pétri et al., 2002).

If the magnetic and rotational axes are misaligned, the geometry of the system changes. Close to the neutron star, the magnetic field lines can be assumed to be co-rotating with the rotational axis of the star. This region is referred to as the pulsar magnetosphere. The speed of co-rotation of particles accelerated on the magnetic field lines with the pulsar can be described by $v = \omega R$ with ω the angular velocity of the pulsar. At a distance of $r_L = c/\omega$, further co-rotation is no longer possible since this would require the particles to become faster than the speed of light. Since R is given as the distance from the rotational axis, the end of the magnetosphere is marked by a region with the cylindrical radius of r_L, called the light cylinder. This relation infers that magnetic field lines that extend beyond the light cylinder cannot be closed

A schematic of the region can be seen in Figure 4.1. The charged particles accelerated along open field lines escape the magnetosphere, resulting in a magnetized supersonic particle wind. This can be observed from Earth if the magnetic axis is oriented such that the beam sweeps across our line of sight. The magnetized particle wind also leads to the gradual decrease of the rotational energy of the pulsar. Under the assumption of a rotating magnetic dipole model, the energy loss rate $\dot{E}$ can be approximated as:

$$\dot{E} = -\frac{B_p R^6 \Omega^4}{6c^3} \sin(\chi)^2 \,, \tag{51}$$

with B_p the magnetic dipole strength and χ the angle between the magnetic field and the pulsar rotation axis, which accounts for the misalignment. The behaviour of the

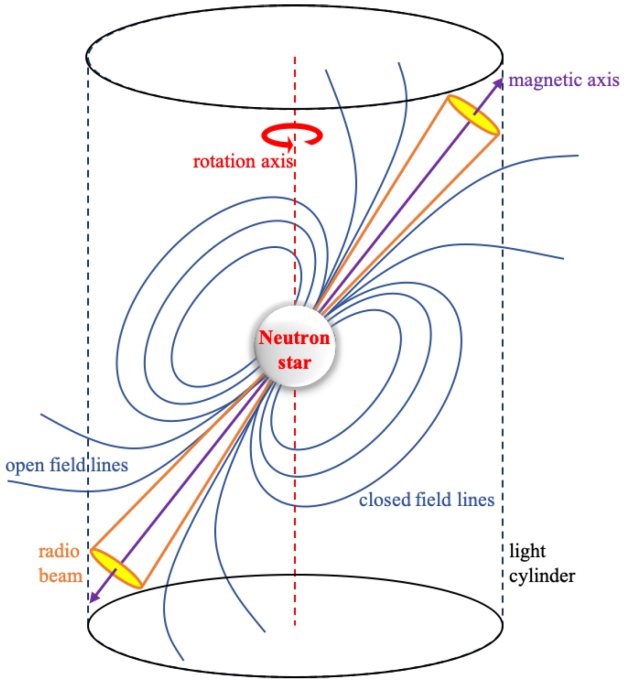

Figure 4.1: Left: Schematic depiction of the light cylinder around a pulsar. Figure taken from Lorimer and Kramer (2004)

spin-down luminosity with time is characterized by:

$$\dot{E} = \frac{\mathrm{d}E}{\mathrm{d}t} = \dot{E}_0 \left(1 + \frac{t}{\tau_{sd}}\right)^{\frac{n+1}{n-1}} , \tag{52}$$

with $\dot{E}_0$ the initial spin-down luminosity, τ_{sd} the spin-down timescale, t the neutron star age and n the braking index, which qualifies how the spin-down rate changes with time. For a simple dipole model the braking index is expected to be $n = 3$. Observations of isolated pulsars have however shown that the measured braking index often deviates from that expectation (Lyne et al., 1996; Hamil et al., 2015; Archibald et al., 2016), implying that the change in spin-down rate cannot be attributed solely to constant dipole radiation.

The number of ejected particles per unit time can be estimated as:

$$\dot{N} = 2.7 \cdot 10^{30}\, \kappa \left(\frac{B}{10^{12}\,\mathrm{G}}\right) \left(\frac{P}{1\,\mathrm{s}}\right)^{-2} \mathrm{s}^{-1} , \tag{53}$$

where κ is the number of pairs produced by a single primary particle at the polar caps. The true value of κ is however still debated and depends strongly on the ion fraction in the pulsar wind (Hibschman and Arons, 2001; Bietenholz et al., 2004).

The age of the pulsar can be calculated as:

$$\tau = \frac{P}{(n-1)\dot{P}} \left(1 - \left(\frac{P_0}{P}\right)^{n-1}\right) , \tag{54}$$

with P_0 the initial spin period of the star. Under the assumption of a simple magnetic dipole model, this can be simplified to the characteristic age of the system:

$$t_{\mathrm{ch}} = \frac{P}{2\dot{P}} \tag{55}$$

with $\dot{P} = \mathrm{d}P/\mathrm{d}t$ the time derivative of the period. While providing a good first estimate of the pulsar age, it should not be seen as the true age of the pulsar, and models of individual sources often find the characteristic age to be inaccurate (Kaspi et al., 2001; Gaensler and Frail, 2000). This inaccuracy is also evident when comparing the characteristic age of the Crab pulsar ($\tau_c = 1260$,yrs) (Manchester et al., 2005) to the historical record of its supernova explosion in 1054 AD (Hillebrandt, 1982).

4.3 Pulsar Wind Nebulae

When the initially low-density particle wind streams out of the light cylinder, it is compressed and slowed by interactions with the ambient medium. This creates a wind termination shock, which serves as an acceleration site for further particles escaping the light cylinder. The shock forms at a radius where the pressure within the surroundings equals the ram pressure of the wind:

$$R_{\mathrm{TS}} = \sqrt{\frac{\dot{E}}{4\pi\omega_c p_{\mathrm{PWN}}}}\,, \tag{56}$$

with ω_c the filling factor for the wind and p_{PWN} the total nebula pressure (Slane, 2017). The acceleration mechanism at this shock front is still debated, it is believed to be dominantly caused by Fermi acceleration, with magnetic reconnection playing a substantial part (Sironi and Spitkovsky, 2011; Sironi and Spitkovsky, 2014).

Overall, it is believed that the injection spectrum of the electrons can be well described by a broken power law:

$$\frac{d\dot{N}}{dE} = \begin{cases} \dot{N}_{\mathrm{break}} \left(\frac{E}{E_{\mathrm{break}}}\right)^{-p_1}, & E_{\mathrm{min}} \leq E \leq E_{\mathrm{break}} \\ \dot{N}_{\mathrm{break}} \left(\frac{E}{E_{\mathrm{break}}}\right)^{-p_2}, & E_{\mathrm{break}} \leq E \leq E_{\mathrm{max}} \end{cases} \tag{57}$$

with typically a high index $p_2 \sim 2.5$ reflecting the dominance of Fermi acceleration at a strong shock as an acceleration mechanism and p_1 considerably lower possibly indicating the influence of magnetic reconnection (Bambi and Santangelo, 2024).

The pulsar wind provides a steady stream of what is thought to be predominantly leptonic particles, with a possible hadronic component, whose contribution remains uncertain (Amato et al., 2003b). The leptons of the particle wind, in turn, produce γ-rays by synchrotron radiation due to interactions of the particles with the uniform magnetic field of the nebula and IC scattering between leptons and photons of the ambient medium. The evolution of the pulsar wind nebula (PWN) around the pulsar can then be divided into a number of different phases, which depend on the interplay between the pulsar and the evolution and density of the surrounding SNR. For young systems, it can be assumed that the pulsar is located in the centre of the SNR. This is not true for later phases since the propagation of the forward shock front of the SNR depends on the density of the ambient medium, which often is highly anisotropic due to

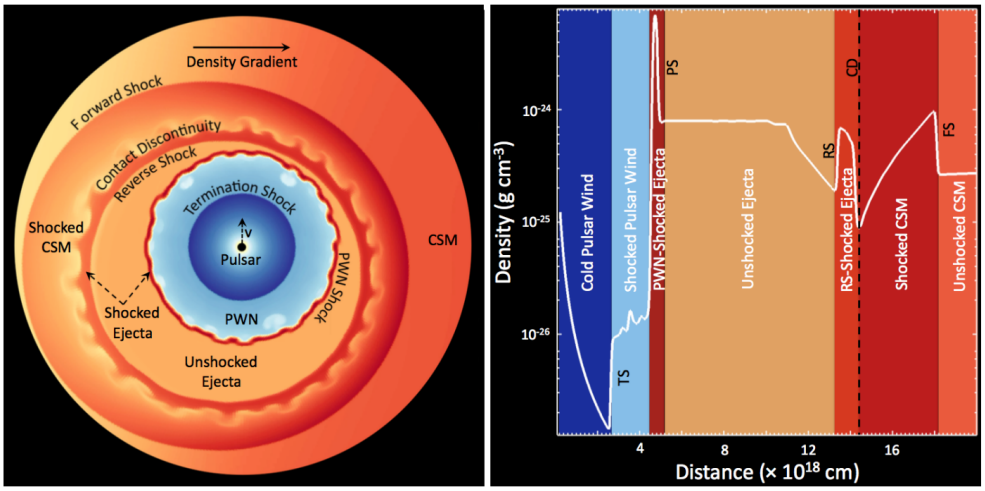

Figure 4.2: Left: Density image for the evolution of a pulsar wind nebula in its host SNR. Right: Density distribution of a radial slice through the system. Figure taken from Slane (2017).

anisotropies in the stellar wind of the progenitor. This leads to an often anisotropic development of the forward shock and in conclusion, also of the reverse shock. An additional factor of asymmetry of the system results from asymmetries in the supernova explosion itself. They result in an imbalance of momentum, which causes the neutron star to move in the opposite direction. These kick velocities are found to be in a range of $\sim 200 - 1500\,\mathrm{kms}^{-1}$ for single star systems (Slane, 2017).

A simulated configuration for the beginning of the evolution of the PWN/SNR system can be seen in Figure 4.2. Initially, the pulsar wind forms a low-density, high-pressure bubble of relativistic particles, which is referred to as pulsar wind nebula (PWN). Due to its high pressure, it expands into the cold, high-density region of unshocked ejecta in the SNR and sweeps up the material in a thin shell, creating a PWN shock. The shell mainly confines the relativistic particles within the PWN, though extreme density gradients might result in particle escape due to instabilities (Chandrasekhar, 1961). The PWN expands rapidly, which results in a decrease of the magnetic field and, therefore a weakening of synchrotron emission. The inverse Compton emission, however, increases in older systems due to the constant injection of particles from the pulsar wind and the γ-ray emission starts to dominate over the observed X-ray and radio emission. This interplay of radiative mechanisms can be used to infer the stage of evolution of a PWN from the observed γ-ray emission. Most of the bright TeV PWNe detected are in this stage, with many of them accompanied by a faint X-ray nebula with magnetic fields in the $\sim 5\,\mu$G range (de Jager, 2008). However, even in TeV Nebulae, the luminosity decreases with increasing age, as it is directly correlated with the spin-down luminosity, with a study finding a correlation of $L \sim \dot{E}^{0.59\pm0.21}$ (H.E.S.S. Collaboration et al., 2018b).

Another characteristic of the signal from PWNe is the energy dependence of their spatial extent. In X-ray PWNe, the most energetic electrons, and therefore the brightest signal, can be found close to the pulsar where the magnetic field is strongest. The

lower energetic electrons farther from the pulsar emit synchrotron radiation in the radio energy range, resulting in a PWN that is more extended at those longer wavelengths.

Particle transport in PWNe involves a complex interplay between diffusion and advection, with both processes contributing to the overall transport of particles. If, for a simplified model, only diffusion is assumed, the spatial extent of the nebula can be approximated as $r_{\mathrm{diff}} = \sqrt{2t \cdot D}$ with D the diffusion coefficient given by:

$$\mathrm{D} = \mathrm{D}_0 \left(\frac{\mathrm{E}_e}{\mathrm{E}_{\mathrm{ref}}} \right)^{\delta} , \tag{58}$$

with the electron energy E_e, the diffusion index δ and the diffusion coefficient D_0 at the reference energy E_{ref}. Based on diffusion alone, it might be expected that nebula extension would increase with increasing lepton energy since more energetic particles diffuse faster. However, this is not observed in studies of TeV PWNe (e.g. see (H.E.S.S. Collaboration et al., 2024), (H.E.S.S. Collaboration, 2019)). Instead, observations show a decrease in extension with increasing energy, which is generally attributed to electron cooling. Higher energetic leptons lose energy faster through synchrotron cooling (only near the pulsar) and IC scattering, meaning they cannot diffuse outwards as far before cooling significantly. As a result, TeV PWNe show a highly energy-dependent morphology, with their extension being smallest at the highest energies (H.E.S.S. Collaboration, 2019; Aharonian et al., 2024).

The free expansion of the PWN stops when it collides with the reverse shock. At this stage, the pressure in the reverse shock is greater than the pressure in the PWN, resulting in deceleration and then later compression of the PWN (Gelfand et al., 2009). Due to the asymmetric nature of the formation of the reverse shock and the kick velocity of the pulsar, the likelihood of an asymmetric collision is high. This can result in a displacement between the pulsar and PWN or even full separation of the two (see page 3544 in Bambi and Santangelo (2024) and references therein). If no separation occurs, the compression leads to an increase in magnetic field strength (Gelfand et al., 2009). This significantly increases the synchrotron radiation from particles injected into the nebula before the interaction, resulting in the existence of low energetic particles in the nebula. The pressure within the nebula also increases until it overcomes the pressure of the ambient medium and expands again. During this interplay between compression and expansion, an increase of instabilities in the PWN is thought to occur, which can lead to 'leakage' of highly relativistic particles into the SNR or even into the surrounding medium (Ohira et al., 2018).

A good way to visualize the evolution of pulsars over time is given by the $P - \dot{P}$ diagram. Such a diagram, containing all pulsars listed in the ATNF (Manchester et al., 2005), can be seen in Figure 4.4. Young energetic pulsars have short spin-periods (P) and high spin-down rates ($\dot{P}$), and are located in the upper left corner of the diagram. These pulsars are expected to power compact and very bright PWNe. Over time, the pulsars lose spin-down energy, moving toward the centre of the diagram. The bulk of the PWNe population is believed to be observable from these pulsars since they still have enough spin-down energy to sustain particle acceleration but are old enough that their nebulae have expanded significantly. When the pulsar age increases further, its position in the diagram shifts further towards the bottom right corner. At this stage, it no longer has enough spin-down energy to power a pulsar wind, and the PWN dissipates into

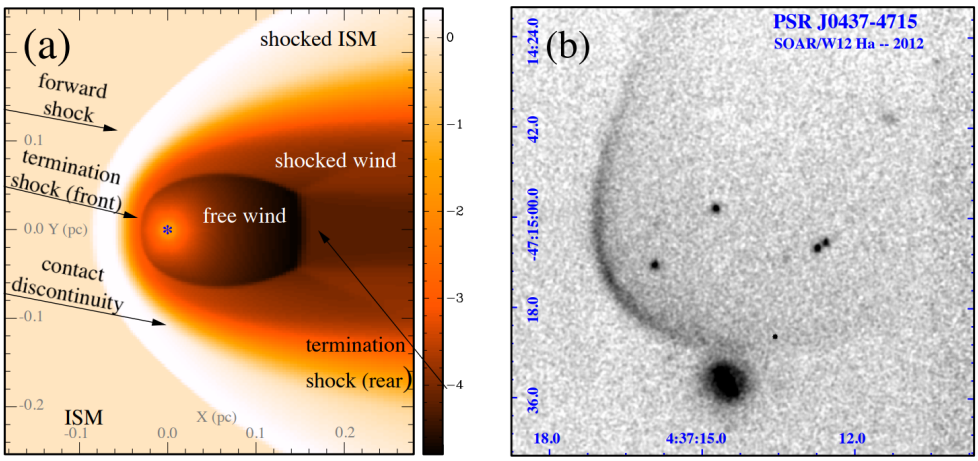

Figure 4.3: Left: Schematic diagram of the last evolution stage of PWNe with a bow-shock nebula forming around the pulsar. Right: Bow-shock nebula around PSR J0437−4715 as seen from Hα observations. Figure taken from Slane (2017)

the ISM. Once the pulsar has crossed the death line, indicated by the orange-shaded region in Figure 4.4, it does not produce further electromagnetic emission. The absence of electromagnetic emission below the death line can be explained by several different scenarios. The most commonly accepted scenarios are changes in the plasma flow or magnetic field of the pulsar, discussed in detail in Beskin and Litvinov (2022), or the lack of further particle acceleration due to the breakdown of pair production and the loss of strong electric fields, discussed in detail in (Beskin and Istomin, 2022).

Pulsars located in the bottom left corner are so-called millisecond pulsars. These pulsars have short, stable periods with small spin-down rates. They are produced either by accretion-induced collapse of white dwarfs or upcycling of old radio pulsars via accretion from a companion. More information on the current studies of millisecond pulsars can be found in Manchester (2017) and Halder et al. (2023). γ-ray emission from these pulsars has recently been detected for a selected few pulsars using *Fermi*-LAT (Abdo et al., 2009a). However, in the TeV energy range, no detection of emission has been reported yet, and a study conducted with HAWC shows that even when all likelihood profiles of the millisecond pulsar population accessible to the Observatory are combined, no significant emission can be found (Abeysekara et al., 2025).

4.4 Pulsar Halos

The third evolutionary stage begins when the pulsar exits the SNR. The kick velocity of the pulsar (around $v \sim 300\text{kms}^{-1}$) is greater than the speed of sound in the ISM (around $v \sim 100\text{kms}^{-1}$ for a hot phase) (Slane, 2017). This leads to a confinement of the pulsar wind due to the pressure resulting from the pulsar motion, and a bow-shock morphology can be assumed. The particles injected by the pulsar wind are no longer confined to a small region by strong magnetic fields. They get upscattered on the shock fronts of the termination shock and forward shock and can then freely diffuse outward into the surrounding ISM. This morphology can be seen in Figure 4.3. At this stage, a constant injection rate of particles can be assumed since the pulsar age typically is much larger than the spin-down timescale.

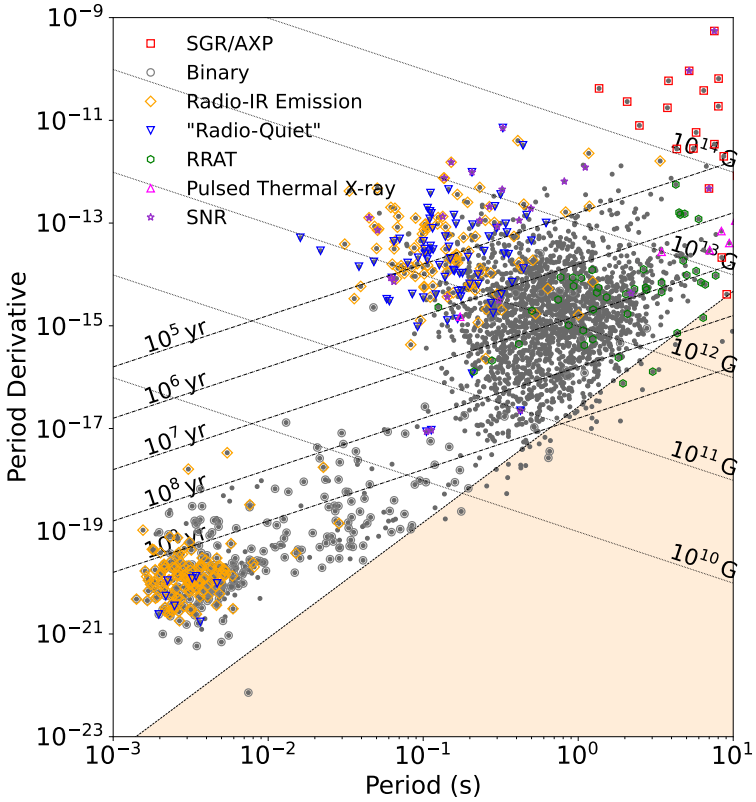

Figure 4.4: $P - \dot{P}$ diagram of all pulsars listed in the ATNF catalogue (Manchester et al., 2005). The death line is indicated by the orange shaded region. This diagram was computed using the python package `psrqpy` (Pitkin, 2018).

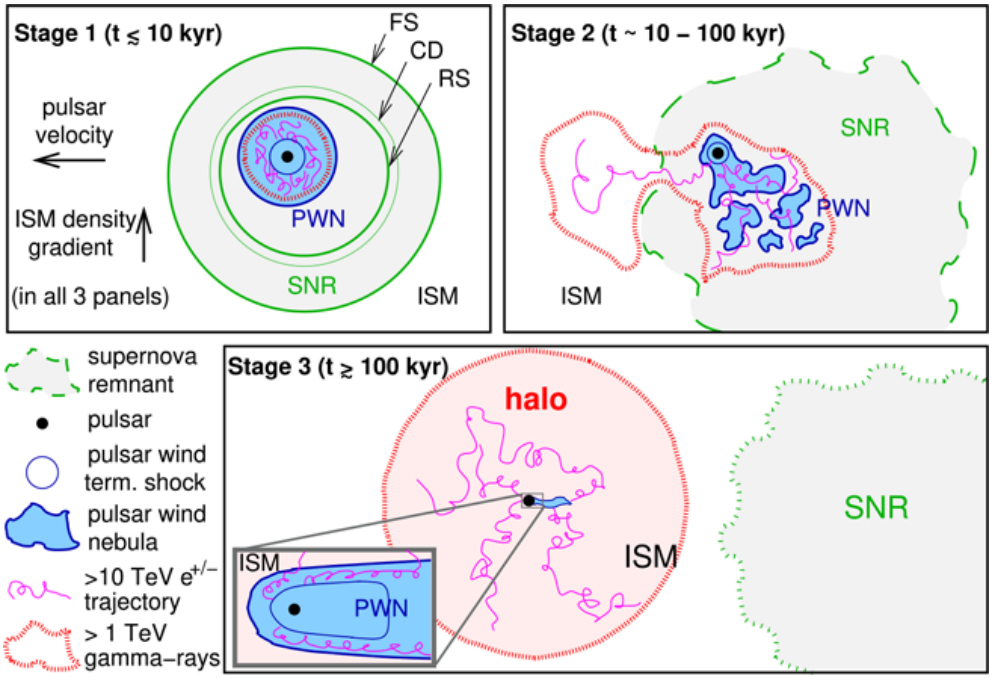

Figure 4.5: Schematic of the evolution of a pulsar system with time. Figure taken from Giacinti et al. (2020)

Following the definition in Giacinti et al. (2020), structures in this evolution state are no longer referred to as PWNe, but pulsar halos, once the pulsar itself no longer dominates the dynamics or the composition of the ISM, that is, when the energy density of the relativistic electrons drops below the energy density of the ISM. Such structures are also characterized by a large extension in the TeV energy range due to IC scattering of the leptons, which are no longer confined around the pulsar. In contrast, the X-ray structure is substantially less extended since synchrotron radiation is only produced in the vicinity of the pulsar, where the magnetic fields are sufficiently strong. A schematic of the three evolutionary stages outlined above and a rough estimate of how much time the system spends in each phase can be seen in Figure 4.5.

At this stage, it can be assumed that diffusion always dominates over advection, with studies having identified that the electron diffusion in these regions is several orders of magnitudes below the diffusion coefficient expected for the ISM (H.E.S.S. Collaboration et al., 2023). The reason for the suppressed diffusion is still highly debated (Quenby, 2018; Fang et al., 2019; Recchia et al., 2021). A detailed summary of the current research in the field of pulsar halos can be found in Fang (2022a).

Following the definition of pulsar halos outlined above, until now, only a few such halos have been detected, with the first being the halos around the Geminga pulsar and PSR B0656+14 (Abeysekara et al., 2017b). The low number of detected halos is, however, not necessarily an accurate depiction of the pulsar halo fraction but could be due to the challenges faced when observing highly extended emission (see Section 3.1).

5 PSR J1813−1749 and its Nebula

The evolution of a PWN depends strongly on the properties of the pulsar that powers the nebula, as well as the environment it evolves in. With a characteristic age of 5600 years (Gotthelf and Halpern, 2009) and a spin-down power of $\dot{E} = 5.6 \cdot 10^{37}$ erg/s, the pulsar PSR J1813−1749 shows the fourth-largest spin-down energy loss rate measured to date (Ho et al., 2020). This combination of properties makes the young, energetic pulsar not only a promising candidate for being observable in γ-rays, but also an interesting object for studying the influence of the high injection power of a central pulsar onto its nebula. Additionally, PSR J1813−1749 is positionally coincident with the SNR G012.8–00.0, which is believed to be its parent SNR. This association provides a rare opportunity to investigate both the evolution of a PWN within its remnant and the complex interactions between the SNR and PWN.

Even before the detection of the pulsar by Gotthelf and Halpern (2009), VHE γ-ray emission in the region had been discovered during the first Galactic plane survey conducted by H.E.S.S. in 2005 (Aharonian et al., 2006c). The bright source HESS J1813−178 is located on the Galactic plane (GLON, $12.82 \pm 0.03°$; and GLAT, $-0.03 \pm 0.02°$) with a compact extension of $\sigma = (0.050 \pm 0.004)°$.

Shortly after this discovery, the young shell-type radio SNR G012.8–00.0 was discovered by the radio telescope Very Large Array (VLA) in the 20 cm and 90 cm band (Brogan et al., 2005). Brogan et al. (2005) also report the detection of X-ray emission from the ASCA telescope, which is contained within the shell of the SNR. The pointing uncertainty of the ASCA, however, was too large to distinguish between the signal from the centre or the shell of the SNR. No pulsed emission was found at this time and no conclusion about the origin of the emission could be made.

These observations triggered a follow-up study of the region using the INTEGRAL telescope, where a composite signal was found in the $2 - 10$ keV energy range (Ubertini et al., 2005). This study finds a softer spectrum than the previous studies and indicates a possible interpretation as a composite system with a pulsar in the centre of an SNR. The IACT array MAGIC later confirmed the detection of excess γ-ray emission compatible with the observations made by H.E.S.S. and a high likelihood of the observed γ-ray emission being of hadronic origin (Albert et al., 2006).

A study conducted with the XMM-Newton telescope, which has a considerably higher angular resolution than the previously mentioned telescopes, detected a point-like X-ray source with a surrounding nebula in the centre of the shell, concluding that the signal was most likely associated with a PWN (Funk et al., 2007). This finding is supported by observations of X-ray emission with a soft spectrum by Chandra (Helfand et al., 2007).

Funk et al. (2007), however, also presented an alternative origin scenario for the observed γ-ray emission from HESS J1813−178. A large, dense molecular cloud is located in the vicinity of the TeV source, at a distance of only $\sim 10'$. The molecular cloud is associated with the star-forming region W33. This connection suggests that the observed γ-rays could be produced by cosmic rays accelerated in the SNR before interacting with protons in the dense molecular cloud. Both scenarios are presented as equally likely, and Funk et al. (2007) notes that no further distinction can be made until a better resolution can be reached or a pulsar is detected.

The discovery of 44.7 ms pulsations in 2009 by another study conducted with XMM-

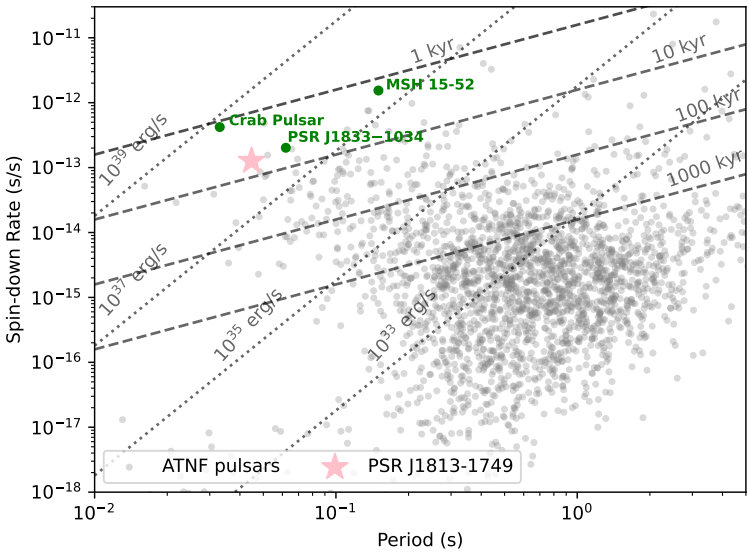

Figure 5.1: $P - \dot{P}$ diagram of the pulsars listed in the ATNF catalogue (Manchester et al., 2005). The position of PSR J1813−1749, the pulsar positionally coincident with HESS J1813−178 is indicated by the pink star. Also shown are the positions of other young, well-known pulsars with similar spin-down powers, which host compact PWNe in green, and the spin-down luminosity and characteristic age of the pulsars as dotted and dashed lines, respectively.

Newton increased the likelihood of a leptonic scenario (Gotthelf and Halpern, 2009). The pulsar PSR J1813−1749 is detected as positionally coincident with the TeV emission, and the rather compact extension observed both in X-ray energies and TeV energies, as well as the position of the pulsar in the centre of the observed shell-type SNR, point toward the system being rather young. The position of PSR J1813−1749 in a $P - \dot{P}$ diagram compared to the other pulsars in the ATNF catalogue (Manchester et al., 2005) can be seen in Figure 5.1.

Additionally shown are three other young pulsars with similar spin-down power, around which a bright, compact PWN has been detected and firmly identified: the crab pulsar, with a spin-down power of $\dot{E} = 4.6 \times 10^{38}\,\mathrm{erg/s}$ and a characteristic age of $\tau_c = 1.24\,\mathrm{kyrs}$; PSR B1509−58, which is the pulsar powering the PWN MSH 15−52, with a spin-down power of $\dot{E} = 1.8 \times 10^{37}\,\mathrm{erg/s}$ and a characteristic age of $\tau_c = 1.54\,\mathrm{kyrs}$; and PSR J1833−1034, with a spin-down power of $\dot{E} = 3.4 \times 10^{37}\,\mathrm{erg/s}$ and a characteristic age of $\tau_c = 4.87\,\mathrm{kyrs}$ (Manchester et al., 2005). The placement of PSR J1813−1749 in the $P - \dot{P}$ diagram shows that, assuming that the development of a PWN is only influenced by the pulsar, it is likely that the compact γ-ray emission from HESS J1813−178 is associated with the pulsar.

The interpretation of the emission was further complicated by the detection of extended emission using data from the *Fermi*-LAT telescope. This emission is positionally coincident with the position reported by Aharonian et al. (2006c), but shows an extension of $(0.6 \pm 0.06)^\circ$ (Araya, 2018). While a similarly extended, weak but diffuse emission was observed during the Galactic plane survey (H.E.S.S. Collaboration, 2018b),

this detection was discarded because of large uncertainties in the background estimation. From their detection of the large extended emission, Araya (2018) concluded that the origin of the GeV and TeV γ-ray emission are disconnected and the GeV emission is more likely to be caused by cosmic rays accelerated at the shock fronts of the SNR or the HII star-forming region W33, while the TeV emission is caused by the central pulsar. Following a study conducted by Halpern et al. (2012) this scenario is, however, less likely because the distance to PSR J1813−1749 is far greater, possibly between $6 - 12\,\mathrm{kpc}$, than the estimated distance of $4.2\,\mathrm{kpc}$ estimated for W33.

An even more recent study of the region with *Fermi*-LAT supports the detection of the extended γ-ray emission and estimates a spatial extent of the emission of $0.56°$, with no uncertainty on the extension given, in an energy range of $1\,\mathrm{GeV} - 20\,\mathrm{GeV}$ (Xin and Guo, 2021). These observations are supported by HAWC, which detected positionally coincident emission with an upper limit for the extension of $0.5°$ (Albert et al., 2020), and LHAASO which detected a source with an extension of $(0.71 \pm 0.07)°$ with WCDA and two source components with an extension of $(0.68 \pm 0.08)°$ and $< 0.27°$ using KM2A (Cao et al., 2023a).

With these contradicting results, it has not been possible to establish which of the origin scenarios is the most likely for the γ-ray emission. The detection of extended emission for both *Fermi*-LAT and the WCDs, as well as the improvements in background rejection and event reconstruction in the last years - particularly regarding the detection of extended emission using IACTs make a reanalysis of the available H.E.S.S. data of this region an important task.

A reanalysis of both the TeV data from H.E.S.S. and the GeV data acquired from *Fermi*-LAT was conducted and published in the Master's Thesis Wach (2022). This work focuses on the improvement of the results presented in Wach (2022), as well as their interpretation using the evolution of different parent particle populations to explain the γ-ray emission. The following section will give a quick overview of the morphology and spectrum of the emission derived in the scope of the Master's Thesis and then move on to an extensive discussion about the systematic uncertainties on the analysis results and the physical modelling. The information about the spectromorphological analysis of the data, as well as the modelling of the emission, has partly been published in H.E.S.S. Collaboration et al. (2024).

5.1 Analysis of H.E.S.S. and *Fermi*-LAT data

The available H.E.S.S. data of the region around PSR J1813−1749 has been acquired in a time window between 2004 to 2010. After the application of spectral quality cuts (see Section 3.2.1), 32 hours of deadtime corrected observation time remain. The background was estimated using the background template model derived in Mohrmann et al. (2019a) and discussed in Section 3.1.4. The analysis was conducted using `gammapy, version 0.18.2` (Deil et al., 2020; Donath et al., 2023), which employs a maximum likelihood fitting algorithm (see Section 2.3.6 for more information). Since this analysis is fully described in the Master's Thesis Wach (2022), no additional information is given here. The main results needed for further interpretation in the scope of this work are given below, while a more in-depth explanation is given in Appendix B.1.

In addition to HESS J1813−178, another known γ-ray source is present in the ROI.

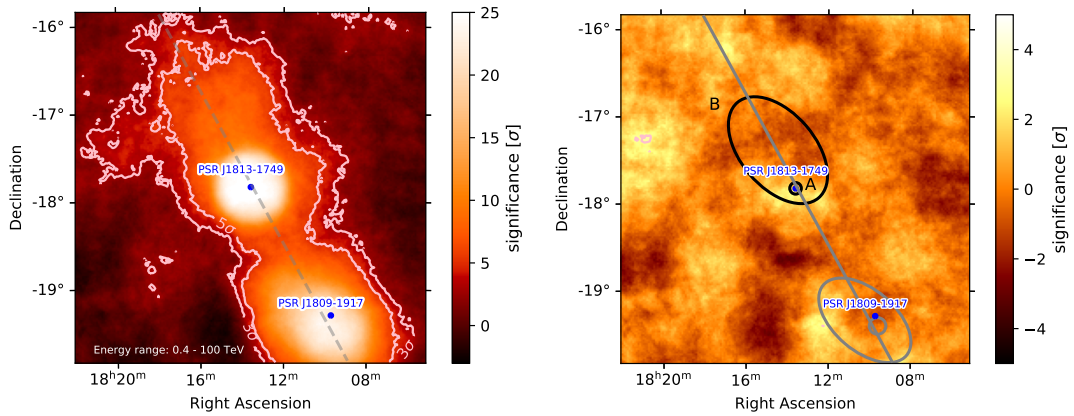

Figure 5.2: Li&Ma (1983) significance maps of the data taken by H.E.S.S. in the energy range between 0.4 TeV to 100 TeV. For both maps, a correlation radius of 0.4° was used. Left: The contours correspond to the $3\,\sigma$ and $5\,\sigma$ regions. The dashed line indicates the position of the Galactic plane. Right: Significance map of the region after subtracting the emission using four components. The blue dots indicate the positions of both pulsars. The $1\,\sigma$ Gaussian extent of the models used to describe the emission is indicated by the grey and black lines.

HESS J1809−193 was discovered using data from the galactic plane survey from H.E.S.S. (Aharonian et al., 2007). A recent reanalysis of the data using the background model template has led to the resolution of the emission into two source components (H.E.S.S. Collaboration, 2023). To account for this emission in the analysis presented here, the best-fit parameters from H.E.S.S. Collaboration (2023) were used.

Through the application of the background model template and improved reconstruction using ImPACT, the reanalysis of the data revealed that the emission can be best described by a compact emission model, as well as a second extended source component, which could be detected with a significance of $13\,\sigma$. It was found that a Gaussian model yields the best description for both components. The symmetric Gaussian source model is defined as:

$$\Phi\left(\Theta\right) = \frac{1}{2\pi\sigma_M^2} \exp\left(-\frac{1}{2}\frac{\Theta^2}{\sigma_M^2}\right) , \tag{59}$$

with σ_M being the $1\,\sigma$ containment radius of the Gaussian and Θ the angular distance to the model centre. In the case of an elongated Gaussian, the major axis σ_M is defined by σ_{eff}, the effective containment radius:

$$\sigma_{\text{eff}}\left(\Delta\phi\right) = \sqrt{\left(\sigma_M \sin\left(\Delta\phi\right)\right)^2 + \left(\sigma_M \cdot \sqrt{\left(1-e^2\right)} \cos\left(\Delta\phi\right)\right)^2} , \tag{60}$$

with e being the eccentricity and $\Delta\phi$ the difference between the position angle of the Gaussian ϕ and the position angle of the evaluation point (Donath et al., 2023). The best spectral description of both components could be achieved using a power law spectral model of the form:

$$\frac{\mathrm{dN}}{\mathrm{dE}} = \mathrm{N}_0 \cdot \left(\frac{\mathrm{E}}{\mathrm{E}_0}\right)^{-\Gamma} , \tag{61}$$

Table 5.1: Best-fit parameters obtained for the likelihood minimisation of H.E.S.S. data.

	HESS J1813−178A	HESS J1813−178B
Γ	$2.17 \pm 0.05_{\mathrm{stat}} \pm 0.03_{\mathrm{sys}}$	$2.36 \pm 0.09_{\mathrm{stat}} \pm 0.05_{\mathrm{sys}}$
$\mathrm{N_0}\,[10^{-12}\mathrm{cm^{-2}\,s^{-1}\,TeV^{-1}}]$	$3.16 \pm 0.18_{\mathrm{stat}} \pm 0.24_{\mathrm{sys}}$	$9.89 \pm 1.40_{\mathrm{stat}} \pm 1.23_{\mathrm{sys}}$
R.A. [°]	$273.400 \pm 0.004_{\mathrm{stat}} \pm 0.001_{\mathrm{sys}}$	$273.61 \pm 0.06_{\mathrm{stat}} \pm 0.07_{\mathrm{sys}}$
Dec. [°]	$-17.831 \pm 0.004_{\mathrm{stat}} \pm 0.001_{\mathrm{sys}}$	$-17.39 \pm 0.07_{\mathrm{stat}} \pm 0.08_{\mathrm{sys}}$
σ_M [°]	$0.056 \pm 0.003_{\mathrm{stat}} \pm 0.001_{\mathrm{sys}}$	$0.72 \pm 0.08_{\mathrm{stat}} \pm 0.09_{\mathrm{sys}}$
e	-	$0.80 \pm 0.06_{\mathrm{stat}} \pm 0.04_{\mathrm{sys}}$
$\Delta\varphi$ [°]	-	$40 \pm 7_{\mathrm{stat}} \pm 6_{\mathrm{sys}}$

where $\mathrm{N_0}$ is the flux normalisation factor, Γ the spectral index and $\mathrm{E_0} = 1\,\mathrm{TeV}$ the reference energy (Donath et al., 2023).

The best-fit parameters for both source components can be seen in Table 5.1. The compact component will hereafter be referred to as HESS J1813−178A, while the extended component will be referred to as HESS J1813−178B. The best-fit parameters of HESS J1813−178A derived from this study are in agreement with the results published in Aharonian et al. (2006c). The region before and after the fit can be seen in Figure 5.2. Additionally shown are the best-fit morphology for the emission around PSR J1813−1749 in black, and the best-fit morphology of the neighbouring source HESS J1809−193 from H.E.S.S. Collaboration (2023) in grey.

To obtain a consistent description of the region, an analysis of *Fermi*-LAT data, with increased exposure compared to the study conducted in Araya (2018), has also been carried out. The *Fermi*-LAT analysis was conducted using data from the beginning of the mission in August 2008 until October 2021. The most recent Instrument Response Functions (IRFs) from Pass 8 version 3 — `P8R3_SOURCE_V2` (Ajello et al., 2021) were used, and other sources in the ROI were described using catalogue models from the 12-year 4FGL source catalogue (Abdollahi et al., 2020).

The import process of the *Fermi*-LAT data, as well as a first analysis of the region, has already been presented in Wach (2022) and Aharonian et al. (2024). Therefore, just like for the H.E.S.S. data, no detailed information is given here. A more in-depth description of the data and analysis can, however, be found in Appendix B.2.

The analysis presented in the Wach (2022) identified only one extended component, described with an elongated Gaussian model and a simple power law as spectral model. This description, however, is not able to account for all observed emission in the FoV, and the simple power law is not a good fit for the shape of the SED.

To account for the remaining emission, a second, symmetric Gaussian component is fitted to the data. Because of the spectral shape below 10 GeV, a simple power-law spectral model cannot describe the observed emission well, so a power law with exponential cutoff was chosen as spectral model. Minimisation yields a compact component, positionally coincident with PSR J1813−1749.

The residual Li&Ma (1983) significance map after the application of both models is shown on the right-hand side of Figure 5.3. In addition to the maps, the SED points were derived. In each energy bin, a SED point was derived if the model fit in the

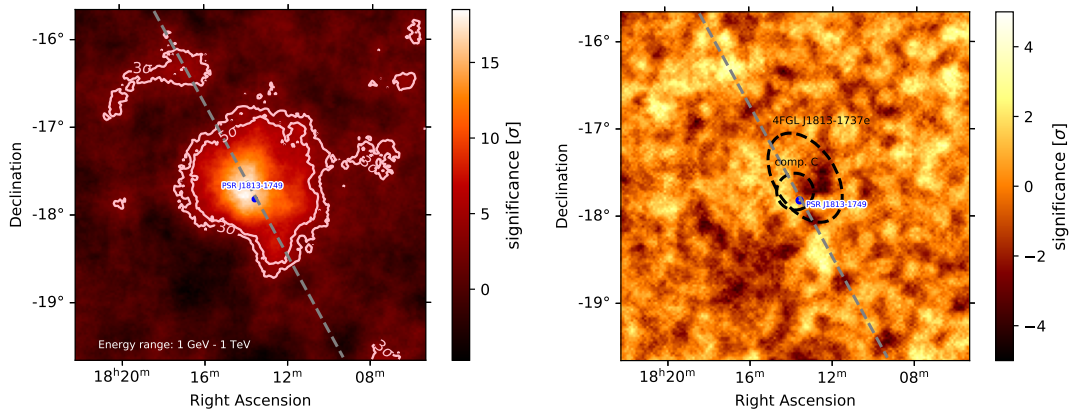

Figure 5.3: Li&Ma (1983) significance maps of the *Fermi*-LAT data around the position of 4FGL J1813-1737e in the energy range from 1 GeV to 1 TeV, with a correlation radius of 0.1°. Left: The position of the Galactic plane is indicated by the dashed line, the pulsar position is indicated by a blue marker, and $3\,\sigma$ and $5\,\sigma$ contours are depicted. Right: Significance map of the region after subtracting the emission using an elongated Gaussian model and a symmetric Gaussian model. The $1\,\sigma$ Gaussian extent of the models is depicted by the black dashed lines.

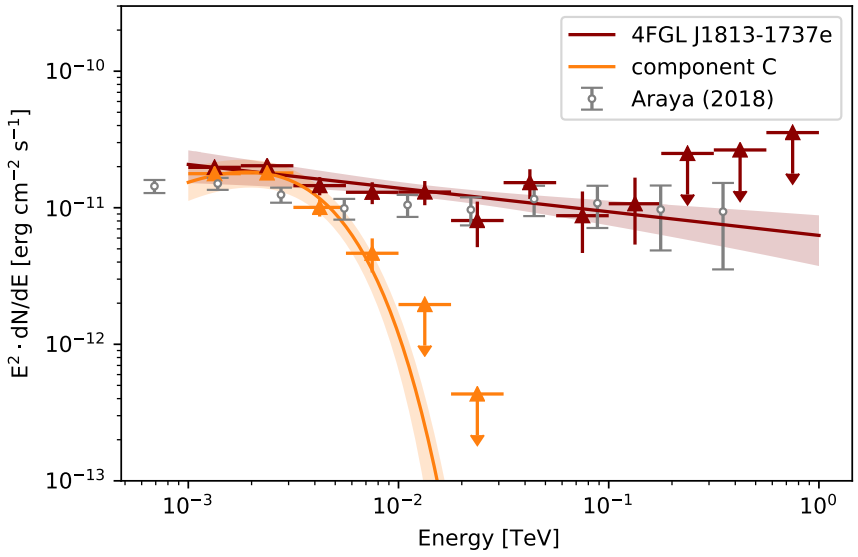

Figure 5.4: SED of the two-component description derived from the analysis of the data obtained by the *Fermi*-LAT, and SED points derived in Araya (2018).

Table 5.2: Best-fit source parameters obtained for the *Fermi*-LAT data for a model consisting of an elongated Gaussian model with a power law and a symmetric Gaussian model with an exponential cutoff power law as a spectral model.

	component C	4FGL J1813−1737e
Γ	$0.95 \pm 0.22_{\mathrm{stat}}$	$2.17 \pm 0.09_{\mathrm{stat}}$
λ [TeV^{-1}]	$551.5 \pm 84.4_{\mathrm{stat}}$	-
N_0 at 2 GeV [10^{-12} cm^{-2} s^{-1} TeV^{-1}]	$8.4 \pm 2.5_{\mathrm{stat}} \pm 3.3_{\mathrm{sys}}$	$2.7 \pm 0.6_{\mathrm{stat}} \pm 0.2_{\mathrm{sys}}$
R.A. [°]	$273.452 \pm 0.004_{\mathrm{stat}}$	$273.33 \pm 0.05_{\mathrm{stat}}$
Dec. [°]	$-17.73 \pm 0.03_{\mathrm{stat}}$	$-17.57 \pm 0.05_{\mathrm{stat}}$
σ_M [°]	$0.21 \pm 0.03_{\mathrm{stat}}$	$0.56 \pm 0.07_{\mathrm{stat}}$
e	-	$0.78 \pm 0.07_{\mathrm{stat}}$
$\Delta\varphi$ [°]	-	$33 \pm 8_{\mathrm{stat}}$

respective energy bin shows a significance above $2\,\sigma$, an SED point is derived, otherwise, an upper limit is calculated. 4 logarithmically spaced energy bins are used per decade. The SED are given in Figure 5.4.

Slight differences to the SED points derived in Araya (2018) can be observed. These can be attributed to the changes in the spectra of the neighbouring sources due to a switch from the 3FGL to the 4FGL catalogue, the usage of newly computed IRFs from Pass 8 version 3, and four years of additional data used in this analysis. Because the shape of the SED does not suggest a possible connection to HESS J1813−178A, this compact component will be referred to as component C. The best-fit parameters for 4FGL J1813−1737e and component C are given in Table 5.2.

The cutoff of this model was estimated to be 1.81 GeV. Component C improved the likelihood of the model only with a significance of $3.8\,\sigma$. It does, however, improve both the amount of remaining emission, as well as the agreement between the spectrum and the SED points and was therefore not discarded. To detect this second component with certainty and probe the nature of its emission, events with energies below 1 GeV would need to be included, and an analysis conducted, which only includes events recorded during a time in which the pulsar's beam axis is misaligned with the line of sight of the telescope.

5.2 Estimation of Systematic uncertainties

The best-fit parameters derived from the model fit are largely influenced by the detector response, which is described by the IRFs of the respective observations, and the accuracy of the background estimation. To get an estimate of the influence of uncertainties in the IRFs on the source parameters, the IRFs were varied within their uncertainties reported in Aharonian et al. (2006a), and the analysis was repeated. Due to the different detector response and reconstruction, this estimation was done differently for both detectors.

H.E.S.S. Data

The IRFs for the H.E.S.S. data reconstruction were obtained by interpolating between IRFs generated from Monte Carlo simulations covering a grid of observational conditions (Bernlöhr, 2008b). This method cannot describe all variations of observational conditions in detail, which leads to systematic uncertainties affecting the likelihood minimisation. In this analysis, three possible sources of uncertainties were considered.

Firstly, a discrepancy between the true and reconstructed pointing positions will lead to uncertainties in source position estimation. As indicated in Acero et al. (2010), the uncertainty of the pointing is $20''$, estimated using the position of known γ-ray sources and stars.

Secondly, the reconstruction of the energy of a γ-ray strongly depends on the optical efficiency of the telescopes, influenced by effects such as degradation of the PMTs or mirrors over time. Additionally, the transparency of the atmosphere, affected by effects such as the presence of aerosols, strongly influences the accuracy of the energy reconstruction. A discrepancy in energy reconstruction particularly influences the estimated spectral parameters of the source.

Thirdly, an important aspect of the data analysis is the correct statistical description of the inferred background event rate as a function of energy. The background model used in this analysis was constructed using archival observation runs. The mean observation conditions, which are reflected in the template, are not necessarily comparable to the observation conditions under which the data used in this analysis is acquired. The statistical and systematic uncertainties in the inferred background model will lead to uncertainty in the prediction of background counts and affect all fit parameters.

The energy threshold of the data has been set by estimating the energy bias of the stacked dataset and excluding data in energy bins for which the energy bias is greater than 10%. This threshold is generally assumed as a safe choice within the H.E.S.S. Collaboration (Unbehaun et al., 2025) and is now assumed as the maximum uncertainty on the energy reconstruction. To assess the systematic error on the source flux, which results from this uncertainty, a large number of pseudo-datasets with a shift of the energy scale ϱ_E is produced. This shift is randomly drawn from a Gaussian distribution with a mean of 1 and a standard deviation of 10%.

Another large systematic uncertainty on the source parameters is the estimation of the background rate. The influence on the source parameters is estimated by introducing a linear gradient with a direction angle α_{bkg} and a gradient amplitude Φ_{bkg} and applying the gradient to the background model. In addition to the gradient parameters, the starting value of the amplitude Φ and index δ of the model is varied by randomly drawing a value from Gaussian distributions. The standard deviation of these distributions was chosen such that they represent the maximum deviation between the fit parameters derived from the fit of the background model template to each observation and the mean value for the fit parameters for the whole dataset. The mean and deviation of these distributions are indicated in table 5.3.

Then, the shift, corresponding to the randomly drawn factor, was applied to the IRFs of the dataset, and the background gradient was introduced. The best-fit model was applied to the dataset, and a likelihood minimisation for these pseudo-datasets was performed. This process was repeated 500 times.

Table 5.3: Parameter distribution used for the computation of the systematic errors.

parameter	distribution	variation
ϱ_E	Gaussian	$\mu = 1, \sigma = 0.1$
Φ	Gaussian	$\mu = 1, \sigma = 0.05$
δ	Gaussian	$\mu = 0, \sigma = 0.05$
α_{bkg}	uniform	$0° - 360°$
Φ_{bkg}	Gaussian	$\mu = 1, \sigma = 0.01$

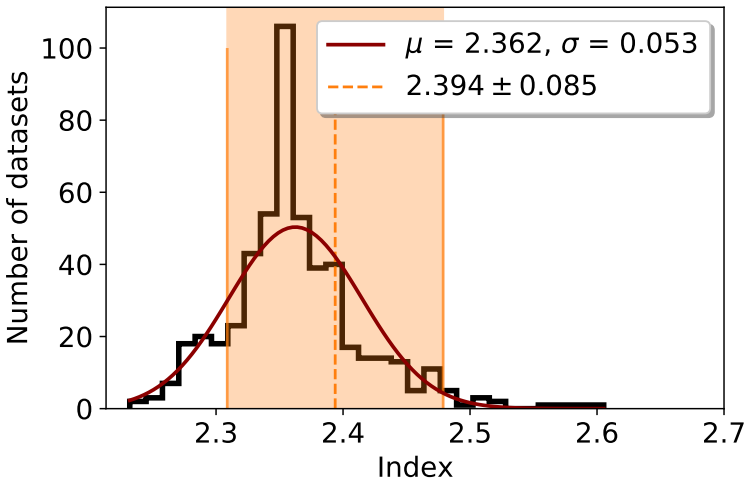

Figure 5.5: Distribution of the best-fit values of the spectral index for HESS J1813−178B. A Gaussian fit to the data is indicated in red. The orange dashed line corresponds to the fit value derived in the analysis of the original dataset, the orange band indicates the statistical error.

An example of the resulting distribution for the spectral index of HESS J1813−178B can be seen in Figure 5.5. The statistical error derived from the fit of the model to the real dataset is indicated by the orange band and the orange dashed line represents the best-fit value derived in the analysis of the original dataset. The standard deviation from a fit of a Gaussian model to this parameter distribution represents the systematic error derived by this method.

In addition to the systematic error derived through this method, the pointing uncertainty of $20''$ is added in quadrature for the position of both sources. The systematic errors estimated through this method are presented in Table 5.1.

Fermi-LAT

The most important systematic uncertainty on the system response of the *Fermi*-LAT is the uncertainty on the effective area. In the energy range of this analysis, the uncertainty is of the order of 3% (LAT Collaboration, 2019). In order to propagate this uncertainty to the derived source flux, a dataset has been created where the effective area has been scaled up and down by 3%. The analysis has then been repeated using these datasets.

The errors estimated from this method are 4.2 % for 4FGL J1813−1737e and 66.3 % for component C.
In order to estimate the error introduced by the background estimation, the residual flux inside a region corresponding to the source region, at an empty position in the ROI, has been calculated. The systematic uncertainty on the number of measured counts can then be derived by dividing the total amount of residual counts by the total amount of background in the shifted region and then multiplying by the total amount of background counts in the original source region. The number of counts per bin is then scaled up and down for the whole ROI, and the likelihood minimisation is repeated. This process was repeated for ten different regions. The estimation yields a systematic uncertainty of 2.1 % for 4FGL J1813−1737e and 13.3 % for component C. Both errors were added in quadrature to derive the total systematic uncertainty on the source parameters and can be found in Table 5.2.

5.3 Energy-dependent Morphology

The spatial association of the γ-ray emission with PSR J1813−1749 and an X-ray PWN detected by the INTEGRAL satellite, XMM-Newton, and Chandra (Ubertini et al., 2005; Funk et al., 2007; Helfand et al., 2007), suggests that a leptonic origin of the emission is plausible. Previous analyses of evolved PWNe suggest an energy-dependent morphology caused by electron diffusion and cooling (H.E.S.S. Collaboration, 2019; MAGIC Collaboration, 2020; Principe et al., 2020). To test for energy dependence of the extended emission, the data observed with H.E.S.S. was divided into three energy ranges (H1 - H3, specified in table 5.4), and the source models for HESS J1813−178A and HESS J1813−178B were fitted in each range. The *Fermi*-LAT data was divided into six energy ranges (F1 - F6, also specified in table 5.4), and the source model for 4FGL J1813−1737e was refitted in each range. The spacing of these energy ranges was chosen to account for the small amount of statistics in the H.E.S.S. data and the high-energy range in the *Fermi*-LAT data and ensure that the fitted source model is still significant. While F1 - F6 each span 3 energy bins, F6 spans 11 energy bins. The H.E.S.S. data was divided such that H1 and H2 contain five energy bins of the dataset, while H3 spans 10 energy bins.

Table 5.4 shows the extension along the semi-major axis, as well as the eccentricity of the ellipse describing the emission in each energy bin and the distance of the centre of the spatial model to the pulsar. In Figure 5.6, the dependence of the $1\,\sigma$ containment area of the ellipse and the offset to the centre of the fitted model from the pulsar position as a function of the energy is depicted. The area of the ellipse is defined as $A = \pi\sigma_M^2\sqrt{(1-e^2)}$.

The extension of the emission is compatible within errors in the overlapping energy ranges of the *Fermi*-LAT and H.E.S.S. data. There is no significant indication for energy-dependence of the best-fit containment area of the emission. This study does, however, reveal that the distance between the pulsar and the centre of the emission increases with increasing energy. The increased offset of the best-fit position towards higher energies, visualised in Figure 5.6, may indicate that the particle transport occurs preferentially towards a single direction before spreading out more isotropically as the particles lose energy and cool. Alternatively, this could indicate that a second faint source is present in the region.

Table 5.4: Best-fit parameters for the morphology of HESS J1813−178B in different energy bands, for both *Fermi*-LAT (F1 - F6) and H.E.S.S. datasets (H1 large - H3 large). An elongated Gaussian model was assumed in all cases, and the $1\,\sigma$ statistical uncertainties are given. Additionally, the best-fit values for the symmetrical Gaussian were used to account for the emission from HESS J1813−178A (H1 small - H3 small).

	Energy [GeV]	RA [°]	Dec [°]	σ_M [°]	e
F1	$1.0\ -\ 2.0$	273.46 ± 0.02	-17.67 ± 0.02	0.39 ± 0.04	0.81 ± 0.05
F2	$2.0\ -\ 4.0$	273.48 ± 0.03	-17.69 ± 0.03	0.42 ± 0.04	0.85 ± 0.04
F3	$4.0\ -\ 7.5$	273.38 ± 0.04	-17.66 ± 0.06	0.39 ± 0.08	0.87 ± 0.07
F4	$7.5\ -\ 18$	273.26 ± 0.09	-17.52 ± 0.12	0.53 ± 0.11	0.75 ± 0.19
F5	$18\ -\ 58$	273.17 ± 0.10	-17.77 ± 0.08	0.57 ± 0.16	0.77 ± 0.21
F6	$58\ -\ 1.0 \times 10^3$	273.22 ± 0.20	-17.75 ± 0.13	0.71 ± 0.19	0.92 ± 0.08
H1 small	$(0.4\ -\ 1.3) \times 10^3$	273.393 ± 0.005	-17.832 ± 0.005	0.054 ± 0.004	$--$
H2 small	$(1.3\ -\ 5.7) \times 10^3$	273.397 ± 0.006	-17.834 ± 0.007	0.064 ± 0.005	$--$
H3 small	$(5.7\ -\ 100) \times 10^3$	273.408 ± 0.009	-17.817 ± 0.009	0.035 ± 0.006	$--$
H1 large	$(0.4\ -\ 1.3) \times 10^3$	273.61 ± 0.08	-17.48 ± 0.09	0.87 ± 0.12	0.88 ± 0.04
H2 large	$(1.3\ -\ 5.7) \times 10^3$	273.41 ± 0.09	-17.42 ± 0.11	0.48 ± 0.09	0.48 ± 0.38
H3 large	$(5.7\ -\ 100) \times 10^3$	273.65 ± 0.11	-17.18 ± 0.10	0.41 ± 0.09	0.00 ± 0.02

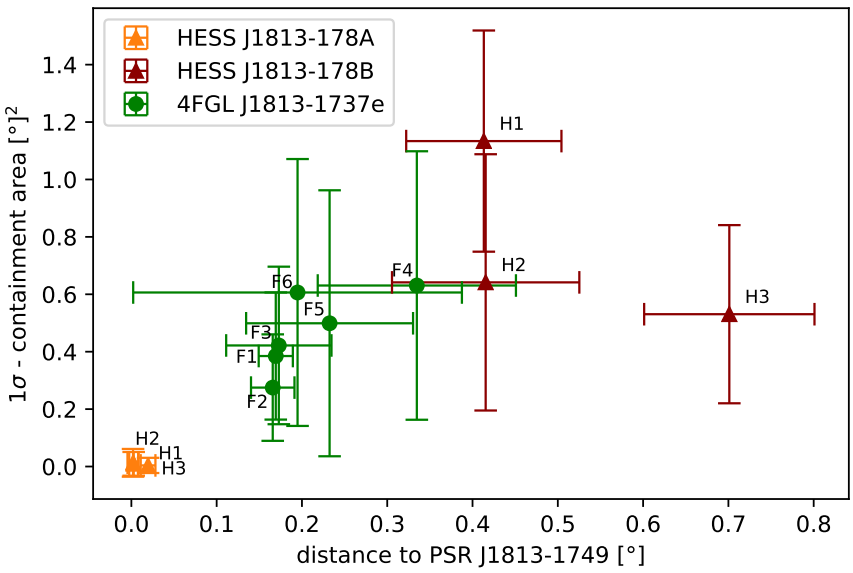

Figure 5.6: Best-fit angular offset and area of the ellipse of HESS J1813−178A and HESS J1813−178B with $1\,\sigma$ uncertainties, as well as 4FGL J1813−1737e data in independent energy bins (see Table 5.4) H1 - H3 and F1 - F6.

5.4 Joint model fit

A consistent description of the ROI through the GeV-TeV range can be reached with a joint likelihood minimization of the *Fermi*-LAT and H.E.S.S. data. Following the results derived in the analysis of the respective datasets, three source models were used to describe the data across the five decades of energy. First, a symmetric Gaussian model, as well as an elongated Gaussian model was added to both datasets. A logarithmic parabola model was used for the spectral description:

$$\frac{\mathrm{dN}}{\mathrm{dE}} = \mathrm{N}_0 \cdot \left(\frac{\mathrm{E}}{\mathrm{E}_0}\right)^{-\Gamma-\beta\log\left(\frac{\mathrm{E}}{\mathrm{E}_0}\right)} , \tag{62}$$

where β is the curvature, as well as a power law with a generalised exponential cutoff. Based on the results derived from the analysis of the H.E.S.S. data, these models will be referred to as components A and B, respectively. Additionally, a symmetric Gaussian model with an exponential cutoff power-law spectral model was added only to the *Fermi*-LAT data. The exponential cutoff power-law model is described by:

$$\frac{\mathrm{dN}}{\mathrm{dE}} = \mathrm{N}_0 \cdot \left(\frac{\mathrm{E}}{\mathrm{E}_0}\right)^{-\Gamma} \cdot \exp\left(-\lambda \mathrm{E}\right) , \tag{63}$$

with λ, the inverse of the cutoff energy. This model component corresponds to component C, which was found in the analysis of the *Fermi*-LAT data. The likelihood minimisation was then performed on both datasets at the same time.

Table 5.5: Best-fit parameters derived in the joint analysis of the H.E.S.S. and *Fermi*-LAT data.

	comp. A	comp. B	comp. C
Γ	2.05 ± 0.03	2.17 ± 0.03	-0.12 ± 0.02
β	0.0620 ± 0.003	0.0437 ± 0.008	-
α	-	-	0.66 ± 0.01
λ $[10^3 \cdot \mathrm{TeV}^{-1}]$	-	-	3.93 ± 0.20
N_0 at 1 TeV $[10^{-12}\,\mathrm{cm}^{-2}\,\mathrm{s}^{-1}\,\mathrm{TeV}^{-1}]$	3.16 ± 0.14	6.47 ± 0.43	9.89 ± 1.64
RA [°]	273.400 ± 0.003	273.39 ± 0.03	273.48 ± 0.02
Dec [°]	-17.832 ± 0.003	-17.50 ± 0.04	-17.67 ± 0.02
σ_M [°]	0.056 ± 0.003	0.54 ± 0.03	0.29 ± 0.02
e	-	0.73 ± 0.04	-
$\Delta\varphi$ [°]	-	33 ± 7	-

The best-fit parameters are shown in Table 5.5. Figure 5.7 depicts the spectra and SED of the best-fit models, together with the sensitivity of the *Fermi*-LAT for 12 years of exposure in blue. The curve shows the broadband sensitivity for sources located in the Galactic plane (Ajello et al., 2021).

While the best-fit parameters of the models were estimated using the data from both datasets at the same time, the flux points were computed in the respective datasets. This results in an energy range where both the H.E.S.S. and *Fermi*-LAT data show significant flux or upper limits. If the spectrum of component A does not change

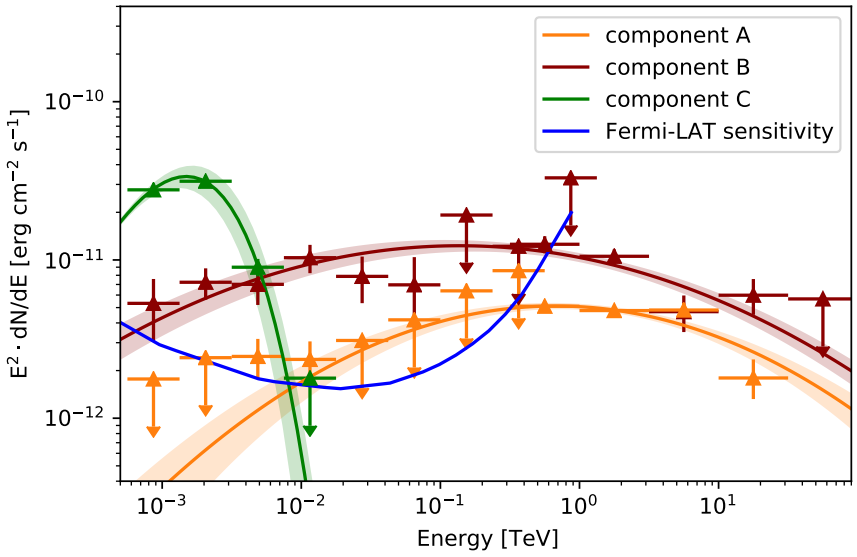

Figure 5.7: SED from a joint-analysis of the combined H.E.S.S. and *Fermi*-LAT data. The 12 year sensitivity of the *Fermi*-LAT is indicated by the blue line.

drastically at the lower energies, measuring it in the *Fermi*-LAT data would not be possible as components A and C are positionally coincident and the detector sensitivity is insufficient. Together, these three different source models describe the emission of the ROI well.

The advantage of this joint model becomes evident in the GeV energy regime. The spatial separation between 4FGL J1813−1737e and the compact emission component detected in the *Fermi*-LAT data is complicated, but using the assumption that 4FGL J1813−1737e and HESS J1813−178B have the same origin, the influence of the second component on the model parameters can be reduced. This becomes evident when comparing the flux from 4FGL J1813−1737e around 1 GeV, which has been reduced by a factor of two in the joint model with the emission being attributed to component C.

5.5 Spectral modelling of the emission

The above-presented analysis could resolve the previously observed discrepancy in the extension of the γ-ray emission observed by IACTs and *Fermi*-LAT. The question about the origin of the emission, however, still remains. In order to employ the results presented above to investigate whether the γ-ray emission results from the SNR G012.8–00., the young pulsar PSR J1813−1749, or even interactions of the star-forming region W33, the expected γ-ray spectrum for two emission scenarios was computed and fitted to the data.

In the first scenario, a magnetised wind of charged particles, primarily electrons and positrons, originating from PSR J1813−1749, forms a PWN. The diffuse γ-ray emission produced by these electrons is typically observed around middle-aged pulsars, and one can distinguish between a majority of the particles still confined in the PWN and one where most particles have escaped into the ISM (Giacinti et al., 2020).

This leptonic emission scenario has been favoured in previous analyses of the X-ray

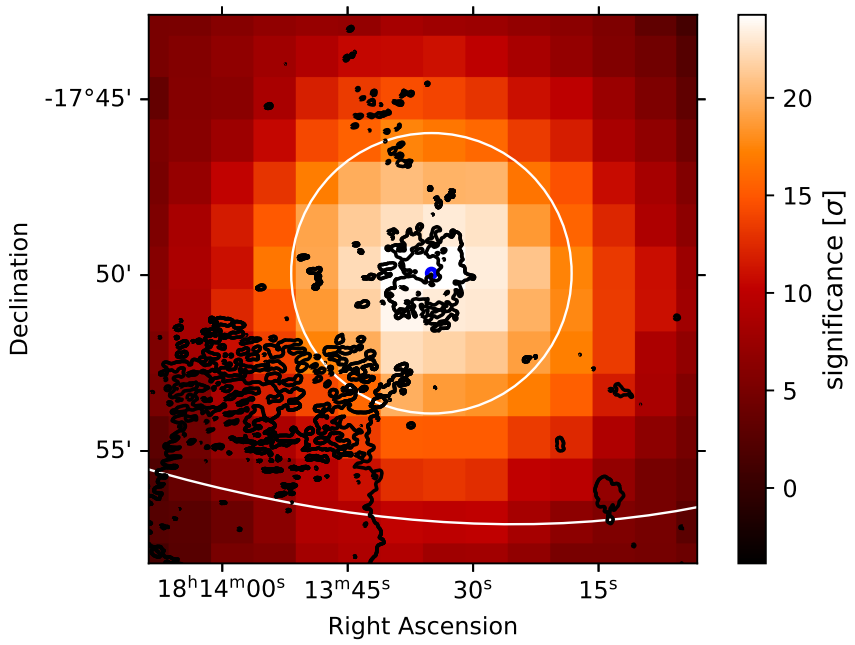

Figure 5.8: Zoom-in on a Li&Ma (1983) significance map with a correlation radius of 0.06° of the region around PSR J1813−1749 as seen with H.E.S.S.. The best-fit morphology of HESS J1813−178A and HESS J1813−178B are indicated by the white lines, the black contours depict SNR G012.8–00.0 and CL J1813−178 as observed by VLA. The position of PSR J1813−1749 is indicated in blue.

and TeV emission (Ubertini et al., 2005; Funk et al., 2007). In systems older than 10 kyr, the electrons can escape the confines of the PWNe and diffuse through the ISM, which would result in large extended γ-ray emission, with a more confined X-ray counterpart. For the system around PSR J1813−1749 to be in this state would, however, be rather unusual, since the characteristic age of the pulsar is only 5600 years. It should, however, be noted that the system does not evolve in a typical environment since it is located in the vicinity of the active star-forming region W33, and the pulsar itself is highly energetic.

The positioning and distance between the different objects in the region can be seen in Figure 5.8. The Figure shows a Li&Ma (1983) significance map of the H.E.S.S. data, overlayed with contours derived from VLA data. The Figure is centred on the SNR G12.82 − 0.02, which is positionally coincident with the pulsar PSR J1813−1749 and believed to be the pulsar's host SNR (see Figure 5.8). The best-fit position and extension of HESS J1813−178A are shown in white. Towards the bottom left, the stellar cluster Cl J1813-178, which is part of the star-forming region W33, becomes visible.

Another possible origin of the extended emission are cosmic ray nuclei which are accelerated at shock fronts and since then have escaped from their accelerator. A possible candidate for such an acceleration site is SNR G12.82 − 0.02. After acceleration and propagation, the cosmic ray nuclei may interact within dense molecular clouds in the region, producing high-energy γ rays. This emission scenario has been favoured in an analysis of nine years of *Fermi*-LAT data, performed by Araya (2018), who suggested

Table 5.6: The assumed properties of PSR J1813−1749 following newest estimates from Camilo et al. (2021). For the braking index and break energy canonical values are assumed.

Parameter	Value
Distance, d	6.2 kpc
spin-down power, $\dot{E}$	5.6×10^{37} erg/s
spin period, P	$44.7 \cdot 10^{-3}$ s
change in spin period, $\dot{P}$	1.27×10^{-13} s/s
characteristic age τ_c	5.585 kyr
Braking index, n	3.0
Break energy, E_b	100 GeV

the stellar cluster Cl J1813-178 as a possible origin. This scenario is, however, also not able to fully explain the extent of the observed γ-ray emission, since it exceeds the extension of the star-forming region, and therefore an unknown component of star formation would be necessary.

Leptonic scenario

To describe the γ-ray emission in the region using a time-dependent model of electrons originating from PSR J1813−1749, the GAMERA package (Hahn, 2015) was used. Additionally to the SED derived in the joint analysis, measurements of the region in the $20 - 100$ keV band, showing an unresolved hard X-ray source observed by the INTEGRAL satellite (Ubertini et al., 2005), XMM-Newton (Funk et al., 2007) (with an extraction region of $75''$), and Chandra (Helfand et al., 2007, with an elliptical extraction region of $6'' \times 8''$) were used.

The SED used for this model was not derived using the same spatial extent. While one possible solution for this discrepancy would be to scale the observed flux for the different observation regions, this would require the assumption that a linear scaling can be applied. Additionally, X-ray emission generally traces higher energy electrons, and hence younger electrons, than the TeV emission.

To account for these differences, three electron 'generations' were defined, following a procedure outlined also in H.E.S.S. Collaboration (2023). The first electron generation, the relic electrons, have been injected since the birth of the pulsar and are now detected as extended high-energy γ-ray emission. The second electron generation, the middle-aged electrons, were injected since $t_e = t_\mathrm{true} \cdot t_\mathrm{PWN}$, with t_true the age of the system, and are now detected as PWN around PSR J1813−1749. The third electron generation, the young electrons injected since $t_e = t_\mathrm{true} \cdot t_\mathrm{X\text{-}ray}$ are responsible for the X-ray synchrotron emission in the vicinity of the pulsar.

For this model, an electron injection spectrum following a power law with a spectral index of α, a break energy of E_b and a cutoff E_cut:

$$N(E_\mathrm{e}) = \left(1 + \frac{E_e}{E_b}\right)^{\alpha} \cdot \exp\left(\frac{-E_\mathrm{e}}{E_\mathrm{cut}}\right) , \tag{64}$$

where E_e the electron energy, was used.

The distance to the pulsar, as well as pulsar-specific parameters, such as spin-down period P, change in spin period $\dot{\mathrm{P}}$, and spin-down power $\dot{\mathrm{E}}$ were taken from Camilo et al. (2021). All assumed properties of the pulsar used for this model are given in Table 5.6.

The injection index α, the birth period P_0, and the conversion fraction of the spin-down luminosity to electrons ϑ, as well as the magnetic field present at the time of the observation of the γ-ray emission $\mathrm{B}_{\mathrm{now}}$, and the age of the electron populations were free parameters of the model. The spin-down power of the pulsar was assumed to evolve in time with:

$$\dot{\mathrm{E}} = \dot{\mathrm{E}}_0 \left(1 + \frac{t}{\tau_0}\right)^{-2}, \tag{65}$$

with $\tau_0 = \mathrm{P}_0/(2\,\dot{\mathrm{P}}_0)$, the spin-down time at the birth of the pulsar and $\dot{\mathrm{E}}_0$ the initial spin-down energy loss rate at birth of the pulsar. Similarly the pulsar period was assumed to evolve as $\mathrm{P(t)} = \mathrm{P}_0 \left(1 + \frac{t}{\tau_0}\right)^{0.5}$, with P_0 the birth period of the pulsar and the magnetic field as $\mathrm{B(t)} = \mathrm{B}_0 \left(1 + \left(\frac{t}{\tau_0}\right)^{0.5}\right)^{-1}$ (Gaensler and Slane, 2006; Venter and de Jager, 2007) with B_0 the magnetic field at birth of the pulsar. The spin-down luminosity is defined as:

$$\mathrm{L} = \mathrm{L}_0 \cdot \vartheta \cdot \left(1 + \frac{t}{t_0}\right)^{-2}, \tag{66}$$

with the initial spin down luminosity $L_0 = \dot{\mathrm{E}} \cdot (1 + (t_{\mathrm{true}}/t_0))^2$ and $t_0 = P_0^2/(2P\dot{P})$.

Since the time at which the escape of the particles from the PWN first occurs is unknown, this modelling approach assumes that the particles have been able to escape instantly and therefore, the relic electrons have been injected since the birth of the pulsar. An additional caveat of this model is that while this model is time-dependent and cooling losses of electrons were taken into account, no spatial dependence or spatial evolution was added. The fit of the different electron generations was performed only on the SED.

The free parameters of the model were fitted to the observation data from the X-ray satellites, as well as the SEDs derived in the joint-analysis from components A and B. For optimisation, the package *EMCEE* (Foreman-Mackey et al., 2013), which applies a Markov chain Monte Carlo (MCMC) method, was used.

The optimised model is shown in Figure 5.9, while the parameter space that yields the highest numerical probability ($16 - 84\%$ range of the probability distribution) for the MCMC method is listed in Table 5.7. The corner plot showing the posterior distributions and parameter correlations for the MCMC modeling of the leptonic particle population is shown in the Appendix in Figure B.2. The diagonal panels display the one-dimensional distributions for each parameter, while the off-diagonal panels illustrate the two-dimensional correlations between the respective parameter pairs.

This morphology-independent model can account well for the observed emission. In addition to the SED points from X-ray and γ-ray observations, data from the Very Large Array in the 20 cm and 90 cm band is shown (Brogan et al., 2005). This data on SNR G12.82–0.02 is only shown for comparison and was not included in the modelling.

The observed X-ray data in the vicinity of PSR J1813−1749 can be well explained by

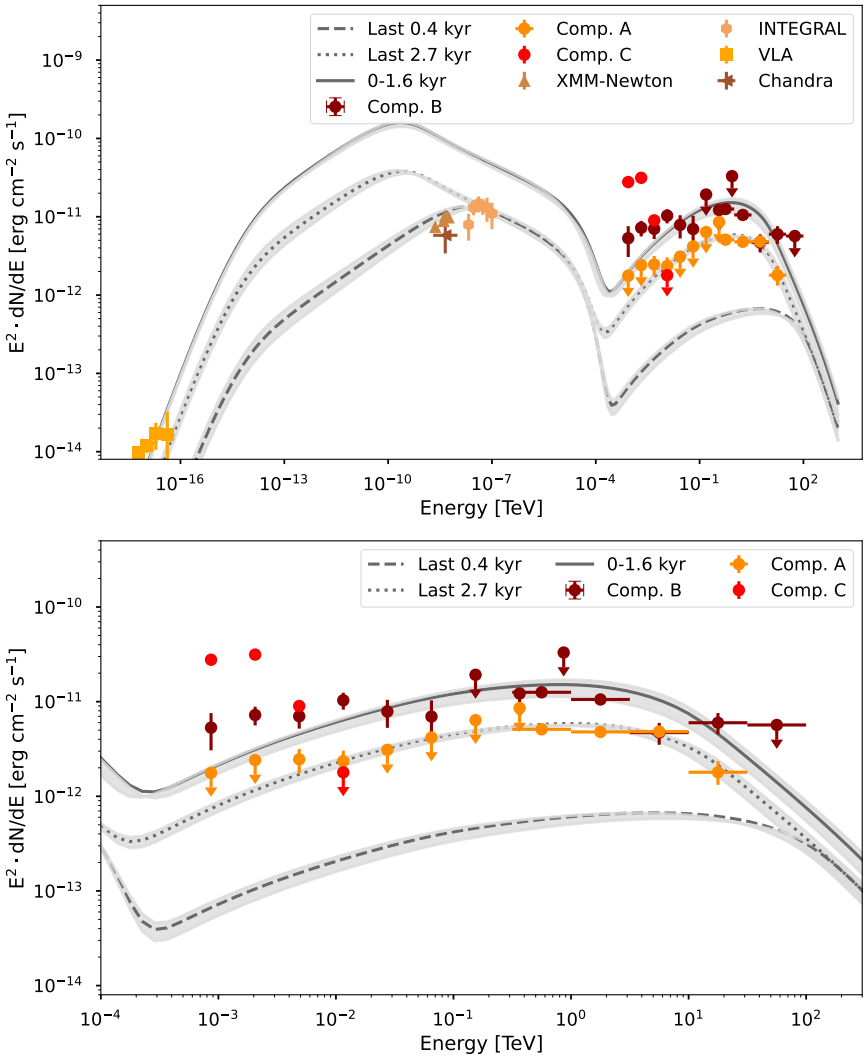

Figure 5.9: SED derived in this analysis, as well as X-ray SED by XMM-Newton (Funk et al., 2007), Chandra (Helfand et al., 2007), and INTEGRAL (Ubertini et al., 2005), and the SED derived in the analysis of VLA data (Brogan et al., 2005), compared to the SED curves expected from the leptonic model obtained with GAMERA. Top: Full energy range. Bottom: Comparison between the γ ray flux estimated from the leptonic model from $0 - 1.6$ kyrs and the last 2.5 kyrs and the emission observed from HESS J1813−178B and HESS J1813−178A, respectively. The shaded grey error bands indicate the possible parameter space, given in Table 5.7.

Table 5.7: Validity range of the parameters used in the evolution of the leptonic model. The parameter combination presented here should be interpreted as a range of possible combinations, not best-fit values.

Parameter	Validity range
B_{now}	$[11.36 - 13.18]\,\mu$G
P_0	$[20.19 - 22.97\,]$ ms
ϑ	$[0.15 - 0.17]$
α	$[2.35 - 2.40]$
$\Delta t_{\mathrm{X\text{-}ray}}$	$[0.88 - 0.91]$
Δt_{PWN}	$[0.35 - 0.39]$

young electrons that were produced only in the last 0.4 kyr, the electrons of the third generation. The electrons produced in the last 2.7 kyr, the second generation, were observed by H.E.S.S. as compact emissions around the pulsar. Taking into account the low statistics at high energies, the population of relic electrons from the first generation, released from the birth of the pulsar up to an age of 1.6 kyrs, can describe the extended emission from HESS J1813−178B reasonably well but fails to describe the emission from component C. To describe this emission in a leptonic scenario, a second electron population and an unreasonably high photon density, only experienced by the second electron generation, would need to be introduced.

Using the parameters of the model, the true age of the system was estimated, following Gaensler and Slane (2006):

$$t_{\mathrm{true}} = \frac{\mathrm{P}}{(n-1)\dot{\mathrm{P}}}\left(1 - \left(\frac{\mathrm{P}_0}{\mathrm{P}}\right)^{n-1}\right), \tag{67}$$

with n the braking index of the pulsar. For the validity range of parameters in this analysis, the true age of the system was estimated to be ~ 4.7 kyrs.

With this information, together with an estimation of the extension of 4FGL J1813−1737e and HESS J1813−178B in different energy bands, an estimation of the diffusion coefficient and diffusion index can be made by comparing the observed angular size to that expected for the relic electron population at different γ-ray energies. In order to estimate a diffusion coefficient, radial symmetric diffusion was assumed. To get an estimation of the radial symmetric extent of the emission from HESS J1813−178B, a symmetric Gaussian model was fitted to the emission in the energy bands defined in Table 5.4. This derived extension, as well as the age of the system, derived using Equation (67), were then used to estimate the distance which the relic electrons have diffused since they were injected, with the expected angular size calculated as $r_{\mathrm{diff}} = \sqrt{2t_{\mathrm{age}} \cdot D}$, with D the diffusion coefficient. The diffusion coefficient was derived using the electron energy E_e, the diffusion index δ and the diffusion coefficient D_0 at the reference energy of 1 TeV:

$$\mathrm{D} = \mathrm{D}_0 \left(\frac{\mathrm{E}_e}{1\,\mathrm{GeV}}\right)^{\delta}. \tag{68}$$

Using this method, the diffusion coefficient is estimated to be $\mathrm{D}_0 = (6.98 \pm 0.69) \times 10^{28}\,\mathrm{cm}^2/\mathrm{s}$ with a diffusion index $\delta = (0.30 \pm 0.06)$. The estimated radius as a function

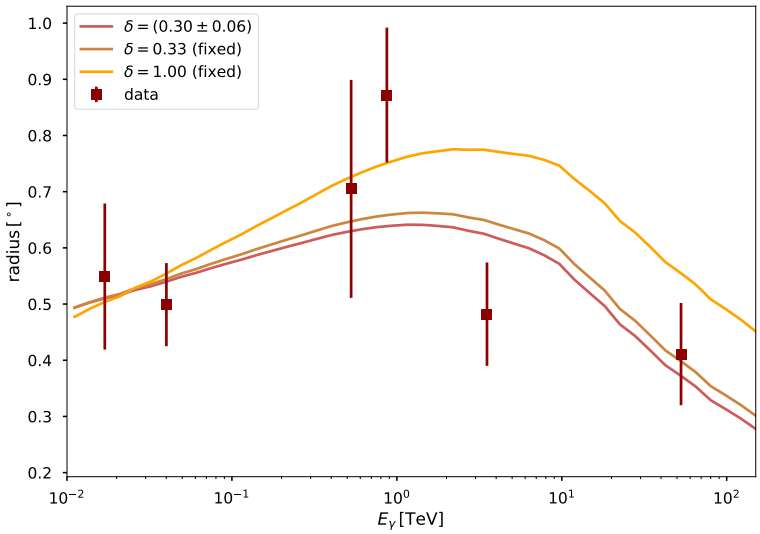

Figure 5.10: The measured extension of HESS J1813−178B in continuous energy bands is shown in red. The figure also shows the expected $1\,\sigma$ containment radius for different diffusion coefficients.

of γ-ray energy, as well as the measurement, can be seen in Figure 5.10. The estimated diffusion index is comparable with Kolmogorov turbulence ($\delta = 0.33$, (Kolmogorov, 1991)), which is the canonical diffusion index typically assumed for PWNe. The best-fit diffusion coefficient is comparable with the diffusion coefficient estimated for the ISM (Strong and Moskalenko, 1998).

To compare the results to the population of known pulsars, the energy density of both HESS J1813−178A and HESS J1813−178B in the TeV energy range was estimated, following the scheme in Giacinti et al. (2020). The energy density of the electrons was estimated using $\epsilon_e = \frac{\mathrm{E_{inj}}}{\mathrm{V}}$, or using the properties of the pulsar:

$$\epsilon_e \quad = \quad \frac{\dot{\mathrm{E}}\tau_c}{\mathrm{V}} \ , \tag{69}$$

with $\dot{E}$ the present-day spin-down power and τ_c the present-day characteristic age. Since the emission is best described by an elongated gaussian model, the Volume is calculated as $V = 4\pi(\mathrm{R}_1^2 \cdot \mathrm{R}_2)/3$, with R_1 the semi-major axis of the ellipse and R_2 the semi-minor axis.

The energy density using the total TeV γ-ray luminosity was estimated by integrating over the electron population inferred by the best-fit model. This study finds a total injection energy of E_{inj} =$3.62{\cdot}10^{48}$ erg. The derived electron densities are given in Table 5.8. The energy density calculated from the γ-ray luminosity is lower than that estimated from the properties of the pulsar. This effect was already observed by Giacinti et al. (2020), a possible reason could be that only the estimation using the γ-ray luminosity takes the evolution into account, while the estimation using the current pulsar properties cannot sufficiently describe this evolution. The energy density calculated for HESS J1813−178A is compatible with the energy densities estimated for other PWNe, while the energy density of HESS J1813−178B is close to $0.1\,\mathrm{eV/cm^3}$ and,

Table 5.8: Estimated electron density following Equation ((69)).

ϵ_e [eV/cm^3]	HESS J1813−178A	HESS J1813−178B
estimated from $\dot{\mathrm{E}}$	65.29 ± 4.49	0.11 ± 0.02
estimated from L_γ	23.95 ± 1.64	0.04 ± 0.01

therefore comparable to the values estimated for pulsar halos (Giacinti et al., 2020).

Hadronic origin

Due to the positional coincidence of the emission and the SNRs G012.8–00.0 and G012.7–00.0 or the star-forming region W33, there is also the possibility that the observed emission is a superposition of γ-ray emission produced by different sources that overlap along the line of sight. While there is no information available for SNR G012.7-00.0, the distance to PSR J1813−1749 and SNR G012.8–00.0 is estimated to be $6.2 - 12\,\mathrm{kpc}$ (Camilo et al., 2021), while the stellar cluster is expected to be located at a much smaller distance of 4.8 kpc (Messineo et al., 2011). It is therefore possible that the emission observed as HESS J1813−178A is a PWN powered by PSR J1813−1749, while the extended emission observed in the *Fermi*-LAT and H.E.S.S. data is caused by protons accelerated at the SNR shock front or the stellar cluster and only spatially overlaps with the PWN along the line of sight.

In order to produce high energy γ rays via hadronic interactions, target material is necessary. Using the molecular cloud catalogues provided in Rice et al. (2016) and Miville-Deschênes et al. (2017), three molecular clouds, positionally coincident with the best-fit position of the emission from HESS J1813−178B were identified. Their location compared to the emission observed in the analysis of the *Fermi*-LAT data can be seen in Figure 5.11. In order to investigate the feasibility of this scenario as the origin of the emission observed from 4FGL J1813−1737e and HESS J1813−178, a proton and electron population, accelerated at the shock front of the SNR, were evolved over time. Following Diesing and Caprioli (2019), the protons were injected with:

$$f(p) \quad = \quad N_p \cdot E^{-\alpha_p} \cdot \exp\left(\frac{-E}{E_{\mathrm{max}}}\right) \cdot \exp\left(-\frac{E_{\mathrm{min}}}{E}\right), \tag{70}$$

where N_p is the normalisation factor, E is the energy of the injected particles, $E_{\mathrm{min}} = m_p$, the rest mass of the proton, E_{max} is assumed to be 1 PeV, and α_p is the spectral index of the injected protons. The injection spectrum of the electrons was defined as:

$$f_e(p) \quad = \quad N_p \cdot k_{ep} \cdot E^{-(\alpha_p+\Delta\alpha)} \cdot \exp\left(\frac{E}{E_{\mathrm{max}}}\right) \cdot \exp\left(-\frac{E_{\mathrm{min}}}{E}\right), \tag{71}$$

with $\Delta\alpha$ the difference between the injection index of the electrons and protons, k_{ep} the electron-to-proton ratio, and $E_{\mathrm{min}} = 100 m_e$, with the electron rest mass, as well as $E_{\mathrm{max}} = 1\,\mathrm{TeV}$. This particle population is evolved in an environment with the ambient magnetic field B_{now} and a particle density d, for simplicity, neglecting any time dependence in the magnetic field. We assume a particle density of $d = 60\,\mathrm{cm}^{-3}$, which corresponds to the density of one of the molecular clouds in the region (see figure 5.11).

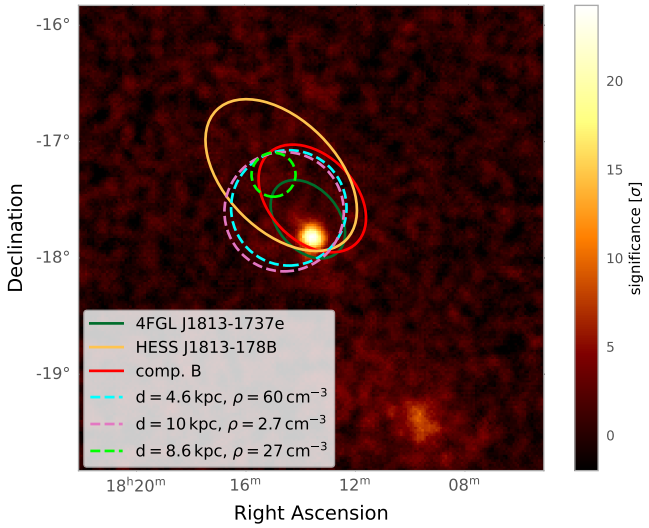

Figure 5.11: Li&Ma (1983) significance map computed from the H.E.S.S data with a correlation radius of 0.06°. The estimated position and density of molecular clouds in the region are indicated by the dashed lines. Additionally, the morphologies of the best-fit models derived from the analyses of the respective datasets and the joint-fit are indicated. Only clouds with a distance between 4 kpc and 12 kpc and a large positional overlap with the extended emission observed in *Fermi*-LAT and H.E.S.S. are depicted in the counts map.

This particle population was evolved with time following the approach in Section 5.5, using an MCMC-Chain. The fit parameters of the model, as well as the adjusted parameter range, can be seen in table 5.9. The corner plot visulising the posterior distributions of the model parameters can be seen in the Appendix in Figure B.3. A comparison of the leptonic model derived in Section 5.5 and the hadronic model can be seen in Figure 5.12, while Figure B.4 shows the comparison of both models with the SED derived in this analysis, as well as the spectra derived from the emission observed in HAWC (Albert et al., 2020) and LHAASO (Cao et al., 2023a).

Both models exhibit good agreement with the SED points from component B derived from the joint-model, while only the leptonic model shows good agreement with the spectrum of 1LHAASO J1814−1719u* measured by KM2A. The spectrum of 3HWC J1813−174 does not show good agreement with either model.

In addition to the discrepancy with the spectra derived by HAWC and LHAASO, the hadronic model has further caveats. The estimated distance between the molecular cloud at 4.6 kpc and the SNR at $6.2 - 12$ kpc are not compatible, and the location of the molecular cloud can account for the emission observed in the GeV energy range but not the extension of the TeV emission. Assuming a particle density of $d = 1\,\mathrm{cm}^{-3}$, corresponding to ISM level, however, results in the need for a very powerful SNR with the energy of the protons required to be $\log_{10}(E_p/\mathrm{erg}) = [51.2 - 51.7]$, to describe the emission well. Since there is no evidence supporting this scenario, an origin of the observed emission only from acceleration of cosmic rays on the SNR seems unlikely.

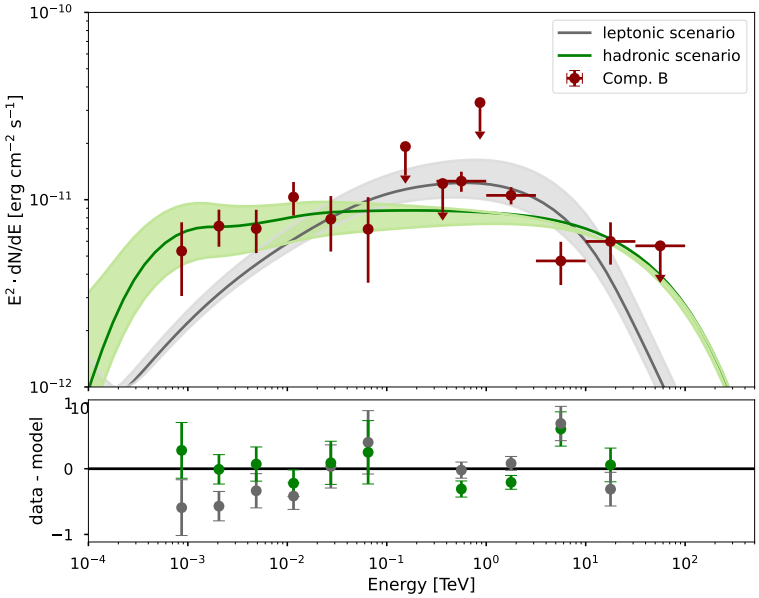

Figure 5.12: Estimated γ-ray flux for the hadronic model compared to the γ-ray flux expected for the leptonic model computed in Section 5.5. The deviation of the SED points to the respective model curves are shown in the bottom panel.

While such a high energy output seems unlikely in the case of only one object, collective effects of a population of young stars in the stellar cluster CL J1813−178 (located at a distance of 4.8 kpc Messineo et al. (2011)) could account for the required energy. For example, for a kinetic luminosity of 3×10^{38} erg/s and an age of 3-10 Myr, as may be typical for a young, massive stellar cluster, the available total energy budget is $\log_{10}(E_p/\mathrm{erg}) = [52.5 - 53]$ (Morlino et al., 2021b). Acceleration of protons in the stellar cluster remains, therefore a valid possible origin for the observed extended γ-ray emission, a detailed examination is, however, beyond the scope of this work.

Table 5.9: The validity range of the free parameters of the hadronic model.

α_p	$[2.01 - 2.08]$
$\log_{10}(E_p)$	$[48.49 - 49.65]$ log (erg)
$\Delta\alpha$	$-[0.15 - 0.27]$
k_{ep}	$-[1.72 - 6.05]$
B_now	$[73 - 271]\,\mu G$

5.6 Discussion

In previous analyses of the region around PSR J1813−1749 the analysis of H.E.S.S. data revealed compact emission with an extension of 0.06° around the pulsar (Aharonian et al., 2006c), while the analysis of *Fermi*-LAT data, as well as data acquired by HAWC and LHAASO showed largely extended emission. With these results, no connection between the *Fermi*-LAT source 4FGL J1813−1737e and the H.E.S.S. source HESS J1813−178 could be established. In the master's thesis Wach (2022), the data

was analysed using an improved reconstruction for the TeV data and increased exposure in the GeV energy range.

This resulted in the detection HESS J1813−178A, a bright, TeV γ-ray source, centred at the position of the PSR J1813−1749, with an extension of 0.06°. The results derived for this emission component are consistent with the results derived in H.E.S.S. Collaboration (2018b). And also the detection of a fainter, previously undetected γ-ray structure, with an extension of 0.7° enclosing the pulsar and HESS J1813−178A, which was referred to as HESS J1813−178B.

In the GeV energy range observed with *Fermi*-LAT, this work finds γ-ray emission with an extension of 0.4°, positionally coincident with the extended emission observed in the H.E.S.S. dataset. Additionally, compact emission positionally coincident with the pulsar was observed. This emission has already been reported by Araya (2018) but was not significant. While this work also cannot claim a significant detection, adding component C improves the region's description by $3.8\,\sigma$.

By combining the datasets in a joint analysis this work finds that the extended emission detected in the H.E.S.S. and *Fermi*-LAT data can be connected and described by a single source model, while the emission from HESS J1813−178A can only be observed in the H.E.S.S. data, since the emission drops below the sensitivity of the detector in the *Fermi*-LAT energy range. This work can, therefore establish a consistent description of the region over five decades of energy and conclude that the emission observed by *Fermi*-LAT and H.E.S.S. have the same origin.

Araya (2018) concluded that the emission was most likely of hadronic origin due to the spectral shape. While Araya (2018) only took γ rays in the GeV energy range into account, in this work, a combined model of GeV and TeV photons was used, as well as X-ray data included. A physical model was computed that can describe the observed γ-ray emission by evolving an electron population, or alternatively a proton population, over time. This work finds that the leptonic emission scenario describes the combined data well, while acceleration at the SNR shock front seems less justified since the present target material cannot explain the observed extension of the TeV emission. The energetics necessary to produce the observed γ-ray emission could also be explained by the acceleration of protons inside the stellar cluster but has not been further investigated in this study.

This work finds that the data from HESS J1813−178A, as well as HESS J1813−178B, can be described well by γ-ray emission from synchrotron and IC emission of electrons originating from the pulsar. This indicates that HESS J1813−178A, is likely a PWN, while the extended emission is possibly caused by electrons and positrons escaping the confines of the PWN and diffusing into the ISM. The effect of constructing a model that considers only time dependence but not spatial dependence leads to an overprediction in the keV energy range.

Since the measurement of the flux observed by INTEGRAL and XMM-Newton only includes a small area (with an extension of less than 80"), while the measurement of the flux from HESS J1813−178B was conducted in an area of $\sim 0.5°$, we can assume that a low surface brightness, as well as the limitations of the detectors cause the difference between predicted flux and measured flux in the X-ray energy range.

Diffuse leptonic emission around a pulsar is usually only observed in systems older

than $\sim 10\,\mathrm{kyr}$ (Giacinti et al., 2020). The true age estimated in this study, as well as previous observations of PSR J1813−1749 (Dzib and Rodríguez, 2021), indicate that the system is younger than 5 kyrs, but it is not implausible that environmental factors, such as the local ISM density distribution or the pulsar proper motion, might lead to particles diffusing outwards faster than in previously observed systems.

The estimated diffusion coefficient for HESS J1813−178B is within the expected range of diffusion in the ISM (Strong and Moskalenko, 1998) and comparable to the diffusion coefficient estimated for the γ-ray emission observed around PSR B1823−13, the pulsar powering the highly extended PWN HESS J1825−137 (H.E.S.S. Collaboration, 2019). Assuming the same diffusion coefficient for HESS J1813−178A, would lead to an extension far bigger than the observed emission, implying that the diffusion coefficient is non-uniform, which is expected for a pulsar environment. Additionally, the energy density estimated for the extended emission is comparable to the densities estimated for the halos observed around the evolved systems around PSR J0633+1746 and PSR B0656+14 (Giacinti et al., 2020). While the diffusion coefficient in a TeV halo is expected to be below the diffusion observed in the ISM, the low energy density and lack of other accelerators in the area suggest that the system around PSR J1813−1749 shows characteristics of an older, evolved system despite its young age. Although it would be unusual to note electron escape from young PWNe, this may occur if the system becomes disrupted at an early stage, such as due to an early return of the supernova reverse shock preferentially from one direction. Such a disruption is, for example, thought to have occurred for HESS J1825−137 (H.E.S.S. Collaboration, 2019).

This study also investigates the possibility of a hadronic origin of the emission by evolving a proton population originating from SNR G012.8–00.0. In order to estimate the statistical description of both models, the absolute chi-squared (χ^2) goodness-of-fit was estimated using the SED points of component B derived in the joint-fit. This study finds $\chi^2_{\mathrm{had}} = 18.56$ for the hadronic model and $\chi^2_{\mathrm{lep}} = 30.62$ for the leptonic model. The hadronic model is therefore preferred at a 3.47σ level. Whilst the hadronic model yields a marginally better statistical description for the emission, the target material identified in the region is not sufficient to account for the extent of the detected γ-ray emission and target material with a density of the level of the ISM would require an unreasonably high proton energy to explain the detected γ-ray flux.

For the data below 10 GeV, observed as component C, no evidence can be found that convincingly points towards either a leptonic or hadronic origin. A hadronic scenario cannot be supported since no association with a nearby interstellar cloud or target material can be made. A leptonic scenario would imply the existence of a second electron population or an unreasonably high particle density, which is only experienced by this second electron population. Another possible leptonic scenario might be a pulsar origin, which may alternatively account for the emission component, but this study cannot find convincing evidence for such an explanation. For a firm identification of the soft γ-ray emission as originating from the pulsar, a dedicated study of the emission at lower energies needs to be performed.

To further add to the understanding about this source, more observations at high-energy γ rays are necessary, especially the addition of further data taken by HAWC or LHAASO into the joint-fit and the addition of further data taken by *Fermi*-LAT will

be of great value in constraining the possible origin of the different components.

6 The third Musketeer PSR B1055−52

The analysis of the region around PSR J1813−1749 has shown the importance of a correct background estimation for the reconstruction of the morphology of extended γ-ray structures. Whilst the nebula around PSR J1813−1749 shows a quite unexpected extension, all of the emission is still contained in the FoV of the detector, and the background could be estimated from regions within the observations.

For systems older than 100 kyrs, the pulsar has typically left its parent SNR, and electrons of the pulsar wind can escape into the ISM, resulting in the formation of a pulsar halo. This structure is expected to be substantially more extended than the PWN and can potentially fill a region larger than the FoV of IACTs. Two such pulsar halos were detected around the Geminga Pulsar (PSR J0633+1746) and the Monogem Pulsar (PSR B0656+14) (Abdo et al., 2009b). Both are middle aged pulsars ($\tau_c = 342\,\mathrm{kyr}$ and $\tau_c = 110\,\mathrm{kyr}$ respectively) and have similar spin-down energies ($\dot{E} = 3.2 \cdot 10^{34}\,\mathrm{ergs}^{-1}$ and $\dot{E} = 3.8 \cdot 10^{34}\,\mathrm{ergs}^{-1}$), and a similar magnetic field strength at the light cylinder ($B_{\mathrm{LC}} = 1.15 \cdot 10^3\,\mathrm{G}$ and $B_{\mathrm{LC}} = 0.77 \cdot 10^3\,\mathrm{G}$).

A third pulsar with similar properties, PSR B1055−52 (or PSR J1057−5226), was detected in 1972 in radio energies by the Molonglo Radio Observatory (Vaughan and Large, 1972). Pulsed emission has since been detected in soft X-ray using ROSAT (Oegelman and Finley, 1993) and in γ-ray energies, by the Compton Gamma-ray Observatory in 1993 (Fierro et al., 1993). The pulsar is estimated to have a spin-down luminosity of $\dot{E} = 3.0 \cdot 10^{34}\,\mathrm{erg/s}$, and a magnetic field strength of $B = 1.1 \cdot 10^{12}\,\mathrm{G}$ (Jankowski et al., 2018). From the observed spin frequency and its derivative, a characteristic age of $\tau_c = 535\,\mathrm{kyr}$ can be inferred. The placement of the pulsar in the $P - \dot{P}$ diagram can be seen in Figure 6.1.

Aside from showing similar spin-down energy loss rates and magnetic fields, Geminga, Monogem, and PSR B1055−52 share another important characteristic: thermal X-ray emission can be detected from all three pulsars. This thermal emission results from the cooling of the neutron star and is difficult to observe in younger pulsars since their spectrum is dominated by interactions of relativistic particles in the pulsar wind. For very old pulsars, the surface has cooled significantly, and the thermal emission becomes very weak and hard to detect. This prominent thermal component of their spectrum, as well as overall common properties, has earned them the nickname the 'three musketeers' (Becker and Truemper, 1997).

Due to these similarities, it is plausible to assume that the evolution of the environment around these pulsars should be similar. While all three pulsars are established as γ-ray pulsars (Smith et al., 2023a), until now, an extended γ-ray halo was only detected in the region around Geminga and Monogem. This detection was made by the WCD array MILAGRO (Abdo et al., 2009b) and later confirmed by HAWC (Abeysekara et al., 2017b). A detection of this halo with IACTs has proven to be complicated (Akerlof et al., 1993; Aharonian et al., 1999) due to the large extent of the emission, which leaves no emission-free region for the background estimation. Using a classical ON-OFF background estimation (for more information see Chapter 3.1), H.E.S.S. Collaboration et al. (2023) was able to obtain a detection, a morphological study or estimation of the flux of the whole emission region was however still not possible.

The detection of a TeV halo around PSR B1055−52 could also help to explain the observation of an unexpected excess of positrons at energies between 10 GeV and

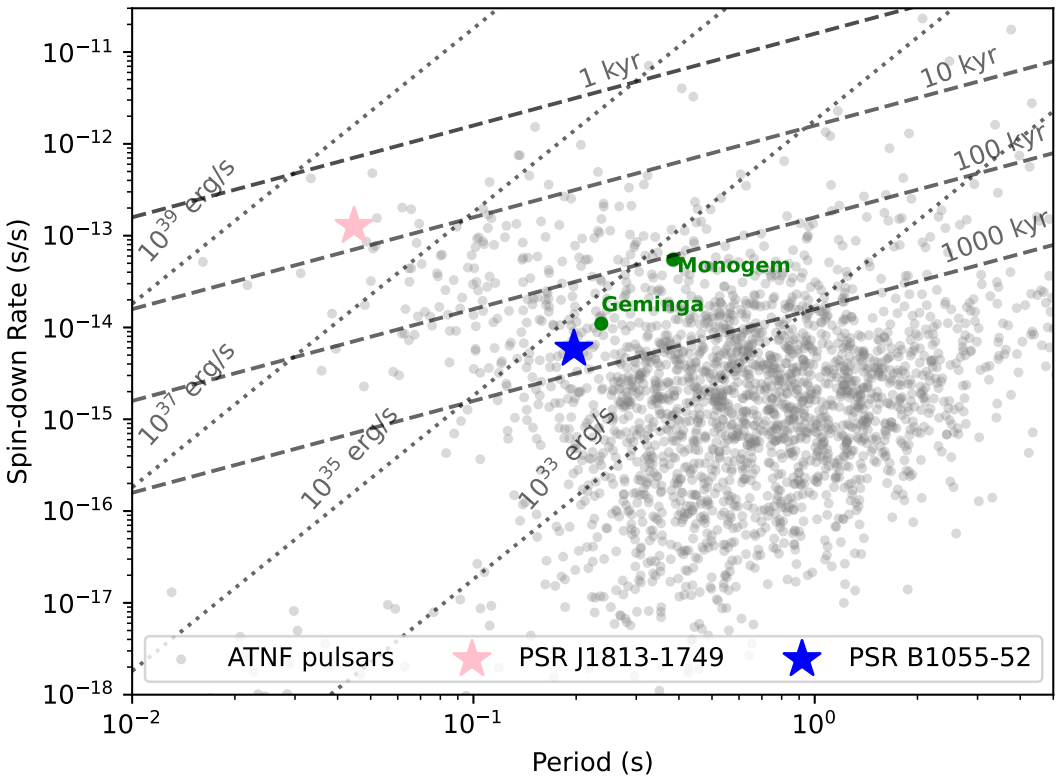

Figure 6.1: $P - \dot{P}$ diagram of the pulsars listed in the ATNF catalogue (Manchester et al., 2005). The position of PSR B1055−52 is indicated by the blue star. Also shown are the positions of the Geminga and Monogem pulsars in green.

1 TeV the Alpha Magnetic Spectrometer (AMS-02), a particle detector mounted to the International Space Station (Aguilar et al., 2013). This significant increase in the positron fraction is not accounted for by traditional cosmic ray propagation models, suggesting the presence of one or more unknown sources of positrons.

PWNe and pulsar halos are prime candidates for the origin of these positrons at such high energies due to their efficient acceleration and relatively ineffective confinement of cosmic ray leptons. However, leptons at TeV energies cool rapidly through processes such as IC scattering and synchrotron radiation. This implies that the pulsar responsible for the observed positron excess must be relatively nearby to ensure that the accelerated positrons retain sufficient energy.

The distance estimated for PSR B1055−52 is not well constrained, with estimates ranging from 92 pc to 1.53 kpc, depending on the electron density model that is used for the estimation (Posselt et al., 2023; Taylor and Cordes, 1993). Given this range of estimates, PSR B1055−52 is sufficiently close to the International Space Station that its TeV halo could contribute significantly to the observed positron flux (Orusa et al., 2025).

Due to its location (GLON = 285.98°, GLAT = 6.65° (Manchester et al., 2005)), the region around PSR B1055−52 is not observable by γ-ray detection facilities located in the northern hemisphere, including all currently operating WCD arrays. This sky region is, however, observable with H.E.S.S.. The following work will present an analysis of the available H.E.S.S. data on the region, using two different background estimation approaches. The morphological and spectral properties of the γ-ray emission in the region will be analysed in detail, and the results used to compute an injection spectrum of electrons from the pulsar, which can explain the γ-ray emission.

6.1 Data selection and background estimation

A total of 157 observation runs on the region around PSR B1055−52 were acquired from January to March in 2019. The observations were taken with an offset of 1.0° from the pulsar position listed in Manchester et al. (2005). Of these, 42 observations do not pass spectral quality cuts (see Section 3.2.1) or have one of CT $1-4$ missing. Since no background template model for data with less than four telescopes is available, these observations are excluded. The data was reduced using the H.E.S.S. analysis package (see (Aharonian et al., 2006a)) and reconstructed using the ImPACT algorithm (Parsons and Hinton, 2014). The analysis was performed using `gammapy` version 1.2 (Donath et al., 2023; Acero et al., 2024).

The background estimation is performed using two different methods. The first background estimation method used is the run matching approach outlined in Chapter 3.2. As a second method, the background model template is applied directly to the data. Since the emission is expected to be largely extended, and the application of the background model template requires a normalization in a γ-ray free region of the respective observation, an underestimation of the source extension and energy flux using this method is likely. This dataset is therefore only used to cross-check the results obtained using the run matching. Since no background template model for mono or hybrid observations is currently available, events observed by CT5 are not included in this analysis.

During the matching of the observation pairs for the background estimation, only

78 run pairs within the validity range of the matching parameters could be found. To avoid a significant drop in exposure due to these restrictions, the validity range was slightly increased for all parameters until the exposure loss dropped below 20% (see Table C.1). The implications for the background estimation have been checked by repeating the analysis of the empty-field regions outlined in Chapter 3.2. The mean and standard deviation of the Li&Ma (1983) significance distribution for the direct application of the background template (Case 0), the run matching approach using the nominal validity range for all parameters (Case 3) and the increased validity range (Case 5) can be seen in Table 6.1. Despite the slight decrease in comparability between both background estimation methods, the fit parameters of the Gaussian fit to the Li&Ma (1983) significance distribution for the Case 5 dataset indicate a valid background description and are still within the systematic uncertainties estimated for the respective dataset in Chapter 3.2.

Table 6.1: Fit parameters of a Gaussian distribution to the Li&Ma (1983) significance values of the background events derived from the empty-field observations around Reticulum II, Tucana II and Sculptor before and after the validity range of the matching parameters was increased.

Case	Reticulum II		Tucana II		Sculptor	
	μ	σ	μ	σ	μ	σ
Case 0	-0.06	1.04	-0.05	1.01	-0.10	1.04
Case 3	-0.08	1.04	-0.06	1.06	-0.14	1.03
Case 5	-0.14	1.03	-0.01	1.02	-0.18	1.03

The dataset containing all observations for which OFF runs could be identified consists of 99 observation runs, with a deadtime corrected observation time of 44.9 hours, acquired in a zenith angle range of $29 - 51°$. The fractional run deviation of the dataset is $\overline{f} = 0.53$, which is comparable to the datasets used in the validation of the run matching approach ($\overline{f} \in [0.22 - 0.89]$).

For the dataset using the direct application of the background model template, the observations for which no matching OFF run was found could also be included in the observation. However, to ensure comparability between both datasets, the same observation list was used. The region around PSR B1055−52 does not contain other known γ-ray sources, so the background rate of the template model is normalised to the observation counts outside of a region with a radius of 2.3° around the nominal pulsar position. The choice of radius for this region was made to ensure that as much of the suspected emission around the pulsar is excluded, while at the same time retaining enough statistics (at least 100 counts per observation) for a successful fit of the template.

The adjusted background rate is calculated following Equation (43), with large deviations in Φ corresponding either to strong deviations in the atmospheric conditions or the detector response from the mean conditions in this optical phase or the absorption of emission into the background fit. The distribution of the spectral norm for all observations in this dataset for both background estimation methods can be seen in Figure 6.2.

Additionally shown is a Gaussian fit to the distribution. The direct application of the background model template to the observation on average results in a 14% higher

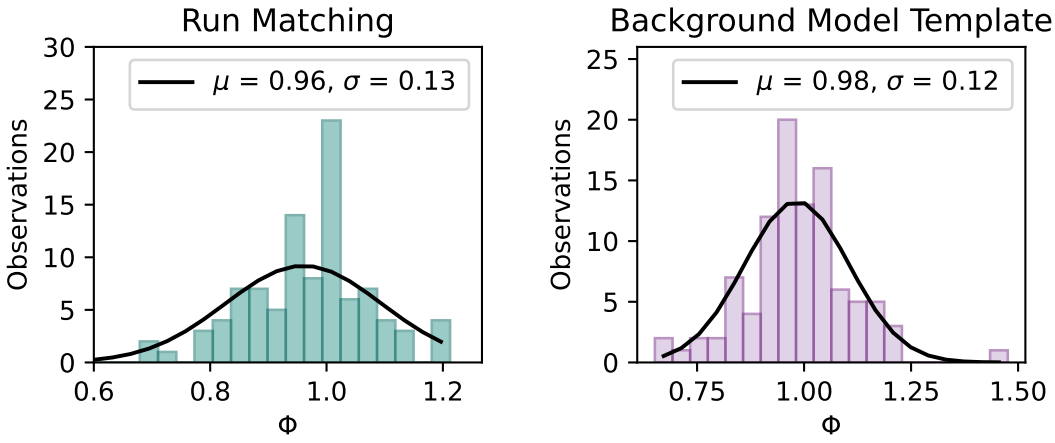

Figure 6.2: Distribution of the spectral norm Φ for the background fit. Additionally shown is a Gaussian fit to the data. Left: Distribution for the fit for Dataset 2. Right: Distribution for the fit for Dataset 1.

normalisation. This deviation has also been computed for the four different wobble pointing positions that were used to acquire the data.

The pointing positions at higher Right Ascension and equal Declination of the pulsar, as well as the pointing position at equal Right Ascension but lower Declination, show only a deviation of $\sim 3\%$.

The observations taken at a pointing position that has equal declination but lower right ascension show that the normalisation of the background model is 10% higher for the application of the background model template.

At the pointing position with higher declination, the deviation is even larger, with the normalisation derived from the application of the background model template being 38% higher than the values derived from the run matching approach. This indicates that some emission, especially for observations taken on the latter two pointing positions, might be absorbed into the background.

The dataset using the established method of the direct application of the background model template will hereafter be referred to as Dataset 1, while the dataset computed using the run matching approach will be referred to as Dataset 2. For the analysis region, a size of $6° \times 6°$ with a spatial bin size of $0.02°$ was chosen. The energy axis of the IRFs is binned into 48 bins between 0.1 TeV and 100 TeV. The reconstructed energy is binned in 24 bins in the same energy range. The energy threshold for every run was set so that all data for which the energy bias is above 10% is discarded. Additionally, all data with $E < E_{\text{peak}}$, where E_{peak} is the energy of the peak of the background spectrum, is discarded. This threshold was applied to both datasets. Only events with a reconstructed offset of less than $2.0°$ from the camera centre were retained for the analysis. After the background estimation for each observation, the observations are stacked into one dataset.

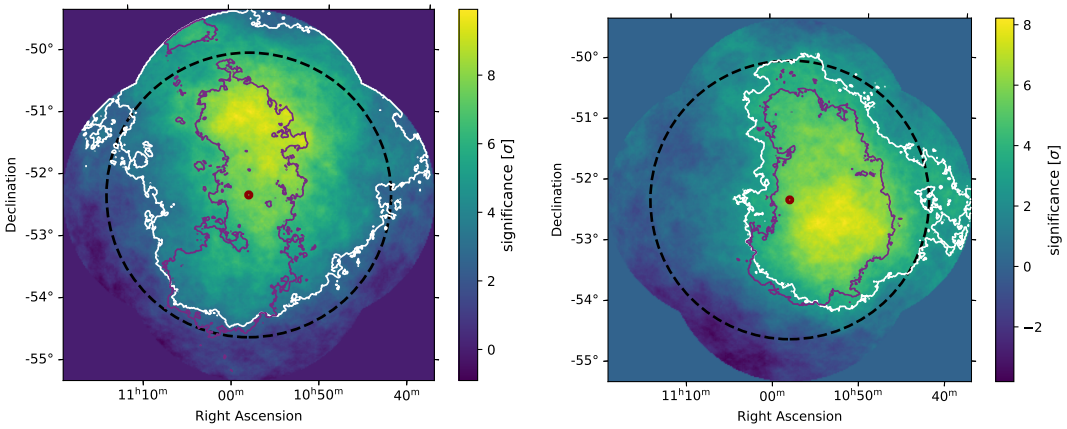

Figure 6.3: Li&Ma (1983) significance map of the region around PSR B1055−52 with a 1° correlation radius, estimated using Dataset 2. The $3\,\sigma$ contours of the emission from this dataset are added in white, while the $3\,\sigma$ contours of the emission derived from Dataset 1 are added in purple. Left: Map calculated from events above the energy threshold derived from the energy bias and background peak. Right: Map calculated only from events with a reconstructed energy above 1 TeV.

6.2 Spectromorphological Modelling

Figure 6.3 shows two Li&Ma (1983) significance maps computed using Dataset 2, both with a correlation radius of 1.0 °. While the left panel shows the data above the energy threshold derived from the background peak and the energy bias, the right panel shows a Li&Ma (1983) significance map computed using only events with a reconstructed energy above 1 TeV.

The region excluded from the background fit for Dataset 1 is depicted as black dashed circle in both panels. Additionally shown are the $3\,\sigma$ contours computed from Dataset 2 in white and the $3\,\sigma$ contours of Dataset 1 in purple. The left panel shows that for Dataset 2, the γ-ray emission extends to the edges of the observed region at a Declination above $\sim 52°$. This means that despite the choice of a large exclusion region for the background estimation, γ-ray contaminated regions have been included in the background normalisation for Dataset 1, which leads to the overprediction of background counts, and reduces the flux substantially. This explains the deviation in extension observed from the $3\,\sigma$ contours between both datasets. For this reason, all further analysis is done using Dataset 2, except stated otherwise.

As shown in the right panel of Figure 6.3, this effect is less pronounced at energies above 1 TeV where almost all emission observed in Dataset 2 are contained within the region excluded from the fit of the background spectrum. In this case, the observed emission shows a comparable extension for both datasets.

The Li&Ma (1983) significance map, as well as contours shown on the left in Figure 6.3, also suggest that the γ-ray emission might not fully be contained within the region observed by H.E.S.S.. For this reason, many of the results presented in the following should be interpreted as lower limits. An additional limitation of this is that no spectromorphological fit over the whole energy range is possible.

To circumvent this problem, the centre of gravity of the observed emission is estimated.

This is done by computing the acceptance-corrected excess counts summed over the total energy range in every spatial bin. This data is then evaluated using the python package `scipy` (Virtanen et al., 2020), and a centre of mass is calculated. The estimated position is then used as the centre of a spatial model and fixed for the subsequent fitting. The best-fit extension of the model, as well as the parameters of the spectral model, are derived from a maximum likelihood fit.

To describe the emission different spectromorphological models were applied to the region. As a spatial model a disc model, as well as a Gaussian model, both symmetric and with elongation, were tested. The Gaussian model is defined in Equation (59), while the disk model is given by:

$$\phi(r_0) = \frac{1}{2\pi(1-\cos r_0)} \cdot \begin{cases} 1 & \text{for } \theta \leq r_0 \\ 0 & \text{for } \theta > r_0 \end{cases} \tag{72}$$

with r_0 the radius of the containment area in which the emission is uniformly distributed. The width of the edge of this uniform distribution is defined as the range within which the edge of the model drops from 95% to 5% of the initial amplitude (Donath et al., 2023). In this study, the edge width was fixed to 1% of the radius of the containment area. As spectral model, a simple power-law (Equation (61)), an exponential cutoff power-law (Equation 63) as well as a broken power-law spectral model, were tested. The latter is defined as:

$$\phi(E) = \phi_0 \cdot \begin{cases} \left(\frac{E}{E_{\text{break}}}\right)^{-\Gamma_1} & \text{if } E < E_{\text{break}} \\ \left(\frac{E}{E_{\text{break}}}\right)^{-\Gamma_2} & \text{otherwise} \end{cases} \tag{73}$$

with E_{break} the energy of the spectral break, Γ_1 the spectral index before the break and Γ_2 the spectral index after the break (Donath et al., 2023).

For every model, a test statistic was calculated, and the ΔTS between the model hypothesis and the null hypothesis (no source model) was calculated. After the application of a source model, a histogram of the Li&Ma (1983) significance of the emission in every pixel of the region was computed. The significance of all models, as well as the parameters of the Gaussian fit to the histogram for all model hypotheses, can be seen in Table 6.2.

The best description of the γ-ray emission around PSR B1055−52 can be reached by applying a symmetric Gaussian model. The best-fit parameters of this model can be seen in Table 6.3. The extension derived in this analysis is to be interpreted as a lower limit on the true extension of the γ-ray emission. A significance map of the emission, overlaid with the best-fit morphology of the model, as well as the $3\,\sigma$ contours, can be seen in the left panel of Figure 6.4, the distribution of pixel significance values before and after the fit is depicted in the right panel of Figure 6.4.

The significance distribution derived from the data after the fit deviates slightly from the expected distribution of a good description of all emission in the region, and some significant emission remains even after the application of the Gaussian model. A second Gaussian model was added to the data, did, however, not improve the description of the region significantly, and the model significance is estimated to be only $3.72\,\sigma$.

Adding a spectral break or a cutoff in the power-law spectrum is preferred by $1.68\,\sigma$ and $0.98\,\sigma$ with respect to the simple power law. The SED for the three models tested

Table 6.2: Model significance σ_M and Gaussian distributions of the Li&Ma (1983) significance values in the region after the model fit, for all model assumptions. The tested spectral models are a power law (PL), an exponential cutoff power law (Ecut PL) as well as a broken power law (BPL).

Spatial Model	Spectral Model	σ_M	μ	σ
Disk	PL	13.63	0.15	1.11
Elongated Disk	PL	13.31	0.21	1.11
Gauss	PL	13.84	0.04	1.07
Elongated Gauss	PL	13.64	0.05	1.06
Gauss	Ecut PL	13.70	0.05	1.07
Gauss	BPL	13.72	0.06	1.07

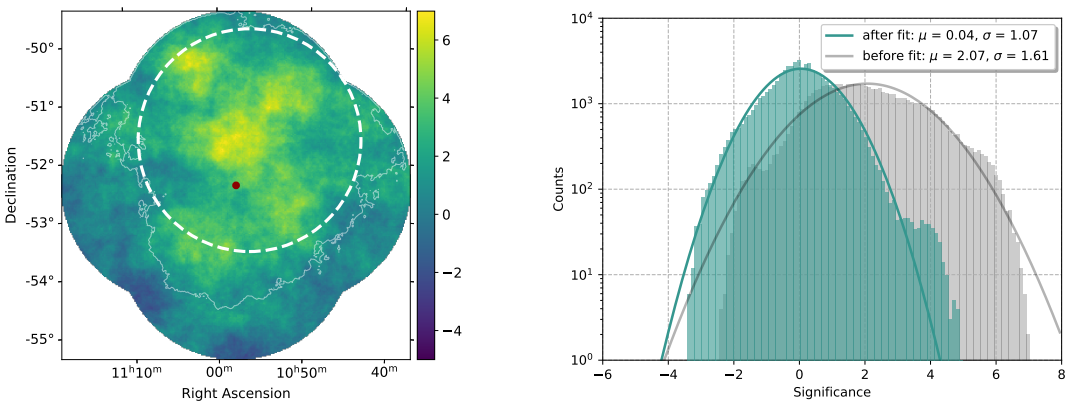

Figure 6.4: Left: Li&Ma significance map for Dataset 2, with a correlation radius of 1.0°. The $3\,\sigma$ contours are depicted in white, the best-fit morphology of the Gaussian model is depicted by the white-dashed circle. Right: Significance distribution of the emission in the region before and after the application of the Gaussian model.

Table 6.3: Best-fit parameters obtained for the analysis of the data above the energy threshold, using a Gaussian model with a power law as spectral model.

	PSR B1055−52 region
Γ	$2.79 \pm 0.08_{\text{stat}} \pm 0.42_{\text{sys}}$
N_0 $[10^{-11}\text{cm}^{-2}\,\text{s}^{-1}\,\text{TeV}^{-1}]$	$2.12 \pm 0.42_{\text{stat}} \pm 1.57_{\text{sys}}$
R.A. [°]	$164.12 \pm 0.35_{\text{sys}}$
Dec. [°]	$-51.67 \pm 1.40_{\text{sys}}$
σ [°]	$1.92 \pm 0.23_{\text{stat}} \pm 0.72_{\text{sys}}$

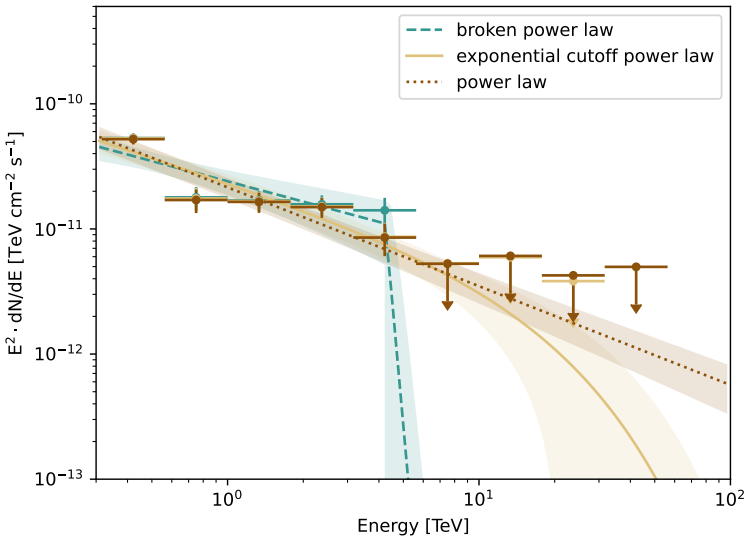

Figure 6.5: The SED of the emission for the three different spectral models.

in this work can be seen in Figure 6.5. For the computation of the SED points 12 logarithmically spaced energy bins between 0.1 TeV and 100 TeV were used. Since the addition of the spectral break or cutoff does not result in a significant improvement, the power law is retained as spectral model for the analysis.

6.3 Compatibility of the background estimation methods

In order to compare the results derived using both background estimation techniques, different tests were conducted. At first, the data of both datasets were analysed only including events with a reconstructed energy above 1 TeV. A Li&Ma (1983) significance map of Dataset 2 using this energy threshold can be seen on the right in Figure 6.3. Most of the significant γ-ray emission in this energy range is contained within a circle of 2.3° around the position of PSR B1055−52, which was ignored for the background estimation using the background model template. Since only a minimal contamination is expected, the results obtained from both datasets can be compared above 1 TeV.

Another advantage in this energy range is that the observed emission is fully contained within the ROI, and it becomes possible to derive not only the best-fit extension but also the position from a maximum likelihood fit. For this test, only a simple power-law model is used since the energy range of the datasets is restricted between 1 TeV and 100 TeV. As spatial model, a disc model and a Gaussian model were tested.

The Gaussian model is preferred over the disc model with a significance of $2.37\,\sigma$ ($9.03\,\sigma$ as opposed to $6.66\,\sigma$ for the disc model) for Dataset 2. The significance of the Gaussian model for Dataset 1 $6.28\,\sigma$, is slightly below the significance derived for Dataset 2. This is, however, expected due to the slight contamination of the background estimation region. Adding an elongation is not significantly preferred for either dataset.

The best-fit parameters for the Gaussian models for both datasets can be found in Table 6.4. After the application of the model, a distribution of the significance in the ROI is computed, and a 1-dimensional Gaussian model is fitted to this data. The

Table 6.4: Best-fit parameters obtained for the analysis of the data above 1 TeV, using the direct application of the background model template (Dataset 1) and the run matching approach (Dataset 2). A Gaussian model with a power law as spectral model was fit to the data.

	Dataset 1	Dataset 2
Γ	2.53 ± 0.12	2.89 ± 0.15
N_0 $[10^{-11}\mathrm{cm}^{-2}\,\mathrm{s}^{-1}\,\mathrm{TeV}^{-1}]$	0.86 ± 0.31	1.77 ± 0.62
R.A. [°]	163.17 ± 0.41	162.82 ± 0.54
Dec. [°]	-53.00 ± 0.35	-51.73 ± 0.36
σ_M [°]	1.11 ± 0.23	1.36 ± 0.23

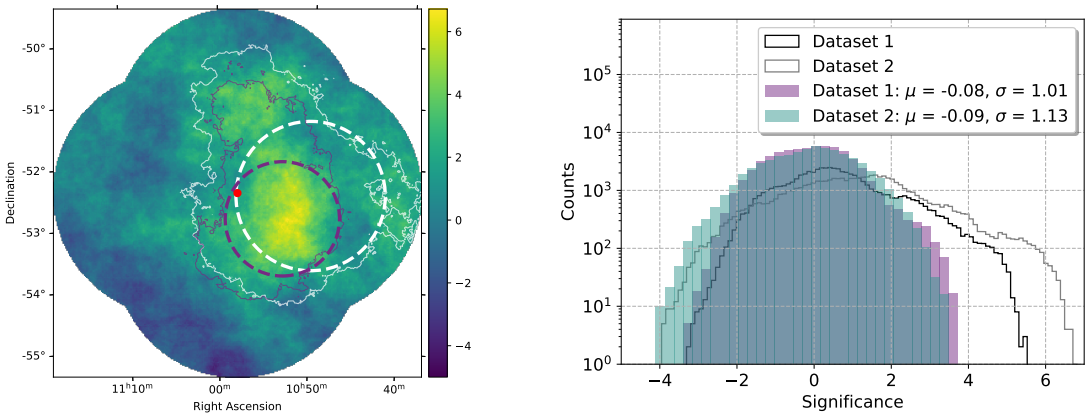

Figure 6.6: Significance map of the region around PSR B1055−52 using only events with a reconstructed energy above 1 TeV. Left: The 3σ contours as well as position and extension of the best-fit model for Dataset 1 are shown in purple, while the contours and model for Dataset 2 are shown in white. Right: Histogram of the significance distribution before the addition of the model in black/grey and after the addition of the model in blue/purple.

histogram and fit results can be seen in the right panel of Figure 6.6, no significant γ-ray emission remains after the application of the respective model.

The SED of both power-law models can be seen in Figure 6.7. The SED points agree reasonably well, a deviation of $\sim 2\,\sigma$ can be observed around 1 TeV, which can be explained by the contamination of the background estimation region with γ-ray source flux towards lower energies.

From this analysis, it can be concluded that there is no significant deviation in the observed γ-ray emission between the two different background estimation techniques at high energies.

A second test conducted to compare the compatibility of the background estimation with both methods is the computation of radial profiles.

The Li&Ma (1983) significance map presented in Figure 6.3 shows that the observed

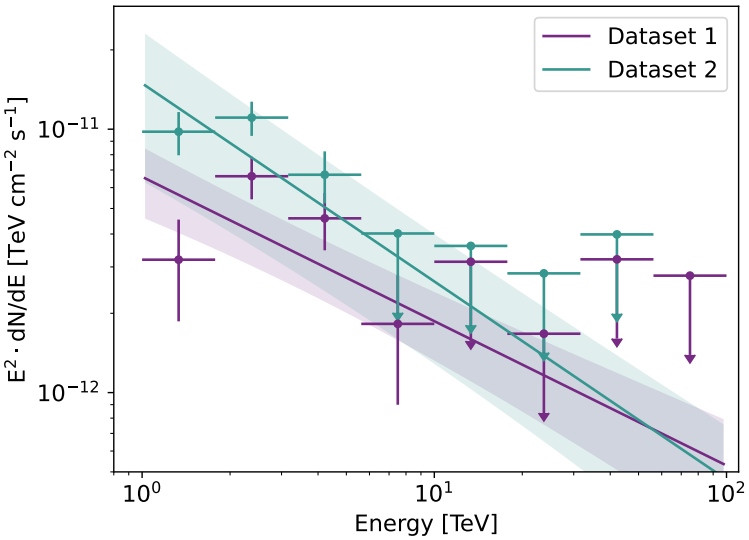

Figure 6.7: The SED derived from the fit to the dataset computed using the direct application of the background model template (Dataset 1) and the run matching approach (Dataset 2) above 1 TeV.

emission is not symmetrically distributed around the pulsar position but offset to the north. To estimate the direction along which the most emission is observed, a power-law spectral model with the best-fit parameters presented in Table 6.3 is used to compute an acceptance-corrected counts map. Then the observed excess counts, out to a radial distance of 2.5° from the pulsar position, are integrated over triangular regions originating at the pulsar position, with an opening angle of 20°. The zero angle is defined as the direction of decreasing declination, i.e., south. The resulting integrated counts are then depicted over the angle of the integration region, and their profile for both datasets can be seen in Figure 6.8.

The number of counts derived for both datasets is within errors comparable in the regions towards the south, while Dataset 1 overall shows a lower number of counts towards the north. This finding is consistent with the suspected overestimation of the background for especially the northern pointing for Dataset 1, whereas the southern pointing is not influenced by this due to the presence of a large enough source-free region to fit the background model template.

The azimuthal distribution for Dataset 2 is fit with a Gaussian model, obtaining the main emission angle α as the mean of the Gaussian $\mu = (182.91 \pm 35.44)°$. The direction of the main emission angle compared to the proper motion of the pulsar is shown in Figure 6.9.

For a bow-shock PWN, it would be expected that the emission is primarily influenced by the direction of the proper motion of the pulsar. In this case the emission is aligned almost perpendicular to the velocity vector of the pulsar. In case the emission is associated with PSR B1055−52, this suggests that other factors, such as anisotropies of the local magnetic field, particle diffusion, or inhomogeneities in the surrounding medium, are the main influence on the diffusion of the high energetic cosmic ray leptons. This is in agreement with a pulsar halo scenario, where it is expected that particle

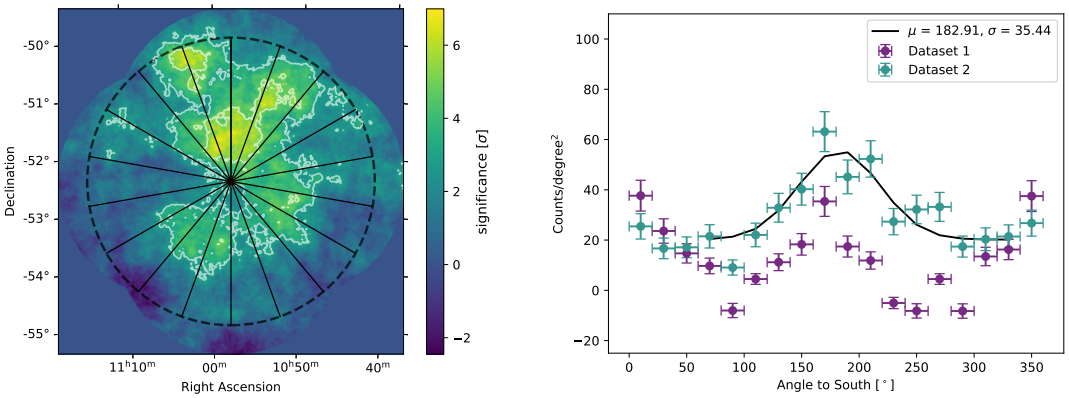

Figure 6.8: Right: Li&Ma (1983) significance map computed with a correlation radius of 0.5°. The triangular wedges used to compute the anular emission profile are shown in black. Left: Angular profile of the emission around PSR B1055−52 for both datasets. A Gaussian fit to the excess counts estimated from Dataset 2 is depicted in black.

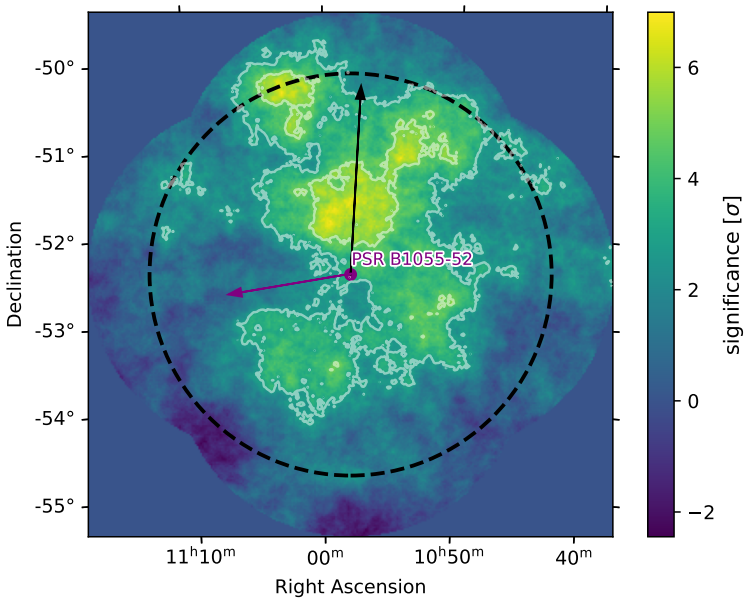

Figure 6.9: Li&Ma (1983) significance map of the region around PSR B1055−52 with a correlation radius of 0.5°. The $5\,\sigma$ and $8\,\sigma$ contours are shown in white. The region from which the angular profile shown in Figure 6.8 is derived is shown by the black circle. The black arrow depicts the main emission direction, and the purple arrow shows the direction of proper motion of the pulsar derived from measurements in the optical band (Mignani et al., 2010b).

diffusion is influenced mainly by the ambient medium and not the pulsar motion.

6.4 Energy Dependence

In order to further characterise the γ-ray emission, energy flux profiles are estimated from the emission in Dataset 2. Due to the asymmetry of the emission compared to the pulsar position, the region was split into two semicircles perpendicular to the main emission angle. Then, the energy flux as a function of radial distance from the pulsar was computed in rings of 0.3° width. This is shown in the Appendix in Figure C.1.

The radial profiles for both semi-circular areas can be seen in Figure 6.10. The radial profile in the region south of PSR B1055−52 shows a significant decrease in energy flux to background level at around 1.5°. The radial profile in the region north of PSR B1055−52 shows an overall higher energy flux, without a significant decrease and background level is not reached, implying that the emission is likely to extend further from the pulsar and further underlining that the overall source flux measured in this study should be treated as a lower limit. The negative energy flux values computed for some bins can be explained due to statistical fluctuations in the differential flux introduced by the background subtraction.

To characterise the energy dependence of this result, taking the available statistics into account, the data was split into four logarithmically spaced energy bands, also shown in Figure 6.10, and the radial profiles were recomputed in each energy band.

The profiles computed for the southern region in the first three energy bins are within $1\,\sigma$ uncertainties comparable. Above 4.22 TeV, the energy flux drops to background level.

The profiles derived from the northern segment show a strong energy dependence, with the energy flux detected in the bin below 0.75 TeV containing the highest concentration of flux. This suggests that the contribution to the total energy flux from the lower energy bins is disproportionately larger than from the higher energy range and that the flux in the total range is dominated by the low-energy tail of the spectrum. This leads to the energy flux over the whole energy range being smaller than the flux in a smaller energy bin where the source's emission is more concentrated. For energies below 0.75 TeV, the energy flux increases with increasing distance to the pulsar, which is consistent with the centre of gravity of the emission being offset from the pulsar position and supports the finding that the emission likely extends beyond the observed ROI. A similar behaviour, but less significant, is also observed in the second bin. Above 4.22 TeV, the energy flux is independent of the distance to the pulsar and comparable to background level.

The differences in extension observed between the significance maps in Figure 6.3, as well as the surface brightness profile in the northern segment, suggest a possible energy-dependence of the extension of the γ-ray emission. To further investigate a possible energy-dependence, the data was divided into the same four logarithmically spaced energy bands as used for the computation of the radial profiles and the Gaussian source model was fitted in each band.

Since no fit of the position was possible for the first two energy bands, two different methods were used to estimate the source extension. First, the position of the spatial model was fixed to the centre of gravity of the emission estimated over the whole energy range. Second, the position of the spatial model was fixed to the centre of gravity in

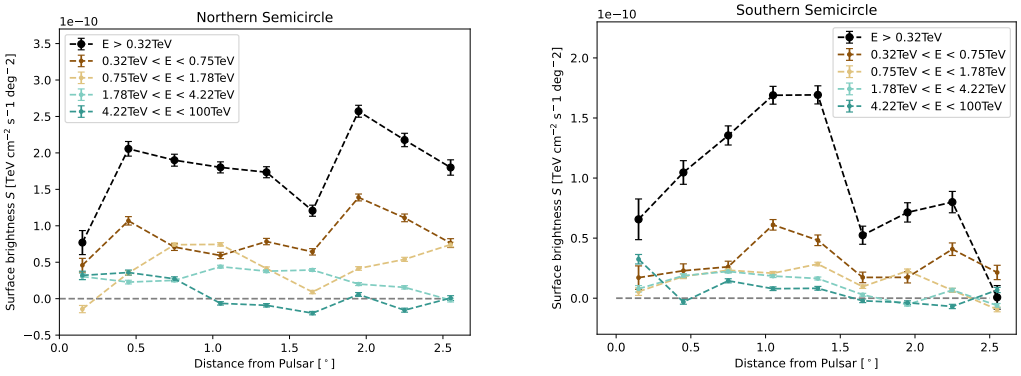

Figure 6.10: Radial energy flux profiles derived from the regions around PSR B1055−52 as shown in Figure C.1. The left panel shows the integrated energy flux in the northern half, while the right panel depicts the integrated energy flux profile in the southern half.

Table 6.5: Best-fit parameters obtained for the morphology of the emission around PSR B1055−52 in different energy bands for a fixed and free position of the spatial model.

Energy [TeV]	free position			fixed position		
	R.A. [°]	Dec [°]	σ_M	R.A. [°]	Dec [°]	σ_M
$[0.32 - 0.75]$ TeV	164.57	−51.64	1.96 ± 0.36	164.12	−51.67	2.02 ± 0.38
$[0.75 - 1.78]$ TeV	163.53	−51.82	2.54 ± 0.57	164.12	−51.67	2.55 ± 0.59
$[1.78 - 4.22]$ TeV	162.74 ± 0.31	-52.61 ± 0.18	0.91 ± 0.16	164.12	−51.67	1.70 ± 0.32
$[4.22 - 100.00]$ TeV	163.42 ± 0.35	-52.47 ± 0.18	0.48 ± 0.18	164.12	−51.67	0.92 ± 0.73

each of the respective energy bands. In the second approach, the centre of gravity was estimated in each of the first two energy bands, while the position was included as a fit parameter for the latter two energy bands.

The energy range of the respective bands, as well as the best-fit position and extension of the Gaussian model for both cases, can be seen in Table 6.5. A visualisation of the $1\,\sigma$ containment radius for the Gaussian model in the different energy bands is shown in Figure 6.11. The extension of the Gaussian model estimated with the fixed model centre at the centre of gravity of the emission estimated over the whole energy range does not show a significant trend. However, the extension of the model for which the model centre was estimated in each energy bin shows that the emission in the first two energy bins is comparable but then decreases significantly. The analysis in which the position is not fixed also shows that the centre of the emission shifts closer to the position of PSR B1055−52. These two effects are a further indication that the emission is most likely leptonic, with the parent particles originating from PSR B1055−52 and diffusing outward while they cool.

6.5 Spectral Analysis of the Region

The large extension of the emission raises the question of whether the whole region can be described with a single spectral model. To estimate the uniformity of the emission,

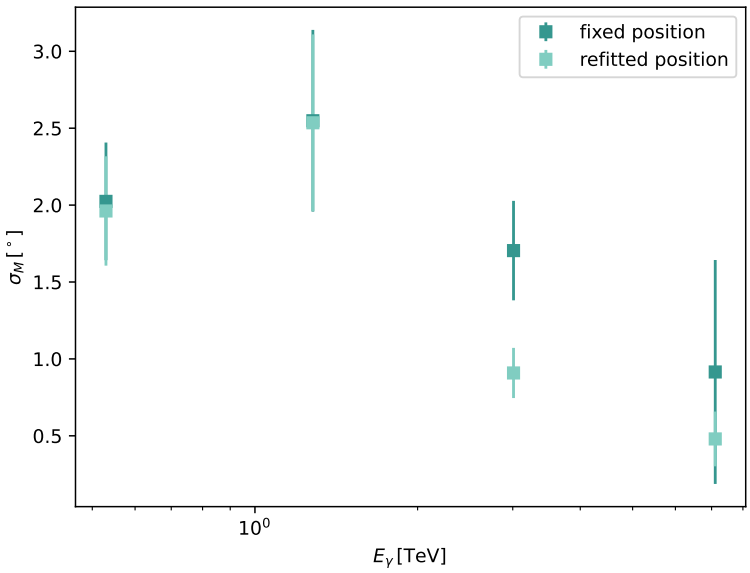

Figure 6.11: Extension of the Gaussian model fitted in the different energy bins shown in Table 6.5. The fixed position refers to the analysis where the center of gravity was estimated over the whole energy range and fixed to this value in the analysis in each energy bin. Refitted position refers to the analysis where the center of gravity or best-fit position was estimated for each energy bin, respectively.

the FoV is divided into 25 signal regions. Then, a power-law model is fitted to the emission in each of these regions, and regions in which a signal with a significance of less than $2\,\sigma$ is detected are discarded. The 14 regions in which a signal with a significance of more than $2\,\sigma$ is found are shown in Figure 6.12, overlaid with the $5\,\sigma$ and $8\,\sigma$ contours of the emission.

Table 6.6 shows the best-fit parameters in all regions with a signal above the $2\,\sigma$ threshold. The spectra derived from all significant boxes are comparable both in spectral index as well as in flux normalisation. For the spectral index, the deviations between the different boxes are visualised in a heat map in the left panel of Figure 6.13. The index values compared to the spectral index derived from the fit of the model to the whole region (see Table 6.3) are shown in the right panel of Figure 6.13. The behaviour of the Flux normalisation at 1 TeV is shown in Figure 6.14. The values derived for the individual boxes are within $2\,\sigma$ compatible with each other, and no significant trend can be identified.

Additionally, a Pearson correlation coefficient between the distance to the pulsar and the spectral index was calculated and found to be $r = 0.31$. The correlation coefficient between the flux normalization and the pulsar position was found to be $r = 0.51$. For both Pearson correlation coefficients, a t-score can be calculated as:

$$t = \frac{r\sqrt{n-2}}{\sqrt{1-r^2}}\,, \tag{74}$$

with n the sample size. The p-value can then be derived from the t-distribution as $p = 2 \cdot (1 - F_t(|t|, df))$, with $F_t(|t|, df)$ the cumulative distribution function (CDF) of

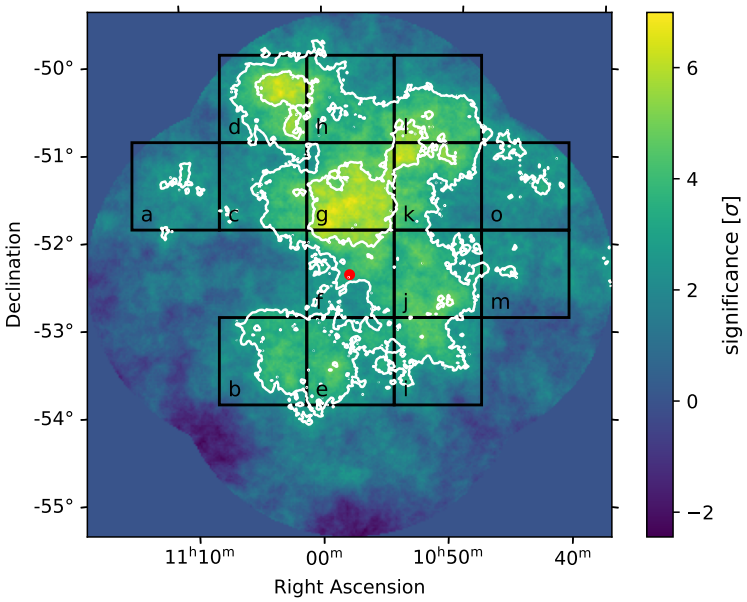

Figure 6.12: Li&Ma (1983) significance map of the region computed using a correlation radius of 0.5°. The 5 and 8 σ contours of the emission are shown in white, and all grid boxes for which a spectral model could be fitted with a significance higher than 2σ are shown in black.

Table 6.6: Parameters of the spectral fit and significance of the emission in the different signal boxes.

Signal Region	Spectral Index	N_0 $[10^{-13}\mathrm{cm}^{-2}\,\mathrm{s}^{-1}\,\mathrm{TeV}^{-1}]$	Significance σ
a	4.34 ± 2.07	2.55 ± 5.04	2.10
b	3.10 ± 0.38	7.42 ± 2.38	3.66
c	3.38 ± 0.48	4.26 ± 2.01	2.45
d	3.23 ± 0.45	1.16 ± 3.97	4.55
e	2.54 ± 0.20	7.34 ± 1.81	3.81
f	2.81 ± 0.32	5.81 ± 1.59	3.50
g	3.14 ± 0.25	9.44 ± 2.00	5.99
h	2.87 ± 0.34	9.46 ± 2.79	3.29
i	2.33 ± 0.13	9.30 ± 2.11	4.83
j	2.38 ± 0.12	9.78 ± 1.85	5.49
k	2.73 ± 0.40	7.25 ± 2.13	3.08
l	3.09 ± 0.39	1.16 ± 3.60	3.96
m	2.33 ± 0.26	7.20 ± 2.96	2.65
o	3.11 ± 0.57	7.69 ± 3.69	2.26

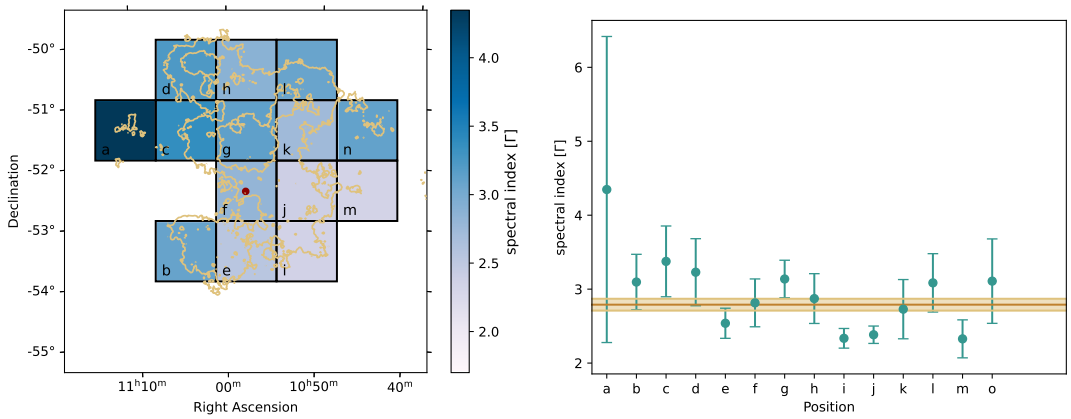

Figure 6.13: Left: Heat map for the spectral index derived from a fit of a power-law model to each of the boxes indicated in black. The $5\,\sigma$ and $8\,\sigma$ contours of the emission are shown in brown. Right: spectral indices for every box compared to the value derived from the fit over the whole region.

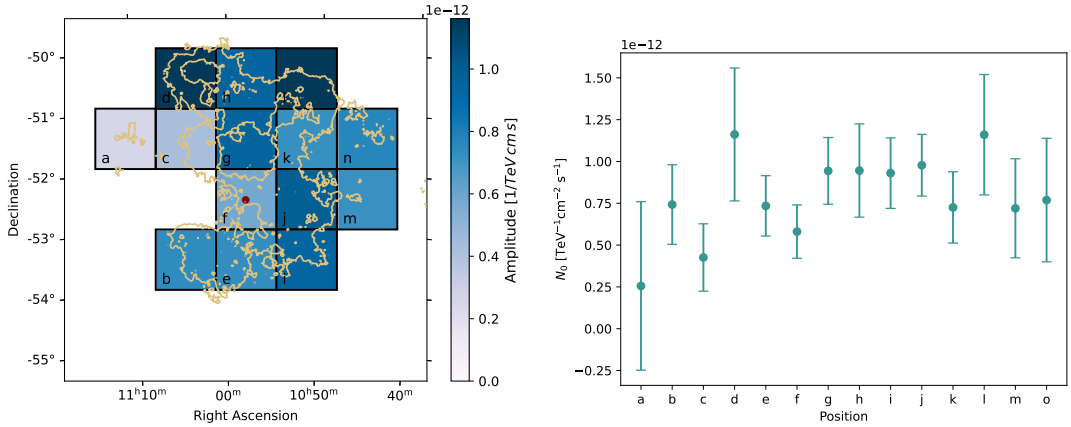

Figure 6.14: Left: Heat map for the flux normalisation at 1 TeV derived from a fit of a power-law model to each of the boxes indicated in black. The $5\,\sigma$ and $8\,\sigma$ contours of the emission are shown in brown. Right: comparison of the flux normalisation for every box.

the t-distribution with *df* the number of degrees of freedom. This can be converted into a z-score under a normal distribution as $z = \Phi^{-1} \cdot (1 - 0.5p)$.

For a correlation coefficient of $r = 0.31$ and $r = 0.51$ this results in a significance of $1.08\,\sigma$ and $1.86\,\sigma$ respectively. This lack of a correlation for both the spectral index, as well as the flux normalization, and the uniformity of the results obtained for all boxes supports the theory that all emission observed in the region has a single point of origin. It, however, also indicates that the propagation of the cosmic-ray particles responsible for the γ-ray emission is not significantly impacted by cooling, which would be expected for a γ-ray source powered by electrons and positrons.

6.6 Estimation of the Systematic Uncertainties

In order to estimate the influence of the background estimation on the significance of the source detection and the source parameters, two different tests were conducted.

6.6.1 Simulation of a γ-ray source

For this test, a simulated dataset was created. For this purpose, the IRFs and the background spectrum from Dataset 2 were used, and a simulated source, with the properties derived for the best-fit source model describing the emission around PSR B1055−52, depicted in Table 6.3, was injected into the ROI.

A Gaussian model has then been applied to the data, finding a significance of the model of $\sigma_M = 13.38$, which is comparable to the significance of the emission in the real data. The background rate was then increased until the significance of the model dropped below $5\,\sigma$. This study finds that a systematic uncertainty of 2.5% on the background rate can be introduced before the source detection is no longer significant. In the next step, the background rate of the real dataset is increased by 2.5%. We find that the significance of the detection drops down to $5.9\,\sigma$, showing a similar behaviour between the simulated source and the detected emission.

6.6.2 Estimation of the influence of the ON run sequence on the background rate

To provide an estimate of the systematic uncertainties of the best-fit parameters and the significance of the source detection due to the background estimation, a second independent matching list is created. For this purpose, the order of the ON runs was randomly rearranged before performing the run matching. Since a run is removed from the pool of potential OFF runs once it has been assigned to an ON run, this leads to a random shuffle of run pairs, which are then used to create a third dataset, hereafter referred to as Dataset 3. A visual comparison of the fractional run deviation between both lists can be seen in Figure 6.15. The shuffled run list shows a larger fractional run deviation, indicating that the identified run pairs are less compatible and that the quality of the background estimation is slightly worse.

A Gaussian model with a power-law spectral model was fitted to the data. The position of the Gaussian has been estimated by computing the centre of gravity of the emission, which was then fixed in the fit of the model to the data for both datasets. We find that the significance of the detection decreases from $13.53\,\sigma$ to $11.78\,\sigma$ in Dataset 3. A significance map and histogram visually comparing the emission and best-fit position

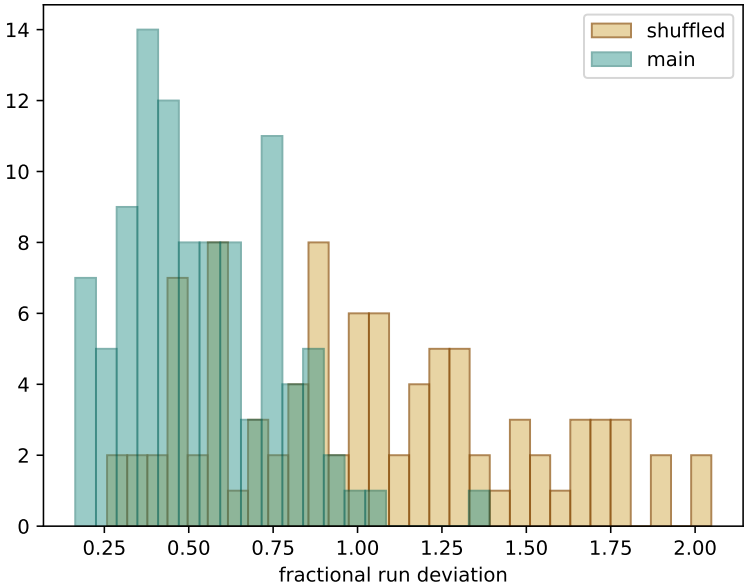

Figure 6.15: Distribution of the fractional run deviation for all run pairs in Dataset 2, as well as in the shuffled dataset.

of the Gaussian model for Dataset 2 and Dataset 3 can be found in the left panel of Figure 6.16. The significance histograms for both datasets are shown in the right panel. The source parameters for both datasets, as well as the SED, can be found in the Appendix in Table C.2 and Figure C.2, respectively.

The differences between the source parameters of the ON-OFF list used to create Dataset 2 and the list used to create Dataset 3 can be used as a first approximation on the systematic uncertainties of the best-fit model parameters.

However, the deviation between the observed emission for Dataset 2 and Dataset 3 is smaller than the deviation between the emission for the two different background estimation methods. This is not surprising since it is expected that the direct application of the background template used for Dataset 1 overestimates the background flux. In order to give the most conservative estimate of the source parameters, it was therefore decided to fit a Gaussian model to Dataset 1 and use the difference on the source parameters derived for this fit and the fit to Dataset 2 as the systematic uncertainties on the source parameters. From this fit also a lower limit on the significance of the detection can be established to $6.31\,\sigma$. The systematic uncertainties derived through this method are given in Table 6.3.

6.7 Analysis of *Fermi*-LAT data

Before this work, no detection of the pulsar halo around PSR B1055−52 using *Fermi*-LAT data was made. This is possibly due to a lack of appropriate background models for the detection and analysis of largely extended emission (see discussion in Ackermann et al. (2012) as well as on the website of the *Fermi*-LAT Collaboration [3], where caveats

[3] `https://fermi.gsfc.nasa.gov/ssc/data/analysis/LAT_caveats.html`

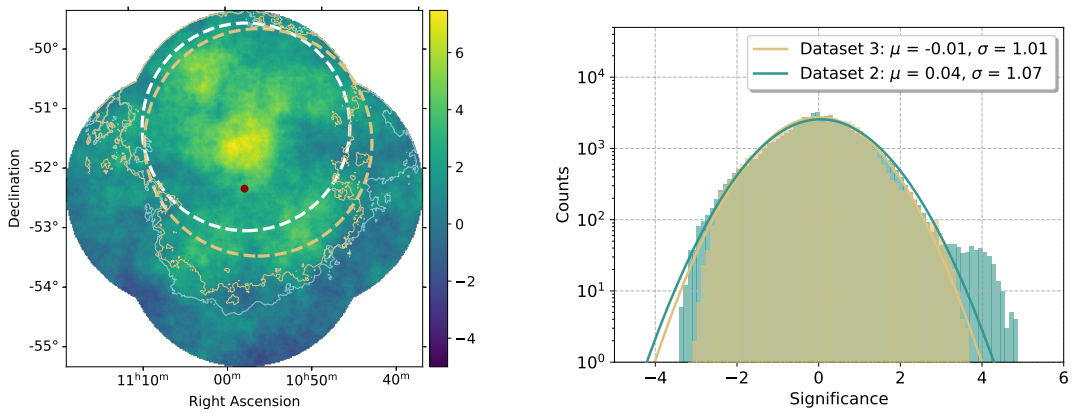

Figure 6.16: Left: Li&Ma significance map computed with a correlation radius of 1.0° from Dataset 2. The $3\,\sigma$ contours of the main dataset are depicted in white and the contours of the shuffled dataset in gold. The best-fit position of the Gaussian models is depicted by the dashed circle in the respective colour. Right: Significance distributions of the emission in the region after the application of the Gaussian model for both ON-OFF lists.

for the data released by the Collaboration are listed).

These restrictions, however, can be overcome when a joint-modeling approach is used. For this, LAT data from October 2008 to January 2025 was used. The diffuse class was used to achieve the best background rejection. The IRFs from the third version of Pass 8, `P8R3_SOURCE_V3` (Ajello et al., 2021) were used and all sources in the ROI were described using their respective models from the 12-year 4FGL source catalogue (Abdollahi et al., 2020). The ROI is chosen as a 15° degree region around the nominal position of the pulsar. A binsize of 0.025° and 8 energy bins per decade with logarithmic spacing were used.

The energy range analysed in this work is 10 GeV to 500 GeV. These thresholds were set to exclude significant emission from the pulsar itself and still stay within the energy range for which the background model has been computed, without any extrapolation. To account for isotropic background emission, the model `iso_P8R3_SOURCE_V3_v1.txt` was used.

To account for the diffuse emission, the newest version of the Interstellar Emission Model (`gll_iem_v07.fits`) was slightly modified. The LAT Collaboration has released the Interstellar Emission Model with the caveat that it is likely that structures with an extension of more than 2° will be absorbed into the background due to their iterative fitting process of the patch models (Ackermann et al., 2012). Since the emission observed in the H.E.S.S. data is likely more extended than 2°, a background model in which the patch models are removed was created by the *Fermi*-LAT member Dmitry Malyshev and provided for this work. The data was then exported to `gammapy`, since a spectromorphological analysis is not possible using the analysis tools provided by the *Fermi*-LAT collaboration.

For the estimation of the normalisation and the spectral tilt following Equation (43) of both background models, a circular region with a radius 4 ° has been excluded around the nominal pulsar position. Additionally, excluded was the region around the

Table 6.7: Best-fit parameters for the background fit of the *Fermi*-LAT dataset for the Interstellar Emission Model (IEM) and the isotropic background model.

	Φ	δ
IEM	$[1.15 \pm 0.03]$	$[0.05 \pm 7.67] \cdot 10^{-6}$
isotropic	$[0.88 \pm 0.20]$	$[0.01 \pm 5.87] \cdot 10^{-4}$

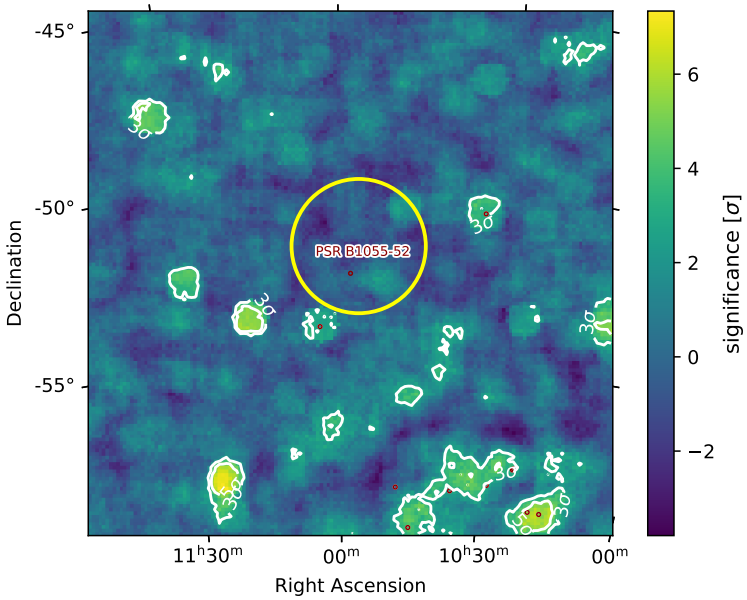

Figure 6.17: Li&Ma (1983) significance map of the ROI around PSR B1055−52 as seen by *Fermi*-LAT. The best-fit morphology derived from an analysis of the H.E.S.S. data is indicated by the yellow circle.

stellar cluster Westerlund 2, from which significant emission has been detected before (Yang et al., 2018), as well as three point sources. The exclusion regions can be found in Appendix C.4. The background models are then fit to the ROI outside of the exclusion regions, and the best-fit values for both background models are shown in Table 6.7. For the subsequent analysis, the background models are fixed to these best-fit values.

A Li&Ma (1983) significance map of the region is shown in Figure 6.17. Additionally, the best-fit position and extension derived in the H.E.S.S. analysis are displayed. No significant emission around PSR B1055−52 can be observed. Nevertheless, a source model is fitted to the region, with a power law as spectral model. For the morphology of the model, a Gaussian source with the best-fit parameters derived in the H.E.S.S. analysis and presented in Table 6.3 is used. The significance of the model is found to be $1.67\,\sigma$, and no SED point with a significance above $2\,\sigma$ can be derived.

A second analysis was performed, taking the statistical uncertainties of the fit of both background models into account. For this, the statistical error on the flux normalisation of the respective background models was subtracted from the nominal value of the normalisation, and the Gaussian source model was refitted. The significance of the model fit is $3.30\,\sigma$, and despite the model itself not being significant, one significant

Table 6.8: Best-fit parameters obtained for the analysis of the LAT data, using a Gaussian model fixed to the best-fit position derived from the analysis of the H.E.S.S. data with a power law as spectral model.

	PSR B1055−52
Γ	$1.84 \pm 1.52_{\mathrm{stat}} \pm 0.002_{\mathrm{sys}}$
$\mathrm{N_0}$ $[10^{-12}\mathrm{cm^{-2}\,s^{-1}\,TeV^{-1}}]$	$4.17 \pm 19.1_{\mathrm{stat}} \pm 0.11_{\mathrm{sys}}$

SED point and some upper limits can be derived. The SED points are calculated with an energy binning of 4 bins per decade. The best-fit parameters of the power-law model can be seen in Table 6.8. It, however, needs to be stressed here that the results and SED derived from this analysis, as well as the joint analysis of this dataset and the H.E.S.S. data described in this section, can only be interpreted as upper limits due to the decreased background flux normalisation.

The SED compared to the SED points derived in the analysis of the H.E.S.S. data for Dataset 1 and Dataset 2 can be seen in Figure 6.18. The last energy bin in which an SED point was derived for the *Fermi*-LAT data overlaps with the first energy bin in which an SED point was derived in the H.E.S.S. dataset. The upper limit from the LAT data is consistent with the shape of all SED points of Dataset 1, and with all but the first SED point derived from Dataset 2. It does however need to be iterated here that the systematics on the background model of the *Fermi*-LAT data are not known, the energy flux derived in the first bin of Dataset 2 should therefore not be interpreted as wrong, and a more conclusive answer on whether these results are in tension with each other can only be made once a realistic evaluation of the systematic uncertainty on the LAT background model becomes public, or once a background model template for data including CT 5 becomes available and the H.E.S.S. data analysis can be extended to lower energies.

To solidify these results and leverage the combined statistics of both instruments, a source model was fit jointly to the data. Two fits were performed using the LAT data together with either Dataset 1 or Dataset 2 separately. For the joint-fit of the LAT data and Dataset 2, the centre of gravity estimated in the H.E.S.S.-only analysis was used as centre of a Gaussian source model and fixed for the fit. As spectral model, a simple power law, as well as a logarithmic parabola model, a broken power law, and an exponential cutoff power law were tested. For the joint-fit of the LAT data and Dataset 1, the position of the Gaussian is included as a fit parameter.

The significance of each model for the joint modelling can be seen in Table 6.9. The best-fit parameters of the respective models can be seen in Table 6.10 for the logarithmic parabola model and in Appendix C.5 for the other three models. For the joint fit with Dataset 2, the highest combined significance between both datasets is found for the exponential cutoff power-law model. For the joint-fit with Dataset 1, the broken power law yields the highest model significance for the LAT and H.E.S.S. data. However, no valid minimum in the parameter space could be found during the fit.

It was, therefore, decided to retain the exponential cutoff power-law model, which shows the second-highest significance for both datasets, as the best choice for the emission. The SED for the exponential cutoff power-law model jointly fit to the LAT

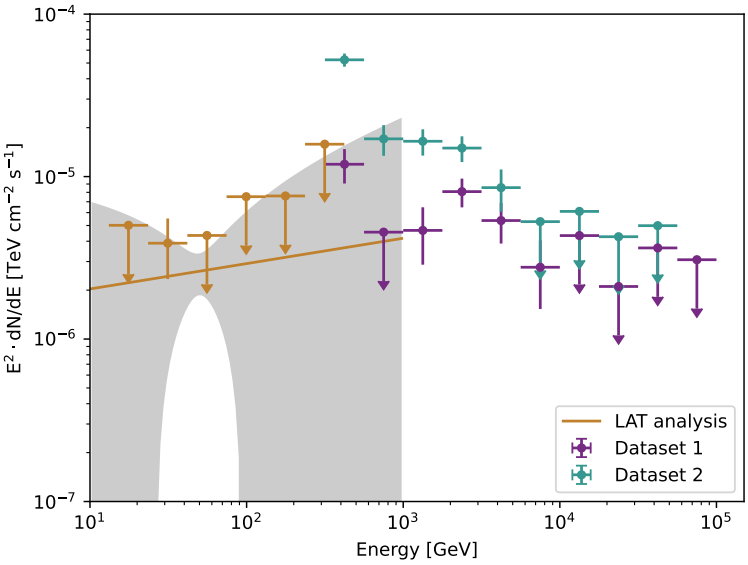

Figure 6.18: SED of the source model for the extended emission around PSR B1055−52 derived from a separate analysis of the *Fermi*-LAT and H.E.S.S. data.

data and Dataset 2 can be seen in the left panel of Figure 6.19, the SED of the fit of the logarithmic parabola model to the LAT data and Dataset 1 can be seen in the right panel of Figure 6.19. The SED of the other models can be found in Appendix C.5

In the visual comparison of the SED from the analysis of the separate datasets shown in Figure 6.18, the SED point in the first energy bin of Dataset 1 is in agreement with the upper limit derived in the last energy bin of the LAT data. In the joint analysis of the datasets, neither of the models is able to explain the energy flux in the first energy bin for both Dataset 1 and Dataset 2. This might indicate the presence of a threshold effect in the H.E.S.S. data or a too high estimation of the background in the *Fermi*-LAT data. However, without information about the systematic uncertainty of the *Fermi*-LAT background model or an analysis of the H.E.S.s. data including CT 5 no conclusions can be drawn from this mismatch.

Except the disagreement in the energy bin at around 300 GeV, the SED agree well with the derived model and the emission can be detected with a significance above $3\,\sigma$ in the fit including Dataset 2, and above $5\,\sigma$ in the fit including Dataset 1. From this, it can be inferred that even if large systematic uncertainties need to be considered, the LAT data supports the detection of a highly extended source around PSR B1055−52.

6.8 Electron Diffusion Model

The ROI covered by the observations conducted on the region around PSR B1055−52 contains only two known physical objects, PSR B1055−52 and PSR J1103−5403, located at R.A. = 165.8875° and Dec = −54.0619°. The latter is an old millisecond pulsar, with an age of $\tau_c = 1.46 \cdot 10^7$ kyr and a period of $P = 3.39$ ms. Its spin-down power is estimated to $\dot{E} = 3.7 \cdot 10^{33}$ erg/s. With such a low spin-down power, it is unlikely that the pulsar contributes to the production of VHE γ-ray photons. The position of both pulsars is shown on a significance map computed from Dataset 2 in Figure 6.20.

Table 6.9: Model significance values for the joint fit of different spectral models to the LAT data and either Dataset 1 or Dataset 2. As spatial model, a Gaussian centred on the centre of gravity of the emission in Dataset 2 was used. The spectral models used were a simple power law (PL), a logarithmic parabola model (LP), a broken power law (BPL) as well as an exponential cutoff power law (EPL).

	Dataset 2		Dataset 1	
	LAT	H.E.S.S.	LAT	H.E.S.S.
PL	$2.58\,\sigma$	$6.01\,\sigma$	$0.39\,\sigma$	$3.87\,\sigma$
LP	$1.38\,\sigma$	$12.29\,\sigma$	$5.74\,\sigma$	$6.34\,\sigma$
BPL	$0.13\,\sigma$	$13.40\,\sigma$	$6.30\,\sigma$	$6.60\,\sigma$
EPL	$3.11\,\sigma$	$11.87\,\sigma$	$5.99\,\sigma$	$6.59\,\sigma$

Table 6.10: Best-fit parameters derived from the joint model using the *Fermi*-LAT data and the two different H.E.S.S. datasets. For the joint fit of the LAT data and Dataset 2, the position of the Gaussian model was fixed to the centre of gravity of the emission, for the joint model involving Dataset 1 the position of the Gaussian model was included as a fit parameter. As spectral model an exponential cutoff power law was used.

	Dataset 1	Dataset 2
Γ	1.46 ± 0.09	0.80 ± 0.18
N_0 $[10^{-11}\mathrm{cm}^{-2}\,\mathrm{s}^{-1}\,\mathrm{TeV}^{-1}]$	6.41 ± 2.10	14.80 ± 7.60
λ $[\mathrm{TeV}^{-1}]$	0.25 ± 0.06	0.94 ± 0.17
R.A. $[^\circ]$	162.50 ± 0.01	164.12
Dec. $[^\circ]$	-54.45 ± 0.01	-51.67
σ_M $[^\circ]$	4.78 ± 0.96	3.46 ± 0.76

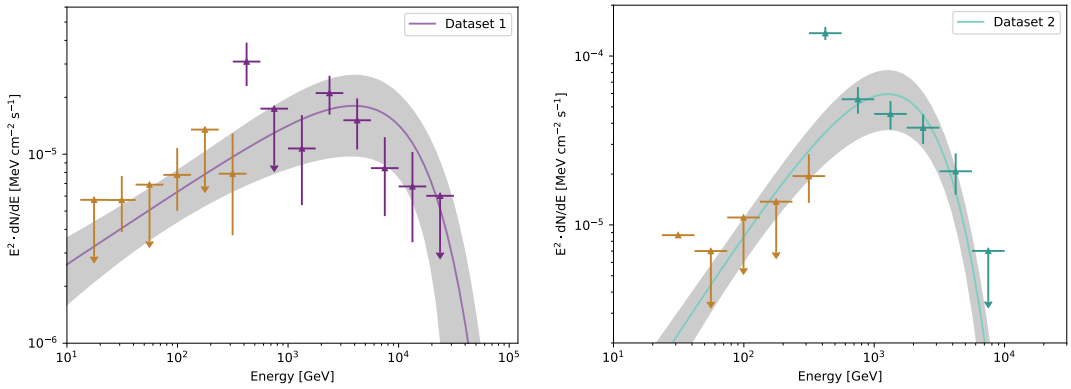

Figure 6.19: SED derived from a joint fit of the LAT data with Dataset 1 (on the left) and Dataset 2 (on the right) for an exponential cutoff power-law spectral model. The exponential cutoff power-law spectral model describes all but the first SED point in the H.E.S.S. data well. A possible reason for the divergence of the model from the SED point could be threshold effects in the H.E.S.S. data or an overestimation of the background in the *Fermi*-LAT data.

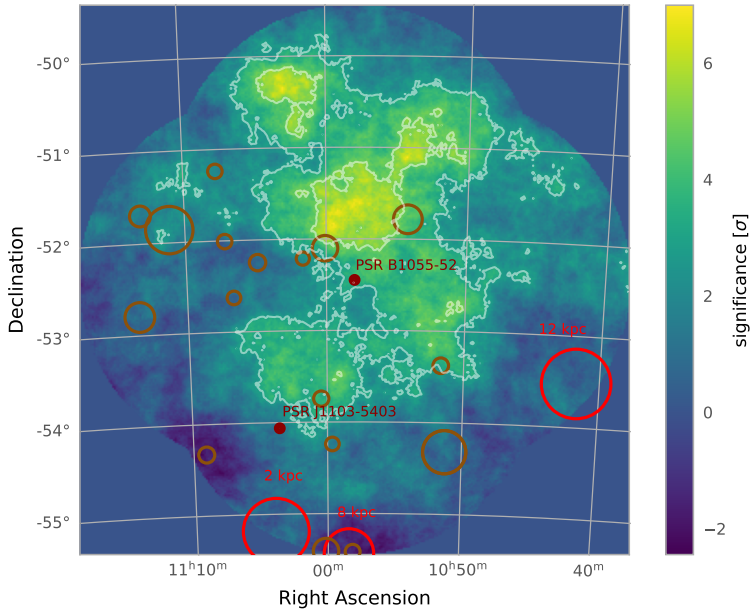

Figure 6.20: Li&Ma (1983) significance map of Dataset 2 computed with a 0.5° correlation radius. The $5\,\sigma$ and $8\,\sigma$ contours are shown in white. The position of PSR J1103−5403 is indicated, and the locations of the molecular clouds present in the region taken from Miville-Deschênes et al. (2017) and Dawson et al. (2008) are shown as circles.

Additionally shown in Figure 6.20 is the position and estimated extension of molecular clouds in the region. The molecular clouds shown in red are taken from Miville-Deschênes et al. (2017), with their respective distance estimate shown in the Figure. The molecular clouds shown in brown are taken from a NANTEN survey of ^{12}CO and ^{13}Co clouds in the Carina Flare Supershell (Dawson et al., 2008). No distance estimate for these clouds is provided.

None of the observed molecular clouds in the region can account for the full extent of the detected γ-ray emission. While some clouds overlap spatially with portions of the emission, the uniformity of its spectral properties suggests that cosmic ray interactions within these clouds are unlikely to be the source of any significant fraction of the emission.

In the absence of any other physical sources within the ROI, and considering the uniformity of the emission and the energy dependence of its extension, it is reasonable to assume that the extended γ-ray emission has a leptonic origin, with PSR B1055−52 as its source.

To further classify the nature of this emission, a distinction between the categorization as a PWN or pulsar halo can be attempted. These two structures are primarily differentiated by the energy density ϵ_e of relativistic electrons, which governs their propagation and confinement.

In a PWN, the relativistic electrons are confined within a strongly magnetised wind bubble. This entrapment of electrons and positrons, combined with a continuous injection of leptons from the pulsar wind into the region, leads to a high energy density with $\epsilon_e > \epsilon_{\mathrm{ISM}}$.

In pulsar halos, the surrounding magnetic fields are too weak to confine the electrons, allowing them to diffuse slowly outward. As they propagate, the leptons experience significant radiative losses, leading to an energy density lower than the density of leptons in the ISM, $\epsilon_e \ll \epsilon_{\mathrm{ISM}}$. Following the population study presented in Giacinti et al. (2020), a γ-ray structure around a pulsar is classified as a pulsar halo when $\epsilon_e < 0.1\,\mathrm{eV/cm^3}$.

Using Equation (69), the energy density for the extended emission can be estimated from the spin-down power $\dot{E} = 3.0 \cdot 10^{34}\,\mathrm{erg/s}$, the characteristic age $\tau_c = 535\,\mathrm{kyr}$ and the radius of the region containing the γ-ray emission R_1. R_1 is estimated using the $3\,\sigma$ containment radius of the Gaussian $3\sigma_M$ fitted to Dataset 2 and the distance d to the source as $R_1 = 3\sigma_M \cdot d$.

The distance to PSR B1055−52 is, however, not well constrained. A distance estimate based on the dispersion measure (DM $= 29.69 \pm 0.01$, (Petroff et al., 2013)) finds $d = (0.75 \pm 0.15)\,\mathrm{kpc}$ for the electron density model presented in Cordes and Lazio (2002), while the electron density model from Taylor and Cordes (1993) suggests a distance of 1.53 kpc. More recently, an investigation into the contributions of thermal components to the multiwavelength spectrum suggests a distance of $350 \pm 150\,\mathrm{pc}$ (Mignani et al., 2010a) while a refined electron density model presented in Yao et al. (2017) results in a distance estimate of 92 pc (Posselt et al., 2023).

For further analysis, the distance estimate from the thermal contributions of $d = 350\,\mathrm{pc}$, as well as the distance estimates from the two newest electron density models ($d = 92\,\mathrm{pc}$ and $d = 750\,\mathrm{pc}$) were used. The energy density for the emission is derived for all three distances to $\epsilon_{\mathrm{e},\,92} = (0.35 \pm 0.11)\,\mathrm{eV/cm^3}$, $\epsilon_{\mathrm{e},\,350} = (5.89 \pm 1.82) \cdot 10^{-2}\,\mathrm{eV/cm^3}$, $\epsilon_{\mathrm{e},\,750} = (5.99 \pm 1.86) \cdot 10^{-3}\,\mathrm{eV/cm^3}$.

Table 6.11: Diffusion coefficient at an electron energy of 100 TeV for Kolmogorov and Kraichnan diffusion.

	$D_0(\delta = 0.33)$ $[10^{27}\,\mathrm{cm}^2/\mathrm{s}]$	$D_0(\delta = 0.5)$ $[10^{27}\,\mathrm{cm}^2/\mathrm{s}]$
$d = 92\,\mathrm{pc}$	0.11	0.23
$d = 350\,\mathrm{pc}$	1.60	3.49
$d = 750\,\mathrm{pc}$	7.33	16.04

Except for the energy density assuming a distance of 92 pc, all energy density values are below the expected value for the ISM. From this, as well as taking into account that the extension of the source is likely to be only a lower limit due to the lack of a large enough observation region, it can be concluded that the region is most likely not dominated by strong magnetic fields of the pulsar, and a diffusive outflow of leptons is happening.

A low energy density is expected for pulsar halos and was already observed in the pulsar halo around the Geminga and Monogem pulsars. A rather surprising finding in the same halo was that despite the low energy density, the diffusion in the region seems to be suppressed with respect to the diffusion expected for the ISM (Abeysekara et al., 2017b). The diffusion coefficient in the pulsar halo around Geminga and Monogem has been estimated to $(4.5 \pm 1.2) \cdot 10^{27}\,\mathrm{cm}^2/\mathrm{s}$ at an electron energy of 100 TeV and a diffusion index of $\delta = 0.33$ using HAWC data (Abeysekara et al., 2017b), and $7.5^{1.5}_{1.2} \cdot 10^{27}\,\mathrm{cm}^2/\mathrm{s}$ for a diffusion index of $\delta = 1.0$ using H.E.S.S. data (H.E.S.S. Collaboration et al., 2023). The diffusion coefficient at the same electron energy has been estimated to $4.5 \cdot 10^{29}\,\mathrm{cm}^2/\mathrm{s}$ for the ISM (Strong and Moskalenko, 1998), a factor 100 larger.

To examine if this behaviour can also be observed for the extended γ-ray emission around PSR B1055−52, the diffusion coefficient in the region is calculated from the observed extension of the γ-ray emission, following Equation (68). For the diffusion index δ, two different regimes of diffusion have been assumed. Kolmogorov diffusion, with $\delta = 1/3$, is usually assumed to describe the ISM under normal conditions (Kolmogorov, 1991). Kraichnan diffusion with $\delta = 0.5$ describes weaker turbulence dominated by magnetohydrodynamic waves (Kraichnan, 1965).

The diffusion coefficients at an electron energy of 100 TeV for both diffusion indices as well as all three distance estimates can be seen in Table 6.11. The reference electron energy was chosen to allow a direct comparison with the diffusion coefficient derived for the pulsar halo around the Geminga pulsar. This study can confirm that the γ-ray emission around PSR B1055−52 also shows diffusion, which is suppressed in comparison to the ISM, with values comparable to the diffusion coefficient estimated for the Geminga and Monogem halo assuming a distance of 350 pc and slightly higher if the distance to PSR B1055−52 is larger. A visual comparison between the diffusion coefficient of the ISM taken from Strong and Moskalenko (1998), the diffusion coefficient for the Geminga halo derived in H.E.S.S. Collaboration et al. (2023) and Abeysekara et al. (2017b), and the diffusion coefficients derived in the work can be seen in Figure 6.21.

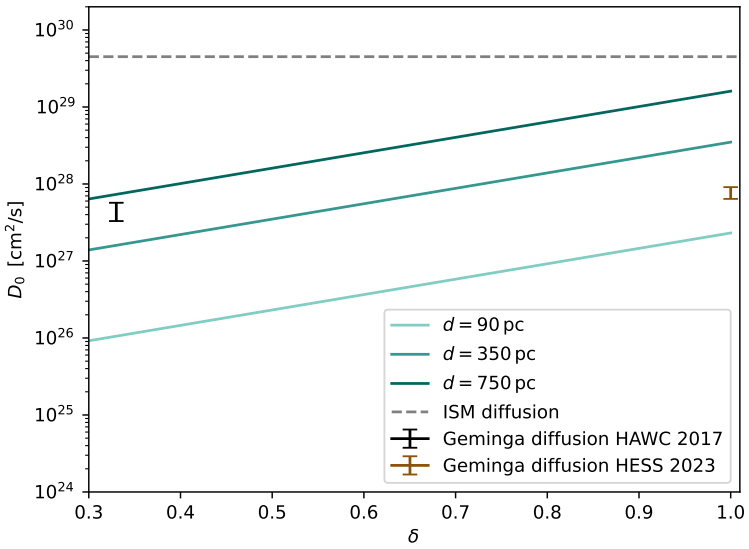

Figure 6.21: Diffusion coefficient for the pulsar halo around PSR B1055−52, estimated from the angular size of the γ-ray emission derived from Dataset 2 using Equation (68) for the three distances. Additionally shown are the diffusion coefficient of the ISM (Strong and Moskalenko, 1998) and the diffusion coefficient estimated for the Geminga halo in H.E.S.S. Collaboration et al. (2023) and Abeysekara et al. (2017b). The reference electron energy for all coefficients is 100 TeV.

To estimate the properties of the electrons responsible for the observed γ-ray emission, a diffusion model was used. The model itself was provided for this work and was already used to derive the properties of the electron spectrum in an analysis of H.E.S.S. data around the Geminga halo presented in H.E.S.S. Collaboration et al. (2023). A thorough definition of the model can be found in H.E.S.S. Collaboration et al. (2023), while only the key points are given below.

The model assumes a point-like source that continuously injects electrons into its surroundings, which then diffuse outwards and cool. The electron density $N(E, r, t)$ is derived as:

$$\partial_t N(E, r, t) = D(E)\Delta N(E, r, t) - \partial_E(b(E)N(E, r, t)) + Q(E, t)\delta(r - r_s) \quad (75)$$

with $D(E)$ the diffusion coefficient and $b(E)$ the energy loss rate. The pulsar position $r_s(t) = v_T(T^* - t)$ is estimated from the proper motion of the pulsar v_T and the current age of the pulsar T^*. The rate $Q(E, t)$ of electrons produced for each pulsar energy E depends on the assumed injection spectrum of the pulsar. For this, an exponential cutoff power law is chosen, which results in an electron rate of:

$$Q(E, t) = Q_0 \left(1 + \frac{t}{\tau_0}\right)^{-\frac{(n+1)}{(n-1)}} \left(\frac{E}{E_0}\right)^{-\alpha} \exp\left(-\frac{E}{E_c}\right), \quad (76)$$

where n is the pulsar braking index, τ_0 the characteristic age of the pulsar, E_c the cutoff of the power law and Q_0 a normalisation factor.

The energy loss was approximated following derivations from Delahaye et al. (2010). Since the dominant energy loss mechanisms for relativistic leptons in the GeV-TeV

Table 6.12: Pulsar parameters used as input values for the computation of the diffusion model.

parameter	value
τ_c [kyr]	535
$\dot{E}$ [10^{34} erg/s]	3.0
v_T [mas/yr]	42
P [1/s]	0.013
ambient B-field [μG]	1.0
δ	0.33

energy range are synchrotron radiation and IC scattering, only energy losses from these two processes were considered.

The strength of the IC losses is strongly dependent on the electron energy and can be classified into two key regimes: In the Thomson regime ($\alpha \ll 1$, with $\alpha = (\gamma k_B T)/m_e$), leptons lose energy gradually in many scattering events. In the Klein-Nishina regime ($\alpha \gg 1$), the electrons and positrons lose most of their energy in one interaction. The target fields for the Inverse Compton scattering are photons from the cosmic microwave background (CMB), dust (IR), and star light (optical). For the CMB photons, the canonical temperature of $T = 2.7\,\mathrm{K}$ and an energy density of $0.26\,\mathrm{eV/cm^3}$ were assumed (Navas et al., 2020).

The energy density of the IR and optical photon fields were estimated using a model presented in Popescu and Tuffs (2013). This model estimates the energy density in a given region by comparing the intrinsic light emission of known stellar objects to the observed light to estimate the absorption and scattering on the ambient medium. For the region around PSR B1055−52, the energy density is estimated to be $0.85\,\mathrm{eV/cm^3}$, with a black-body temperature of $T = 3.66\,\mathrm{K}$.

From these assumptions, the diffusion radius λ can be estimated as:

$$\lambda^2 = 4 \int_E^{E_s} \mathrm{d}E' \frac{D(E')}{b(E')}\,, \tag{77}$$

with $E_s(E, t_0, t)$ the energy of an electron produced at time t_0 and observed at time t with energy E (H.E.S.S. Collaboration et al., 2023). At low energies, the influence of cooling on the electrons is insignificant, and λ is only influenced by the properties of the diffusion. At higher energies, the cooling effects become significant, and λ is limited by the cooling time of the electrons. This results in a peak diffusion radius at which the cooling time of the electrons is equal to the age of the pulsar.

The properties assumed for the diffusion model are given in Table 6.12. Since no X-ray observations of a pulsar wind nebula around PSR B1055−52 have been made yet, the synchrotron part of the spectrum cannot be constrained, and an ISM typical value of $B = 3\,\mu\mathrm{G}$ is chosen (Grasso and Rubinstein, 2001). For the particle transport, a Kolmogorov diffusion behaviour is assumed.

In order to estimate the electron spectrum, which would result in γ-ray emission that can describe the SED derived from the joint models best, a range of different

parameters was tested. For each parameter combination, the electron injection spectrum was computed and translated into a photon spectrum using the Naima package (Zabalza, 2015). Then, a χ^2 between the derived spectrum and the SED was calculated. The model with the smallest χ^2 is then retained. Due to the correlation of the parameters of the diffusion model, the large uncertainty of the background rate in the analysis cannot be directly propagated into the diffusion model. A fit of the SED derived from the diffusion model and the SED derived from the joint-modeling presented above is not possible. This is due to the large number of free parameters in the model and the absence of multiwavelength data in the region. It is, therefore, decided to conduct a parameter scan to find the parameter combination that best describes the SED derived from the two joint models presented above. In order to propagate the large uncertainty of the distance estimation into the model, this scan is conducted for both datasets for a distance of 92 pc and 350 pc.

The free parameters of the diffusion model are the initial period of the pulsar P_0, the braking index n, the injection index of the electrons Γ_e, the cutoff of the injection spectrum E_c and the γ-ray efficiency η_γ of the conversion of electron energy into γ-rays. The tested parameter ranges, as well as the best description derived from the parameter scan, can be seen in Table 6.13.

The minimal χ^2 that can be achieved in the tested parameter range is also given in the respective column in Table 6.13 for each model. The model for which the smallest χ^2 could be found, compared to the SED, can be seen in Figure 6.22 for the joint fit involving Dataset 2, and in Figure 6.23 for the joint fit involving Dataset 1.

The parameter scan yields that in both cases, the emission is almost equally well described assuming either of the two distances. For both datasets, a distance of 350 pc is marginally preferred, does however infer a γ-efficiency higher than 10%. Previous studies have estimated a γ-ray efficiency of $\sim 1\% - 5\%$ for several pulsar systems, among those also the halo around the Geminga pulsar (Fang et al., 2022; Di Mauro et al., 2019). An efficiency of 10%, or higher, as predicted by the model derived from the comparison to the SED, would point to a very dense environment in which the leptons are cooled very effectively. On the other hand, an efficiency of 1.5% and 2.2%, as estimated for a distance of 92 pc, suggests that only a small fraction of electrons undergoes IC scattering. It is, therefore, likely that the true distance to PSR B1055−52 lies somewhere between 92 pc and 350 pc.

The initial period P_0 derived from the model is in both cases similar to the current period of $P = 0.197$ s (Manchester et al., 2005), indicating that the pulsar has not slowed down considerably. This is in agreement with the small period derivative observed from PSR B1055−52 of $\dot{P} = 5.83870 \cdot 10^{-15}$ s/s, does, however, imply that PSR B1055−52 was born with a rather slow initial spin-down period.

A study presented in Bucciantini et al. (2010) found that a number of PWNe can be well described by employing a broken power law injection model, with an injection index exceeding 2 in the γ-ray energy range. In contrast, numerical simulations of older systems suggest that the injection of electrons in bow-shock PWNe happens under a much harder spectral index of around 1 (Bykov et al., 2017). The injection index of the electrons derived for the SED of the fit to Dataset 1 and the LAT data is estimated to $\Gamma_e = 1.80^{+0.03}_{-0.05}$. This is harder than the values derived for the Geminga halo presented in Abeysekara et al. (2017b) but remains significantly above the lower limit expected for bow-shock PWNe. In contrast, the injection index estimated for the SED from the joint

Table 6.13: Free parameters of the diffusion model, with their tested parameter range, as well as the best description for Dataset 1 and Dataset 2. Additionally given are the $1\,\sigma$ uncertainties for all free parameters and the χ^2 value for the best parameter combination.

	parameter range	Dataset 1		Dataset 2	
distance [kpc]	$--$	0.09	0.35	0.09	0.35
D_0 [$10^{27}\,\mathrm{cm}^2/\mathrm{s}$]	$--$	0.11	1.60	0.11	1.60
χ^2	$--$	9.10	8.73	70.60	70.85
η_γ	$[0.001 - 0.500]$	$0.015^{+0.003}_{-0.002}$	$0.300^{+0.037}_{-0.037}$	$0.022^{+0.002}_{-0.002}$	$0.380^{+0.032}_{-0.025}$
P_0 [1/s]	$[0.100 - 0.195]$	$0.193^{+0.001}_{-0.001}$		$0.194^{+0.002}_{-0.002}$	
n	$[1.0 - 30]$	$1.5^{+13.5}_{-0.5}$		$2.5^{+10.5}_{-0.5}$	
Γ_e	$[1.0 - 3.0]$	$1.80^{+0.03}_{-0.05}$		$1.00^{+0.06}_{-0.00}$	
E_c [TeV]	$[1 - 100]$	51^{+14}_{-11}		12^{+1}_{-2}	

fit of Dataset 2 and the LAT data is $\Gamma_e = 1.00^{+0.06}_{-0.00}$. This result is in tension with the expectations for a pulsar halo. However, this parameter is predominantly influenced by the Fermi-LAT SED, and the difference in the shape of these SED from both joint-fits suggests that large systematic uncertainties need to be taken into account.

For a pulsar that is slowed purely by its dipole radiation, a braking index of $n = 3$ is expected. A study presented in Tong and Kou (2017) proposes that the braking index of young pulsars can deviate from this value since energy loss from the pulsar wind needs to be taken into account as well. Due to internal torques and dissipation effects, the magnetic axis aligns more closely with the rotation axis during the evolution of the pulsar. This reduces the energy loss due to dipole radiation, and the pulsar wind losses start to dominate. Following this model, a braking index of $1 < n < 3$ would be expected for PSR B1055−52. The derived parameter of the diffusion model fits this theory well for both datasets, the model does, however, not constrain this parameter, as seen by the large statistical uncertainties.

The diffusion radius, estimated from the parameter combination with the smallest χ^2 of the fit to Dataset 1, can be seen in Figure 6.24. From the diffusion model, a source extension which peaks at 66 pc at an electron energy of 0.57 TeV is estimated. For an electron energy of 4 TeV, the γ-ray emission, observable by both *Fermi*-LAT and H.E.S.S., is predicted to extend over 45 pc. Assuming a distance of 350 pc, this suggests that the emission would extend over 7.36° at an electron energy of 4 TeV. At a distance of 92 pc, the estimated extension of the emission at an electron energy of 4 TeV is 11.51°. The estimated diffusion radius suggests that the emission extends beyond the region observed by H.E.S.S., and the extension derived from Dataset 2 is likely closer to the true extension of the γ-ray emission. However, without further data in different wavelengths, a further reduction of the systematic uncertainties in either the *Fermi*-LAT or H.E.S.S. data, or observations of a larger region in the TeV energy range,

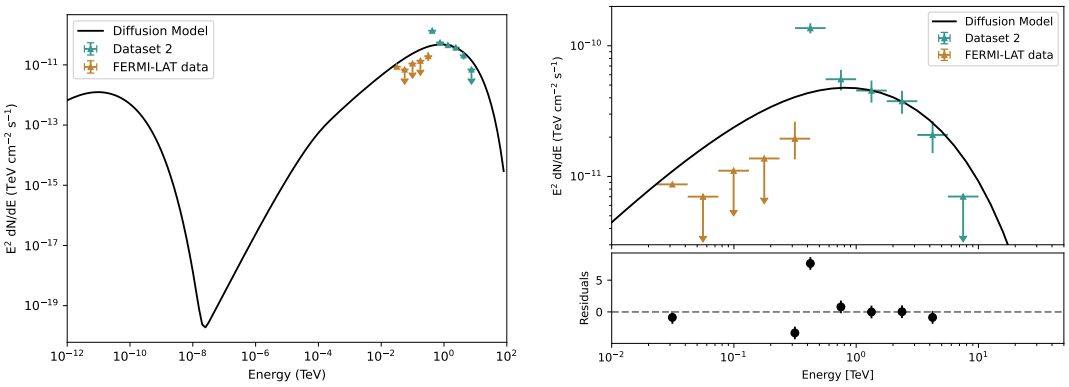

Figure 6.22: Comparison of the model SED derived from the diffusion model and the SED derived from joint analysis of the *Fermi*-LAT data and Dataset 2. The distance assumed for this model is 350 pc. Left: Whole energy range. Right: Zoom-in to the GeV-TeV energy range. The residuals shown are calculated as (data -model)/data.

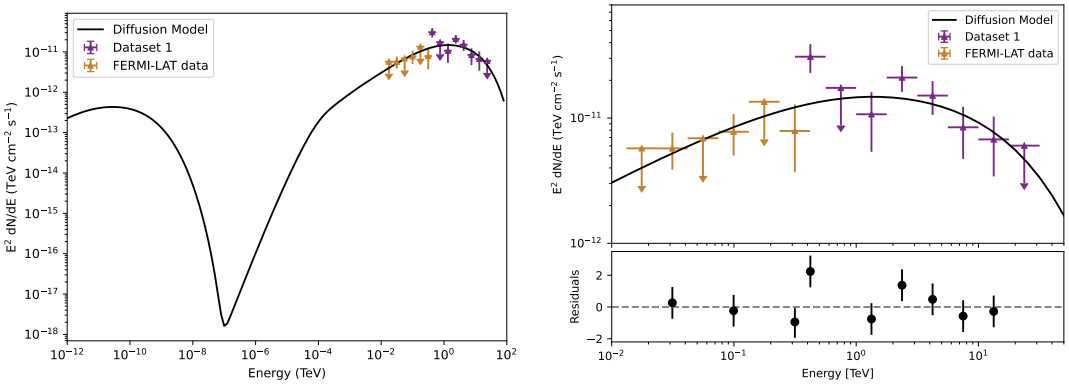

Figure 6.23: Comparison of the model SED derived from the diffusion model and the SED derived from joint analysis of the *Fermi*-LAT data and Dataset 1. The distance assumed for this model is 350 pc. Left: Whole energy range. Right: Zoom-in to the GeV-TeV energy range. The Residuals shown are calculated as (data -model)/data.

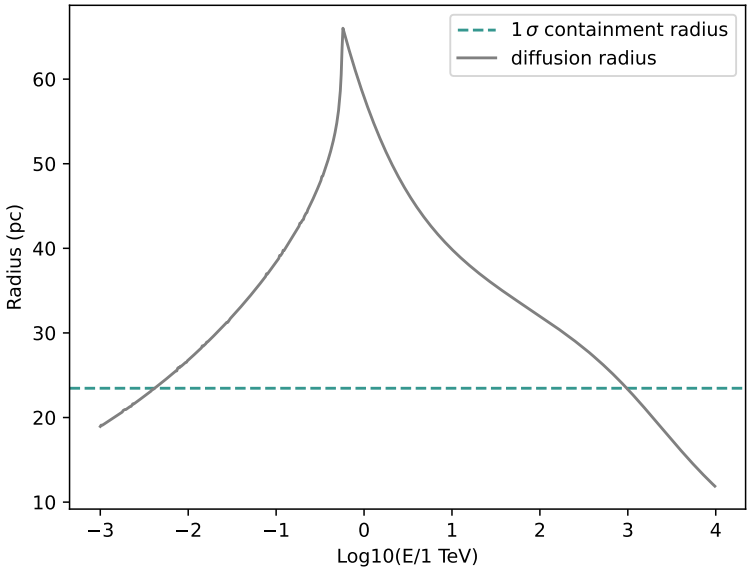

Figure 6.24: Estimated diffusion radius λ for different electron energies for the diffusion model which is best able to describe the SED derived in the joint analysis of the *Fermi*-LAT data and Dataset 1. The best-fit extension of the Gaussian model fitted to Dataset 1 is depicted in blue.

it is not possible to ascertain which of the two parameter combinations presented above is more plausible or how large the true uncertainties on the parameters are.

6.9 Discussion

The detection and analysis of γ-ray emission around older pulsars provide crucial insights into the long-term evolution of pulsar systems and the transport of high-energy electrons in the interstellar medium (ISM). Studying these evolved systems allows us to probe the interplay between particle injection, energy loss, and diffusion processes, which can lead to valuable conclusions for local ISM turbulences and, therefore, cosmic-ray propagation. The population of identified pulsar halos is, however, still rather small, which leads to large uncertainties about the general applicability of the properties derived from only a handful of TeV sources, and each new detection helps to differentiate between commonalities of the population and characteristics of the individual halos.

The middle-aged pulsar PSR B1055−52 has long been expected to be the source of such a TeV pulsar halo (Romero, 1998; Orusa et al., 2025; Fang, 2022b), however the detection of these extended structures with IACTs is challenging due to the large extension of the TeV emission and the lack of γ-ray free regions from which the background contamination can be estimated. Such detections are therefore mostly done using wide field of view survey instruments like HAWC or LHAASO. Since PSR B1055−52 is located on the southern hemisphere, it is currently only observable by the IACT array H.E.S.S., with no observations of γ-ray survey instruments available yet.

To facilitate the analysis of the expected largely extended γ-ray emission, a novel background estimation technique combining a classical ON-OFF background estimation

with a three-dimensional background model template was developed. This method, as well as the direct application of the background model template, was then used to estimate the background contamination in the data around PSR B1055−52.

With these two techniques, this work is able to establish a significant detection of extended TeV γ-ray emission around PSR B1055−52. Despite large differences in source morphology and spectrum between the two background estimation methods, a lower limit of a detection significance of $6.31\,\sigma$ can be given. This work also finds that it is likely that the emission extends further than the observed 6° region, and the source extension of $\sigma_M = (1.92 \pm 0.23_{\mathrm{stat}} \pm 0.72_{\mathrm{sys}})^\circ$ should be interpreted as a lower limit. Across this extension, no significant spectral variations are found, supporting the hypothesis that a single source is responsible for the emission.

In addition to the analysis of the TeV γ-ray data, an analysis of *Fermi*-LAT data is performed. While no significant emission can be detected in this analysis, an SED compatible with the results from H.E.S.S. can be derived, further solidifying the detection of the emission.

An estimation of the energy density in the region suggests that the leptons are not confined by strong magnetic fields to a small region around the pulsar and freely diffuse into the ISM. From this it can be concluded that the extended γ-ray emission around PSR B1055−52 is likely a pulsar halo.

Moreover, the diffusion coefficient derived from the halo extent is significantly lower than the typical ISM diffusion coefficient, with $0.11 \cdot 10^{27}\mathrm{cm}^2\mathrm{s}$ at $E = 100\,\mathrm{TeV}$ and an assumed distance of 0.092 kpc. While diffusion is seen as the main transport mechanism in the magnetic bubble of a PWN (Tang and Chevalier, 2012), the older, more evolved systems of pulsar halos are expected to trace the diffusion in the ISM. A similar result, however, has already been derived from the pulsar halo around the Geminga and Monogem pulsars, which suggests that this might not be a unique property of a single system but may be a general property of the population of pulsar halos. A reason for this could be that the influence of the pulsar creates a region of slow diffusion in its vicinity, in which the accelerated electrons still largely influence the ISM. If further observations of pulsar halos confirm these results, it could have strong implications on our understanding of cosmic ray propagation and allow for pulsars as a central part of the solution of the cosmic ray positron excess observed by ASM-02 (Aguilar et al., 2013).

This work also derives the properties of the electron spectrum, which is needed to explain the observed γ-ray emission using a diffusion model. For this model, an exponential cutoff power law and Kolmogorov diffusion, which is the expected turbulence regime for the ISM, was assumed. Employing a parameter scan, it is found that a cutoff of the electron spectrum at 15 TeV/60 TeV describes the SED derived from a joint fit of the LAT data and both H.E.S.S. datasets best.

From this model, the diffusion radius at a given energy can be estimated. The parameter scan finds that the SED derived in the analysis can only be explained with a reasonable γ-ray efficiency if the distance to PSR B1055−52 is below 350 pc. At this distance, the diffusion radius, derived from the model at 0.5 TeV, amounts to 7.36°. This is far larger than the region observed by H.E.S.S..

This strongly supports the conclusion that the analysis of the currently available data of the region provides convincing evidence for the existence of a pulsar halo around

PSR B1055−52. However, to be able to draw well-founded conclusions, observations of a larger sky area, preferably by survey instruments, are needed. Only with further observations will it be possible to fully characterise the source morphology, confirm the spectral properties, and refine the diffusion model.

For this purpose, especially observations of future wide-field γ-ray detection instruments such as the upcoming detector array ALPACA (Kawashima and The ALPACA Collaboration, 2022) located in Bolivia and the planned detector array SWGO (Hinton and SWGO Collaboration, 2022) at the Atacama astronomical park in Chile will be essential to establishing a more complete picture of this region.

7 Outlook: Pulsar population study

Pulsar environments can be broadly classified into three distinct categories. In young systems, γ-ray emission is contained to a well-defined region around the pulsar. For older systems, the interaction between the pulsar wind nebula and the reverse shock of the SNR has caused leakage of relativistic leptons into the ISM, and a more extended and distorted PWN can be observed in γ-rays. In even older systems, where the pulsar has left the SNR, very extended γ-ray structures are expected to be observed since the diffusion of relativistic leptons into the ISM is no longer strongly inhibited by the pulsar (see Figure 4.5). A broad estimate of the duration for each of these stages of the evolution of pulsar systems is given in Giacinti et al. (2020). However, this evolution can be influenced by the properties of the central pulsar, and the environment the system evolves in.

This work has presented the analysis of two environments around pulsars, PSR B1055−52 and PSR J1813−1749. The analysis of the region around PSR B1055−52 revealed the presence of a pulsar halo, which is in accordance with the predictions made for a pulsar with a characteristic age of 535 kyrs. The results of the analysis of the γ-ray structure around PSR J1813−1749, however, indicate that the emission exhibits characteristics only expected from a pulsar halo, despite the young age of the central pulsar suggesting a compact bright PWN. These findings raise important questions regarding the universality of pulsar system evolution and the extent to which both environmental conditions and intrinsic pulsar properties influence the particle transport in the vicinity of the pulsar.

A first attempt to compare the population of TeV PWNe to these expectations, as well as identify other factors influencing the development of PWNe, using H.E.S.S. data was made in H.E.S.S. Collaboration et al. (2018b). This study used nine years of data on pulsars, which are distributed along the galactic plane with $|b| < 3.5°$, and data on a small number of firmly identified PWNe located at higher galactic latitudes. PWNe Candidates were selected based on two criteria: they are located within 0.5° of a source detected during the H.E.S.S. galactic plane survey (Aharonian et al., 2006c), and that they host a pulsar with a spin-down luminosity of $\dot{E}/d^2 > 10^{34}\,\mathrm{erg/s\,kpc^2}$. Applying this selection resulted in a sample of 29 PWNe for detailed analysis, while upper limits were derived for an additional 22 PWNe.

As expected, H.E.S.S. Collaboration et al. (2018b) finds that TeV emission is observed in the region around young, energetic pulsars. However, H.E.S.S. Collaboration et al. (2018b) also find that for 30% of the very energetic pulsars ($\dot{E}/d^2 > 10^{37}\,\mathrm{erg/skpc^2}$), no PWN can be detected.

Another key result is the establishment of a link between the spin-down power and the TeV γ-ray luminosity ($L \propto E^{0.59\pm0.21}$), and an observed offset between pulsar and PWN which, in many cases, cannot be explained by the proper motion of the pulsar and might be related to the interactions of the reverse shock with the PWN.

While this study already presents important results, it is also limited by the usage of only a subset of the available H.E.S.S. data around the galactic plane and a few isolated known pulsar systems at higher galactic latitudes. The work outlined in the following aims to extend the population by analysing a larger dataset, spanning over 15 years and including pulsars independent of their location.

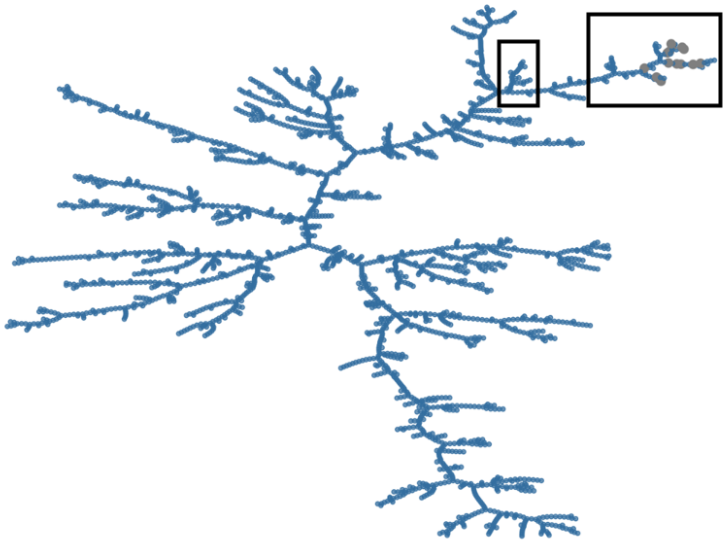

Figure 7.1: Visualization of a principal component analysis of the pulsar population. Pulsars that are known to host TeV PWNe are shown in grey. The regions of the pulsar tree used in this analysis are indicated by the black boxes. Figure adapted from García et al. (2022).

7.1 Selection of PWN candidates

As the first step, possible PWN candidates are selected from two different sources. The first source is the third *Fermi*-LAT pulsar catalogue (Smith et al., 2023b), which lists 294 pulsars. Since the pulsars listed in this catalogue all emit γ-rays in the GeV energy range, they are likely to be efficient electron-positron accelerators and thus promising candidates for PWNe observable also in the TeV energy range.

The second source is the pulsar tree presented in García et al. (2022). This pulsar tree uses principal component analysis to cluster the pulsar population based on their inherent characteristics. Using this approach is advantageous as it does not introduce a bias to the selected pulsar sample but inherently captures multi-dimensional relationships between different parameters. All pulsars for which a firm detection of a TeV PWN has been made in H.E.S.S. Collaboration et al. (2018b) are located on one branch of the pulsar tree, already indicating that a certain combination of parameters is likely to be required for powering a TeV PWN. The non-detection of a PWN for a pulsar located on the same branch can also be used to help constrain the environmental factors necessary for the formation of an extended γ-ray structure around the pulsar. A visualization of the pulsar tree is shown in Figure 7.1. The two black boxes highlight the branch on which the population of pulsars used in this analysis is located. The right black box includes the branch on which the confirmed TeV PWNe are located, which are indicated in grey. The left box shows the branch of the tree on which the pulsars hosting known TeV halos are located.

This selection yields a total of 361 PWN candidates, which are observable by H.E.S.S.. For all candidates, the ATNF catalog (Manchester et al., 2005) is queried, and their estimated distance, spin-down power, spin period, and the derivative of the spin period

are gathered. In case no distance estimate is given in the ATNF, a distance of 4 kpc is assumed. This corresponds to the mean of a Gaussian distribution, which was fitted to the distribution of the known distances of all listed ATNF pulsars, estimated using the electron density model presented in Yao et al. (2017).

7.2 Data Selection and Analysis

For the data analysis, all archival H.E.S.S. observations acquired under a zenith angle of less than 55° are considered. At even higher zenith angles, the increased amount of atmosphere that needs to be traversed until the signal reaches the detector results in the detection of a reduced number of Cherenkov photons. This would result in the inclusion of large systematic uncertainties on the background estimation and signal reconstruction.

For each pulsar, a list of observations with an offset of less than 2° from the nominal pulsar position is computed. Furthermore, the deadtime-corrected observation time for all observations, as well as for all observations passing detection quality cuts and spectral quality cuts, is derived.

In the next step, the regions around all pulsars for which data was acquired before spring 2019 were analysed. This threshold was set since observations recorded at a later date can, at the date of writing, only be analysed using a preliminary, not validated reconstruction, which is not accessible using `gammapy`.

For each pulsar, an ROI of $5° \times 5°$ centred on the pulsar position is analysed. For the analysis, all observations passing detection quality cuts (see Section 3.2.1) are used. The data is then binned into 25 energy bins from 0.1 TeV to 100 TeV, while the IRFs are binned into 49 bins in the same energy range. The background estimation was performed using the background model template described in Section 3.1.4. For the estimation of the flux normalisation and the spectral index of the background model template, all known γ-ray sources are excluded. For the pulsars in the third *Fermi*-LAT catalogue, as well as in the TeV PWNe branch of the pulsar tree, additionally a 0.4° region around the pulsar is excluded from the background fit, to avoid the absorption of potential emission into the background.

Since the extension of pulsar halos is estimated to be much larger, a region of 1.0° is excluded from the background fit for the pulsars on the halo branch. The energy threshold of each observation is determined by a threshold of 10% on the energy bias and the background peak. In this manner, a dataset was created for each of the three hardware phases of H.E.S.S.. A stacked analysis, as presented in Chapter 5, Chapter 3.1 and Chapter 6 of all observations is not possible, due to large differences of the IRFs between the different hardware phases. For this reason, only observations in the same hardware phase are stacked, and a joint maximum likelihood analysis is performed over the resulting datasets.

To account for emission from known γ-ray sources in the analysis, an updated version of the HGPS (H.E.S.S. Collaboration, 2018b) is used, which at the time of finalising this work has not yet been published. From this list, all sources that are associated with SNRs, star-forming regions, molecular clouds, or AGNs are used. The sources marked as unidentified or as associated with pulsars are not used in the analysis. Then, a Gaussian source model with a simple power law as spectral model is fit jointly to the datasets, assuming the position of the pulsar as starting value for the centre of the

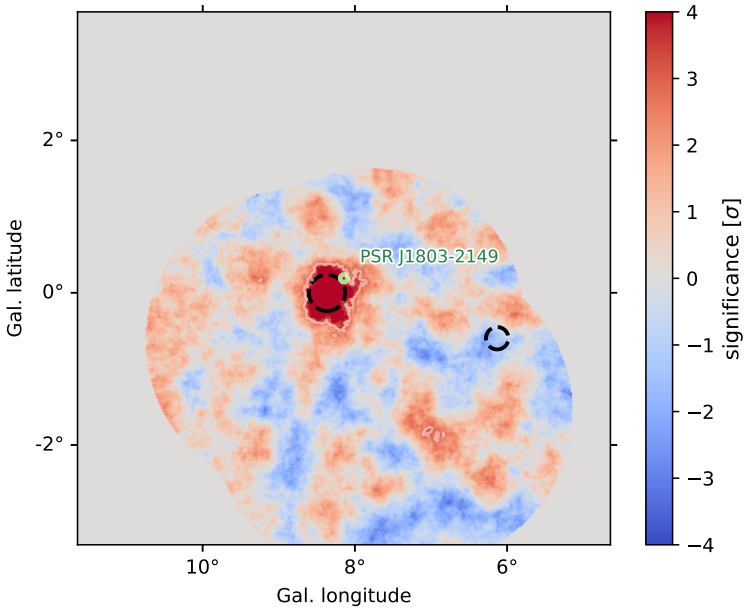

Figure 7.2: Li&Ma (1983) significance map of the region around PSR J1803−2149 derived from data acquired during H.E.S.S. Phase II. The map was computed using a correlation radius of 0.3°. The best-fit position of the Gaussian source model is shown by the black dashed circle. Additionally shown are the positions of known H.E.S.S. sources in the ROI, for which the emission has been removed using the best-fit parameters derived in the updated galactic plane survey.

Gaussian. From this fit, the significance of the model over all datasets was computed.

A significance map of the ROI around an example pulsar, PSR J1803−2149 ($\dot{E} = 6.4 \cdot 10^{35}\,\mathrm{ergs}^{-1}$, $\tau_c = 86.4\,\mathrm{kyrs}$), as observed by H.E.S.S. Phase II can be seen in Figure 7.2. For the computation of the significance map, a correlation radius of 0.3° was used. The pulsar position is indicated by the green dot, while the position of the Gaussian model and two models accounting for known H.E.S.S. sources are shown by the black dashed circles.

The distance to PSR J1803−2149 is unknown, however, assuming a distance of 4 kpc, its high $\dot{E}/d^2$ suggests that the pulsar is likely to host a PWN. In the PWN population study presented in H.E.S.S. Collaboration et al. (2018b), no extended γ-ray emission could be detected around PSR J1803−2149, this study, with increased exposure and improved analysis techniques, finds significant γ-ray emission, which can be described by a Gaussian model with a $1\,\sigma$ containment radius of $\sigma_M = 0.25°$. The detection significance of the Gaussian model is $7.5\,\sigma$

Then, the γ-ray luminosity L of each candidate PWN is calculated as:

$$L = 1.92 \times 10^{44} \frac{I}{\mathrm{cm}^{-2}\mathrm{s}^{-1}} \cdot \frac{\Gamma - 1}{\Gamma - 2} \left(1 - 10^{2-\Gamma}\right) \left(\frac{d}{\mathrm{kpc}}\right)^2 \mathrm{erg\ s}^{-1}\,, \tag{78}$$

with I the integral photon flux and Γ the best-fit spectral index of the power-law model. For sources which are detected above $3\,\sigma$, the integral photon flux is derived directly as the integral over the power-law spectral model above 1 TeV. This energy threshold is

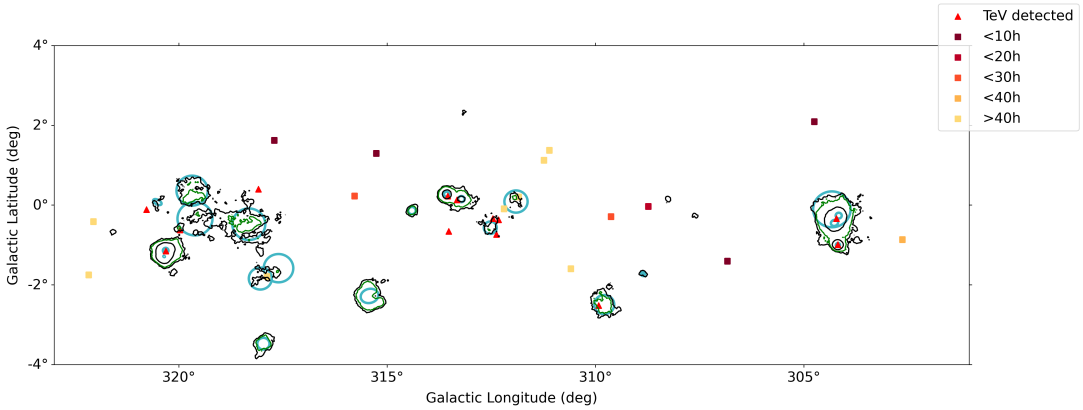

Figure 7.3: Cutout of the galactic plane. The position of the candidate pulsars are shown by the square markers. The colour of the respective marker indicates the exposure of archival H.E.S.S. data used in the analysis. Pulsars for which γ-ray emission is detected above $5\,\sigma$ are indicated by red triangles. Additionally shown are the $3\,\sigma$ and $5\,\sigma$ contours derived from the updated galactic plane survey. The best-fit morphology of the models derived in the updated galactic plane survey are shown in blue.

chosen for consistency with the previous analysis published in H.E.S.S. Collaboration et al. (2018b). For sources which are detected with less than $3\,\sigma$, an upper limit of the flux above 1 TeV is derived. From the γ-ray luminosity, the surface brightness S is derived as:

$$S = \frac{L}{4\pi R_{\mathrm{PWN}}^2}\,, \tag{79}$$

with R_{PWN} the best-fit extension of the Gaussian source model in parsec.

7.3 Results

Of the 361 pulsars in the sample, archival data is available for 288 candidates. Emission with a significance above $5\,\sigma$ can be detected at the position of 98 candidates. For an additional 89 candidates, the maximum likelihood fit of the Gaussian model converges to a valid minimum, and upper limits for the γ-ray flux are extracted. A part of the candidate population distributed along the galactic plane, together with the $3\,\sigma$ and $5\,\sigma$ contours derived from the updated galactic plane survey and the best-fit models derived in that study is shown in Figure 7.3.

Using the information derived in the analysis of the different regions around all pulsars, the most promising candidates for further observations can be identified. These candidates are then collected, and an observation proposal has been submitted to the Observing Committee of the H.E.S.S. Collaboration.

For this purpose, the candidate list is filtered to exclude certain pulsars. The first population to be excluded from the proposal are millisecond pulsars, due to the lack of TeV γ-ray emission observed in previous studies (Abeysekara et al., 2025). Additionally, pulsars for which significant emission is already detected in this analysis are excluded from the proposal, as well as pulsars which have already been observed for more than 20 hours and result in a detection with less than $2\,\sigma$. This threshold is set to maximise the chance that candidates are proposed for which a twofold increase of exposure to

Name	σ	Obs. time (h)	RA (°)	Dec (°)	$\dot{E}/d^2$ (erg/s/kpc^2)	Dist. (kpc)	Priority
PSR J1740+1000	0.00	4.71	265.11	10.00	1.53e+35	1.23	**A**
PSR J1705-1906	0.00	1.41	256.40	-19.11	1.09e+34	0.75	**A**
PSR J1741-2054	1.49	4.98	265.49	-20.90	1.05e+35	0.30	**A**
PSR J1954+2836	2.34	13.86	298.58	28.60	2.73e+35	1.96	**A**
PSR J0729-1448	0.00	0.56	112.32	-14.81	3.91e+34	2.68	**A**
PSR J1846+0919	0.26	0.88	281.61	9.33	1.46e+34	1.53	**A**
PSR J1429-5911	0.00	5.64	217.49	-59.19	2.03e+35	1.96	**B**
PSR J1447-5757	0.00	6.55	221.54	-57.92	1.16e+35	1.00	**B**
PSR J0538+2817	1.25	4.02	84.60	28.29	2.92e+34	1.30	**B**
PSR J0742-2822	0.00	6.17	115.70	-28.38	3.58e+34	2.00	**B**
PSR J0905-5127	0.02	5.57	136.47	-51.46	1.33e+34	1.33	**B**
PSR J1231-6511	0.15	2.65	187.77	-65.28	7.40e+34	1.00	**B**

Table 7.1: List of target pulsars for a H.E.S.S. observation proposal, ranked according to descending their Priority. Obs. time refers to the archival H.E.S.S. data without any further quality selection, σ the the significance of the Gaussian model fitted to the data in this analysis.

30 hours will lead to a significant detection of extended γ-ray emission. These target candidates, the exposure on the regions, as well as the significance achieved without further observations can be seen in Table 7.1.

In order to fully utilize the diversity of the pulsar population and further our understanding of the interplay between pulsars and their surroundings, the PWNe candidates are sorted into two categories based on the properties of the central pulsar and its environment. For this classification, the galactic latitude, characteristic age τ_c, magnetic field at the light cylinder B_{LC}, and the column density of the surrounding medium were used. The latter was derived by Alison Mitchell (priv. Comm.) using the HI and CO gas tracer maps presented in Mertsch and Phan (2023) and Mertsch and Vittino (2021) and a gas flow density presented in Sormani et al. (2015). The properties of the PWNe candidates can be seen in Table 7.2.

The inclusion of PWNe around pulsars assigned to category A will greatly enhance the diversity of the sample that will be used for the following population study.

PSR J1740+1000, PSR J1705−1906, and PSR J1846+0919 are located in dense environments at high galactic latitudes. Observations of these three sources will provide valuable insights into particle acceleration and energy loss mechanisms under distinct environmental conditions, relatively unaffected by the dense photon and magnetic fields of the Milky Way. Notably, extended VHE γ-ray emission, interpreted as a bow-shock PWN, has already been detected around PSR J1740+1000 by LHAASO (Cao et al., 2025). Follow-up observations with H.E.S.S. could play a crucial role in resolving the morphology of the nebula and further constraining its emission properties.

PSR J1741−2054 is a high-spin-down-luminosity pulsar located in a dense environment, making it a strong candidate for hosting a PWN. Furthermore, its proximity at a

Name	GLON (°)	GLAT (°)	τ_c (kyrs)	Type	$B_{\rm LC}$ (10^4 G)	distance (kpc)	$n_{\rm col}$ ($1/{\rm cm}^3$)
PSR J1740+1000	34.01	20.27	114.46	HE	4.70	1.23	29.8
PSR J1705−1906	3.19	13.03	1144.83	HE	0.39	0.75	29.8
PSR J1741−2054	6.42	4.91	385.96	HE	0.36	0.30	29.8
PSR J1954+2836	65.24	0.38	69.41	NRAD	16.68	1.96	30.0
PSR J0729−1448	230.39	1.42	35.18	HE	3.18	2.68	3.2
PSR J1846+0919	40.69	5.34	359.86	NRAD	1.24	1.53	29.8
PSR J1429−5911	315.26	1.30	60.18	NRAD	1.15	1.96	3.2
PSR J1447−5757	317.79	1.55	214.20	NRAD	3.24	1.00	–
PSR J0538+2817	179.72	-1.69	618.13	HE	2.34	1.30	12.7
PSR J0742−2822	243.77	-2.44	157.08	HE	3.43	2.00	1.8
PSR J0905−5127	271.63	-2.85	220.68	-	0.67	1.33	1.8
PSR J1231−6511	300.87	-2.40	137.95	NRAD	1.66	1.00	–

Table 7.2: Additional information for the target pulsars for the 2025-2028 H.E.S.S. legacy program. Listed are the distance to the galactic plane, the characteristic age τ_c, the pulsar type, the strength of the magnetic field on the pulsar surface $B_{\rm surf}$, the strength of the magnetic field at the light cylinder $B_{\rm LC}$, the spin-down power and distance, and the column density $n_{\rm col}$. The pulsar type 'HE' refers to a spin-powered pulsar with pulsed emission from radio to infrared or higher frequencies. In comparison 'NRAD' refers to a spin-powered pulsar with pulsed emission only at frequencies higher than infrared.

distance of only 300 pc enhances its relevance for studies of the cosmic-ray electron and positron spectrum observed at Earth, potentially contributing to our understanding of local cosmic-ray propagation.

For PSR J1954+2836, estimates indicate a high column density and a strong magnetic field at the light cylinder, suggesting favourable conditions for PWN formation. The non-detection of a nebula in this system would offer a unique opportunity to identify additional parameters that significantly influence the emergence of extended γ-ray structures around pulsars.

With a characteristic age of $\tau_c = 35.18$ kyrs, PSR J0729−1448 is exceptionally young. The detection of a PWN associated with this pulsar would provide critical insights into the early stages of neutron star evolution, magnetospheric processes, and interactions with the surrounding supernova remnant, further refining models of PWN evolution.

Pulsars classified as category B exhibit high spin-down luminosities, making them strong candidates for hosting extended γ-ray structures. Observing these systems would significantly expand the sample size for a population study of PWNe. However, they are not as exceptional as those categorized as type A. Therefore, priority should be given to the observation of pulsars in category A to maximize the scientific impact of the study.

7.4 Outlook

The interactions of pulsars with their surrounding environment are well probed by the formation and properties of PWNe. Previous studies of single sources have yielded valuable insights for the population as a whole, however, they also introduce biases in the results through different assumptions throughout the source analyses. A first attempt on an unbiased analysis of the PWNe population was made in H.E.S.S. Collaboration et al. (2018b). While this study provides valuable insights into the characteristics of known TeV PWNe, the sample was limited to pulsars located at a latitude of $|b| < 3.5°$, and approximately 10 years of data. This work presents a pipeline developed to enhance the population covered in H.E.S.S. Collaboration et al. (2018b). For this, a total of 362 pulsars were selected from the third *Fermi*-LAT pulsar catalogue (Smith et al., 2023b), as well as the pulsar tree (García et al., 2022). This selection not only includes a diverse set of pulsars at different distances but also in different environments. Additionally, the dataset was increased to include 15 years of observations by the H.E.S.S. telescopes.

Using this enhanced pipeline, a total of 98 significant γ-ray sources in the vicinity of pulsars could be detected, with a further 89 regions for which upper limits could be derived. Additional observations have been requested for 12 candidate pulsars. The position of the host pulsars of these candidate PWNe in the $P - \dot{P}$ diagram are shown in Figure 7.4. As expected, significant extended γ-ray emission has been detected for many of the pulsars located in the upper left corner. Moving further towards the lower right corner, the number of pulsars for which only an upper limit could be derived, or no extended γ-ray emission is observed at all, increases.

However, it should be stressed that at this point, the detected γ-ray emission has not been firmly identified as being connected to the pulsars. Especially for pulsars which are positionally coincident with other known γ-ray sources, a more cautious analysis needs to be performed to ensure that the detected γ-ray emission does not correspond to emission from a positionally coincident extended source with a different origin or even a neighbouring source. For this reason, no further interpretation of the population is made here.

Once observations of the above outlined PWN candidates are complete, the enhanced population can also be used to refine the theoretical models derived in H.E.S.S. Collaboration et al. (2018b). The increase of the population of candidate PWNe in comparison to the previous study is visualised in Figure 7.5, where the spin-down power of all pulsars listed in the ATNF (Manchester et al., 2005) is plotted over the characteristic age of the pulsars. Shown on the left in Figure 7.5 is the population used in H.E.S.S. Collaboration et al. (2018b). Indicated on the right are the PWN candidates identified in this study. Also indicated are the proposed observation targets for the H.E.S.S. legacy program, as well as the two pulsars analysed in detail in this work, PSR J1813−1749 and PSR B1055−52.

In the future, a more thorough distinction between candidate PWNe and γ-ray emission from other sources positionally coincident with the pulsars will be made. Then, the population as a whole will be probed to derive correlations between pulsars that host a PWN and identify common parameters for pulsars for which no PWN can be detected, and a more thorough discussion of the nature of TeV emission from pulsars and their environments will be given. Identifying these common traits could also help recognize currently unidentified leptonic TeV sources, where no associated pulsar is detected due to an unfavourable beaming orientation.

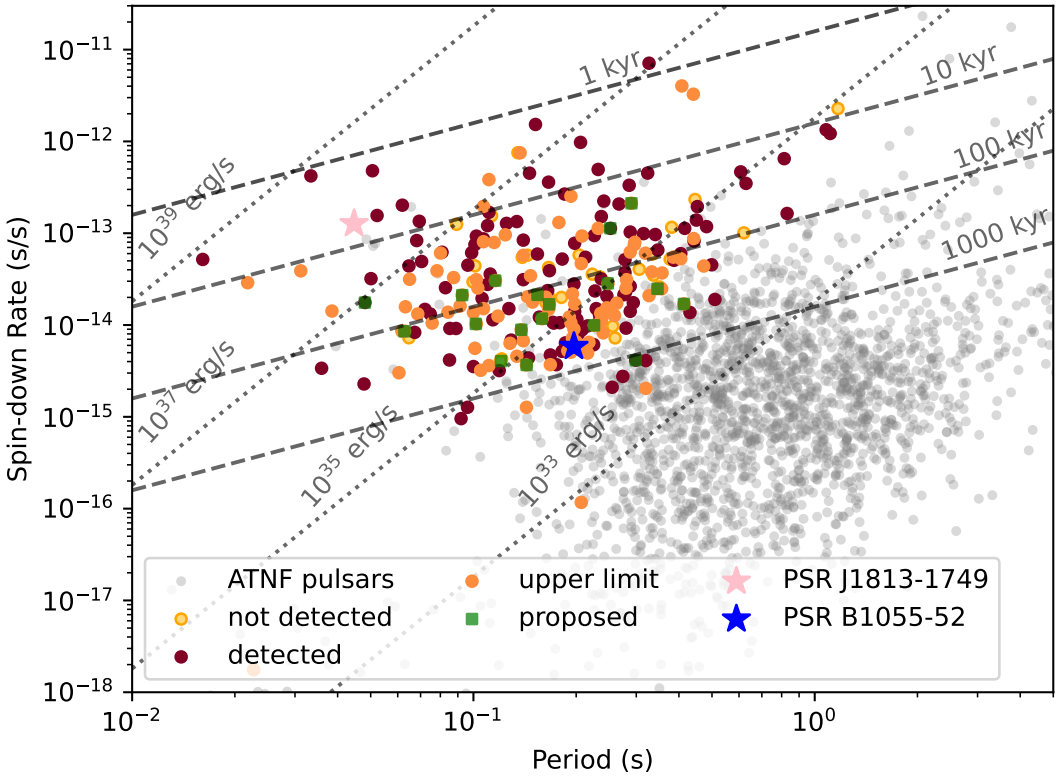

Figure 7.4: $P - \dot{P}$ diagram showing the pulsar population probed in this study. Pulsars listed in the ATNF catalogue (Manchester et al., 2005) are shown in grey. Candidate objects for which emission with a significance of above $5\,\sigma$ was detected are labelled as 'detected'. Candidate objects for which upper limits could be extracted are labelled as 'upper limit'. If the likelihood minimization did not find a valid minimum, i.e., no γ-ray emission could be detected in the region around the pulsar, the candidate is labelled as 'not detected'. PWNe candidates for which further observations are proposed in the scope of the H.E.S.S. legacy observation program are labelled as 'proposed'. Additionally shown are the sources analysed in this work, PSR J1813−1749 and PSR B1055−52.

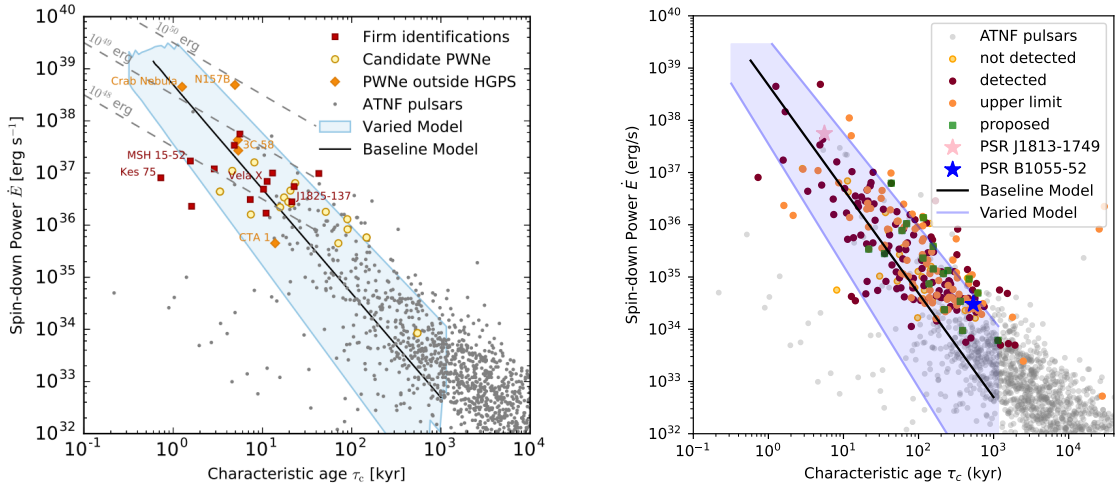

Figure 7.5: Spin-down power $\dot{E}$ and characteristic age τ_c of pulsars listed in the ATNF (Manchester et al., 2005) compared to the model derived in H.E.S.S. Collaboration et al. (2018b). Left: firmly identified PWNe and PWNe candidates from H.E.S.S. Collaboration et al. (2018b). Right: PWNe candidates identified in this study.

dentifying these common traits could also aid in recognizing currently unidentified leptonic TeV sources, where no associated pulsar is detected due to unfavourable beaming geometry.This limitation is non-negligible, as the radio beaming fraction of young, energetic pulsars with high spin-down power is estimated to be only around 60%, implying that a substantial fraction of pulsars may remain unseen despite actively powering nebular emission (Straal and van Leeuwen, 2019).

A Appendix: Run matching approach

A.1 Quality criteria

The quality criteria used to reject observation runs acquired under bad atmospheric conditions or suboptimal telescope response can be seen in Table A.1.

Table A.1: Observation quality thresholds for the different H.E.S.S. Phases.

Parameter	detection	spectral
RA_Dev_mean [°]	$-0.01667 - 0.01667$	$-0.01667 - 0.01667$
Dec_Dev_mean [°]	$-0.01667 - 0.01667$	$-0.01667 - 0.01667$
Az_Dev_rms [″]	$0.0 - 10.0$	$0.0 - 10.0$
Alt_Dev_rms [″]	$0.0 - 10.0$	$0.0 - 10.0$
Num_Hardware	$0.0 - 120.0$	$0.0 - 120.0$
Num_HV_Turned_Off	$0.0 - 50.0$	$0.0 - 50.0$
Duration [s]	$600 - 7200$	$600 - 7200$
Participation_frac	$0.4 - 1.0$	$0.4 - 1.0$
True_Rate_mean [Hz]	$--$	1200.
Transparency_mean	$--$	$0.8, 1.2$
True_Rate_Delta_1	$--$	$0.9 - 1.1$
True_Rate_Delta_2	$--$	$0.9 - 1.1$

A.2 Zenith angle correction

In order to account for differences in mean zenith angle of the observation between ON and OFF run, equation (47) is fitted to the array trigger rates in every optical phase. The resulting fit parameters are given in Table A.2.

Table A.2: Zenith angle correction to the background rate for different optical phases. The fit parameters are estimated from a fit of equation (47) to the trigger rates of the H.E.S.S. telescopes for the different optical phases.

Optical phase	Start date	p_1	p_2
1/1b	01/2004	218.8 ± 1.0	0.92 ± 0.02
1c	07/2007	171.7 ± 0.7	1.10 ± 0.06
1c1	04/2010	174.3 ± 1.9	1.02 ± 0.07
1c2	10/2010	176.5 ± 3.2	0.71 ± 0.05
1c3	04/2011	188.2 ± 1.9	0.61 ± 0.07
1d	11/2011	214.9 ± 2.7	0.81 ± 0.16
2b0	01/2013	258.7 ± 9.7	0.73 ± 0.21
2b2	06/2013	250.9 ± 12.0	0.61 ± 0.04
2b3	05/2014	165.7 ± 1.4	0.91 ± 0.03
2b4	11/2014	205.2 ± 1.6	0.87 ± 0.07
2b5	08/2015	142.2 ± 1.8	0.84 ± 0.19
2c0	01/2017	380.6 ± 17.7	1.31 ± 0.06
2c1	03/2017	495.8 ± 4.9	1.05 ± 0.04
2c2	05/2017	435.0 ± 2.3	0.99 ± 0.02
2d3	10/2019	385.8 ± 1.5	1.08 ± 0.01

A.3 Energy dependence

Since the highest number of misclassified cosmic rays is expected at low energies, it is important that the correlation coefficients presented in Table 3.2 are not biased by the inclusion of data over the whole energy range. To test this behaviour, the coefficients have been calculated including events in the whole energy range, only events with a reconstructed energy below 1 TeV and events with reconstructed energy below 0.56 TeV. A comparison of the matching parameters for these different energy ranges is given in Table A.3.

Table A.3: Distance correlation coefficients computed using data with different energy thresholds.

	$E_\gamma < 100\,\mathrm{TeV}$	$E_\gamma < 1\,\mathrm{TeV}$	$E_\gamma < 0.56\,\mathrm{TeV}$
zenith	0.46	0.52	0.53
duration	0.71	0.62	0.62
NSB	0.24	0.30	0.26
Muon Efficiency	0.15	0.16	0.16
Trigger Rate	0.46	0.36	0.36
Transparency Coeff.	0.55	0.44	0.43
Radiometer Temp.	0.48	0.40	0.40

An additional test to rule out a potential energy dependence of the goodness of the background estimation was done by dividing the datasets for the analysis of the empty-field regions into bins, such that one bin consists of two energy bins of the original datasets. Then, significance histograms were computed for all bins, and a Gaussian fit was performed. The results of the Gaussian fit to the significance distribution for the regions around Reticulum II and Tucana II have been summarised in Table A.4 and Table A.5, respectively.

Table A.4: The fit parameters of the Gaussian fit to the significance distributions estimated from the region around Reticulum II

Energy bin [TeV]	Case 0		Case 3		Case 4+		Case 4-	
	μ	σ	μ	σ	μ	σ	μ	σ
0.32 - 0.56	−0.07	1.01	−0.26	1.01	−0.51	1.01	−0.00	1.02
0.56 - 1.00	−0.03	1.00	−0.01	1.02	−0.25	1.00	0.25	1.04
1.00 - 1.78	−0.12	1.04	−0.02	1.05	−0.18	1.04	0.14	1.07
1.78 - 3.16	−0.14	1.05	−0.04	1.07	−0.14	1.06	0.07	1.09
3.16 - 5.62	−0.20	0.98	−0.10	1.01	−0.16	0.99	−0.03	1.02
5.62 - 10.00	−0.30	0.78	−0.24	0.80	−0.27	0.80	−0.21	0.78

Table A.5: The fit parameters of the Gaussian fit to the significance distributions estimated from the region around Tucana II

Energy bin [TeV]	Case 0		Case 3		Case 4+		Case 4-	
	μ	σ	μ	σ	μ	σ	μ	σ
0.32 - 0.56	-0.13	1.03	-0.19	1.03	-0.58	1.00	0.23	1.09
0.56 - 1.00	-0.08	1.05	-0.12	1.04	-0.39	1.03	0.18	1.07
1.00 - 1.78	-0.15	1.06	-0.18	1.06	-0.36	1.03	0.02	1.09
1.78 - 3.16	-0.16	1.03	-0.18	1.03	-0.30	1.01	-0.06	1.06
3.16 - 5.62	-0.26	0.89	-0.28	0.88	-0.34	0.87	-0.21	0.90
5.62 - 10.00	-0.27	0.67	-0.28	0.67	-0.32	0.66	-0.25	0.68

A.4 Fit Results

Figure A.1, Figure A.2, and Figure A.3 show a visual comparison of the best-fit values, including the systematic errors for the regions around the Crab Nebula, PKS 2155−304, and RX J1713.7−3946, respectively. The best-fit values for the large dataset on RX J1713.7−3946 are shown in Figure A.4.

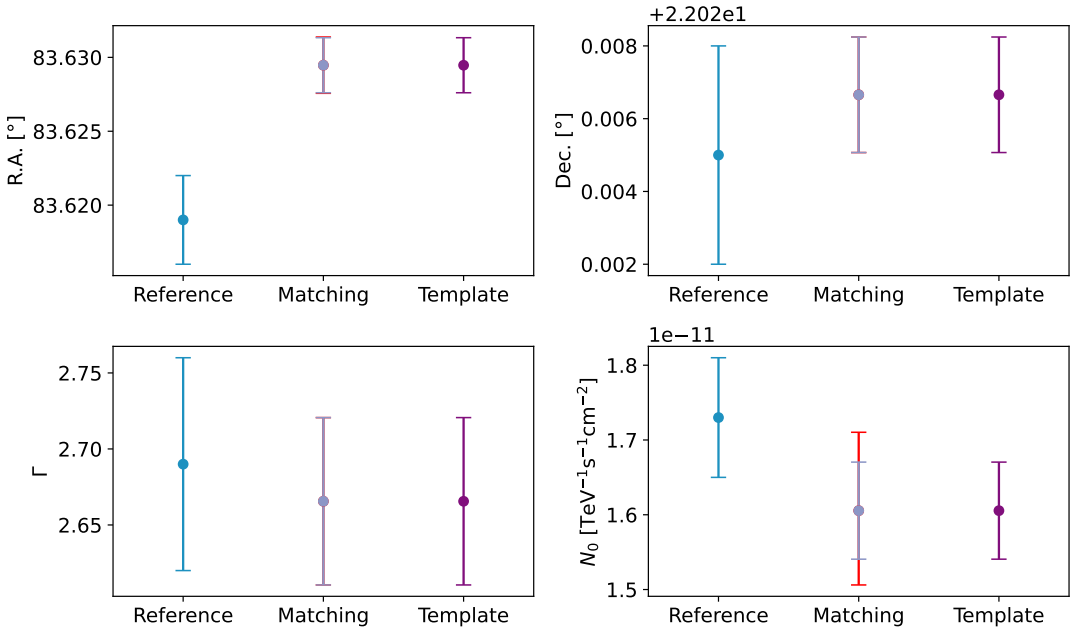

Figure A.1: Comparison between the best-fit values for all parameters of the point model used to describe the emission from the Crab Nebula. The reference values were taken from Mohrmann et al. (2019a). Matching refers to the values derived by using the run-matching approach for the background estimation, while template refers to the background model template. The systematics introduced due to the run-matching approach are indicated in red.

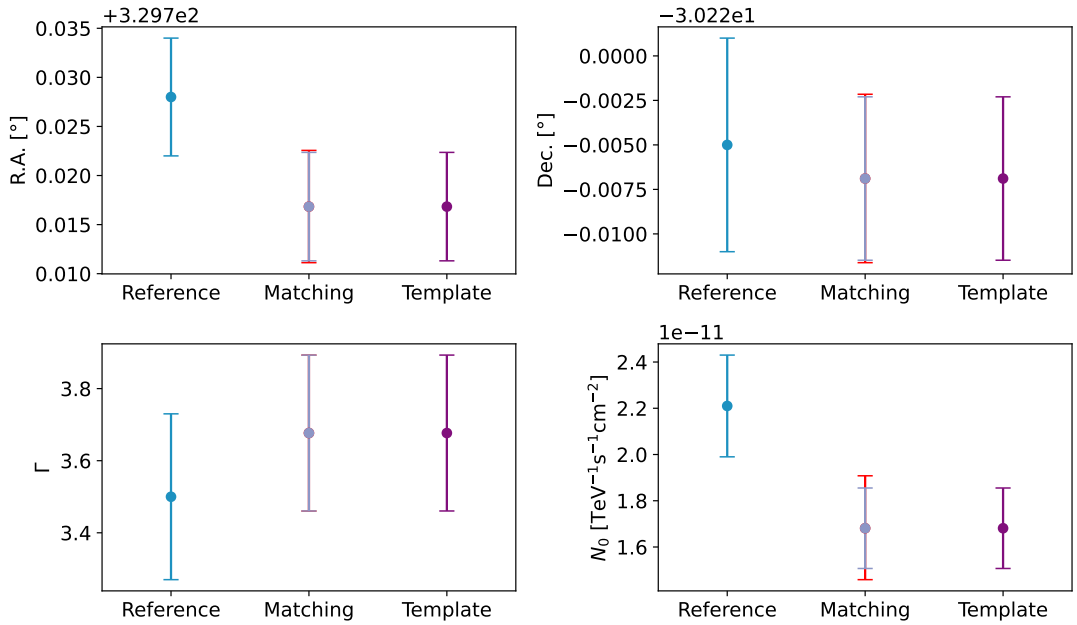

Figure A.2: Comparison between the best-fit values for all parameters of the point model used to describe the emission from PKS 2155−304. The reference values were taken from Mohrmann et al. (2019a). Matching refers to the values derived by using the run-matching approach for the background estimation, while template refers to the background model template. The systematics introduced due to the run-matching approach are indicated in red.

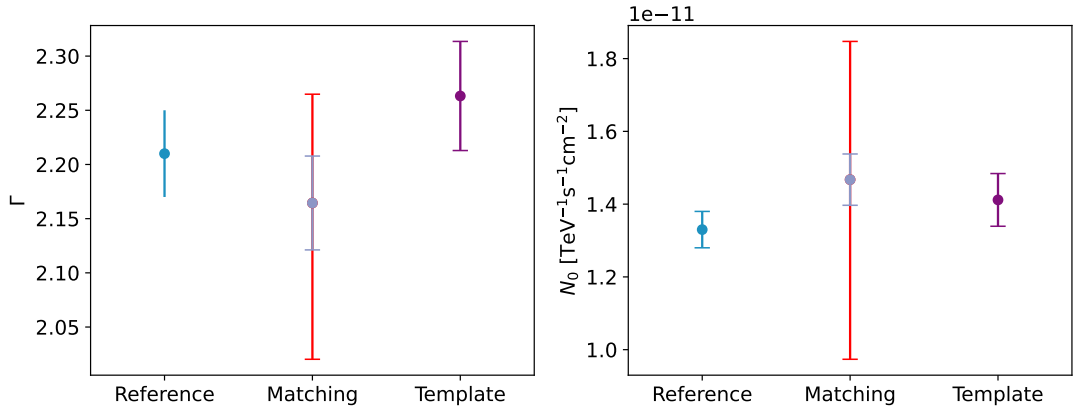

Figure A.3: Comparison between the best-fit values for all fit parameters of the model used to describe the emission from RX J1713.7−3946. The reference values were taken from Mohrmann et al. (2019a). Matching refers to the values derived by using the run-matching approach for the background estimation, while template refers to the background model template. The systematics introduced due to the run-matching approach are indicated in red.

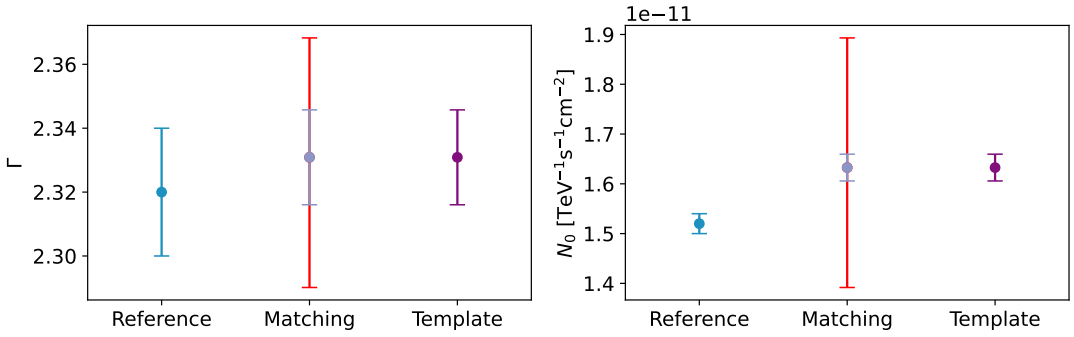

Figure A.4: Comparison between the best-fit values for all fit parameters of the model used to describe the emission from RX J1713.7−3946 for the larger dataset containing 57 hours of data. The reference values were taken from Mohrmann et al. (2019a). Matching refers to the values derived by using the run-matching approach for the background estimation, while template refers to the background model template. The systematics introduced due to the run-matching approach are indicated in red.

A.5 Additional significance maps and spectra

Here the significance maps and distributions of the region around PKS 2155−304 (Figure A.9), MSH 15−5*2* (Figure A.10) and RX J1713.7−3946 (Figure A.11) are shown. Although a small shift in the background distributions for the datasets estimated using the run-matching approach can be observed, this shift is within the systematic uncertainty (see Table 3.6).
The SED estimated for the Crab Nebula, PKS 2155−304 and MSH 15−5*2* are shown in Figures A.5, A.6 and A.7 respectively. The lower panel of these figures shows the deviation between the two sets of SED points and the best-fit spectral model derived in the analysis of the respective Case 3 datasets, defined by $(x_{1/2} - x_{model})/x_{model}$, with x_1 the differential energy flux in the respective energy bin for the reference SED points derived in Mohrmann et al. (2019a), x_2 the differential energy flux for the SED points derived from the Case 3 datasets and x_{model} the differential energy flux estimated from the best-fit spectral model. The SED derived from the large dataset on RX J1713.7−3946 are shown in comparison with the SED published in H.E.S.S. Collaboration et al. (2018a) in Figure A.8. In this case no residual panel is shown due to the large differences in binning between both datasets.

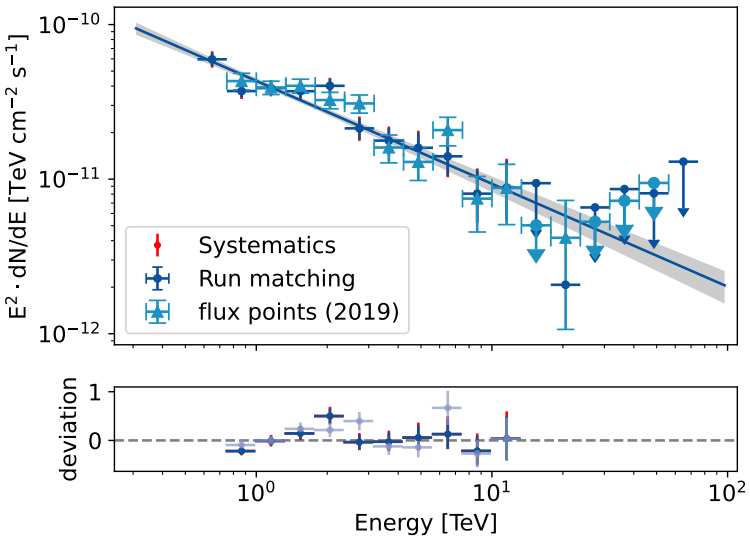

Figure A.5: SED of the Crab Nebula using the run-matching approach for the background estimation compared to the reference SED from (Mohrmann et al., 2019a). The deviation between the two SEDs and the best-fit model derived for the Case 3 datasets is depicted in the lower panel.

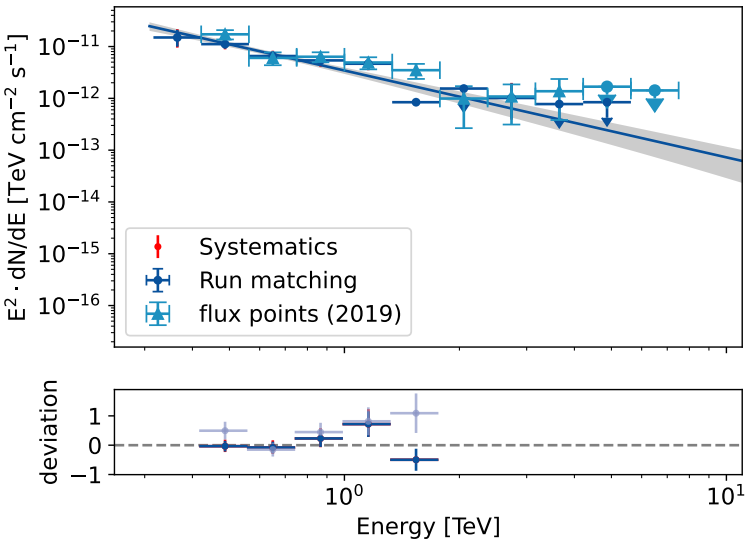

Figure A.6: SED of PKS 2155−304 using the run-matching approach compared to the SED from (Mohrmann et al., 2019a). The deviation between the two SEDs is depicted in the lower panel.

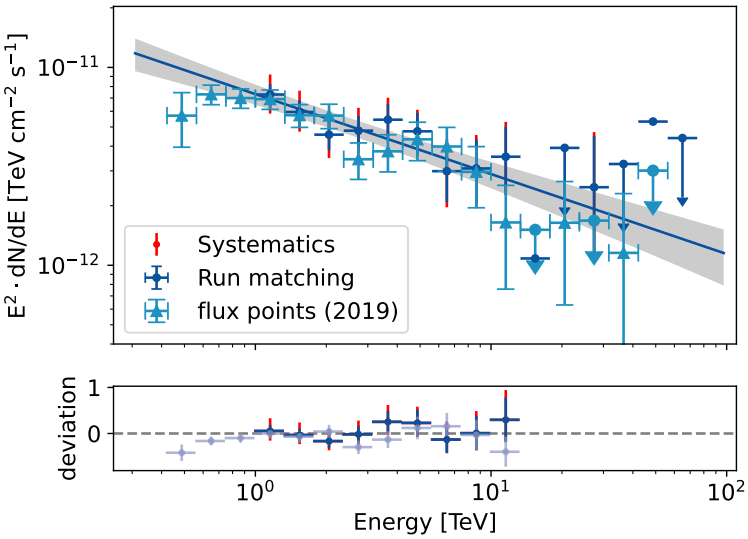

Figure A.7: SED of MSH 15−5*2* using the run-matching approach compared to the SED from (Mohrmann et al., 2019a). The deviation between the two SEDs is depicted in the lower panel.

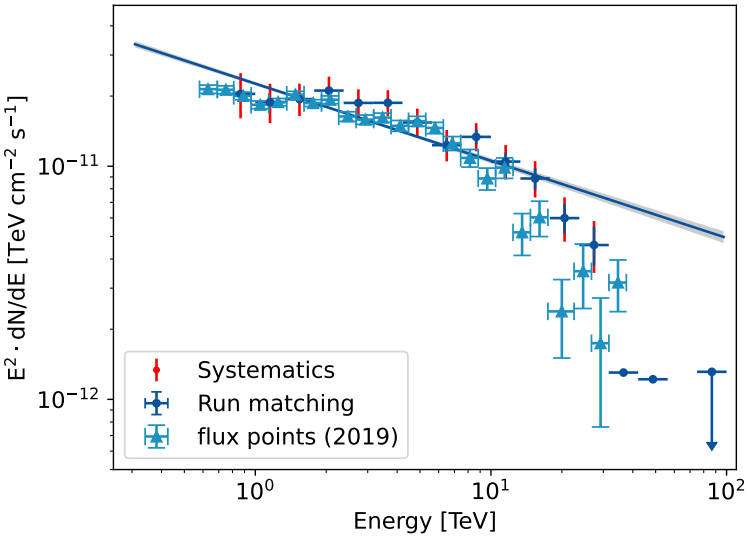

Figure A.8: SED of derived in the analysis of the large dataset on RX J1713.7−3946 using the run-matching approach for the background estimation compared to the reference SED derived in the analysis presented in (H.E.S.S. Collaboration et al., 2018a).

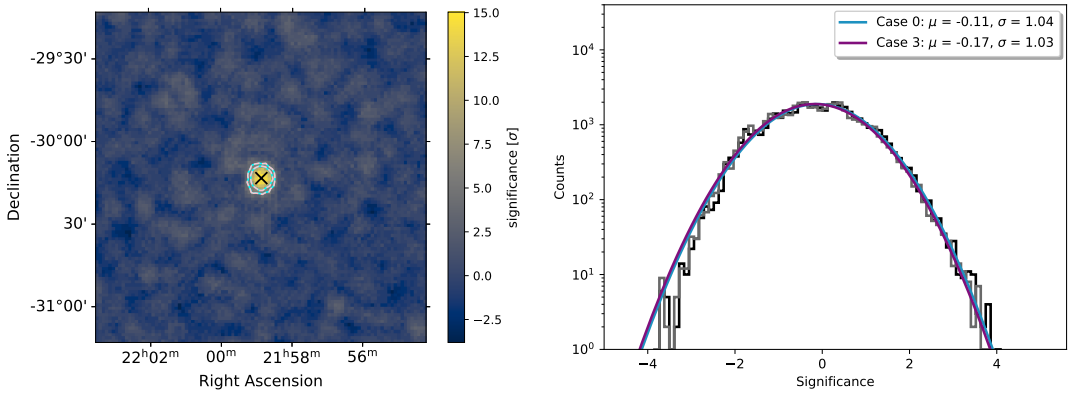

Figure A.9: Left: Li&Ma significance map of the region around PKS 2155−304, with $5\,\sigma$ and $8\,\sigma$ contours, from the Case 0 dataset (blue), and from the Case 3 dataset (pink). The best-fit position is indicated by the black cross. Right: significance distribution of the background in the FoV around PKS 2155−304 for both background estimation techniques, fit with a normal distribution.

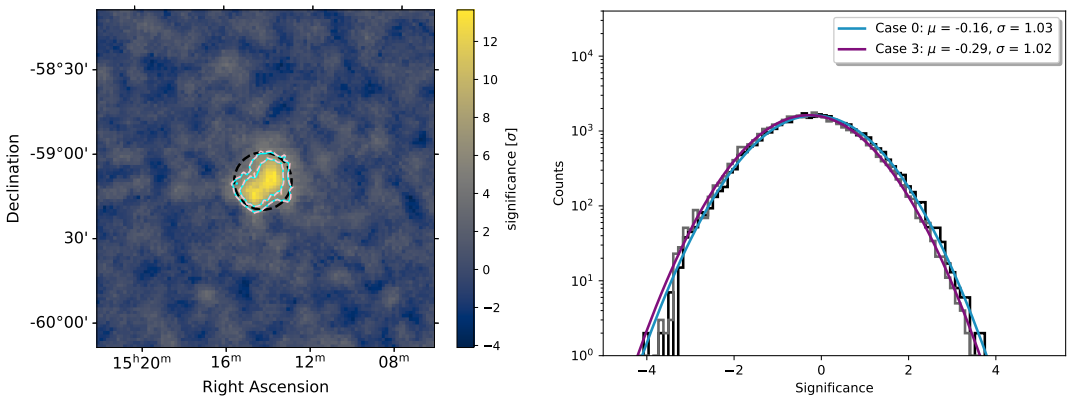

Figure A.10: Left: Li&Ma significance map of the region around MSH 15−5*2*, with $5\,\sigma$ and $8\,\sigma$ contours from the Case 0 dataset (blue) and from the Case 3 dataset (pink). The best-fit morphology is indicated by the black-dashed line. Right: The significance distribution of the background in the FoV for both background estimation techniques fit with a normal distribution.

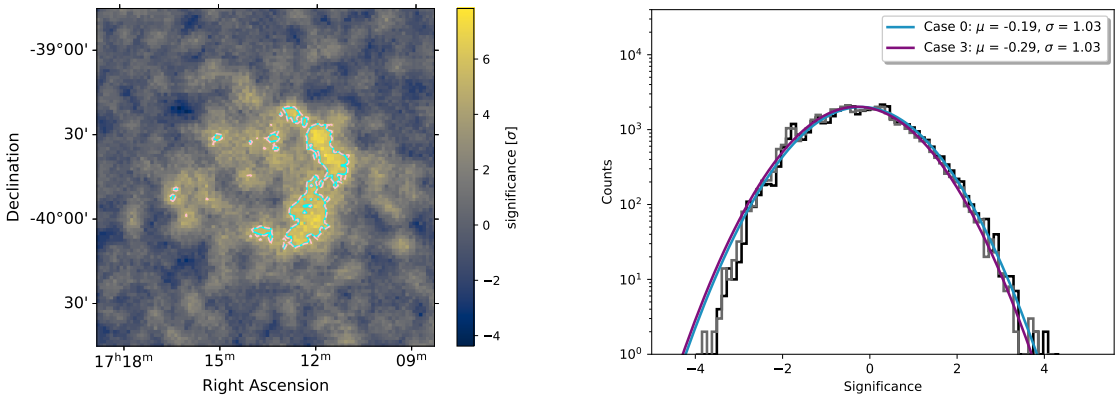

Figure A.11: Left: Li&Ma significance map of the region around RX J1713.7−3946, with $5\,\sigma$ and $8\,\sigma$ contours for Case 0 (blue), and for Case 3 (pink). Right: significance distribution of the background in the FoV for both background estimation techniques, fit with a normal distribution.

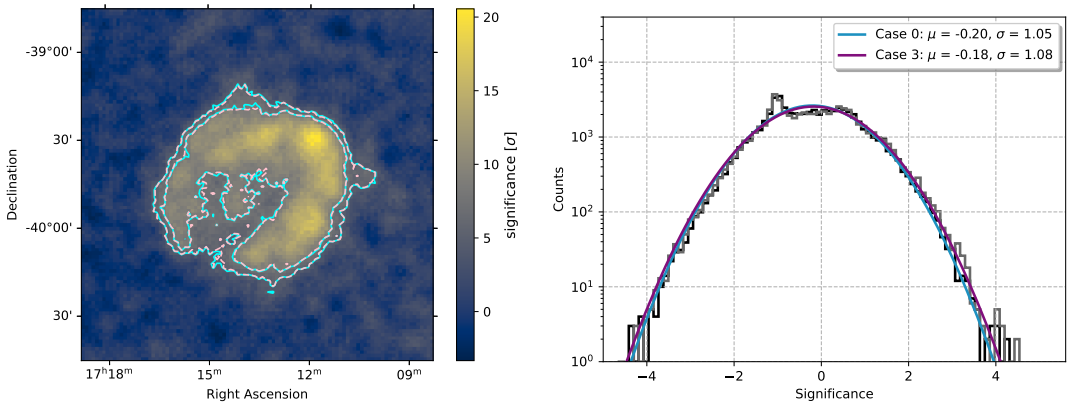

Figure A.12: Left: Li&Ma significance map of the region around RX J1713.7−3946, using a dataset containing 57 hours. Contours are shown at $5\,\sigma$ and $8\,\sigma$ for Case 0 (blue), and for Case 3 (pink). Right: significance distribution of the background in the FoV for both background estimation techniques, fit with a normal distribution.

B Appendix: Analysis of the Region around PSR J1813−1749

B.1 H.E.S.S. Data analysis

The region around PSR J1813−1749 has been observed with H.E.S.S. Phase I between 2004 and 2010 as part of different observation campaigns in the sky region. For the analysis of this data, the participation of all four telescopes was required for every observation. Additionally, the pointing position of the telescopes was required to not be offset by more than 2.0° from RA = 273.40°, Dec = −17.84°, the position of HESS J1813−178 as derived in Aharonian et al. (2006c). After applying spectral selection cuts (see Chapter 3.2.1), a total exposure of 32 hours was available for analysis.

The data was reduced using the H.E.S.S. analysis package (see (Aharonian et al., 2006a)), reconstructed using the ImPACT algorithm (Parsons and Hinton, 2014). For background estimation, the background template model derived in Mohrmann et al. (2019a) and discussed in Chapter 3.1.4 was used.

For each individual run, a safe energy threshold was defined to exclude the threshold region where effective detection areas vary steeply with energy and where the energy reconstruction is biased. The threshold was chosen as the energy at which the energy bias is below 10% (Aharonian et al., 2006a). A second energy threshold was defined as the peak in the field of view background template spectrum (Mohrmann et al., 2019b); the higher of the two thresholds was applied for the run.

The events passing the cut criteria were then stacked into a single dataset, and the field of view background template, as discussed in Mohrmann et al. (2019b), was applied. In addition to the run-wise threshold, a global energy threshold for the dataset of 0.4 TeV was set due to problems with the reconstruction at lower energies. All events below this energy were excluded from the binned-likelihood estimation.

The left side of Figure 5.2 shows a Li&Ma (1983) significance map, where compact, bright γ-ray emission positionally coincident with the pulsar is visible. The emission is well described with a power-law spectral model and detected with a significance of $38\,\sigma$. The best-fit position and extension derived in this analysis are compatible with the results reported in Aharonian et al. (2006c).

A diffuse emission component was already detected during the Galactic plane survey (Aharonian et al., 2006c) but discarded because of large uncertainties in the background estimation. The emission was reported to be located at R.A. $= (273.46 \pm 0.05)^\circ$, Dec. $= (-17.77 \pm 0.06)^\circ$ with a Gaussian width of $\sigma = (0.31 \pm 0.06)^\circ$. Due to using the rather stable background template model, as opposed to a ring-background approach, a firm detection of significant extended emission in the source region is possible. The morphological model that best describes the emission is evaluated, testing both a disc-like model and a Gaussian model, each with and without the possibility of an elongation. This study finds that an elongated Gaussian model centred at R.A. $= (273.61 \pm 0.06)^\circ$, Dec. $= (-17.39 \pm 0.07)^\circ$ with a semi-major axis of $\sigma = (0.72 \pm 0.08)^\circ$ describes the emission best. The Gaussian model is preferred over the disc-like model with $\Delta TS = 59.91$, while the elongated Gaussian model is preferred by $3.4\,\sigma$ compared to the symmetric Gaussian model. The increased size compared to the first report of possible extended emission can be attributed to the difference in background estimation. A power-law model was used to describe the emission. This additional extended emission, HESS J1813−178B, was detected with a significance of $13\,\sigma$.

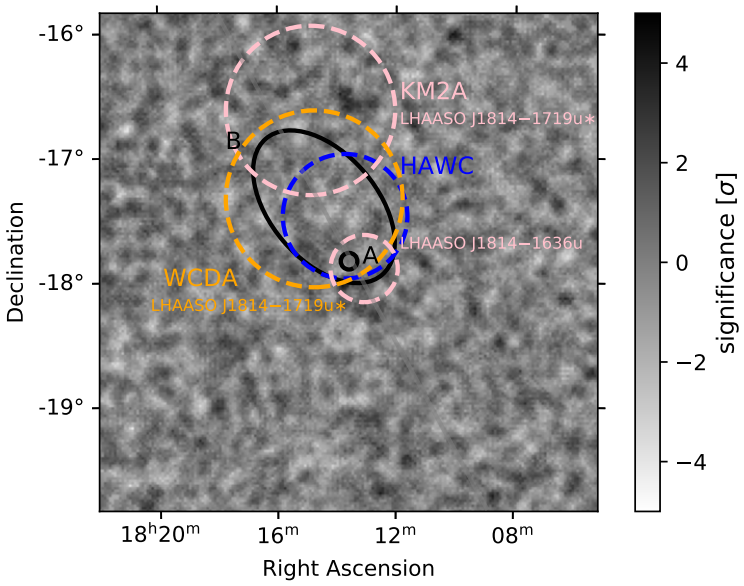

Figure B.1: Li&Ma (1983) significance map of the H.E.S.S. data, with a correlation radius of 0.1°. The best-fit morphology derived from the analysis of the H.E.S.S. data is indicated in black. The best-fit morphology of the source 3HWC J1813−174 is indicated in blue. The description of the region obtained with LHAASO is indicated by the pink and orange dashed circles.

The morphology of HESS J1813−178B is also compared to the sources detected with HAWC and LHAASO. The detection made in this work is in good spatial agreement with the extended emission 3HWC J1813−174 observed by HAWC, as well as 1LHAASO J1814−1719u*, extended emission observed by the WCDA of LHAASO (see figure B.1).

B.2 Fermi-LAT Data analysis

In this study, $\sim$ 13 years of LAT data was analysed. To account for the emission from other sources in the FOV, catalogue models were taken from the 12-year 4FGL source catalogue (Abdollahi et al., 2020). A 6° region of interest (ROI) around the source position of 4FGL J1813−1737e, as derived in Araya (2018), a bin size of 0.025° and 8 energy bins per decade with logarithmic spacing were used. Only events arriving with a maximum zenith angle of 90° were considered, in order to avoid including secondary γ rays from the Earth's horizon.

The remaining γ-ray background was modelled using an isotropic background model (`iso_P8R3_SOURCE_V3_v1.txt`), and a template model for the Galactic diffuse background (`gll_iem_v07.fits`). In order to describe the region well, all known catalogue sources in a region of 10° around the source position were included.

For the analysis, the Python package `fermipy, version 1.0.1` (Wood et al., 2017), optimised for performing a binned likelihood analysis of LAT data using the *Fermi* Science Tools, was used. With `fermipy`, a counts cube and IRF cubes in an energy range between 1 GeV and 1 TeV was created. For the analysis of the source, the data, IRFs, and background models were exported to `gammapy`. In contrast to the standard

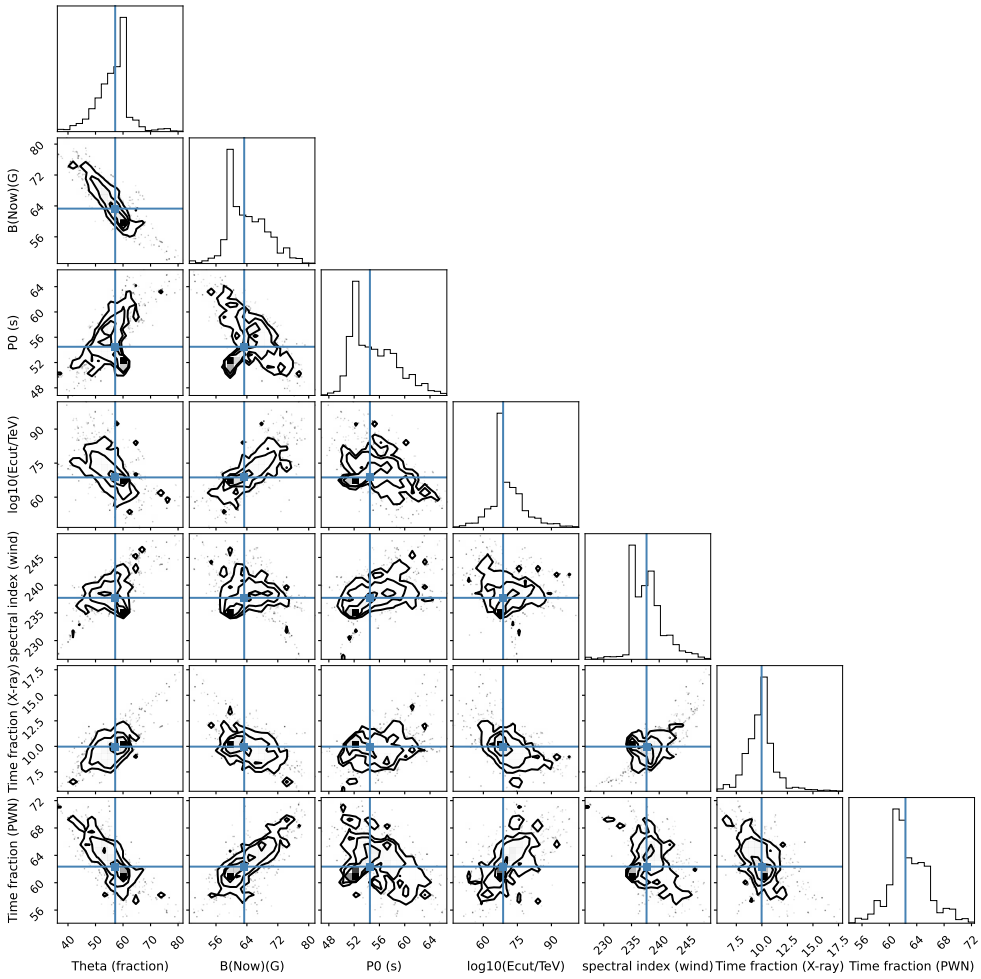

Figure B.2: Corner plot showing the distributions and correlations of the free parameters of the leptonic model.

analysis chain of the *Fermi*-LAT data, this allows for a fit of both morphological and spectral parameters simultaneously.

B.3 Modeling and Multiwavelength Context

The parameters of the leptonic model, used to describe the γ-ray emission, were obtained through an MCMC method, allowing for a thorough exploration of the parameter space. The resulting corner plot showing the posterior distributions and correlations between model parameters can be seen in Figure B.2 for the leptonic model and in Figure B.3 for the hadronic model.

In addition to the morphology comparison between the sources detected by H.E.S.S., HAWC, and LHAASO shown in Figure B.1, the spectra, derived in Albert et al. (2020) and Cao et al. (2023a) are compared. These spectra, together with the leptonic and hadronic model derived in this work are shown in Figure B.4. The spectra of 1LHAASO J1814−1719u*, observed by KM2A and 3HWC J1813−174 show a good agreement with the results derived in this study, while the spectrum of

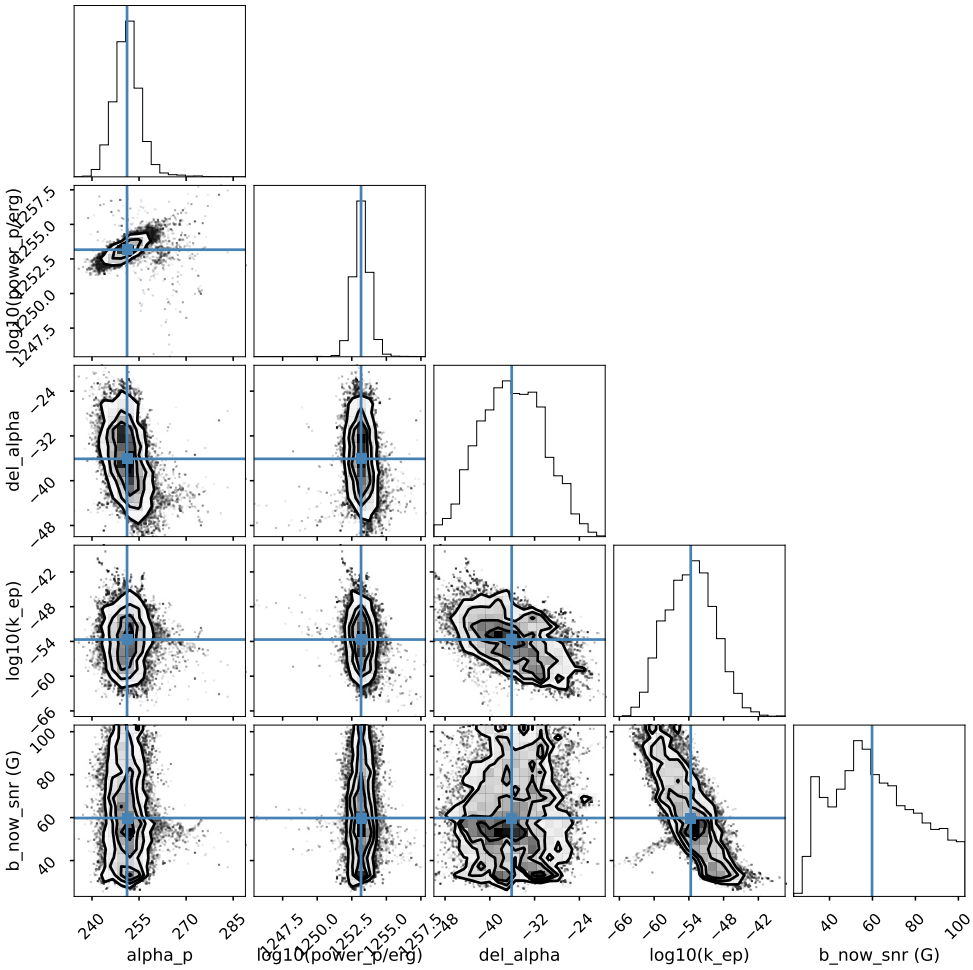

Figure B.3: Corner plot showing the distributions and correlations of the free parameters of the hadronic model.

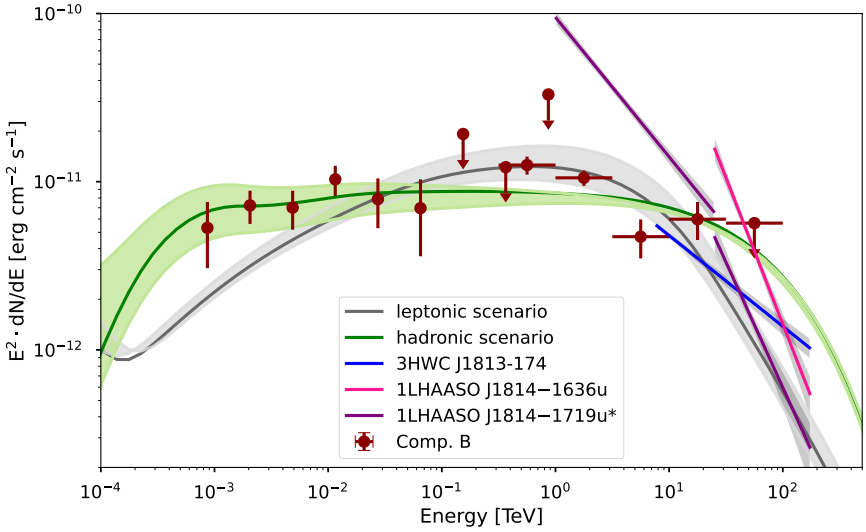

Figure B.4: Estimated γ-ray flux for the hadronic and leptonic model together with the spectra derived in the analysis of the Fermi-LAT, H.E.S.S., HAWC and LHAASO data.

1LHAASO J1814−1719u*, observed by WCDA as well as the spectrum of 1LHAASO J1814−1636u do not agree. A possible reason for this could be the differences in the separation between source emission and diffuse emission along the galactic plane.

C Appendix: Analysis of the Region around PSR B1055−52

C.1 Background estimation

Using the nominal validity range for all matching parameters presented in Chapter 3.2, no OFF run can be found for 37 of the observation runs in the region of PSR B1055−52. To avoid a large loss of exposure, the validity range of the parameters has been relaxed. The old and new validity range can be seen in Table 3.2

Table C.1: Comparison of the validity range of the matching parameters used for the validation and the relaxed criteria for the background estimation in the region around PSR B1055−52.

Matching parameter	nominal range	increased range
Zenith Angle Θ_z	within zenith bins	
Trigger Rate r	$\Delta\, r < 25\%$	$\Delta\, r < 45\%$
Duration t	$\Delta\, t < 7\%$	$\Delta\, t < 25\%$
Transparency Coeff. τ	$\Delta\, \tau < 6\%$	$\Delta\, \tau < 19\%$
Radiometer Temp. R_T	$\Delta\, R_T < 50\%$	$\Delta\, R_T < 55\%$
Muon Efficiency ε_μ	$\Delta\, \varepsilon_\mu < 11\%$	$\Delta\, \varepsilon_\mu < 19\%$
NSB	$\Delta\,\mathrm{NSB} < 80\%$	$\Delta\,\mathrm{NSB} < 90\%$

C.2 Radial Profiles

A visualization of the position of the semicircles used for the extraction of the radial profiles compared to the $3\,\sigma$ and 5σ contours of the emission is given in Figure C.1.

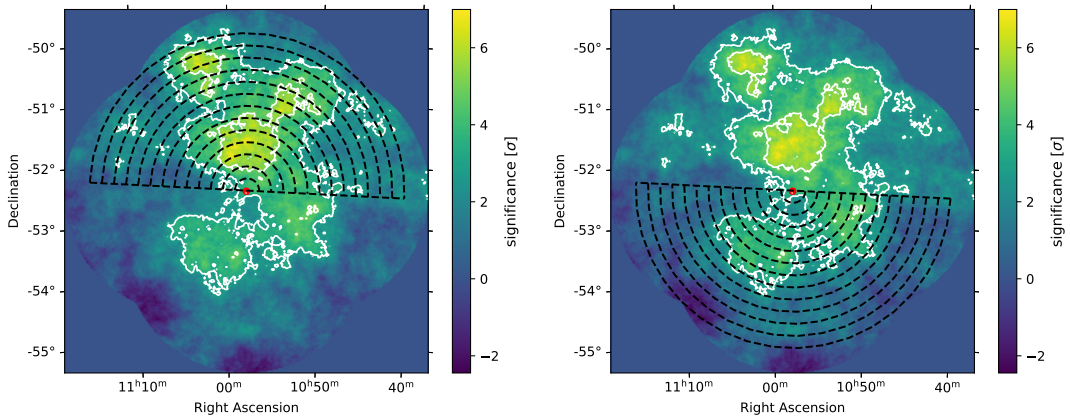

Figure C.1: Li&Ma (1983) significance map of the region around PSR B1055−52 with a correlation radius of 0.5°. The $3\,\sigma$ and $5\,\sigma$ contours are shown in white. The semicircles from which the radial profiles have been extracted are shown in black.

Table C.2: Best-fit parameters for the main dataset and the shuffled dataset, with σ the 1σ containment radius of the gaussian, Γ the spectral index and N_0 the flux normalization at 1 TeV.

	main dataset	shuffled dataset
R.A. [°]	164.12	164.46
Dec. [°]	−51.67	−51.41
σ [°]	1.91 ± 0.23	1.75 ± 0.23
Γ	2.79 ± 0.08	3.20 ± 0.23
N_0 $[10^{-11}\mathrm{cm}^{-2}\,\mathrm{s}^{-1}\,\mathrm{TeV}^{-1}]$	2.15 ± 0.40	1.38 ± 0.34

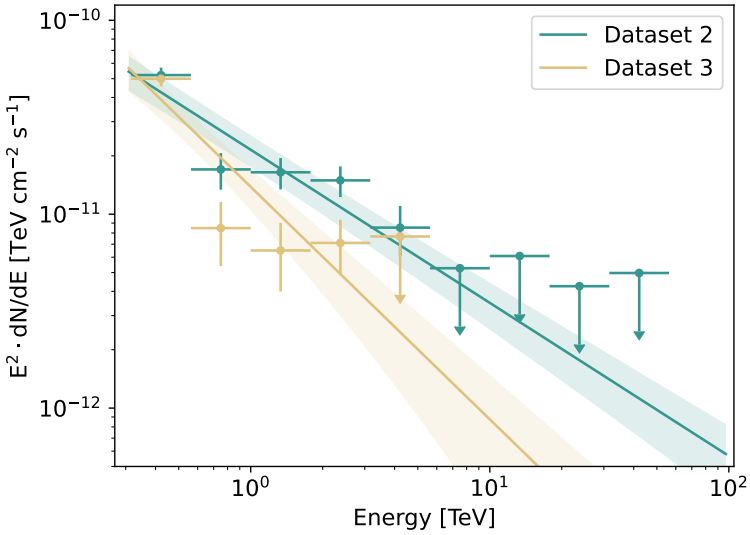

Figure C.2: SED computed from the Gaussian model applied to Dataset 2 and the shuffled Dataset 3, respectively.

C.3 Shuffled dataset

To gauge the level of systematic uncertainty introduced on the source parameters due to the background estimation, a dataset with a randomly shuffled run list was created. Then, a Gaussian source with a power law was fitted to the data. The best-fit parameters and statistical uncertainties can be seen in Table C.2. A visual comparison of the SED from both datasets can be seen in Figure C.2

C.4 *Fermi*-LAT data analysis

The ROI used for the analysis of the *Fermi*-LAT data contains several known γ-ray sources, which need to be excluded from the background fit. The identification of the exclusion regions was performed iteratively. After the addition of an exclusion region, the background models were fit to the ROI, and a distribution of the Li&Ma (1983) significance in each pixel outside of the exclusion region was extracted. After each iteration, further regions were excluded until a Gaussian fit to the significance

Table C.3: Exclusion regions used for the fit of the background models for the analysis of the *Fermi*-LAT data. In addition to the morphology of the exclusion regions, the closest known γ-ray source is indicated. In the case of a circular model, the height parameter corresponds to the radius of the circle. Φ corresponds to the angle of the major axis of the ellipse ot the southern axis.

	R.A. [°]	Dec. [°]	height [°]	width [°]	Φ [°]
PSR B1055−52	164.12	−51.67	4.00	–	–
Westerlund 2	158.00	−58.80	9.00	4.00	30.00
4FGL J1125.0−5804	171.30	−58.30	0.50	–	–
4FGL J1129.1−5230	172.20	−52.30	0.50	–	–
4FGL J1132.2−4736	173.00	−47.70	0.50	–	–

distribution yielded a mean of mean of $\mu = -0.09$ and a standard deviation of $\sigma = 1.09$, which is consistent with a background-only hypothesis and indicates a good estimation of the background. The exclusion regions are listed in Table C.3 and visualized in Figure C.3.

C.5 Joint-modeling with *Fermi*-LAT data

In addition to the analysis of the separate datasets, a joint model between *Fermi*-LAT data above 10 GeV and H.E.S.S. data above 360 GeV has been conducted for both datasets. For the morphological description of the emission, a Gaussian model has been used with a fixed position to the centre of gravity of the emission derived in the analysis of Dataset 2. For the joint analysis using Dataset 1, the position of the Gaussian model is included as a fit parameter. Different spectral models have been used. The top panel in Figure C.4 shows a simple power-law model, which is not able to describe the shape of the SED well. The middle panel of Figure C.4 shows a logarithmic parabola model and the bottom panel a broken power law model. For the joint-fit using Dataset 1, the likelihood minimization did not converge, and no reliable errors on the fit parameters could be derived. The fit parameters for all models are shown in Table C.4, Table **??**, and Table **??**.

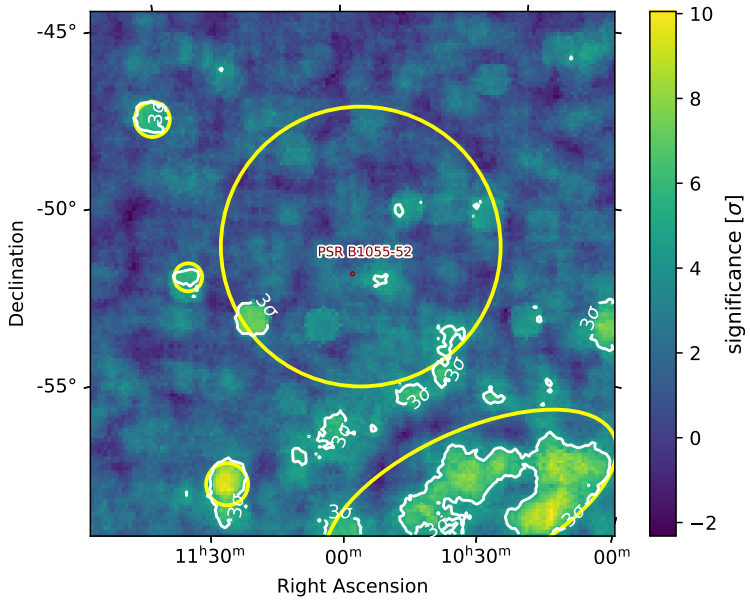

Figure C.3: Li&Ma (1983) significance map of the *Fermi*-LAT data, computed without any exclusion regions for the fit of the background models. A correlation radius of 0.5° was used. The $5\,\sigma$ contours are shown in white, and the exclusion regions listed in Table C.3 are shown in yellow.

Table C.4: Best-fit parameters derived from the joint model using the *Fermi*-LAT data and the two different H.E.S.S. datasets for a simple power-law model (left), a logarithmic parabola model (middle) and a broken power-law model (right). The significances of all three models compared to the best-fit logarithmic parabola model can be seen in Table 6.9.

	Dataset 1	Dataset 2	Dataset 1	Dataset 2	Dataset 1	Dataset 2
Γ_1	1.96 ± 0.04	1.89 ± 0.04	1.98 ± 0.06	2.15 ± 0.13	1.54	0.00 ± 0.00
Γ_2	$--$	$--$	$--$	$--$	3.54	2.83 ± 0.10
E_{break} [TeV]	$--$	$--$	$--$	$--$	3.16	0.48 ± 0.01
$\mathrm{N}_0 \cdot 10^{-11}$ $[\mathrm{cm}^{-2}\,\mathrm{s}^{-1}\,\mathrm{TeV}^{-1}]$	1.63 ± 0.36	4.50 ± 2.30	4.17 ± 0.86	4.31 ± 0.81	0.86	25.50 ± 5.70
R.A. [°]	162.50 ± 0.01	164.12	162.50 ± 0.01	164.12	162.50	164.12
Dec. [°]	-54.45 ± 0.01	-51.67	-54.45 ± 0.01	-51.67	-54.45	-51.67
σ_M [°]	4.87 ± 0.71	9.68 ± 2.70	4.45 ± 0.55	2.67 ± 0.31	4.92	2.47 ± 0.34

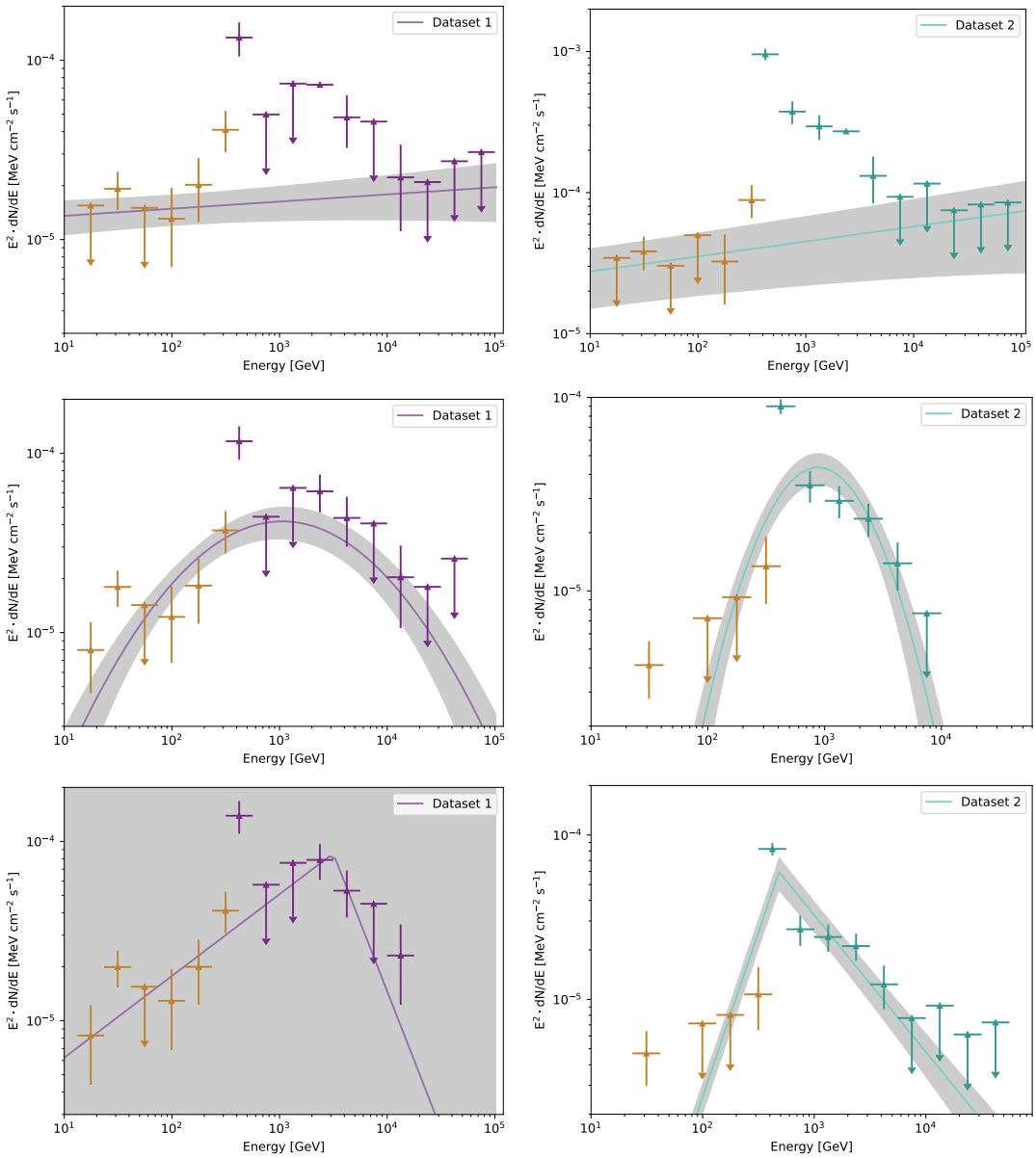

Figure C.4: SED computed from the joint-fit of the *Fermi*-LAT data with Dataset 1 and Dataset 2 respectively, using different spectral models: simple power-law model (top), logarithmic parabola model (middle), broken power-law model (bottom). While the fit of the broken-power law model converges, the uncertainties are unreliable and the model is not a good description of the region. It is therefore not considered as a spectral model to describe the emission.

Bibliography

Aab, A., P. Abreu, M. Aglietta, J. M. Albury, et al. (Sept. 2020). "Features of the Energy Spectrum of Cosmic Rays above 2.5 $\times 10^{18}$ eV Using the Pierre Auger Observatory". In: *Phys. Rev. Lett.* 125.12, 121106, p. 121106. DOI: 10.1103/PhysRevLett.125.121106. arXiv: 2008.06488 [astro-ph.HE].

Abdalla, H., F. Aharonian, F. Ait Benkhali, E. O. Angüner, et al. (Aug. 2021). "TeV Emission of Galactic Plane Sources with HAWC and H.E.S.S." In: *ApJ* 917.1, 6, p. 6. DOI: 10.3847/1538-4357/abf64b. arXiv: 2107.01425 [astro-ph.IM].

Abdallah, H., R. Adam, F. Aharonian, F. Ait Benkhali, et al. (Sept. 2020). "Search for dark matter signals towards a selection of recently detected DES dwarf galaxy satellites of the Milky Way with H.E.S.S." In: *Phys. Rev. D* 102.6, 062001, p. 062001. DOI: 10.1103/PhysRevD.102.062001. arXiv: 2008.00688 [astro-ph.HE].

Abdo, A. A., M. Ackermann, M. Ajello, W. B. Atwood, et al. (Aug. 2009a). "A Population of Gamma-Ray Millisecond Pulsars Seen with the Fermi Large Area Telescope". In: *Science* 325.5942, p. 848. DOI: 10.1126/science.1176113.

Abdo, A. A., M. Ackermann, M. Ajello, L. Baldini, et al. (June 2011). "Fermi Large Area Telescope Observations of Two Gamma-Ray Emission Components from the Quiescent Sun". In: *ApJ* 734.2, 116, p. 116. DOI: 10.1088/0004-637X/734/2/116. arXiv: 1104.2093 [astro-ph.HE].

Abdo, A. A., B. T. Allen, T. Aune, D. Berley, et al. (Aug. 2009b). "Milagro Observations of Multi-TeV Emission from Galactic Sources in the Fermi Bright Source List". In: *ApJ* 700.2, pp. L127–L131. DOI: 10.1088/0004-637X/700/2/L127. arXiv: 0904.1018 [astro-ph.HE].

Abdollahi, S., F. Acero, M. Ackermann, M. Ajello, et al. (Mar. 2020). "Fermi Large Area Telescope Fourth Source Catalog". In: *ApJS* 247.1, 33, p. 33. DOI: 10.3847/1538-4365/ab6bcb. arXiv: 1902.10045 [astro-ph.HE].

Abeysekara, A. (July 2019). "Search for very high energy (E ¿ 100 GeV) Emission from Geminga supernova by VERITAS". In: *36th International Cosmic Ray Conference (ICRC2019)*. Vol. 36. International Cosmic Ray Conference, 616, p. 616. DOI: 10.22323/1.358.0616. arXiv: 1908.05369 [astro-ph.HE].

Abeysekara, A. U., A. Albert, R. Alfaro, C. Alvarez, et al. (July 2017a). "Observation of the Crab Nebula with the HAWC Gamma-Ray Observatory". In: *ApJ* 843.1, 39, p. 39. DOI: 10.3847/1538-4357/aa7555. arXiv: 1701.01778 [astro-ph.HE].

Abeysekara, A. U., A. Albert, R. Alfaro, C. Alvarez, et al. (July 2017b). "The 2HWC HAWC Observatory Gamma-Ray Catalog". In: *ApJ* 843.1, 40, p. 40. DOI: 10.3847/1538-4357/aa7556. arXiv: 1702.02992 [astro-ph.HE].

Abeysekara, A. U., A. Albert, R. Alfaro, C. Alvarez, et al. (July 2023). "The High-Altitude Water Cherenkov (HAWC) observatory in México: The primary detector". In: *Nuclear Instruments and Methods in Physics Research A* 1052, 168253, p. 168253. DOI: 10.1016/j.nima.2023.168253. arXiv: 2304.00730 [astro-ph.HE].

Abeysekara, A. U., R. Alfaro, C. Alvarez, J. C. Arteaga-Velázquez, et al. (Feb. 2025). "Absence of TeV halos around millisecond pulsars". In: *Phys. Rev. D* 111.4, 043014, p. 043014. DOI: 10.1103/PhysRevD.111.043014.

Abramowski, A., F. Acero, F. Aharonian, A. G. Akhperjanian, et al. (Jan. 2012). "Discovery of extended VHE γ-ray emission from the vicinity of the young massive stellar cluster Westerlund 1". In: *A&A* 537, A114, A114. DOI: 10.1051/0004-6361/201117928. arXiv: 1111.2043 [astro-ph.HE].

Abramowski, A., F. Aharonian, F. Ait Benkhali, A. G. Akhperjanian, et al. (Dec. 2014a). "Diffuse Galactic gamma-ray emission with H.E.S.S." In: *Phys. Rev. D* 90.12, 122007, p. 122007. DOI: 10.1103/PhysRevD.90.122007. arXiv: 1411.7568 [astro-ph.HE].

Abramowski, A., F. Aharonian, F. Ait Benkhali, A. G. Akhperjanian, et al. (Dec. 2014b). "Search for dark matter annihilation signatures in H.E.S.S. observations of dwarf spheroidal galaxies". In: *Phys. Rev. D* 90.11, 112012, p. 112012. DOI: 10.1103/PhysRevD.90.112012. arXiv: 1410.2589 [astro-ph.HE].

Acero, F., M. Ackermann, M. Ajello, A. Albert, et al. (June 2015). "Fermi Large Area Telescope Third Source Catalog". In: *ApJS* 218.2, 23, p. 23. DOI: 10.1088/0067-0049/218/2/23. arXiv: 1501.02003 [astro-ph.HE].

Acero, F., M. Ackermann, M. Ajello, A. Albert, et al. (Apr. 2016). "Development of the Model of Galactic Interstellar Emission for Standard Point-source Analysis of Fermi Large Area Telescope Data". In: *ApJS* 223.2, 26, p. 26. DOI: 10.3847/0067-0049/223/2/26. arXiv: 1602.07246 [astro-ph.HE].

Acero, F., F. Aharonian, A. G. Akhperjanian, G. Anton, et al. (Mar. 2010). "Localizing the VHE γ-ray source at the Galactic Centre". In: *MNRAS* 402.3, pp. 1877–1882. DOI: 10.1111/j.1365-2966.2009.16014.x. arXiv: 0911.1912 [astro-ph.GA].

Acero, Fabio, Juan Bernete, Noah Biederbeck, Julia Djuvsland, et al. (Feb. 2024). *Gammapy: Python toolbox for gamma-ray astronomy*. Version v1.2. DOI: 10.5281/zenodo.10726484. URL: https://doi.org/10.5281/zenodo.10726484.

Ackermann, M., M. Ajello, A. Albert, W. B. Atwood, et al. (Apr. 2016). "Measurement of the high-energy gamma-ray emission from the Moon with the Fermi Large Area Telescope". In: *Phys. Rev. D* 93.8, 082001, p. 082001. DOI: 10.1103/PhysRevD.93.082001. arXiv: 1604.03349 [astro-ph.HE].

Ackermann, M., M. Ajello, W. B. Atwood, L. Baldini, et al. (May 2012). "Fermi-LAT Observations of the Diffuse γ-Ray Emission: Implications for Cosmic Rays and the Interstellar Medium". In: *ApJ* 750.1, 3, p. 3. DOI: 10.1088/0004-637X/750/1/3. arXiv: 1202.4039 [astro-ph.HE].

Aguilar, M., G. Alberti, B. Alpat, A. Alvino, et al. (Apr. 2013). "First Result from the Alpha Magnetic Spectrometer on the International Space Station: Precision Measurement of the Positron Fraction in Primary Cosmic Rays of 0.5-350 GeV". In: *Phys. Rev. Lett.* 110.14, 141102, p. 141102. DOI: 10.1103/PhysRevLett.110.141102.

Aharonian, F., F. Ait Benkhali, J. Aschersleben, H. Ashkar, et al. (June 2024). "Spectrum and extension of the inverse-Compton emission of the Crab Nebula from a combined

Fermi-LAT and H.E.S.S. analysis". In: *A&A* 686, A308, A308. DOI: 10.1051/0004-6361/202348651. arXiv: 2403.12608 [astro-ph.HE].

Aharonian, F., A. G. Akhperjanian, K. M. Aye, A. R. Bazer-Bachi, et al. (Nov. 2004). "Calibration of cameras of the H.E.S.S. detector". In: *Astroparticle Physics* 22.2, pp. 109–125. DOI: 10.1016/j.astropartphys.2004.06.006. arXiv: astro-ph/0406658 [astro-ph].

Aharonian, F., A. G. Akhperjanian, K. M. Aye, A. R. Bazer-Bachi, et al. (May 2005). "Discovery of extended VHE gamma-ray emission from the asymmetric pulsar wind nebula in MSH 15-52 with HESS". In: *A&A* 435.1, pp. L17–L20. DOI: 10.1051/0004-6361:200500105. arXiv: astro-ph/0504120 [astro-ph].

Aharonian, F., A. G. Akhperjanian, J. A. Barrio, K. Bernlöhr, et al. (June 1999). "Phase-resolved TeV gamma-ray characteristics of the Crab and Geminga pulsars". In: *A&A* 346, pp. 913–921.

Aharonian, F., A. G. Akhperjanian, A. R. Bazer-Bachi, B. Behera, et al. (Sept. 2007). "Discovery of two candidate pulsar wind nebulae in very-high-energy gamma rays". In: *A&A* 472.2, pp. 489–495. DOI: 10.1051/0004-6361:20077280. arXiv: 0705.1605 [astro-ph].

Aharonian, F., A. G. Akhperjanian, A. R. Bazer-Bachi, M. Beilicke, et al. (Oct. 2006a). "Observations of the Crab nebula with HESS". In: *A&A* 457.3, pp. 899–915. DOI: 10.1051/0004-6361:20065351. arXiv: astro-ph/0607333 [astro-ph].

— (Oct. 2006b). "Observations of the Crab nebula with HESS". In: *A&A* 457.3, pp. 899–915. DOI: 10.1051/0004-6361:20065351. arXiv: astro-ph/0607333 [astro-ph].

Aharonian, F., A. G. Akhperjanian, A. R. Bazer-Bachi, M. Beilicke, et al. (Jan. 2006c). "The H.E.S.S. Survey of the Inner Galaxy in Very High Energy Gamma Rays". In: *ApJ* 636.2, pp. 777–797. DOI: 10.1086/498013. arXiv: astro-ph/0510397 [astro-ph].

Aharonian, F. A., A. M. Atoyan, and T. Kifune (Oct. 1997). "Inverse Compton gamma radiation of faint synchrotron X-ray nebulae around pulsars". In: *MNRAS* 291.1, pp. 162–176. DOI: 10.1093/mnras/291.1.162.

Aharonian, Felix A. (2004). *Very high energy cosmic gamma radiation : a crucial window on the extreme Universe*. Chap. 3. DOI: 10.1142/4657.

Ajello, M., W. B. Atwood, M. Axelsson, R. Bagagli, et al. (Sept. 2021). "Fermi Large Area Telescope Performance after 10 Years of Operation". In: *ApJS* 256.1, 12, p. 12. DOI: 10.3847/1538-4365/ac0ceb. arXiv: 2106.12203 [astro-ph.IM].

Akerlof, C. W., A. C. Breslin, M. F. Cawley, M. Chantell, et al. (July 1993). "Search for TeV gamma-rays from Geminga." In: *A&A* 274, pp. L17–L20.

Alavipanah, Seyed Kazem, Hamid reza Matinfar, Ammar Rafiei Emam, Kamal Khodaei, et al. (June 2008). "Criteria of selecting satellite data for studying land resources". In.

Albert, A., R. Alfaro, C. Alvarez, J. R. Angeles Camacho, et al. (Dec. 2020). "3HWC: The Third HAWC Catalog of Very-high-energy Gamma-Ray Sources". In: *ApJ* 905.1, 76, p. 76. DOI: 10.3847/1538-4357/abc2d8. arXiv: 2007.08582 [astro-ph.HE].

Albert, J., E. Aliu, H. Anderhub, P. Antoranz, et al. (Jan. 2006). "MAGIC Observations of Very High Energy γ-Rays from HESS J1813-178". In: *ApJ* 637.1, pp. L41–L44. DOI: 10.1086/500364. arXiv: astro-ph/0512283 [astro-ph].

Alfvén, H. (Oct. 1942). "Existence of Electromagnetic-Hydrodynamic Waves". In: *Nature* 150.3805, pp. 405–406. DOI: 10.1038/150405d0.

Alves Batista, Rafael, Jonathan Biteau, Mauricio Bustamante, Klaus Dolag, et al. (June 2019a). "Open Questions in Cosmic-Ray Research at Ultrahigh Energies". In: *Frontiers in Astronomy and Space Sciences* 6, 23, p. 23. DOI: 10.3389/fspas.2019.00023. arXiv: 1903.06714 [astro-ph.HE].

— (June 2019b). "Open Questions in Cosmic-Ray Research at Ultrahigh Energies". In: *Frontiers in Astronomy and Space Sciences* 6, 23, p. 23. DOI: 10.3389/fspas.2019.00023. arXiv: 1903.06714 [astro-ph.HE].

Amato, E., D. Guetta, and P. Blasi (May 2003a). "Signatures of high energy protons in pulsar winds". In: *A&A* 402, pp. 827–836. DOI: 10.1051/0004-6361:20030279. arXiv: astro-ph/0302121 [astro-ph].

— (May 2003b). "Signatures of high energy protons in pulsar winds". In: *A&A* 402, pp. 827–836. DOI: 10.1051/0004-6361:20030279. arXiv: astro-ph/0302121 [astro-ph].

Amato, Elena and Sabrina Casanova (Feb. 2021). "On particle acceleration and transport in plasmas in the Galaxy: theory and observations". In: *Journal of Plasma Physics* 87.1, 845870101, p. 845870101. DOI: 10.1017/S0022377821000064. arXiv: 2104.12428 [astro-ph.HE].

Apel, W. D., J. C. Arteaga-Velázquez, K. Bekk, M. Bertaina, et al. (Oct. 2011). "Kneelike Structure in the Spectrum of the Heavy Component of Cosmic Rays Observed with KASCADE-Grande". In: *Phys. Rev. Lett.* 107.17, 171104, p. 171104. DOI: 10.1103/PhysRevLett.107.171104. arXiv: 1107.5885 [astro-ph.HE].

Araya, Miguel (May 2018). "GeV Emission in the Region of HESS J1809-193 and HESS J1813-178: Is HESS J1809-193 a Proton Pevatron?" In: *ApJ* 859.1, 69, p. 69. DOI: 10.3847/1538-4357/aabd7e. arXiv: 1804.03325 [astro-ph.HE].

Archibald, R. F., E. V. Gotthelf, R. D. Ferdman, V. M. Kaspi, et al. (Mar. 2016). "A High Braking Index for a Pulsar". In: *ApJ* 819.1, L16, p. L16. DOI: 10.3847/2041-8205/819/1/L16. arXiv: 1603.00305 [astro-ph.HE].

Atwood, W. B., A. A. Abdo, M. Ackermann, W. Althouse, et al. (June 2009a). "The Large Area Telescope on the Fermi Gamma-Ray Space Telescope Mission". In: *ApJ* 697.2, pp. 1071–1102. DOI: 10.1088/0004-637X/697/2/1071. arXiv: 0902.1089 [astro-ph.IM].

Atwood, W. B., A. A. Abdo, M. Ackermann, W. Althouse, et al. (June 2009b). "The Large Area Telescope on the Fermi Gamma-Ray Space Telescope Mission". In: *ApJ*

697.2, pp. 1071–1102. DOI: 10.1088/0004-637X/697/2/1071. arXiv: 0902.1089 [astro-ph.IM].

Aye, K. M., P. M. Chadwick, C. Hadjichristidis, M. K. Daniel, et al. (July 2003). "Atmospheric Monitoring for the H.E.S.S. Project". In: *International Cosmic Ray Conference*. Vol. 5. International Cosmic Ray Conference, p. 2879.

Baade, W. and F. Zwicky (May 1934). "Cosmic Rays from Super-novae". In: *Proceedings of the National Academy of Science* 20.5, pp. 259–263. DOI: 10.1073/pnas.20.5.259.

Bambi, Cosimo and Andrea Santangelo, eds. (2024). *Handbook of X-ray and Gamma-ray Astrophysics*. Springer. ISBN: 978-981-16-4544-0. DOI: 10.1007/978-981-16-4544-0.

Bartoli, B., P. Bernardini, X. J. Bi, P. Branchini, et al. (Aug. 2014). "Identification of the TeV Gamma-Ray Source ARGO J2031+4157 with the Cygnus Cocoon". In: *ApJ* 790.2, 152, p. 152. DOI: 10.1088/0004-637X/790/2/152. arXiv: 1406.6436 [astro-ph.HE].

Becker, W. and J. Truemper (Oct. 1997). "The X-ray luminosity of rotation-powered neutron stars." In: *A&A* 326, pp. 682–691. DOI: 10.48550/arXiv.astro-ph/9708169. arXiv: astro-ph/9708169 [astro-ph].

Becker Tjus, Julia and Lukas Merten (Aug. 2020). "Closing in on the origin of Galactic cosmic rays using multimessenger information". In: *Phys. Rep.* 872, pp. 1–98. DOI: 10.1016/j.physrep.2020.05.002. arXiv: 2002.00964 [astro-ph.HE].

Bell, A. R. (Mar. 2013). "Cosmic ray acceleration". In: *Astroparticle Physics* 43, pp. 56–70. DOI: 10.1016/j.astropartphys.2012.05.022.

Berge, D., S. Funk, and J. Hinton (May 2007). "Background modelling in very-high-energy γ-ray astronomy". In: *A&A* 466.3, pp. 1219–1229. DOI: 10.1051/0004-6361:20066674. arXiv: astro-ph/0610959 [astro-ph].

Bernlöhr, K., O. Carrol, R. Cornils, S. Elfahem, et al. (Nov. 2003). "The optical system of the H.E.S.S. imaging atmospheric Cherenkov telescopes. Part I: layout and components of the system". In: *Astroparticle Physics* 20.2, pp. 111–128. DOI: 10.1016/S0927-6505(03)00171-3. arXiv: astro-ph/0308246 [astro-ph].

Bernlöhr, Konrad (Oct. 2008a). "Simulation of imaging atmospheric Cherenkov telescopes with CORSIKA and sim_telarray". In: *Astroparticle Physics* 30.3, pp. 149–158. DOI: 10.1016/j.astropartphys.2008.07.009. arXiv: 0808.2253 [astro-ph].

— (Oct. 2008b). "Simulation of imaging atmospheric Cherenkov telescopes with CORSIKA and sim_telarray". In: *Astroparticle Physics* 30.3, pp. 149–158. DOI: 10.1016/j.astropartphys.2008.07.009. arXiv: 0808.2253 [astro-ph].

Beskin, V. S. and A. Yu Istomin (Nov. 2022). "Pulsar death line revisited - II. 'The death valley'". In: *MNRAS* 516.4, pp. 5084–5091. DOI: 10.1093/mnras/stac2423. arXiv: 2207.04723 [astro-ph.HE].

Beskin, V. S. and P. E. Litvinov (Feb. 2022). "Pulsar death line revisited - I. Almost vacuum gap". In: *MNRAS* 510.2, pp. 2572–2582. DOI: 10.1093/mnras/stab3575. arXiv: 2201.02875 [astro-ph.HE].

Bethe, H. A. and J. R. Wilson (Aug. 1985). "Revival of a stalled supernova shock by neutrino heating". In: *ApJ* 295, pp. 14–23. DOI: 10.1086/163343.

Bi, B., M. Barcelo, C. Bauer, F. A. Benkhali, et al. (Mar. 2022). "Performance of the new FlashCam-based camera in the 28m telescope of H.E.S.S." In: *37th International Cosmic Ray Conference*, 743, p. 743. DOI: 10.22323/1.395.0743. arXiv: 2108.03046 [astro-ph.IM].

Bietenholz, M. F., J. J. Hester, D. A. Frail, and N. Bartel (Nov. 2004). "The Crab Nebula's Wisps in Radio and Optical". In: *ApJ* 615.2, pp. 794–804. DOI: 10.1086/424653. arXiv: astro-ph/0408061 [astro-ph].

Blasi, Pasquale (Apr. 2014). "Origin of very high- and ultra-high-energy cosmic rays". In: *Comptes Rendus Physique* 15.4, pp. 329–338. DOI: 10.1016/j.crhy.2014.02.008. arXiv: 1403.2967 [astro-ph.HE].

Bolmont, J., P. Corona, P. Gauron, P. Ghislain, et al. (Oct. 2014). "The camera of the fifth H.E.S.S. telescope. Part I: System description". In: *Nuclear Instruments and Methods in Physics Research A* 761, pp. 46–57. DOI: 10.1016/j.nima.2014.05.093. arXiv: 1310.5877 [astro-ph.IM].

Bradbury, Stella (Jan. 1999). "The Very Energetic Radiation Imaging Telescope Array System (VERITAS)". In: *26th International Cosmic Ray Conference (ICRC26), Volume 5*. Ed. by D. Kieda, M. Salamon, and B. Dingus. Vol. 5. International Cosmic Ray Conference, p. 280. DOI: 10.48550/arXiv.astro-ph/9907248. arXiv: astro-ph/9907248 [astro-ph].

Brogan, C. L., B. M. Gaensler, J. D. Gelfand, J. S. Lazendic, et al. (Aug. 2005). "Discovery of a Radio Supernova Remnant and Nonthermal X-Rays Coincident with the TeV Source HESS J1813-178". In: *ApJ* 629.2, pp. L105–L108. DOI: 10.1086/491471. arXiv: astro-ph/0505145 [astro-ph].

Bucciantini, N., J. Arons, and E. Amato (Dec. 2010). "Modelling spectral evolution of pulsar wind nebulae inside supernova remnants". In: *Monthly Notices of the Royal Astronomical Society* 410.1, pp. 381–398. ISSN: 0035-8711. DOI: 10.1111/j.1365-2966.2010.17449.x. eprint: https://academic.oup.com/mnras/article-pdf/410/1/381/18446661/mnras0410-0381.pdf. URL: https://doi.org/10.1111/j.1365-2966.2010.17449.x.

Bütikofer, R. (2018). "Cosmic Ray Particle Transport in the Earth's Magnetosphere". In: *Solar Particle Radiation Storms Forecasting and Analysis: The HESPERIA HORIZON 2020 Project and Beyond*. Ed. by Olga E. Malandraki and Norma B. Crosby. Cham: Springer International Publishing, pp. 79–94. ISBN: 978-3-319-60051-2. DOI: 10.1007/978-3-319-60051-2_5. URL: https://doi.org/10.1007/978-3-319-60051-2_5.

Bykov, A. M., E. Amato, A. E. Petrov, A. M. Krassilchtchikov, and K. P. Levenfish (July 2017). "Pulsar Wind Nebulae with Bow Shocks: Non-thermal Radiation and Cosmic Ray Leptons". In: *Space Sci. Rev.* 207.1-4, pp. 235–290. DOI: 10.1007/s11214-017-0371-7. arXiv: 1705.00950 [astro-ph.HE].

Camilo, F., S. M. Ransom, J. P. Halpern, and D. Anish Roshi (Aug. 2021). "Radio Detection of PSR J1813-1749 in HESS J1813-178: The Most Scattered Pulsar Known". In: *ApJ* 917.2, 67, p. 67. DOI: 10.3847/1538-4357/ac0720. arXiv: 2106.00386 [astro-ph.HE].

Cao, Zhen, F. Aharonian, Q. An, Axikegu, et al. (May 2023a). "The First LHAASO Catalog of Gamma-Ray Sources". In: *arXiv e-prints*, arXiv:2305.17030, arXiv:2305.17030. DOI: 10.48550/arXiv.2305.17030. arXiv: 2305.17030 [astro-ph.HE].

— (Nov. 2023b). "Very high-energy gamma-ray emission beyond 10 TeV from GRB 221009A". In: *Science Advances* 9.46, eadj2778, eadj2778. DOI: 10.1126/sciadv.adj2778. arXiv: 2310.08845 [astro-ph.HE].

Cao, Zhen, F. Aharonian, Q. An, Bai Axikegu Y. X., et al. (Oct. 2023c). "Measurement of Ultra-High-Energy Diffuse Gamma-Ray Emission of the Galactic Plane from 10 TeV to 1 PeV with LHAASO-KM2A". In: *Phys. Rev. Lett.* 131.15, 151001, p. 151001. DOI: 10.1103/PhysRevLett.131.151001. arXiv: 2305.05372 [astro-ph.HE].

Cao, Zhen, F. Aharonian, Y. X. Bai, Y. W. Bao, et al. (Feb. 2025). "Ultra-high-energy γ-ray emission associated with the tail of a bow-shock pulsar wind nebula". In: *arXiv e-prints*, arXiv:2502.15447, arXiv:2502.15447. DOI: 10.48550/arXiv.2502.15447. arXiv: 2502.15447 [astro-ph.HE].

Cao, Zhen, D. della Volpe, Siming Liu, Editors, et al. (May 2019). "The Large High Altitude Air Shower Observatory (LHAASO) Science Book (2021 Edition)". In: *arXiv e-prints*, arXiv:1905.02773, arXiv:1905.02773. DOI: 10.48550/arXiv.1905.02773. arXiv: 1905.02773 [astro-ph.HE].

Caprioli, D. and C. Haggerty (July 2019). "The Issue with Diffusive Shock Acceleration". In: *36th International Cosmic Ray Conference (ICRC2019)*. Vol. 36. International Cosmic Ray Conference, 209, p. 209. DOI: 10.22323/1.358.0209. arXiv: 1909.06288 [astro-ph.HE].

Caprioli, Damiano (July 2023). "Particle Acceleration at Shocks: An Introduction". In: *arXiv e-prints*, arXiv:2307.00284, arXiv:2307.00284. DOI: 10.48550/arXiv.2307.00284. arXiv: 2307.00284 [astro-ph.HE].

Cardillo, Martina, Elena Amato, and Pasquale Blasi (Sept. 2015). "On the cosmic ray spectrum from type II supernovae expanding in their red giant presupernova wind". In: *Astroparticle Physics* 69, pp. 1–10. DOI: 10.1016/j.astropartphys.2015.03.002. arXiv: 1503.03001 [astro-ph.HE].

Celli, S., A. Specovius, S. Menchiari, A. Mitchell, and G. Morlino (June 2024). "Mass and wind luminosity of young Galactic open clusters in Gaia DR2". In: *A&A* 686, A118, A118. DOI: 10.1051/0004-6361/202348541. arXiv: 2311.09089 [astro-ph.GA].

Chandrasekhar, S. (July 1931). "The Maximum Mass of Ideal White Dwarfs". In: *ApJ* 74, p. 81. DOI: 10.1086/143324.

Chandrasekhar, Subrahmanyan (1961). *Hydrodynamic and hydromagnetic stability*.

Cherenkov Telescope Array Consortium, B. S. Acharya, I. Agudo, I. Al Samarai, et al. (2019). *Science with the Cherenkov Telescope Array*. DOI: 10.1142/10986.

Cocconi, G. (Jan. 1960). "An air shower telescope and the detection of 10^{12} eV photon sources". In: *International Cosmic Ray Conference*. Vol. 2. International Cosmic Ray Conference, p. 309.

Cordes, J. M. and T. J. W. Lazio (July 2002). "NE2001.I. A New Model for the Galactic Distribution of Free Electrons and its Fluctuations". In: *arXiv e-prints*, astro-ph/0207156, astro–ph/0207156. DOI: 10.48550/arXiv.astro-ph/0207156. arXiv: astro-ph/0207156 [astro-ph].

Dame, T. M. and P. Thaddeus (Dec. 2004). "A Large Extension of the CfA Galactic CO Survey". In: *Milky Way Surveys: The Structure and Evolution of our Galaxy*. Ed. by Dan Clemens, Ronak Shah, and Teresa Brainerd. Vol. 317. Astronomical Society of the Pacific Conference Series, p. 66. DOI: 10.48550/arXiv.astro-ph/0310102. arXiv: astro-ph/0310102 [astro-ph].

Dawson, Joanne R., Akiko Kawamura, Norikazu Mizuno, Toshikazu Onishi, and Yasuo Fukui (Dec. 2008). "Catalogue of 12CO(J = 10) and 13CO(J = 10) Molecular Clouds in the Carina Flare Supershell". In: *Publications of the Astronomical Society of Japan* 60.6, pp. 1297–1315. ISSN: 0004-6264. DOI: 10.1093/pasj/60.6.1297. eprint: https://academic.oup.com/pasj/article-pdf/60/6/1297/54715220/pasj_60_6_1297.pdf. URL: https://doi.org/10.1093/pasj/60.6.1297.

de Jager, O. C. (May 2008). "Estimating the Birth Period of Pulsars through GLAST LAT Observations of Their Wind Nebulae". In: *ApJ* 678.2, p. L113. DOI: 10.1086/588283. arXiv: 0803.2104 [astro-ph].

de la Torre Luque, Pedro (Feb. 2022). "Cosmic-ray propagation and production of secondary particles in the Galaxy". In: *arXiv e-prints*, arXiv:2202.07063, arXiv:2202.07063. DOI: 10.48550/arXiv.2202.07063. arXiv: 2202.07063 [astro-ph.HE].

de Vega, H. J. and N. Sanchez (2003). "Extreme Energy Cosmic Rays: Bottom-up vs. Top-down scenarii". In: *The Early Universe and the Cosmic Microwave Background: Theory and Observations*. Ed. by Norma G. Sánchez and Yuri N. Parijskij. Vol. 130, p. 433. DOI: 10.48550/arXiv.astro-ph/0301039.

Deil, Christoph, Axel Donath, Régis Terrier, Jose Enrique Ruiz, et al. (Nov. 2020). *gammapy/gammapy: v.0.18.2*. Version v0.18.2. DOI: 10.5281/zenodo.4701500. URL: https://doi.org/10.5281/zenodo.4701500.

Delahaye, T., J. Lavalle, R. Lineros, F. Donato, and N. Fornengo (2010). "Galactic electrons and positrons at the Earth: new estimate of the primary and secondary fluxes". In: *Astronomy Astrophysics* 524, A51. DOI: 10.1051/0004-6361/201014225. arXiv: 1002.1910 [astro-ph.HE].

Dermer, Charles Dennison and Berrie Giebels (June 2016). "Active galactic nuclei at gamma-ray energies". In: *Comptes Rendus Physique* 17.6, pp. 594–616. DOI: 10.1016/j.crhy.2016.04.004. arXiv: 1602.06592 [astro-ph.HE].

Di Mauro, Mattia, Silvia Manconi, and Fiorenza Donato (Dec. 2019). "Detection of a γ -ray halo around Geminga with the Fermi-LAT data and implications for the positron flux". In: *Phys. Rev. D* 100.12, 123015, p. 123015. DOI: 10.1103/PhysRevD.100.123015. arXiv: 1903.05647 [astro-ph.HE].

Diesing, Rebecca and Damiano Caprioli (Aug. 2019). "Spectrum of Electrons Accelerated in Supernova Remnants". In: *Phys. Rev. Lett.* 123.7, 071101, p. 071101. DOI: 10.1103/PhysRevLett.123.071101. arXiv: 1905.07414 [astro-ph.HE].

Donath, Axel, Régis Terrier, Quentin Remy, Atreyee Sinha, et al. (2023). "Gammapy: A Python package for gamma-ray astronomy". In: *A&A* 678, A157. DOI: 10.1051/0004-6361/202346488. URL: https://doi.org/10.1051/0004-6361/202346488.

Dubus, Guillaume (Aug. 2015). "Gamma-ray emission from binaries in context". In: *Comptes Rendus Physique* 16.6-7, pp. 661–673. DOI: 10.1016/j.crhy.2015.08.014. arXiv: 1507.00935 [astro-ph.HE].

Dwek, Eli and Frank Krennrich (Mar. 2013). "The extragalactic background light and the gamma-ray opacity of the universe". In: *Astroparticle Physics* 43, pp. 112–133. DOI: 10.1016/j.astropartphys.2012.09.003. arXiv: 1209.4661 [astro-ph.CO].

Dzib, Sergio A. and Luis F. Rodríguez (Dec. 2021). "Radio Proper Motions of the Energetic Pulsar PSR J1813-1749". In: *ApJ* 923.2, 228, p. 228. DOI: 10.3847/1538-4357/ac312f. arXiv: 2110.09727 [astro-ph.HE].

Fang, Kun (Oct. 2022a). "Gamma-ray pulsar halos in the Galaxy". In: *Frontiers in Astronomy and Space Sciences* 9, 1022100, p. 1022100. DOI: 10.3389/fspas.2022.1022100. arXiv: 2209.13294 [astro-ph.HE].

— (Oct. 2022b). "Gamma-ray pulsar halos in the Galaxy". In: *Frontiers in Astronomy and Space Sciences* 9, 1022100, p. 1022100. DOI: 10.3389/fspas.2022.1022100. arXiv: 2209.13294 [astro-ph.HE].

Fang, Kun, Xiao-Jun Bi, and Peng-Fei Yin (Sept. 2019). "Possible origin of the slow-diffusion region around Geminga". In: *MNRAS* 488.3, pp. 4074–4080. DOI: 10.1093/mnras/stz1974. arXiv: 1903.06421 [astro-ph.HE].

Fang, Kun, Shao-Qiang Xi, Li-Zhuo Bao, Xiao-Jun Bi, and En-Sheng Chen (Dec. 2022). "Features of the gamma-ray pulsar halo HESS J 1831 -098". In: *Phys. Rev. D* 106.12, 123017, p. 123017. DOI: 10.1103/PhysRevD.106.123017. arXiv: 2207.13533 [astro-ph.HE].

Fegan, S. (June 2024). "The performance of generalised Davies–Cotton optical systems with infinitesimal mirror facets". In: *Astroparticle Physics* 158, 102948, p. 102948. DOI: 10.1016/j.astropartphys.2024.102948. arXiv: 2411.16434 [astro-ph.IM].

Fermi, E. (Jan. 1954). "Galactic Magnetic Fields and the Origin of Cosmic Radiation." In: *ApJ* 119, p. 1. DOI: 10.1086/145789.

Fermi, Enrico (Apr. 1949). "On the Origin of the Cosmic Radiation". In: *Physical Review* 75.8, pp. 1169–1174. DOI: 10.1103/PhysRev.75.1169.

Fichtel, C. E., D. L. Bertsch, J. Chiang, B. L. Dingus, et al. (Oct. 1994). "The First Energetic Gamma-Ray Experiment Telescope (EGRET) Source Catalog". In: *ApJS* 94, p. 551. DOI: 10.1086/192082.

Fierro, J. M., D. L. Bertsch, K. T. S. Brazier, J. Chiang, et al. (Aug. 1993). "Pulsed High-Energy Gamma Rays from PSR 1055-52". In: *ApJ* 413, p. L27. DOI: 10.1086/186951.

Fisher, R. A. (Jan. 1922a). "On the Mathematical Foundations of Theoretical Statistics". In: *Philosophical Transactions of the Royal Society of London Series A* 222, pp. 309–368. DOI: 10.1098/rsta.1922.0009.

— (Jan. 1922b). "On the Mathematical Foundations of Theoretical Statistics". In: *Philosophical Transactions of the Royal Society of London Series A* 222, pp. 309–368. DOI: 10.1098/rsta.1922.0009.

Flinders, Andrew (2016). "Towards a Detection of the Geminga Supernova Remnant with VERITAS ". In: *Proceedings of The 34th International Cosmic Ray Conference — PoS(ICRC2015)*. Vol. 236, p. 795. DOI: 10.22323/1.236.0795.

Foreman-Mackey, Daniel, David W. Hogg, Dustin Lang, and Jonathan Goodman (Mar. 2013). "emcee: The MCMC Hammer". In: *PASP* 125.925, p. 306. DOI: 10.1086/670067. arXiv: 1202.3665 [astro-ph.IM].

Funk, S., G. Hermann, J. Hinton, D. Berge, et al. (Nov. 2004). "The trigger system of the H.E.S.S. telescope array". In: *Astroparticle Physics* 22.3-4, pp. 285–296. DOI: 10.1016/j.astropartphys.2004.08.001. arXiv: astro-ph/0408375 [astro-ph].

Funk, S., J. A. Hinton, Y. Moriguchi, F. A. Aharonian, et al. (July 2007). "XMM-Newton observations of HESS J1813-178 reveal a composite Supernova remnant". In: *A&A* 470.1, pp. 249–257. DOI: 10.1051/0004-6361:20066779. arXiv: astro-ph/0611646 [astro-ph].

Funk, Stefan (Oct. 2015). "Ground- and Space-Based Gamma-Ray Astronomy". In: *Annual Review of Nuclear and Particle Science* 65, pp. 245–277. DOI: 10.1146/annurev-nucl-102014-022036. arXiv: 1508.05190 [astro-ph.HE].

Gaensler, B. M. and D. A. Frail (July 2000). "A large age for the pulsar B1757-24 from an upper limit on its proper motion". In: *Nature* 406.6792, pp. 158–160. DOI: 10.1038/35018010. arXiv: astro-ph/0005526 [astro-ph].

Gaensler, Bryan M. and Patrick O. Slane (Sept. 2006). "The Evolution and Structure of Pulsar Wind Nebulae". In: *ARA&A* 44.1, pp. 17–47. DOI: 10.1146/annurev.astro.44.051905.092528. arXiv: astro-ph/0601081 [astro-ph].

García, C. R., Diego F. Torres, and Alessandro Patruno (Sept. 2022). "Visualizing the pulsar population using graph theory". In: *MNRAS* 515.3, pp. 3883–3897. DOI: 10.1093/mnras/stac1997. arXiv: 2207.06311 [astro-ph.HE].

Gelfand, Joseph D., Patrick O. Slane, and Weiqun Zhang (Oct. 2009). "A Dynamical Model for the Evolution of a Pulsar Wind Nebula Inside a Nonradiative Supernova Remnant". In: *ApJ* 703.2, pp. 2051–2067. DOI: 10.1088/0004-637X/703/2/2051. arXiv: 0904.4053 [astro-ph.HE].

Giacinti, G., A. M. W. Mitchell, R. López-Coto, V. Joshi, et al. (Apr. 2020). "Halo fraction in TeV-bright pulsar wind nebulae". In: *A&A* 636, A113, A113. DOI: 10.1051/0004-6361/201936505. arXiv: 1907.12121 [astro-ph.HE].

Giavitto, G., S. Bonnefoy, T. Ashton, M. Backes, et al. (July 2017). "Performance of the upgraded H.E.S.S. cameras". In: *35th International Cosmic Ray Conference*

(ICRC2017). Vol. 301. International Cosmic Ray Conference, 805, p. 805. DOI: 10.22323/1.301.0805. arXiv: 1708.04550 [astro-ph.IM].

Gill, Ramandeep and Jonathan Granot (May 2022). "Gamma-Ray Bursts at TeV Energies: Theoretical Considerations". In: *Galaxies* 10.3, 74, p. 74. DOI: 10.3390/galaxies10030074. arXiv: 2205.06312 [astro-ph.HE].

Gold, T. (May 1968). "Rotating Neutron Stars as the Origin of the Pulsating Radio Sources". In: *Nature* 218.5143, pp. 731–732. DOI: 10.1038/218731a0.

Gotthelf, E. V. and J. P. Halpern (Aug. 2009). "Discovery of a Highly Energetic X-Ray Pulsar Powering HESS J1813-178 in the Young Supernova Remnant G12.82-0.02". In: *ApJ* 700.2, pp. L158–L161. DOI: 10.1088/0004-637X/700/2/L158. arXiv: 0907.0137 [astro-ph.HE].

Grasso, D. and H. R. Rubinstein (July 2001). "Magnetic fields in the early Universe". In: *Phys. Rep.* 348.3, pp. 163–266. DOI: 10.1016/S0370-1573(00)00110-1. arXiv: astro-ph/0009061 [astro-ph].

Greisen, Kenneth (Apr. 1966). "End to the Cosmic-Ray Spectrum?" In: *Phys. Rev. Lett.* 16.17, pp. 748–750. DOI: 10.1103/PhysRevLett.16.748.

Grieder, Peter (Jan. 2010). *Extensive air showers. High energy phenomena and astrophysical aspects. A tutorial, reference manual and data book. Vol. I and II*. Vol. 1. ISBN: 978-3-540-76940-8. DOI: 10.1007/978-3-540-76941-5.

Hahn, J. (July 2015). "GAMERA - a new modeling package for non-thermal spectral modeling". In: *34th International Cosmic Ray Conference (ICRC2015)*. Vol. 34, 917, p. 917. DOI: 10.22323/1.236.0917.

Hahn, J., R. de los Reyes, K. Bernlöhr, P. Krüger, et al. (Feb. 2014a). "Impact of aerosols and adverse atmospheric conditions on the data quality for spectral analysis of the H.E.S.S. telescopes". In: *Astroparticle Physics* 54, pp. 25–32. DOI: 10.1016/j.astropartphys.2013.10.003. arXiv: 1310.1639 [astro-ph.IM].

— (Feb. 2014b). "Impact of aerosols and adverse atmospheric conditions on the data quality for spectral analysis of the H.E.S.S. telescopes". In: *Astroparticle Physics* 54, pp. 25–32. DOI: 10.1016/j.astropartphys.2013.10.003. arXiv: 1310.1639 [astro-ph.IM].

Halder, Priyam, Satyaki Goswami, Protyusha Halder, Uday Ghosh, and Sushan Konar (Oct. 2023). "Defining Millisecond Pulsars". In: *Research Notes of the American Astronomical Society* 7.10, 213, p. 213. DOI: 10.3847/2515-5172/ad00ac. arXiv: 2310.06230 [astro-ph.HE].

Halpern, J. P., E. V. Gotthelf, and F. Camilo (July 2012). "Spin-down Measurement of PSR J1813-1749: The Energetic Pulsar Powering HESS J1813-178". In: *ApJ* 753.1, L14, p. L14. DOI: 10.1088/2041-8205/753/1/L14. arXiv: 1206.2338 [astro-ph.HE].

Hamil, O., J. R. Stone, M. Urbanec, and G. Urbancová (Mar. 2015). "Braking index of isolated pulsars". In: *Phys. Rev. D* 91.6, 063007, p. 063007. DOI: 10.1103/PhysRevD.91.063007. arXiv: 1608.01383 [astro-ph.HE].

Haslam, C. G. T., C. J. Salter, H. Stoffel, and W. E. Wilson (Jan. 1982). "A 408-MHZ All-Sky Continuum Survey. II. The Atlas of Contour Maps". In: *A&AS* 47, p. 1.

He, Hao-Ning, B. Theodore Zhang, and Yi-Zhong Fan (Mar. 2024). "A Detectable Ultra-high-energy Cosmic-Ray Outburst from GRB 221009A". In: *ApJ* 963.2, 109, p. 109. DOI: 10.3847/1538-4357/ad2352. arXiv: 2401.11566 [astro-ph.HE].

Heck, D., J. Knapp, J. N. Capdevielle, G. Schatz, and T. Thouw (1998). *CORSIKA: a Monte Carlo code to simulate extensive air showers.*

Heitler, W. (1954). *Quantum theory of radiation.*

Helfand, D. J., E. V. Gotthelf, J. P. Halpern, F. Camilo, et al. (Aug. 2007). "Discovery of the Putative Pulsar and Wind Nebula Associated with the TeV Gamma-Ray Source HESS J1813-178". In: *ApJ* 665.2, pp. 1297–1303. DOI: 10.1086/519734. arXiv: 0705.0065 [astro-ph].

Hess, Victor (1912). "On the Observations of the Penetrating Radiation during Seven Balloon Flights". In: *arXiv e-prints*, arXiv:1808.02927, arXiv:1808.02927. DOI: 10.48550/arXiv.1808.02927. arXiv: 1808.02927 [physics.hist-ph].

H.E.S.S. Collaboration (Sept. 2018a). *H.E.S.S. first public test data release.* https://doi.org/10.5281/zenodo.1421099. DOI: 10.5281/zenodo.1421099. URL: https://doi.org/10.5281/zenodo.1421099.

— (Apr. 2018b). "The H.E.S.S. Galactic plane survey". In: *A&A* 612, A1, A1. DOI: 10.1051/0004-6361/201732098. arXiv: 1804.02432 [astro-ph.HE].

— (Jan. 2019). "Particle transport within the pulsar wind nebula HESS J1825-137". In: *A&A* 621, A116, A116. DOI: 10.1051/0004-6361/201834335. arXiv: 1810.12676 [astro-ph.HE].

— (Apr. 2023). "HESS J1809−193: A halo of escaped electrons around a pulsar wind nebula?" In: *A&A* 672, A103, A103. DOI: 10.1051/0004-6361/202245459. arXiv: 2302.13663 [astro-ph.HE].

H.E.S.S. Collaboration, H. Abdalla, A. Abramowski, F. Aharonian, et al. (Feb. 2017). "Characterizing the γ-ray long-term variability of PKS 2155-304 with H.E.S.S. and Fermi-LAT". In: *A&A* 598, A39, A39. DOI: 10.1051/0004-6361/201629419. arXiv: 1610.03311 [astro-ph.HE].

H.E.S.S. Collaboration, H. Abdalla, A. Abramowski, F. Aharonian, et al. (Apr. 2018a). "H.E.S.S. observations of RX J1713.7-3946 with improved angular and spectral resolution: Evidence for gamma-ray emission extending beyond the X-ray emitting shell". In: *A&A* 612, A6, A6. DOI: 10.1051/0004-6361/201629790. arXiv: 1609.08671 [astro-ph.HE].

H.E.S.S. Collaboration, H. Abdalla, A. Abramowski, F. Aharonian, et al. (Apr. 2018b). "The population of TeV pulsar wind nebulae in the H.E.S.S. Galactic Plane Survey". In: *A&A* 612, A2, A2. DOI: 10.1051/0004-6361/201629377. arXiv: 1702.08280 [astro-ph.HE].

H.E.S.S. Collaboration, A. Abramowski, F. Acero, F. Aharonian, et al. (Jan. 2011). "Revisiting the Westerlund 2 field with the HESS telescope array". In: *A&A* 525, A46, A46. DOI: 10.1051/0004-6361/201015290. arXiv: 1009.3012 [astro-ph.HE].

H.E.S.S. Collaboration, F. Aharonian, F. Ait Benkhali, J. Aschersleben, et al. (May 2023). "Detection of extended γ-ray emission around the Geminga pulsar with H.E.S.S." In: *A&A* 673, A148, A148. DOI: 10.1051/0004-6361/202245776. arXiv: 2304.02631 [astro-ph.HE].

H.E.S.S. Collaboration, F. Aharonian, F. Ait Benkhali, J. Aschersleben, et al. (June 2024). "Unveiling extended gamma-ray emission around HESS J1813-178". In: *A&A* 686, A149, A149. DOI: 10.1051/0004-6361/202348374. arXiv: 2403.16802 [astro-ph.HE].

Hewish, A., S. J. Bell, J. D. H. Pilkington, P. F. Scott, and R. A. Collins (Feb. 1968). "Observation of a Rapidly Pulsating Radio Source". In: *Nature* 217.5130, pp. 709–713. DOI: 10.1038/217709a0.

HI4PI Collaboration, N. Ben Bekhti, L. Flöer, R. Keller, et al. (Oct. 2016). "HI4PI: A full-sky H I survey based on EBHIS and GASS". In: *A&A* 594, A116, A116. DOI: 10.1051/0004-6361/201629178. arXiv: 1610.06175 [astro-ph.GA].

Hibschman, Johann A. and Jonathan Arons (June 2001). "Pair Multiplicities and Pulsar Death". In: *ApJ* 554.1, pp. 624–635. DOI: 10.1086/321378. arXiv: astro-ph/0102175 [astro-ph].

Hillas, A. M. (Oct. 1982). "Angular and energy distributions of charged particles in electron-photon cascades in air". In: *Journal of Physics G Nuclear Physics* 8.10, pp. 1461–1473. DOI: 10.1088/0305-4616/8/10/016.

— (Jan. 1984). "The Origin of Ultra-High-Energy Cosmic Rays". In: *ARA&A* 22, pp. 425–444. DOI: 10.1146/annurev.aa.22.090184.002233.

Hillebrandt, W. (June 1982). "An exploding 10 M. star: a model for the Crab supernova." In: *A&A* 110, pp. L3–L6.

Hinton, J. and SWGO Collaboration (Mar. 2022). "The Southern Wide-field Gamma-ray Observatory: Status and Prospects". In: *37th International Cosmic Ray Conference*, 23, p. 23. DOI: 10.22323/1.395.0023. arXiv: 2111.13158 [astro-ph.IM].

Hinton, Jim and Edna Ruiz-Velasco (Feb. 2020). "Multi-messenger astronomy with very-high-energy gamma-ray observations". In: *Journal of Physics Conference Series*. Vol. 1468. Journal of Physics Conference Series. IOP, 012096, p. 012096. DOI: 10.1088/1742-6596/1468/1/012096. arXiv: 1911.06097 [astro-ph.HE].

Ho, Wynn C. G., Sebastien Guillot, P. M. Saz Parkinson, B. Limyansky, et al. (Nov. 2020). "Proper motion, spectra, and timing of PSR J1813-1749 using Chandra and NICER". In: *MNRAS* 498.3, pp. 4396–4403. DOI: 10.1093/mnras/staa2653. arXiv: 2009.00031 [astro-ph.HE].

Hooper, Dan and Lisa Goodenough (Mar. 2011). "Dark matter annihilation in the Galactic Center as seen by the Fermi Gamma Ray Space Telescope". In: *Physics*

Letters B 697.5, pp. 412–428. DOI: 10.1016/j.physletb.2011.02.029. arXiv: 1010.2752 [hep-ph].

Jankowski, F., W. van Straten, E. F. Keane, M. Bailes, et al. (Feb. 2018). "Spectral properties of 441 radio pulsars". In: *MNRAS* 473.4, pp. 4436–4458. DOI: 10.1093/mnras/stx2476. arXiv: 1709.08864 [astro-ph.HE].

Kalman, Rudolph Emil (1960). "A New Approach to Linear Filtering and Prediction Problems". In: *Transactions of the ASME–Journal of Basic Engineering* 82.Series D, pp. 35–45.

Kampert, K. H. (Sept. 2001). "Cosmic Rays and Particle Physics". In: *Acta Physica Hungarica Heavy Ion Physics* 14.1-4, pp. 203–215. DOI: 10.1556/APH.14.2001.1-4.20. arXiv: astro-ph/0101331 [astro-ph].

Karpov, S. N., I. M. Khaerdinov, N. M. Nikolskaya, and T. M. Roganova (2006). "Cherenkov light in electron-induced air showers". In: *Astroparticle Physics* 25, pp. 233–241. DOI: 10.1016/j.astropartphys.2006.02.002. URL: https://ui.adsabs.harvard.edu/abs/2006APh....25..233S/abstract.

Kaspi, V. M., M. E. Roberts, G. Vasisht, E. V. Gotthelf, et al. (Oct. 2001). "Chandra X-Ray Observations of G11.2-0.3: Implications for Pulsar Ages". In: *ApJ* 560.1, pp. 371–377. DOI: 10.1086/322515. arXiv: astro-ph/0107292 [astro-ph].

Kawashima, T. and The ALPACA Collaboration (Aug. 2022). "The ALPACA experiment: The project of the first sub-PeV gamma-ray observation in the southern sky". In: *arXiv e-prints*, arXiv:2208.14659, arXiv:2208.14659. DOI: 10.48550/arXiv.2208.14659. arXiv: 2208.14659 [astro-ph.IM].

Khelifi, Bruno, Roberta Zanin, Karl Kosack, Laura Olivera-Nieto, and Jutta Schnabel (2023). "The Very-high-energy Open Data Format: towards a shared, open data format in very-high-energy astronomy". In: *PoS* ICRC2023, p. 1510. DOI: 10.22323/1.444.1510.

Kochanek, C. S. (Jan. 2015). "Constraints on core collapse from the black hole mass function". In: *MNRAS* 446.2, pp. 1213–1222. DOI: 10.1093/mnras/stu2056. arXiv: 1407.5622 [astro-ph.SR].

Kolmogorov, A. N. (July 1991). "The Local Structure of Turbulence in Incompressible Viscous Fluid for Very Large Reynolds Numbers". In: *Proceedings of the Royal Society of London Series A* 434.1890, pp. 9–13. DOI: 10.1098/rspa.1991.0075.

Konopelko, A. K., A. V. Plyasheshnikov, F. A. Aharonian, M. Hemberger, et al. (Jan. 1997). "Study on the Cosmic Ray Spectrum and Chemical Composition using the Imaging Air Cherenkov Technique". In: *International Cosmic Ray Conference*. Vol. 3. International Cosmic Ray Conference, p. 349.

Kraichnan, Robert H. (July 1965). "Inertial-Range Spectrum of Hydromagnetic Turbulence". In: *Physics of Fluids* 8.7, pp. 1385–1387. DOI: 10.1063/1.1761412.

Kraushaar, W., G. W. Clark, G. Garmire, H. Helmken, et al. (Apr. 1965). "Explorer XI Experiment on Cosmic Gamma Rays." In: *ApJ* 141, p. 845. DOI: 10.1086/148179.

Kraushaar, W. L., G. W. Clark, G. P. Garmire, R. Borken, et al. (Nov. 1972). "High-Energy Cosmic Gamma-Ray Observations from the OSO-3 Satellite". In: *ApJ* 177, p. 341. DOI: 10.1086/151713.

Kuempel, Daniel (Sept. 2014). "Extragalactic Propagation of Ultra-High Energy Cosmic Rays". In: *arXiv e-prints*, arXiv:1409.3129, arXiv:1409.3129. DOI: 10.48550/arXiv.1409.3129. arXiv: 1409.3129 [astro-ph.HE].

Kulkarni, Shrinivas R. and Carl Heiles (1988). "Neutral hydrogen and the diffuse interstellar medium." In: *Galactic and Extragalactic Radio Astronomy*. Ed. by K. I. Kellermann and G. L. Verschuur, pp. 95–153.

Kulsrud, Russell and William P. Pearce (May 1969). "The Effect of Wave-Particle Interactions on the Propagation of Cosmic Rays". In: *ApJ* 156, p. 445. DOI: 10.1086/149981.

LAT Collaboration, *Fermi* (2019). *Propagating the Uncertainties on the Effective Area (Aeff)*. [Online; accessed 12-September-2023]. URL: https://fermi.gsfc.nasa.gov/ssc/data/analysis/scitools/Aeff_Systematics.html.

Lebohec, S. and J. Holder (May 2003). "The cosmic ray background as a tool for relative calibration of atmospheric Cherenkov telescopes". In: *Astroparticle Physics* 19.2, pp. 221–233. DOI: 10.1016/S0927-6505(02)00201-3. arXiv: astro-ph/0208396 [astro-ph].

Lemoine, Martin, Kumiko Kotera, and Jérôme Pétri (July 2015). "On ultra-high energy cosmic ray acceleration at the termination shock of young pulsar winds". In: *J. Cosmology Astropart. Phys.* 2015.7, pp. 016–016. DOI: 10.1088/1475-7516/2015/07/016. arXiv: 1409.0159 [astro-ph.HE].

Liebendörfer, Matthias, Anthony Mezzacappa, Friedrich-Karl Thielemann, O. E. Messer, et al. (May 2001). "Probing the gravitational well: No supernova explosion in spherical symmetry with general relativistic Boltzmann neutrino transport". In: *Phys. Rev. D* 63.10, 103004, p. 103004. DOI: 10.1103/PhysRevD.63.103004. arXiv: astro-ph/0006418 [astro-ph].

Li&Ma (Sept. 1983). "Analysis methods for results in gamma-ray astronomy." In: *ApJ* 272, pp. 317–324. DOI: 10.1086/161295.

Liu, Zheng-Wei, Friedrich K. Röpke, and Zhanwen Han (Aug. 2023). "Type Ia Supernova Explosions in Binary Systems: A Review". In: *Research in Astronomy and Astrophysics* 23.8, 082001, p. 082001. DOI: 10.1088/1674-4527/acd89e. arXiv: 2305.13305 [astro-ph.HE].

Lombardi, Saverio (Jan. 2011). "Advanced stereoscopic gamma-ray shower analysis with the MAGIC telescopes". In: *International Cosmic Ray Conference*. Vol. 3. International Cosmic Ray Conference, p. 266. DOI: 10.7529/ICRC2011/V03/1150. arXiv: 1109.6195 [astro-ph.IM].

Longair, Malcolm S. (2011). *High Energy Astrophysics*. Chap. 15.

Lorimer, D. R. and M. Kramer (2004). *Handbook of Pulsar Astronomy*. Vol. 4.

Luhman, Kevin L. (Sept. 2012). "The Formation and Early Evolution of Low-Mass Stars and Brown Dwarfs". In: *ARA&A* 50, pp. 65–106. DOI: 10.1146/annurev-astro-081811-125528. arXiv: 1208.5800 [astro-ph.GA].

Luongo, Orlando and Marco Muccino (Oct. 2021). "A Roadmap to Gamma-Ray Bursts: New Developments and Applications to Cosmology". In: *Galaxies* 9.4, 77, p. 77. DOI: 10.3390/galaxies9040077. arXiv: 2110.14408 [astro-ph.HE].

Lynch, Gerald R. and Orin I. Dahl (May 1991). "Approximations to multiple Coulomb scattering". In: *Nuclear Instruments and Methods in Physics Research B* 58.1, pp. 6–10. DOI: 10.1016/0168-583X(91)95671-Y.

Lyne, A. G., R. S. Pritchard, F. Graham-Smith, and F. Camilo (June 1996). "Very low braking index for the Vela pulsar". In: *Nature* 381.6582, pp. 497–498. DOI: 10.1038/381497a0.

MAGIC Collaboration (Sept. 2020). "Studying the nature of the unidentified gamma-ray source HESS J1841-055 with the MAGIC telescopes". In: *MNRAS* 497.3, pp. 3734–3745. DOI: 10.1093/mnras/staa2135. arXiv: 2007.09321 [astro-ph.HE].

Manchester, R. N. (Sept. 2017). "Millisecond Pulsars, their Evolution and Applications". In: *Journal of Astrophysics and Astronomy* 38.3, 42, p. 42. DOI: 10.1007/s12036-017-9469-2. arXiv: 1709.09434 [astro-ph.HE].

Manchester, R. N., G. B. Hobbs, A. Teoh, and M. Hobbs (Apr. 2005). "The Australia Telescope National Facility Pulsar Catalogue". In: *The Astronomical Journal* 129.4, 1993–2006. ISSN: 1538-3881. DOI: 10.1086/428488. URL: http://dx.doi.org/10.1086/428488.

Matthews, J. (Jan. 2005). "A Heitler model of extensive air showers". In: *Astroparticle Physics* 22.5-6, pp. 387–397. DOI: 10.1016/j.astropartphys.2004.09.003.

Matthews, James H. and Andrew M. Taylor (June 2021). "Particle acceleration in radio galaxies with flickering jets: GeV electrons to ultrahigh energy cosmic rays". In: *MNRAS* 503.4, pp. 5948–5964. DOI: 10.1093/mnras/stab758. arXiv: 2103.06900 [astro-ph.HE].

Meli, A. (Dec. 2012). "First- and second-order Fermi acceleration in thick relativistic shocks". In: *High Energy Gamma-Ray Astronomy: 5th International Meeting on High Energy Gamma-Ray Astronomy*. Ed. by Felix A. Aharonian, Werner Hofmann, and Frank M. Rieger. Vol. 1505. American Institute of Physics Conference Series. AIP, pp. 626–630. DOI: 10.1063/1.4772338.

Mertsch, P. and V. H. M. Phan (Mar. 2023). "Bayesian inference of three-dimensional gas maps. II. Galactic HI". In: *A&A* 671, A54, A54. DOI: 10.1051/0004-6361/202243326. arXiv: 2202.02341 [astro-ph.GA].

Mertsch, P. and A. Vittino (Nov. 2021). "Bayesian inference of three-dimensional gas maps. I. Galactic CO". In: *A&A* 655, A64, A64. DOI: 10.1051/0004-6361/202141000. arXiv: 2012.15770 [astro-ph.GA].

Messineo, Maria, Ben Davies, Donald F. Figer, R. P. Kudritzki, et al. (May 2011). "Massive Stars in the Cl 1813-178 Cluster: An Episode Of Massive Star Formation in

the W33 Complex". In: *ApJ* 733.1, 41, p. 41. DOI: 10.1088/0004-637X/733/1/41. arXiv: 1103.4975 [astro-ph.GA].

Mignani, R. P., A. C. Jackson, and A. Spiers (Sept. 2010a). "VLT observations of the middle-aged pulsar PSR B1055-52". In: *A&A* 520, A21, A21. DOI: 10.1051/0004-6361/201015495.

Mignani, R. P., G. G. Pavlov, and O. Kargaltsev (Sept. 2010b). "Optical-Ultraviolet Spectrum and Proper Motion of the Middle-aged Pulsar B1055-52". In: *ApJ* 720.2, pp. 1635–1643. DOI: 10.1088/0004-637X/720/2/1635. arXiv: 1007.2940 [astro-ph.HE].

Miville-Deschênes, Marc-Antoine, Norman Murray, and Eve J. Lee (Jan. 2017). "Physical Properties of Molecular Clouds for the Entire Milky Way Disk". In: *ApJ* 834.1, 57, p. 57. DOI: 10.3847/1538-4357/834/1/57. arXiv: 1610.05918 [astro-ph.GA].

Mohrmann, L., A. Specovius, D. Tiziani, S. Funk, et al. (Dec. 2019a). "Validation of open-source science tools and background model construction in γ-ray astronomy". In: *A&A* 632, A72, A72. DOI: 10.1051/0004-6361/201936452. arXiv: 1910.08088 [astro-ph.IM].

— (Dec. 2019b). "Validation of open-source science tools and background model construction in γ-ray astronomy". In: *A&A* 632, A72, A72. DOI: 10.1051/0004-6361/201936452. arXiv: 1910.08088 [astro-ph.IM].

Morcuende, Daniel, Rubén López-Coto, Abelardo Moralejo, Seiya Nozaki, and Thomas Vuillaume (Sept. 2023). "Performance of the Large-Sized Telescope prototype of the Cherenkov Telescope Array". In: *arXiv e-prints*, arXiv:2309.11315, arXiv:2309.11315. DOI: 10.48550/arXiv.2309.11315. arXiv: 2309.11315 [astro-ph.HE].

Morlino, G., P. Blasi, E. Peretti, and P. Cristofari (July 2021a). "Particle acceleration in winds of star clusters". In: *MNRAS* 504.4, pp. 6096–6105. DOI: 10.1093/mnras/stab690. arXiv: 2102.09217 [astro-ph.HE].

— (July 2021b). "Particle acceleration in winds of star clusters". In: *MNRAS* 504.4, pp. 6096–6105. DOI: 10.1093/mnras/stab690. arXiv: 2102.09217 [astro-ph.HE].

Moskalenko, Igor V., Troy A. Porter, Seth W. Digel, Peter F. Michelson, and Jonathan F. Ormes (July 2008). "A Celestial Gamma-Ray Foreground Due to the Albedo of Small Solar System Bodies and a Remote Probe of the Interstellar Cosmic-Ray Spectrum". In: *ApJ* 681.2, pp. 1708–1716. DOI: 10.1086/588425. arXiv: 0712.2015 [astro-ph].

Naumann, C. L., E. Delagnes, J. Bolmont, P. Corona, et al. (Dec. 2012). "New electronics for the Cherenkov Telescope Array (NECTAr)". In: *Nuclear Instruments and Methods in Physics Research A* 695, pp. 44–51. DOI: 10.1016/j.nima.2011.11.008.

Navas, S. et al. (2020). "Review of particle physics". In: *Phys. Rev. D* 110.3, p. 030001. DOI: 10.1103/PhysRevD.110.030001.

Nigro, Cosimo, Tarek Hassan, and Laura Olivera-Nieto (Oct. 2021). "Evolution of Data Formats in Very-High-Energy Gamma-Ray Astronomy". In: *Universe* 7.10, p. 374. DOI: 10.3390/universe7100374. arXiv: 2109.14661 [astro-ph.IM].

Oegelman, Hakki and John P. Finley (Aug. 1993). "ROSAT Observations of Pulsed Soft X-Ray Emission from PSR 1055-52". In: *ApJ* 413, p. L31. DOI: 10.1086/186952.

Ohira, Yutaka, Shota Kisaka, and Ryo Yamazaki (July 2018). "Pulsar Wind Nebulae inside Supernova Remnants as Cosmic-Ray PeVatrons". In: *MNRAS* 478.1, pp. 926–931. DOI: 10.1093/mnras/sty1159. arXiv: 1702.05866 [astro-ph.HE].

Ohm, S., C. van Eldik, and K. Egberts (June 2009). "γ/hadron separation in very-high-energy γ-ray astronomy using a multivariate analysis method". In: *Astroparticle Physics* 31.5, pp. 383–391. DOI: 10.1016/j.astropartphys.2009.04.001. arXiv: 0904.1136 [astro-ph.IM].

Olsen, Haakon (July 1963). "Opening Angles of Electron-Positron Pairs". In: *Physical Review* 131.1, pp. 406–415. DOI: 10.1103/PhysRev.131.406.

Orusa, Luca, Silvia Manconi, Fiorenza Donato, and Mattia Di Mauro (Feb. 2025). "Disclosing the catalog pulsars dominating the Galactic positron flux". In: *J. Cosmology Astropart. Phys.* 2025.2, 029, p. 029. DOI: 10.1088/1475-7516/2025/02/029. arXiv: 2410.10951 [astro-ph.HE].

Pacini, D. (Dec. 1912). "La radiazione penetrante alla superficie ed in seno alle acque". In: *Il Nuovo Cimento* 3.1, pp. 93–100. DOI: 10.1007/BF02957440. arXiv: 1002.1810 [physics.hist-ph].

Pacini, F. (Nov. 1967). "Energy Emission from a Neutron Star". In: *Nature* 216.5115, pp. 567–568. DOI: 10.1038/216567a0.

Parsons, R. D. and J. A. Hinton (Apr. 2014). "A Monte Carlo template based analysis for air-Cherenkov arrays". In: *Astroparticle Physics* 56, pp. 26–34. DOI: 10.1016/j.astropartphys.2014.03.002. arXiv: 1403.2993 [astro-ph.IM].

Perri, Silvia, Andrei Bykov, Hans Fahr, Horst Fichtner, and Joe Giacalone (June 2022). "Recent Developments in Particle Acceleration at Shocks: Theory and Observations". In: *Space Sci. Rev.* 218.4, 26, p. 26. DOI: 10.1007/s11214-022-00892-5.

Peters, B. (Nov. 1961). "Primary cosmic radiation and extensive air showers". In: *Il Nuovo Cimento* 22.4, pp. 800–819. DOI: 10.1007/BF02783106.

Pétri, J., J. Heyvaerts, and S. Bonazzola (Mar. 2002). "Global static electrospheres of charged pulsars". In: *A&A* 384, pp. 414–432. DOI: 10.1051/0004-6361:20020044.

Petroff, E., M. J. Keith, S. Johnston, W. van Straten, and R. M. Shannon (Oct. 2013). "Dispersion measure variations in a sample of 168 pulsars". In: *MNRAS* 435.2, pp. 1610–1617. DOI: 10.1093/mnras/stt1401. arXiv: 1307.7221 [astro-ph.GA].

Pitkin, M. (Feb. 2018). "psrqpy: a python interface for querying the ATNF pulsar catalogue". In: *Journal of Open Source Software* 3.22, p. 538. DOI: 10.21105/joss.00538. URL: https://doi.org/10.21105/joss.00538.

Planck Collaboration, P. A. R. Ade, N. Aghanim, M. Arnaud, et al. (Dec. 2011). "Planck early results. XIX. All-sky temperature and dust optical depth from Planck and IRAS. Constraints on the "dark gas" in our Galaxy". In: *A&A* 536, A19, A19. DOI: 10.1051/0004-6361/201116479. arXiv: 1101.2029 [astro-ph.GA].

Popescu, Cristina C. and Richard J. Tuffs (Dec. 2013). "Radiation fields in star-forming galaxies: the disc, thin disc and bulge". In: *MNRAS* 436.2, pp. 1302–1321. DOI: 10.1093/mnras/stt1666. arXiv: 1305.0232 [astro-ph.CO].

Porter, T. A., G. Jóhannesson, and I. V. Moskalenko (Sept. 2017). "High-energy Gamma Rays from the Milky Way: Three-dimensional Spatial Models for the Cosmic-Ray and Radiation Field Densities in the Interstellar Medium". In: *ApJ* 846.1, 67, p. 67. DOI: 10.3847/1538-4357/aa844d. arXiv: 1708.00816 [astro-ph.HE].

Posselt, B., G. G. Pavlov, O. Kargaltsev, and J. Hare (Aug. 2023). "X-Ray and Near-Infrared Observations of the Middle-aged Pulsar B1055-52, Its Multiwavelength Spectrum, and Proper Motion". In: *ApJ* 952.2, 134, p. 134. DOI: 10.3847/1538-4357/acd9d1. arXiv: 2306.00185 [astro-ph.HE].

Principe, G., A. M. W. Mitchell, S. Caroff, J. A. Hinton, et al. (Aug. 2020). "Energy dependent morphology of the pulsar wind nebula HESS J1825-137 with Fermi-LAT". In: *A&A* 640, A76, A76. DOI: 10.1051/0004-6361/202038375. arXiv: 2006.11177 [astro-ph.HE].

Quenby, J J (July 2018). "The Low Geminga Halo Diffusion Coefficient and a Gradient Driven Alfven Instability". In: *arXiv e-prints*, arXiv:1807.01608, arXiv:1807.01608. DOI: 10.48550/arXiv.1807.01608. arXiv: 1807.01608 [astro-ph.HE].

Recchia, S., M. Di Mauro, F. A. Aharonian, L. Orusa, et al. (Dec. 2021). "Do the Geminga, Monogem and PSR J0622+3749 γ -ray halos imply slow diffusion around pulsars?" In: *Phys. Rev. D* 104.12, 123017, p. 123017. DOI: 10.1103/PhysRevD.104.123017. arXiv: 2106.02275 [astro-ph.HE].

Rice, Thomas S., Alyssa A. Goodman, Edwin A. Bergin, Christopher Beaumont, and T. M. Dame (May 2016). "A Uniform Catalog of Molecular Clouds in the Milky Way". In: *ApJ* 822.1, 52, p. 52. DOI: 10.3847/0004-637X/822/1/52. arXiv: 1602.02791 [astro-ph.GA].

Romero, Gustava E. (Apr. 1998). "On the High-Energy Emission of the Pulsar PSR B1055–52". In: *Rev. Mexicana Astron. Astrofis.* 34, pp. 29–35.

Scully, S. T. and F. W. Stecker (Jan. 2002). "On the spectrum of ultrahigh energy cosmic rays and the /γ-ray burst origin hypothesis". In: *Astroparticle Physics* 16.3, pp. 271–276. DOI: 10.1016/S0927-6505(01)00133-5. arXiv: astro-ph/0006112 [astro-ph].

Shaffer, Travis M., Edwin C. Pratt, and Jan Grimm (Feb. 2017). "Utilizing the power of Cerenkov light with nanotechnology". In: *Nature Nanotechnology* 12.2, pp. 106–117. DOI: 10.1038/nnano.2016.301.

Sironi, Lorenzo and Anatoly Spitkovsky (Nov. 2011). "Acceleration of Particles at the Termination Shock of a Relativistic Striped Wind". In: *ApJ* 741.1, 39, p. 39. DOI: 10.1088/0004-637X/741/1/39. arXiv: 1107.0977 [astro-ph.HE].

— (Mar. 2014). "Relativistic Reconnection: An Efficient Source of Non-thermal Particles". In: *ApJ* 783.1, L21, p. L21. DOI: 10.1088/2041-8205/783/1/L21. arXiv: 1401.5471 [astro-ph.HE].

Skilling, J. (Sept. 1975a). "Cosmic ray streaming - I. Effect of Alfvén waves on particles." In: *MNRAS* 172, pp. 557–566. DOI: 10.1093/mnras/172.3.557.

— (Nov. 1975b). "Cosmic ray streaming - II. Effect of particles on Alfvén waves." In: *MNRAS* 173, pp. 245–254. DOI: 10.1093/mnras/173.2.245.

— (Nov. 1975c). "Cosmic ray streaming - III. Self-consistent solutions." In: *MNRAS* 173, pp. 255–269. DOI: 10.1093/mnras/173.2.255.

Slane, Patrick (2017). "Pulsar Wind Nebulae". In: *Handbook of Supernovae*. Ed. by Athem W. Alsabti and Paul Murdin, p. 2159. DOI: 10.1007/978-3-319-21846-5_95.

Smith, D. A., S. Abdollahi, M. Ajello, M. Bailes, et al. (Dec. 2023a). "The Third Fermi Large Area Telescope Catalog of Gamma-Ray Pulsars". In: *ApJ* 958.2, 191, p. 191. DOI: 10.3847/1538-4357/acee67. arXiv: 2307.11132 [astro-ph.HE].

— (Dec. 2023b). "The Third Fermi Large Area Telescope Catalog of Gamma-Ray Pulsars". In: *ApJ* 958.2, 191, p. 191. DOI: 10.3847/1538-4357/acee67. arXiv: 2307.11132 [astro-ph.HE].

Sormani, Mattia C., James Binney, and John Magorrian (May 2015). "Gas flow in barred potentials". In: *MNRAS* 449.3, pp. 2421–2435. DOI: 10.1093/mnras/stv441. arXiv: 1502.02740 [astro-ph.GA].

Stecker, Floyd William (1971). *Cosmic gamma rays*. Vol. 249.

Straal, S. M. and J. van Leeuwen (Mar. 2019). "A LOFAR search for steep-spectrum pulsars in supernova remnants and pulsar wind nebulae". In: *A&A* 623, A90, A90. DOI: 10.1051/0004-6361/201833922. arXiv: 1902.00356 [astro-ph.HE].

Strong, A. W. and I. V. Moskalenko (2000). "Galactic cosmic rays and gamma rays: a unified approach". In: *Book "Topics in Cosmic Ray Astrophysics" (vol.230 in Horizons in World Physics*, pp. 81–103. DOI: 10.48550/arXiv.astro-ph/9812260.

Strong, Andrew W. and Igor V. Moskalenko (Dec. 1998). "Propagation of Cosmic-Ray Nucleons in the Galaxy". In: *ApJ* 509.1, pp. 212–228. DOI: 10.1086/306470. arXiv: astro-ph/9807150 [astro-ph].

Su, Meng, Tracy R. Slatyer, and Douglas P. Finkbeiner (Dec. 2010). "Giant Gamma-ray Bubbles from Fermi-LAT: Active Galactic Nucleus Activity or Bipolar Galactic Wind?" In: *ApJ* 724.2, pp. 1044–1082. DOI: 10.1088/0004-637X/724/2/1044. arXiv: 1005.5480 [astro-ph.HE].

Sumiyoshi, K., S. Yamada, H. Suzuki, H. Shen, et al. (Aug. 2005). "Postbounce Evolution of Core-Collapse Supernovae: Long-Term Effects of the Equation of State". In: *ApJ* 629.2, pp. 922–932. DOI: 10.1086/431788. arXiv: astro-ph/0506620 [astro-ph].

Szanecki, M., K. Bernlöhr, D. Sobczyńska, A. Niedźwiecki, et al. (May 2014). "Geomagnetic field and altitude effects on the performance of future IACT arrays". In: *arXiv e-prints*, arXiv:1405.1846, arXiv:1405.1846. DOI: 10.48550/arXiv.1405.1846. arXiv: 1405.1846 [astro-ph.IM].

Székely, Gábor J., Maria L. Rizzo, and Nail K. Bakirov (2007). "Measuring and Testing Dependence by Correlation of Distances". In: *The Annals of Statistics* 35.6, pp. 2769–2794. ISSN: 00905364. URL: http://www.jstor.org/stable/25464608 (visited on 09/03/2024).

Tanabashi, M., K. Hagiwara, K. Hikasa, K. Nakamura, et al. (Aug. 2018). "Review of Particle Physics*". In: *Phys. Rev. D* 98.3, 030001, p. 030001. DOI: 10.1103/PhysRevD.98.030001.

Tang, Xiaping and Roger A. Chevalier (June 2012). "Particle Transport in Young Pulsar Wind Nebulae". In: *ApJ* 752.2, 83, p. 83. DOI: 10.1088/0004-637X/752/2/83. arXiv: 1204.3913 [astro-ph.HE].

Taylor, J. H. and J. M. Cordes (July 1993). "Pulsar Distances and the Galactic Distribution of Free Electrons". In: *ApJ* 411, p. 674. DOI: 10.1086/172870.

The Pierre Auger Collaboration (Feb. 2015). "The Pierre Auger Cosmic Ray Observatory". In: *arXiv e-prints*, arXiv:1502.01323, arXiv:1502.01323. DOI: 10.48550/arXiv.1502.01323. arXiv: 1502.01323 [astro-ph.IM].

Thompson, David J. (Aug. 2015). "Space detectors for gamma rays (100 MeV-100 GeV): From EGRET to Fermi LAT". In: *Comptes Rendus Physique* 16.6-7, pp. 600–609. DOI: 10.1016/j.crhy.2015.07.002. arXiv: 1506.07733 [astro-ph.IM].

Thompson, David J. and Colleen A. Wilson-Hodge (2022). "Fermi Gamma-Ray Space Telescope". In: *Handbook of X-ray and Gamma-ray Astrophysics*. Ed. by Cosimo Bambi and Andrea Sangangelo, 29, p. 29. DOI: 10.1007/978-981-16-4544-0_58-1.

Tong, H. and F. F. Kou (Mar. 2017). "Possible Evolution of the Pulsar Braking Index from Larger than Three to About One". In: *ApJ* 837.2, 117, p. 117. DOI: 10.3847/1538-4357/aa60c6. arXiv: 1604.01231 [astro-ph.HE].

Ubertini, P., L. Bassani, A. Malizia, A. Bazzano, et al. (Aug. 2005). "INTEGRAL IGR J18135-1751 = HESS J1813-178: A New Cosmic High-Energy Accelerator from keV to TeV Energies". In: *ApJ* 629.2, pp. L109–L112. DOI: 10.1086/447766. arXiv: astro-ph/0505191 [astro-ph].

Unbehaun, Tim, Rodrigo Guedes Lang, Anita Deka Baruah, Prajath Bedur Ramesh, et al. (Feb. 2025). "Improvements to monoscopic analysis for imaging atmospheric Cherenkov telescopes: Application to H.E.S.S." In: *A&A* 694, A162, A162. DOI: 10.1051/0004-6361/202452927. arXiv: 2501.08671 [astro-ph.IM].

Vacanti, G., P. Fleury, Y. Jiang, E. Paré, et al. (Feb. 1994). "Muon ring images with an atmospheric Čerenkov telescope". In: *Astroparticle Physics* 2.1, pp. 1–11. DOI: 10.1016/0927-6505(94)90012-4.

Vaughan, A. E. and M. I. Large (Jan. 1972). "Discovery of three pulsars". In: *MNRAS* 156, 27P. DOI: 10.1093/mnras/156.1.27P.

Čerenkov, P. A. (Aug. 1937). "Visible Radiation Produced by Electrons Moving in a Medium with Velocities Exceeding that of Light". In: *Physical Review* 52.4, pp. 378–379. DOI: 10.1103/PhysRev.52.378.

Veh, Johannes (2018). "Dark Matter -line search in the Galactic Centre with H.E.S.S. using an On-Off technique ". PhD thesis. Erlangen Centre for Astroparticle Physics (ECAP), Friedrich-Alexander-Universität Erlangen-Nürnberg, Germany. URL: https://ecap.nat.fau.de/wp-content/uploads/2018/09/2018_Veh_Dissertation.pdf.

Venter, C. and O. C. de Jager (Jan. 2007). "Constraints on the Parameters of the Unseen Pulsar in the PWN G0.9+0.1 from Radio, X-Ray, and VHE Gamma-Ray Observations". In: *WE-Heraeus Seminar on Neutron Stars and Pulsars 40 years after the Discovery*. Ed. by W. Becker and H. H. Huang, p. 40. arXiv: astro-ph/0612652 [astro-ph].

Vidaña, Isaac (Oct. 2018). "A short walk through the physics of neutron stars". In: *European Physical Journal Plus* 133.10, 445, p. 445. DOI: 10.1140/epjp/i2018-12329-x. arXiv: 1805.00837 [nucl-th].

Vink, Jacco (2020). *Physics and Evolution of Supernova Remnants*. DOI: 10.1007/978-3-030-55231-2.

Virtanen, Pauli, Ralf Gommers, Travis E. Oliphant, Matt Haberland, et al. (2020). "SciPy 1.0: Fundamental Algorithms for Scientific Computing in Python". In: *Nature Methods* 17, pp. 261–272. DOI: 10.1038/s41592-019-0686-2.

Völk, Heinrich J. and Konrad Bernlöhr (Aug. 2009). "Imaging very high energy gamma-ray telescopes". In: *Experimental Astronomy* 25.1-3, pp. 173–191. DOI: 10.1007/s10686-009-9151-z. arXiv: 0812.4198 [astro-ph].

Wach, T., A. Mitchell, and L. Mohrmann (Oct. 2024). "A background-estimation technique for the detection of extended gamma-ray structures with IACTs". In: *A&A* 690, A250, A250. DOI: 10.1051/0004-6361/202451020. arXiv: 2409.02527 [astro-ph.IM].

Wach, Tina (2022). "Detailed multi-insturment analysis of the very high -ray emission in the region of HESS J1813-178". Available at https://ecap.nat.fau.de/wp-content/uploads/2022/07/Tina_Wach_MA_280322.pdf. Master's thesis. Erlangen Centre for Astroparticle Physics, FAU.

Weekes, T. C., M. F. Cawley, D. J. Fegan, K. G. Gibbs, et al. (July 1989). "Observation of TeV Gamma Rays from the Crab Nebula Using the Atmospheric Cerenkov Imaging Technique". In: *ApJ* 342, p. 379. DOI: 10.1086/167599.

Wilks, S. S. (1938). "The Large-Sample Distribution of the Likelihood Ratio for Testing Composite Hypotheses". In: *The Annals of Mathematical Statistics* 9.1, pp. 60–62. ISSN: 00034851, 21688990. URL: http://www.jstor.org/stable/2957648 (visited on 01/25/2025).

Winchen, Tobias and Stijn Buitink (Nov. 2018). "Energy spectrum of fast second order Fermi accelerators as sources of ultra-high-energy cosmic rays". In: *Astroparticle Physics* 102, pp. 25–31. DOI: 10.1016/j.astropartphys.2018.04.004. arXiv: 1612.03675 [astro-ph.HE].

Wood, M., R. Caputo, E. Charles, M. Di Mauro, et al. (Jan. 2017). "Fermipy: An open-source Python package for analysis of Fermi-LAT Data". In: *35th International*

Cosmic Ray Conference (ICRC2017). Vol. 301, 824, p. 824. arXiv: 1707.09551 [astro-ph.IM].

Wulf, T. (1910). "Beobachtungen über die Strahlung hoher Durchdringungsfähigkeit auf dem Eiffelturm". In: *Physikalische Zeitschrift* 11, pp. 811–813.

Xin, Yuliang and Xiaolei Guo (2021). "The gamma-ray emission toward HESS J1813-178 with Fermi-LAT". In: *Proceedings of 37th International Cosmic Ray Conference — PoS(ICRC2021)*. Vol. 395, p. 625. DOI: 10.22323/1.395.0625.

Yang, Rui-zhi, Emma de Oña Wilhelmi, and Felix Aharonian (Apr. 2018). "Diffuse γ-ray emission in the vicinity of young star cluster Westerlund 2". In: *A&A* 611, A77, A77. DOI: 10.1051/0004-6361/201732045. arXiv: 1710.02803 [astro-ph.HE].

Yao, J. M., R. N. Manchester, and N. Wang (Jan. 2017). "A New Electron-density Model for Estimation of Pulsar and FRB Distances". In: *ApJ* 835.1, 29, p. 29. DOI: 10.3847/1538-4357/835/1/29. arXiv: 1610.09448 [astro-ph.GA].

Zabalza, V. (2015). "naima: a Python package for inference of relativistic particle energy distributions from observed nonthermal spectra". In: *Proc. of International Cosmic Ray Conference 2015*, p. 922. eprint: 1509.03319.

Zatsepin, G. T. and V. A. Kuz'min (Aug. 1966). "Upper Limit of the Spectrum of Cosmic Rays". In: *Soviet Journal of Experimental and Theoretical Physics Letters* 4, p. 78.

Acknowledgements

First and foremost, I would like to thank Dr. Alison Mitchell for providing me with the opportunity to work on a variety of fascinating topics. I have greatly enjoyed my time in her group and am incredibly grateful for the support and guidance I have received over the past years. Her valuable suggestions have greatly improved both my work and my thesis, and I am especially thankful for the opportunities she has provided for me to present my research across the world. Thank you for fostering an environment that has allowed me to grow both as a researcher and as an individual.

I would also like to thank Dr. Johannes Schäfer, not only for meticulously reviewing large portions of this thesis but also for his technical support and for always being available to lend an ear.

Thank you also to Katharina Egg, who not only assisted in proofreading significant parts of this thesis but also provided emotional support throughout the process.

I am deeply thankful to Prof. Dr. Christopher Eldik and Prof. Dr. Stefan Funk for their insightful ideas and assistance whenever I encountered difficulties.

Thanks to Dr. Vikas Joshi for his guidance and support in getting me started with the analysis of HESS J1813-178, as well as for his patience in advising me on good scientific writing practices.

I am also grateful to Dr. Lars Mohrmann for always being willing to answer my questions and for sharing his expertise, without which key aspects of this work would not have been possible.

Thanks to Tim Unbehaun for taking the time to discuss technical details with me and for providing invaluable assistance whenever I encountered challenges with statistical analyses.

Furthermore, I would like to thank Dr. Samuel Spencer, Dr. Rodrigo Guedes-Lang, Dr. Pedro Silva Batista, Matheus Genaro Dantas Xavier, Jelena Celic, and Tim Unbehaun for their time and effort in proofreading parts of this thesis.

To all the wonderful people at ECAP, thank you for making these past four years so enjoyable. Your support and the welcoming atmosphere you fostered have made working at this institute a great experience.

Thank you also to all my friends and family for supporting me throughout this time and for brightening my days.

Lastly, I am grateful to all my colleagues from the H.E.S.S. collaboration across various institutes for their support and for creating a truly collaborative and enriching research environment.